We shall not cease from exploration

And the end of all our exploring

Will be to arrive where we started

And know the place for the first time.

T.S. Eliot

LEED STUDIES OF SOME ADSORPTION SYSTEMS ON THE (100) AND (110) SURFACES OF NICKEL

by

JULIA H. ONUFERKO, B.Sc.

A Thesis submitted for the degree of
Doctor of Philosophy
of the University of Warwick

December, 1978

ACKNOWLEDGEMENTS

I should like to express my sincere thanks to my supervisor, Dr. D.P. Woodruff, for his continual support and invaluable advice during the course of this work, and for his aid in running the dynamical LEED calculations. Thanks are also due to Professor A.J. Forty for the provision of facilities within the Department of Physics.

Members of the Surface Physics group, past and present, have been of great assistance at all times. In particular I should like to thank Drs. P.D. Johnson and B.D. Powell for their willing help and advice, and Dr. B.W. Holland for making available his computer programme for the dynamical LEED calculations. The excellent technical support of Mr. O.S. Simpson is acknowledged with great appreciation.

The financial support of the Science Research Council during this work is gratefully acknowledged.

I should also like to thank Jacynth McKeand for her accurate and speedy typing of this thesis.

Finally, I thank my parents for their continued support, encouragement and infinite patience during the course of this work.

ABSTRACT

A LEED study of the Ni(100) and Ni(110) surfaces has been performed using analysis of intensity-energy (I-V) spectra.

Spectra have been obtained for the clean surfaces and compare favourably with previously available data. Extensive data have been obtained for the Ni(110)(1x2)H and Ni(100)(2x2)C-p4g systems.

Qualitative adsorption studies were undertaken to investigate adsorption conditions and electron beam effects in relation to acquiring reliable I-V spectra. These include the adsorption of hydrogen and ethylene on both surfaces.

Ni(110)(1x2)H spectra compare well with previous work. A model involving pairwise distortion of the top layer of nickel atoms gives reasonable agreement between this experiment and theoretical calculations of other workers.

Symmetry requirements for the Ni(100)(2x2)C-p4g structure have led to the postulation of a model involving distortions of the nickel substrate atoms. The expansion thus caused is consistent with certain peak shifts in I-V spectra. Full dynamical calculations have been performed for various combinations of distortions and carbon positions. Encouraging agreement is obtained for such a model with carbon atoms situated in 4-fold hollows, 0.1 Å above the nickel layer.

In addition to this, I-V data from the clean surfaces and the Ni(110)(1x2)H and Ni(100)(2x2)C-p4g surfaces were used for Constant Momentum Transfer Averaging. The clean Ni(100) surface averages compare well with previous work. Ni(110) surface averages do not indicate the probable 5% surface layer contraction, and the 8½% contraction proposed by dynamical theory is not seen for the Ni(110)(1x2)H surface averages. Averages obtained from the Ni(100)(2x2)C-p4g surface do contain features indicative of top layer expansion; however, many multiple scattering features remain and peak shapes cannot be explained by purely kinematical arguments.

CONTENTS

CHAPTER ONE
INTRODUCTION

The nature of solid materials has been the subject of investigation for many years. Magnetic and electrical properties and electronic structures are now fairly well understood and techniques such as X-ray diffraction have enabled crystal structures and atomic positions to be ascertained. Similarly, the gas phase has been extensively studied, atomic and molecular scattering cross-sections and binding energies of both electrons in an atom or molecule and between atoms or molecules being well tabulated; a wide variety of techniques is used, including infra-red/ultra-violet spectroscopy.

An understanding of the nature of surfaces is very important since in any chemical reaction involving a solid it is necessarily the surface which reacts first. Problems such as catalysis are poorly understood and catalysts are chosen empirically; in electronic devices the surface and interface regions are the most important areas; bonds between dissimilar materials such as metals and insulators could be improved if there were a greater understanding of the problem involved and, of course, the case of corrosion is a perennial problem.

In order to begin to tackle these practical problems a great simplification has to be made, e.g. the catalyst in a methanol plant works, often for years, in a harsh environment of about 20 atmospheres and is subject to large numbers of contaminants; a starting point in this problem must be to examine the clean surface and gradually progress from there. An atomically clean surface can only be maintained for reasonable periods in ultra high vacuum conditions. It was only about 20 years ago that vacuum engineering techniques made surface investigations feasible; nowadays, vacua of the order of 10^{-10} to 10^{-11} τ are routinely possible.

There are many questions which need to be answered about any particular crystal surface, including:-

What is the chemical composition of the surface ?

What is the electronic structure of these surface atoms ?

What is the nature of any chemical bonding ?

What is the vibrational frequency of the atoms ?

How are these atoms arranged relative to the bulk and if an ordered overlayer is present, where do these adsorbed atoms sit relative to the substrate ?

Many techniques can be employed to investigate these problems. The chemical composition of a surface is generally determined by the use of Auger Electron Spectroscopy (AES) in which a core level of a surface atom is ionized by an incident electron, an electron from a higher level fills this hole and any surplus energy is given to an electron which escapes into the vacuum and is subsequently detected. The energy of this ejected electron is characteristic of the atom from which it originated and hence the composition of the surface can be determined (Appendix I). Other techniques (1, 2) indicating the surface chemical composition include X-ray Photoelectron Spectroscopy (XPS), Disappearance Potential Spectroscopy (DAPS) and Appearance Potential Spectroscopy (APS). In general, AES is the most widely used tool for chemical analysis since it basically involves the use of only an electron source and an electron detector and can be readily incorporated into most UHV systems.

The problem of ascertaining surface electronic energy levels is currently being tackled primarily by Ultraviolet Photoelectron Spectroscopy (UPS) in which electrons are ejected by incident photons and have energies characteristic of the states from which they originated. Electron Energy Loss Spectroscopy (EELS) is a technique which provides information about the vibrations of surface atoms.

The arrangements of atoms on a surface have been determined most successfully by the oldest surface technique, Low Energy Electron Diffraction (LEED). LEED intensity-energy spectra contain sufficient information to allow a determination of the positions of atoms on the surface.

Theoretical calculations are lengthy because of the need to include multiple scattering; nevertheless much has been achieved since full dynamical calculations started to be used. Techniques such as Reflection High Energy Electron Diffraction (RHEED) (2), Ion Scattering Spectroscopy (ISS), angular resolved UPS and angular resolved AES are currently being developed and may provide interesting alternatives.

Most of the surface structure investigations carried out to date have been on the low index faces of solids. The clean surfaces of most metals are generally just truncations of the bulk structures, the atoms on the surface having the same registry and interlayer spacing as would be expected from the bulk. Notable exceptions are the Ag(110) and Mo(100) surfaces which suffer 10% and 11.5% surface layer contraction (3) respectively, and the Au(100), Au(110), Ir (100), Pt(100) and low temperature W(100) surfaces (4-7) which are reconstructed relative to the expected bulk termination structure.

When a gas is allowed to interact with a surface, it is usually done in such a manner that the overlayer is an ordered arrangement, usually of less than a monolayer. Elemental gases have been widely used, e.g. O_2, S_2, N_2 and a generalization which can be made is that there are preferred sites for the chemisorption of atoms, these being quite often the positions where the next layer of substrate atoms would have gone. This is especially true of the (100) surface of both bcc and fcc crystals. The Ni(110)(2x1) O (8) structure is an example of where the "expected" site is not occupied by the adsorbed oxygen atom: instead it is thought to reside in the two-fold bridge position. Obviously, the less expected the adsorption site, the more interesting the system since it implies a directionality in the bonding between the adsorbate atom and the substrate and is not the most energetically preferred site from first considerations.

The two systems, Ni(100)(2x2) C-p4g and Ni(110)(1x2) H studied in detail in the present work, are of particular interest in that both adsorbates appear to cause a reconstruction of the metal substrate.

In the present work, LEED I-V spectra have been used to investigate the adsorption of hydrogen, carbon and ethylene on the (100) and (110) faces of nickel. A knowledge of how the two elements behave individually on the surface is necessary if an understanding of hydrocarbon reactions on the surface is ever to be achieved. Experimentally, the adsorption of ethylene and subsequent acquisition of I-V data is not trivial, since both the temperature of the sample and the incident electron beam are important considerations.

Chapter Two of this Thesis presents a discussion of LEED: why it is a surface technique, what it is able to say about a surface and the problems involved in extracting this information.

Chapter Three describes the experimental equipment used in this work and also the methods used to obtain and characterize the clean surfaces.

In the Fourth Chapter is presented a qualitative study of the adsorption of hydrogen, carbon and ethylene on the Ni(100) and (110) surfaces together with a review of the results of other workers. Using I-V spectra as a sensitive tool, electron beam effects are gauged; in the case of the adsorption of C_2H_4 on a cold surface where the diffuseness of the resulting LEED pattern made obtaining I-V data unfeasible, an investigation of the effect of varying the adsorption temperature is described through a study of LEED patterns. Conditions under which I-V spectra can be obtained which are consistent and characteristic of the surface structure, not of the various desorption effects, are described and provide a basis for the two systems, the Ni(110)(1x2) H and the Ni(100)(2x2) C-p4g, which are discussed in detail in Chapters Five and Six respectively. Chapter Six includes a comparison of I-V spectra with spectra obtained from full dynamical calculations.

Finally, in view of the difficult and time consuming nature of dynamical calculations, methods of reducing experimental data to leave only kinematical features are very attractive propositions. Constant Momentum Transfer Averaging (CMTA) is one such method and its application to the clean surfaces and the Ni(110)(1x2) H and Ni(100)(2x2) C-p4g systems is described in Chapter Seven.

CHAPTER ONE

REFERENCES

1. R.H. Williams, Cont. Phys., 19 (1978) 389.

2. M. Prutton, Surface Physics, Clarendon Press, Oxford (1975).

3. A. Ignatiev, F. Jona, H.D. Shih, D.W. Jepsen & P.M. Marcus, Phys. Rev. B, 11 (1975) 4787.

4. D. Wolf, H. Jagodzinski & W. Moritz, Surface Sci., 77 (1978) 265.

5. A. Ignatiev, A.V. Jones & T.N. Rhodin, Surface Sci., 30 (1972) 573.

6. H.P. Bonzel, C.R. Helms & S. Kelemen, Phys. Rev. Lett., 35 (1975) 1237.

7. M. Debe & D.A. King, Phys. Rev. Lett., 39 (1978) 708.

8. P.M. Marcus, J.E. Demuth & D.W. Jepsen, Surface Sci., 53 (1975) 501.

CHAPTER TWO
LOW ENERGY ELECTRON DIFFRACTION

In the previous chapter, LEED was stated to be a surface sensitive technique; why this is thought to be the case will now be explained, together with a description of methods developed over the years to obtain and explain LEED information.

2.1 Diffraction and Surface Sensitivity

When a beam of low energy electrons in the range 30 eV - 300 eV is incident on a surface, it undergoes very strong attenuation. If only the electrons which have been elastically scattered from the sample are collected, then this necessarily restricts them to having interacted with the first few surface layers of the sample. Attenuation of the flux of elastically scattered electrons is characteristic of the surface region. The range 30 eV - 300 eV is one for which the mean escape depth is fairly constant and surface sensitive, i.e. 2-3 atomic spacings or approximately 10 Å (Fig. 2.1) (1).

Intensities of elastically scattered electrons, even at peak values, are only about 2% of the incident current. Plasmon creation is a major loss method; before electrons can excite plasmons, they must have a minimum energy of about 15 eV and below this energy the elastic beam is much less strongly attenuated. Many electrons suffer inelastic collisions and cascade processes to form the so-called "slow peak" of the energy loss spectrum, N(E), shown in Fig. 2.2.

Electrons having undergone the small energy changes due to phonon interactions or thermal losses cannot usually be resolved from the true elastic peak; energy losses due to phonons are of the order of $\hbar$ x the phonon frequencies, or approximately kT, where k is the Boltzmann constant and T is the temperature in degrees Kelvin, i.e. < 1/10 eV.

The intermediate region of the N(E) spectrum usually consists of a slowly varying background with humps characteristic of Auger electrons (2) (see Appendix I).

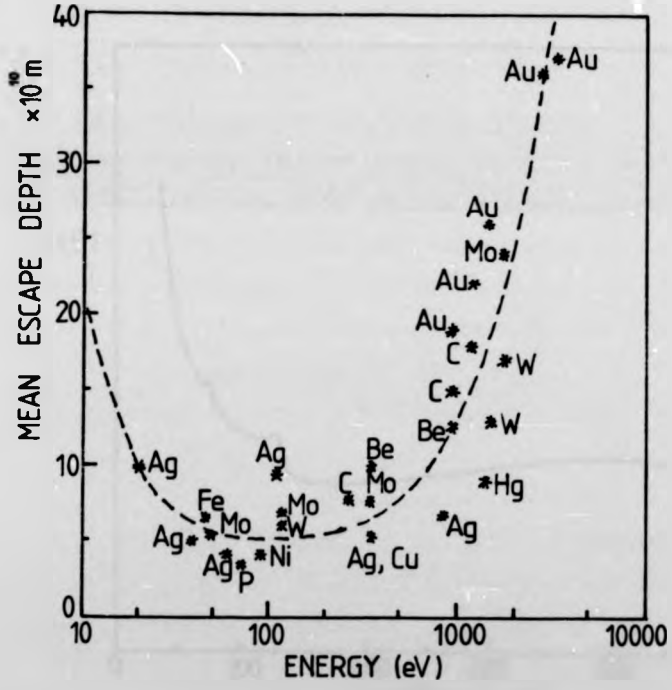

Fig. 2.1

The variation of mean escape depth with energy, (after Riviere (11)).

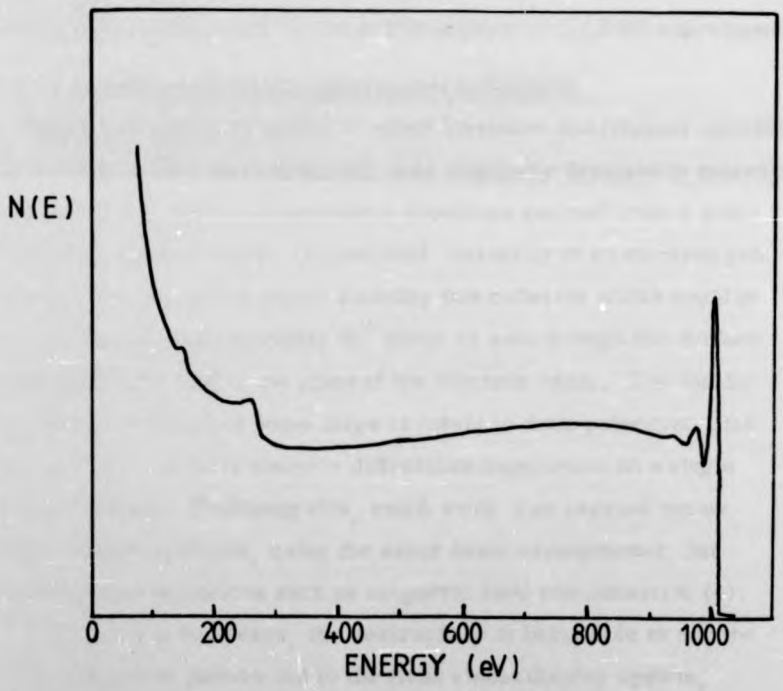

Fig. 2.2

Typical energy loss spectrum for a 1000 eV incident electron beam.

2.2 Methods of Obtaining LEED Information

Having ascertained that low energy electrons scattered elastically from a sample must contain some information about the surface region, the questions arise of how an experimental system to obtain such information might be arranged, and what some of the experimental constraints are likely to be. This section is divided into two parts: the first describes the development and present state of experimental LEED systems, while the second discusses some of the factors which must be taken into account in a LEED experiment.

2.2.1 The development of experimental techniques

The experimental chamber in which Davisson and Germer carried out the first LEED experiment (3) was originally designed to measure the angular dependence of secondary electrons emitted from a polycrystalline nickel sample. It consisted basically of an electron gun aimed at a target, and a double Faraday box collector which could be rotated through approximately 90^{o} about an axis through the surface of the specimen, and in the plane of the electron beam. The totally accidental formation of some large crystals in their polycrystalline sample led to the first electron diffraction experiment on a single crystal surface. Following this, much work was carried out on single crystal surfaces, using the same basic arrangement, but including sophistications such as magnetic field compensation (4).

Within only a few years, the desirability of being able to see the whole diffraction pattern led to the first visual display system, developed by Ehrenberg (5). This sytem employed a cylindrical, transparent fluorescent screen, which, as currents of about 10^{-12} Å had to be detectable by eye and would therefore need an electron of about 3 keV (hardly LEED energies), was itself biased at approximately 3kV. The need to filter out inelastically scattered electrons was realised and was achieved by placing a wire grid at a negative potential before the screen. In order that the diffracted electrons would travel through a field-free space before filtering, a second grid was placed in front of the first and was maintained at the same potential as the specimen.

Systems such as that of Scheibner et al. (6) employed a planar transparent screen and grid assembly, and patterns were sometimes viewed from behind the specimen. Subsequent developments in the theory of electron diffraction demanded a more precise knowledge of the variation of the intensity with either incident angle or beam energy. Display systems were improved and intensity variations measured with a spot photometer. Lander et al. (7) moved to a spherical screen and grids, which is the arrangement found in most commercially available LEED systems. An extremely complex detection system involving a rapidly rotating sample, a pulsed incident beam and a moving Faraday cup, was developed by Park and Farnsworth (8) in the early 1960's, but has not been used by other workers in view of the technical problems involved. De Bersuder (9) has developed a very elegant LEED goniometer and optics which allow almost 180^{o} of the diffraction pattern to be viewed on the screen. The use of an image intensifier in a spot photometer by Felter and Estrup (10) has made photometer measurements easier and quicker.

In the past few years, photographic techniques have been employed by some workers, and are particularly useful in the study of systems where time dependent changes occur, or where the incident electron beam causes alterations in surface conditions, as a rapid acquisition of information is possible. The photographic method used by Stair et al. (11) involves measuring the photographed intensities with a microdensitometer, but, although the time involved in acquiring the data is reduced, there is no immediate feedback of information for the experimentalist. Also, only relative beam intensities can be obtained. These are also the problems encountered in the method employed by Frost et al. (12) where the negatives are scanned by a computer-controlled videcon camera. Heilmann et al. (13) use a standard TV system to view the fluorescent screen directly, and a processing computer which provides instant feedback during the experiment and takes 0.5 s or less to obtain one point in the I-V spectrum for one beam.

This section has described briefly how LEED systems have developed. At present, spherical grid display systems are the usual type of equipment found, utilising either a Faraday cup, a spot photometer, or some type of photographic technique to collect I-V data.

The basic requirements of a LEED system are to be capable of acquiring reliable intensity information about the diffracted beams and to ascertain the geometrical structure of the surface. The ability to measure the intensity of beams over a wide angle is desirable, as this allows non-specular beams at or near emergence to be monitored. In addition to this, there must obviously be in situ specimen preparation facilities, surface and vacuum contamination monitoring capabilities and a vacuum sufficiently good to ensure that the specimen remains clean for a reasonable length of time. Of course, the addition of a specimen cooling stage enables a greater variety of surface investigation experiments to be performed and reduces thermal diffuse scattering. For experiments involving the reaction or adsorption of gases such as hydrocarbons on surfaces, it is especially important to minimise the time of interaction of the electron beam with the surface and so any refinement which might allow a more rapid acquisition of data is highly desirable.

2.2.2 Experimental constraints

In addition to the need mentioned above to speed the collection of LEED data, other basic experimental constraints arise.

(a) Coherence .- The energy spread of the electron beam and its angular divergence limit the distance over which the atoms of a surface can be thought of as having a plane wave incident on them. This distance, known as the coherence length, defines the maximum distance over which a surface structure can be determined (14).

For an incident beam of wavevector $\underline{k}$

$$E = \frac{\hbar^2 k^2}{2m}$$

where m = mass of electron
E = electron energy
$\hbar$ = Planck's constant/2π

giving the spread

$$\Delta k = \frac{k \Delta E}{2E}$$

This section has described briefly how LEED systems have developed. At present, spherical grid display systems are the usual type of equipment found, utilising either a Faraday cup, a spot photometer, or some type of photographic technique to collect I-V data.

The basic requirements of a LEED system are to be capable of acquiring reliable intensity information about the diffracted beams and to ascertain the geometrical structure of the surface. The ability to measure the intensity of beams over a wide angle is desirable, as this allows non-specular beams at or near emergence to be monitored. In addition to this, there must obviously be in situ specimen preparation facilities, surface and vacuum contamination monitoring capabilities and a vacuum sufficiently good to ensure that the specimen remains clean for a reasonable length of time. Of course, the addition of a specimen cooling stage enables a greater variety of surface investigation experiments to be performed and reduces thermal diffuse scattering. For experiments involving the reaction or adsorption of gases such as hydrocarbons on surfaces, it is especially important to minimise the time of interaction of the electron beam with the surface and so any refinement which might allow a more rapid acquisition of data is highly desirable.

2.2.2 Experimental constraints

In addition to the need mentioned above to speed the collection of LEED data, other basic experimental constraints arise.

(a) Coherence .- The energy spread of the electron beam and its angular divergence limit the distance over which the atoms of a surface can be thought of as having a plane wave incident on them. This distance, known as the coherence length, defines the maximum distance over which a surface structure can be determined (14).

For an incident beam of wavevector $\underline{k}$

$$E = \frac{\hbar^2 k^2}{2m}$$

where m = mass of electron
E = electron energy
$\hbar$ = Planck's constant/2π

giving the spread

$$\Delta k = \frac{k \Delta E}{2E}$$

In the case of normal incidence, if β is the half-angle subtended at the crystal surface by the source, the spread in the surface component of $\underline{k}$ due to divergence is approximately $2\underline{k}\beta$.

Combining the uncertainties leads to the uncertainty in the component of $\underline{k}$ parallel to the surface.

$$\Delta k_{\parallel} \simeq 2[(k\beta)^2 + (\Delta k\beta)^2]^{\frac{1}{2}}$$

$$\simeq 2\beta \frac{2\pi}{\lambda}[1 + (\frac{\Delta E}{2E})^2]^{\frac{1}{2}}$$

Using $\Delta X . \Delta k_{\parallel} = 2\pi$ where ΔX is the diameter of the coherence zone

$$\Delta X \simeq \frac{\lambda}{2\beta(1 + (\frac{\Delta E}{2E})^2)^{\frac{1}{2}}}$$

i.e. no area larger than $\simeq (\Delta X)^2$ can contribute coherently to the diffraction pattern.

Assuming $\Delta E \simeq 3kT/2 \simeq 0.2$ eV where T = filament temperature $\simeq 1100^{\circ}$ K

and $\beta \simeq 0.005$ radians,

for a beam of energy E = 150 eV

$$\Delta X \simeq 100 \text{ Å}$$

Disorder in the crystal surface gives rise to beam broadening. Steps, kinks and other defects cause electrons to be scattered into the diffuse background (15). Disorder due to out of phase domains may cause the diffracted beams to be split or enlarged (16).

When overlayer structures are considered, care must be given to the question of coherence since the periodicity of the adsorbate relative to the substrate could be of the order of the coherence length.

(b) Temperature effects and the Debye-Waller factor.- An important consideration is the effect of temperature on the diffracted beams. When the temperature of a specimen is raised, the intensities of the beams decrease and there is a general increase in background intensity, although the structure of an intensity-energy spectrum is usually only very slightly modified.

Atomic vibration periods are usually larger by a factor of about 10^4 than the interaction time between an atom and an incident electron. This means that the Born-Oppenheimer, or adiabatic approximation, which considers atoms to be stationary during the diffraction time, is reasonably valid. It is also assumed that there is zero correlation of displacements. However, the intensity collection time is such that an average over atomic displacements is obtained.

The intensity I of a beam may be defined by

$$I = I_o e^{-2W} + \text{phonon scattering}$$

where I_o is the scattered intensity from the rigid lattice and e^{-2W} is the Debye-Waller factor.

For elemental crystals

$$2W = 4\pi^2(\underline{k} - \underline{k}')^2 \langle u^2 \rangle$$

where $\langle u^2 \rangle$ is the mean square displacement of an atom in the direction of the diffraction vector, and $\underline{k}$ and $\underline{k}'$ are the incident and diffracted wavevectors respectively.

In the high temperature limit

$$2W = 3(\underline{k} - \underline{k}')^2 \frac{hT}{mk_B\theta_D^2}$$

θ_D is the Debye temperature.

The inclusion of this factor implies that not all of the incident electrons are scattered coherently into well defined beams, but that some go to form the thermal diffuse background.

Measurement of the elastically diffracted beam should ideally not include such contributions; most detection systems cannot resolve the small change in energy caused by losses to phonons. A compromise has to be made so that the collector aperture is large enough to include all true elastic components but at the same time small enough to exclude most of the thermal diffuse scattering contributions. To minimise thermal diffuse scattering contributions at higher energies, the collection aperture should be reduced further, but a varying aperture on a Faraday cup collector is not easily obtainable; however, in most cases the diffraction spots remain reasonably constant in size over the range 30 - 300 eV, and the need to alter the collection aperture does not arise.

2.3 LEED and Surface Crystallography

LEED can provide surface information in two main ways:

(i) the diffracted electrons form a pattern which contains information about the surface net size.

(ii) the diffracted beams vary both in position and intensity as the incident beam energy is varied. Intensity-energy, or I-V plots, contain information about the positions of atoms within the unit cell.

In this section the surface crystallographic information, i.e. the diffraction pattern, will be discussed.

An electron beam of energy E eV has an associated wavelength λ given in angstroms by

$$\lambda = \left(\frac{150.4}{E} \right)^{\frac{1}{2}}$$

If the wavelength is comparable to the atomic spacings, then elastic scattering by the periodic array of atoms gives rise to diffraction.

An X-ray diffraction pattern (formed by the Laue back-reflection of a polychromatic beam) has similarities to a LEED pattern as regards the spatial distribution of diffraction spots. The major difference is, of course, that an X-ray beam samples the bulk of the crystal and diffracted beams contain information about the 3-D nature of the sample; LEED patterns are a display of the 2-D nature of the surface. In two dimensions, the terms lattice and cell are replaced by net and mesh respectively.

The Ewald sphere construction is used to interpret the formation of X-ray diffraction patterns and the idea may be useful in helping to describe the formation of LEED beams. For LEED, the 3-D reciprocal lattice points become rods perpendicular to the crystal surface and passing through points corresponding to the surface atoms (Fig. 2.3). For the X-ray case, the probability for a given wavelength that a reciprocal lattice point lies on the Ewald sphere is low, so a polychromatic beam is used. For the 2-D case, there is always an intersection of the sphere with a reciprocal lattice rod if the wavelength is of the order of the lattice spacing, and so a monochromatic beam is used. If the incident beam energy is varied, it can be seen that this merely alters where the Ewald sphere cuts the rods, and hence alters the magnification of the projection.

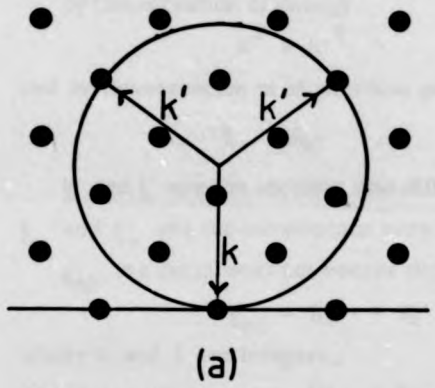

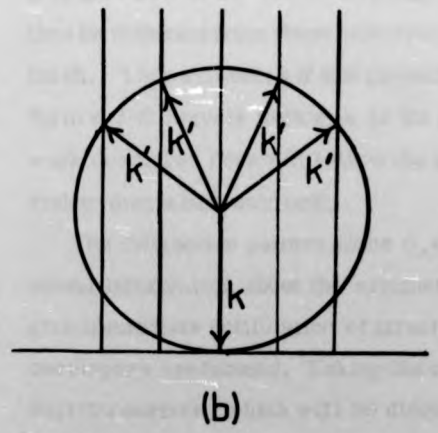

Fig. 2.3

(a) the Ewald Sphere Construction for X-ray scattering

(b) the Ewald Sphere Construction applied to LEED

If the 2-D unit mesh is described by the vectors $\underline{a}$ and $\underline{b}$ lying in the plane of the surface, then the reciprocal net has the unit vectors $\underline{a}^*$ and $\underline{b}^*$ (see Appendix II).

In two dimensions there are five kinds of Bravais lattice (Fig. 2.4). Crystallographic conventions regarding such lattices are described by Wood (17) and in the International Tables for X-ray Crystallography (18).

By Conservation of Energy

$$k^2 = k'^2$$

and by Conservation of Momentum parallel to the surface

$$\underline{k}'_{\parallel} = \underline{k}_{\parallel} + \underline{g}_{hl} \qquad \text{- 2-D Bloch Theorem}$$

$\underline{k}$ and $\underline{k}'$ are the incident and diffracted wavevectors respectively. $\underline{k}_{\parallel}$ and $\underline{k}'_{\parallel}$ are the components parallel to the surface.

$\underline{g}_{hl}$ is a reciprocal net vector defined by

$$\underline{g}_{hl} = h\underline{a}^* + l\underline{b}^*$$

where h and l are integers.

These are illustrated in Fig. 2.5.

One confusion in beam nomenclature is caused by the discrepancy in unit mesh definitions. The bulk unit cell, if applied to a surface, may give rise to so-called "missing spots" and indexing of beams will then be different from those obtained by defining a purely surface unit mesh. This will occur if the projection of the bulk unit cell does not form a 2-D Bravais lattice as is the case for the bcc crystal. All work described here will follow the convention of using a surface mesh rather than a bulk unit cell.

The diffraction pattern alone (i.e. the location of beams) gives useful information about the symmetry of the real surface and can give immediate notification of structure changes, e.g. when ordered overlayers are formed. Taking the case of hydrogen adsorption on the Ni(110) surface, which will be discussed in detail in Chapter Five, extra spots are formed mid-way along the shorter reciprocal lattice vector (Fig. 2.6). This indicates that for some reason the period of the surface in the <100> direction has doubled. The structure is written as the Ni(110)(1x2) H structure.

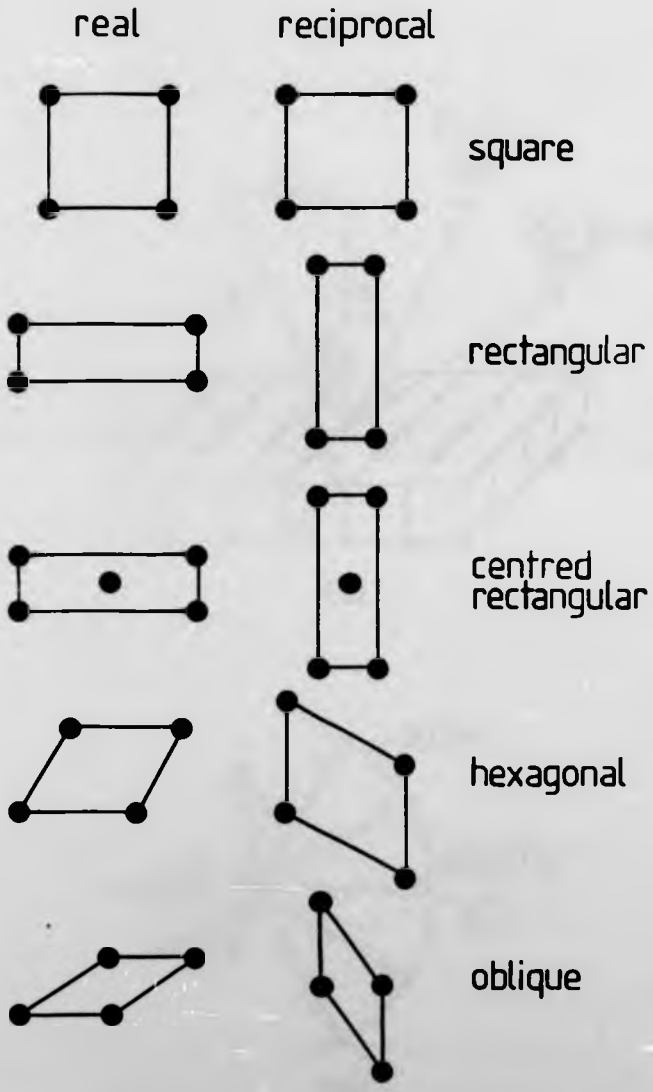

Fig. 2.4

The five 2-D Bravais lattices

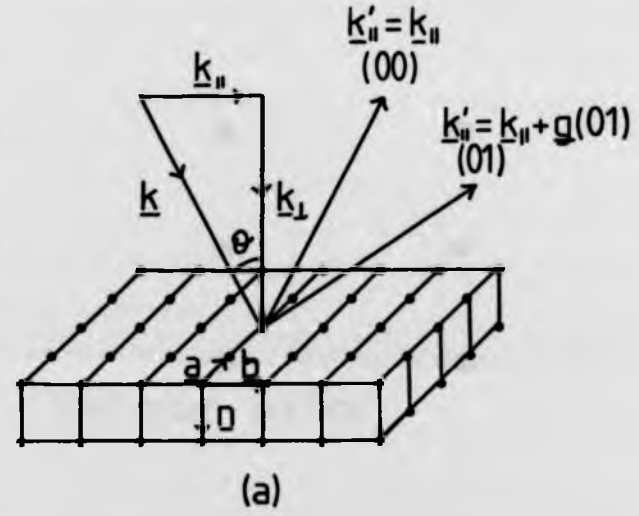

(a)

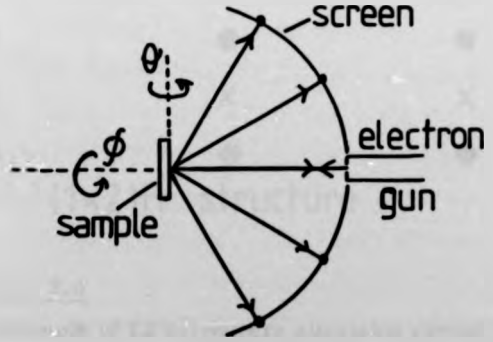

(b)

Fig. 2.5

Definition of scattering geometry

(a) crystal surface

(b) experimental arrangement

NI(110) DIFFRACTION PATTERNS

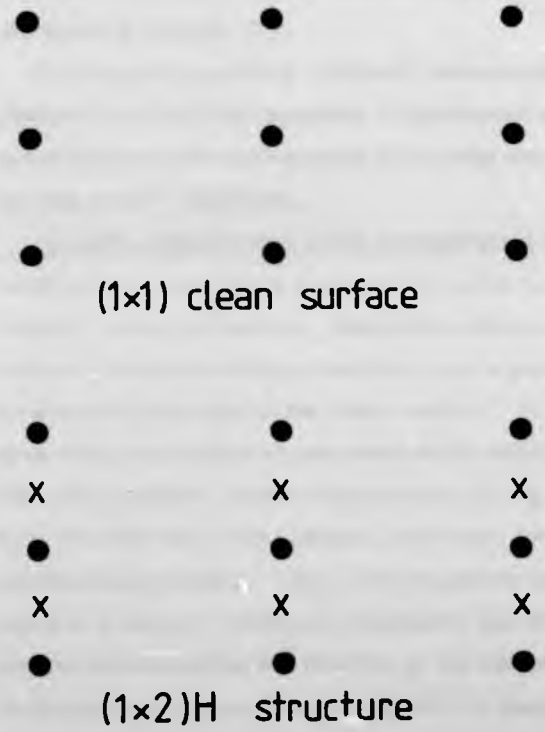

Fig. 2.6

Example of LEED pattern alteration caused by adsorption (Hydrogen on NI(110))

The symmetry of a particular diffraction pattern can occasionally be a useful clue as to the possible surface structures. The Ni(100) (2x2) C system, which is studied in detail in this thesis, has a LEED pattern which exhibits p4g symmetry by virtue of the absence of certain beams. These symmetry arguments are described in detail in Appendix II and I-V spectra for this system are presented and discussed in Chapter Six.

A diffraction pattern is relatively insensitive to many structure changes and also to the presence of disordered adsorbates. Ordered adsorbates are also undetectable by viewing the pattern if they happen to form a (1x1) overlayer.

An added complication in the interpretation of LEED patterns for overlayers is sometimes encountered by the existence of equivalent islands, known as domains. Equivalent domains occur on a surface when an adsorbate forms a structure with a unit mesh less symmetrical than that of the clean surface. An example of such a case is the adsorption of potassium on the Ni(100) surface. The diffraction pattern, shown schematically in Fig. 2.7 (c), might at first be taken for a (4x4) pattern; however, the $(\frac{1}{4}\ \frac{1}{4})$ type spots are systematically absent. This can be explained by the presence of two types of structure which are equivalent and differ in that the unit meshes are rotated by 90° relative to one another. A possible structure could be composed of domains of each of the two structures shown in Fig. 2.7 (d) and (e). Domain effects mean that the identification of the surface net is by no means trivial, and that the LEED pattern displays only the substrate symmetry and not that of the overlayer.

Only the size and shape of the unit mesh are obtainable from the diffraction pattern alone. The positions of adsorbate atoms relative to the substrate, or the spacing of the top layer of atoms relative to the bulk is information which is contained in the intensities of the beams, measured as functions of energy or angle of incidence. Intensity analyses will be discussed in the following sections of this Chapter.

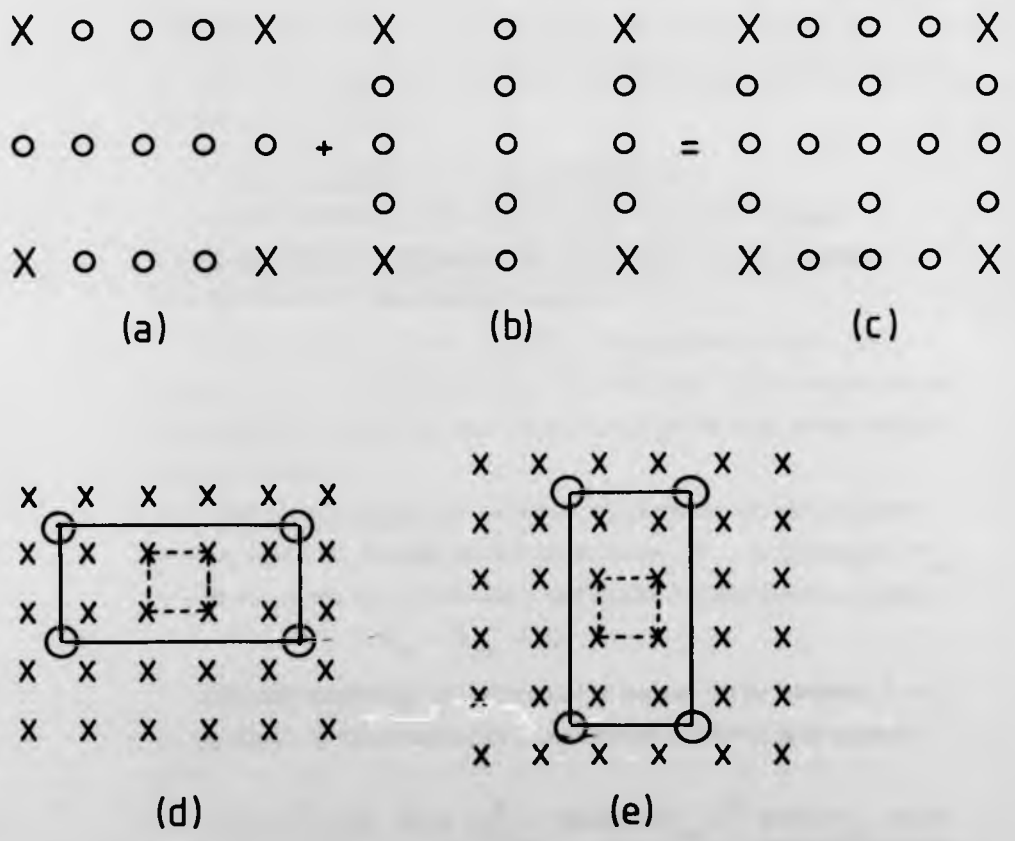

Fig. 2.7

Possible domains formed by an adsorbate on an f.c.c. (100) surface. (a) and (b) are the (4x2) and (2x4) domains which cause the observed LEED pattern (c).
(d) and (e) are the corresponding crystal surfaces (adsorbate atoms (circles) have been arbitrarily placed in the 4-fold position).

2.4 The Interpretation of LEED Beam Intensities

Low energy electrons penetrate sufficiently far into a crystal to be influenced by the periodicity normal to the surface. In a simple view considering the Ewald sphere construction of Fig. 2.3, the intensity varies along reciprocal lattice rods with maxima at or near positions which would correspond to 3-D lattice points. However, the problem is drastically complicated through the occurrence of multiple scattering of the electrons, and several parameters must be included in any models.

2.4.1 Physical models for LEED calculations

Before describing some of the methods used to calculate theoretical LEED I-V spectra, the basic model and parameters thought to be valid will be described.

When an electron enters a crystal, it undergoes various interactions which include interactions with electrons in the conduction or valence bands, with ion-cores and at the potential step at the surface-vacuum boundary.

(a) The optical potential.- When an electron enters the potential well of a crystal, it experiences an increase, V_o, in its energy. V_o is defined as the optical potential and can be divided into two parts:

$$V_o = V_{or} + i\beta$$

Inelastic scattering is considered in terms of the lifetime τ of an electron. If the intensity of a wavefunction decays with time as $e^{2\beta t}$,

then $\beta = -\frac{1}{2\tau}$ or $= \frac{\hbar}{m\lambda_{ee}}[2m(E + V_{or})]^{\frac{1}{2}}$ where λ_{ee} is the inelastic collision damping length.

Attenuation of elastically scattered beams is thus simulated by the addition of a constant imaginary potential.

The potential well itself is taken to have a depth V_{or}, which is the spatially averaged potential between the atoms in the crystal referred to the vacuum, and is known as the inner potential. V_{or} can be calculated and shown to be energy dependent. One of the most successful procedures for its determination has been devised by Jepsen et al. (19), whereby a calculation of LEED spectra is carried out for normal incidence using

$V_{or} = E_F + \varphi$, where E_F is the Fermi energy,
φ is the work function.

The resulting spectra are compared with experimental data and a value of V_o obtained by shifting the energy scale until a good fit is obtained. This value of V_{or} is then used for all other calculations off normal incidence, since V_{or} affects the refraction of the electrons at the surface-vacuum boundary. Energy dependent inner potentials have been used to improve the fit of curves (20).

(b) Ion-core scattering.- Electrons are scattered by the ion-core potentials which are composed of potentials due to the nucleus and the core electrons. There is also an exchange potential which exists between the incident electrons and those core electrons which have parallel spin.

For many materials the problem of adequately describing the ion-core potential can be simplified by certain approximations. Charge densities at atoms are usually calculated by a linear superposition of charge densities (21). Exchange and correlation effects are included by the use of a Hartree-Fock approximation or by using the simplification suggested by Slater (22).

$$V_{ex}(\underline{r}) \simeq -3\left[-\frac{3\rho(\underline{r})}{8\pi}\right]^{1/3}$$

where ρ is the uniform electron density.

The differential cross-section for elastic scattering $\frac{d\sigma}{d\Omega}$ caused by the ion-cores is usually described in terms of phase shifts δ_l.

Using $f(\theta) = (2ik)^{-1} \sum_l (2l + 1)(e^{2i\delta_l} - 1) P_l \cos\theta$

where $f(\theta)$ is the atomic scattering factor and $P_l \cos\theta$ is the Legendre polynomial, and

$$k = \left[\frac{2m(E + V_o)}{\hbar^2}\right]^{\frac{1}{2}}$$

then $$\frac{d\sigma}{d\Omega} = |f(\theta)|^2$$

(c) The Muffin-Tin model.- Near the centre of atoms, at the ion-cores, the potential is given by $-\frac{Ze^2}{r}$ where Z is the atomic number.

Further out, the potential is weaker and it is reasonably accurate to describe the situation by a spherically symmetric potential, simulated by drawing the largest possible non-overlapping spheres about each nucleus. A further approximation proposes that the potential outside these spheres is constant. This model is known as the "muffin-tin" approximation. It has been widely used in band structure calculations and has proved very successful for many materials.

A physical model incorporating muffin-tins is shown in Fig. 2.8, following the scheme of Marcus et al. (23); the structural parameters for the bulk and adsorbate spacings are labelled d_1 and d_o respectively.

2.4.2 Kinematic theory

X-ray diffraction intensities have been successfully predicted by the application of a kinematic theory, and this type of approach has also been used to try to predict LEED intensities.

Applying the Bragg condition

$$(\underline{k} - \underline{k}'). \underline{d} = 2\pi n$$

where $\underline{d}$ is the displacement from one plane to the next

and n is an integer,

the positions of Bragg peaks in I-V spectra can be calculated, as can the energy of emergence of non-specular beams (see Appendix III).

The basic assumption of kinematic theory is that scattering of the incident electrons by ion-cores is weak, and that we can neglect electrons which have been scattered more than once.

The scattered amplitude A is given by

$$A = A_o \sum_j f_j(\theta, E) e^{i\underline{S}.\underline{r}_j}$$

where $\underline{S}$ is the scattering vector

$\underline{r}_j$ is the position of the j^{th} atom

f_j are the atomic scattering factors.

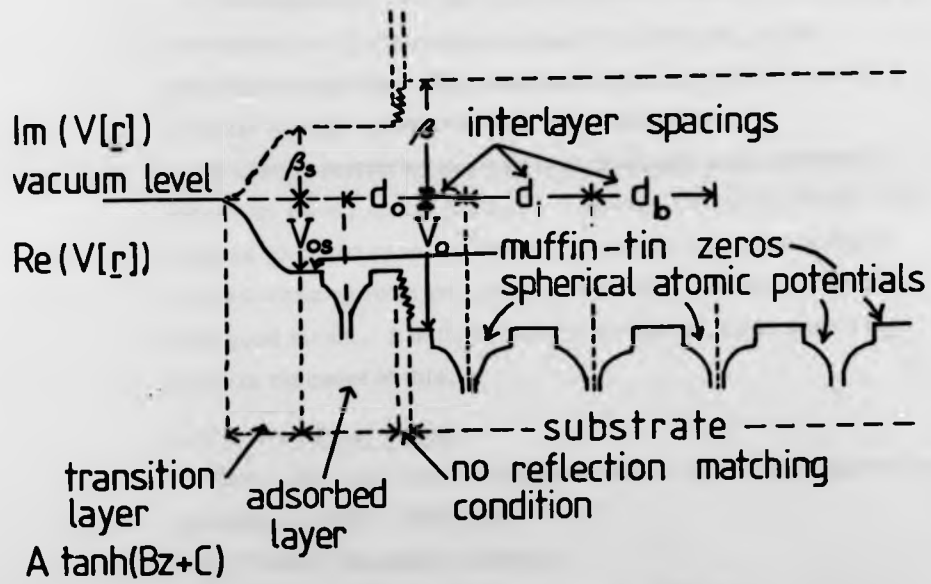

Fig. 2.8

The Muffin-Tin Model (after Marcus et al. (23))

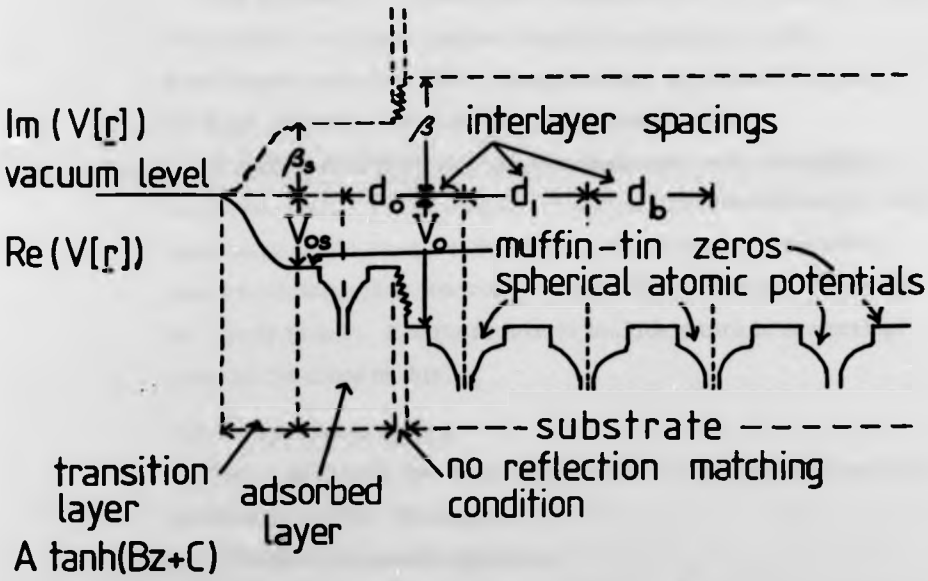

Fig. 2.8

The Muffin-Tin Model (after Marcus et al. (23))

The intensity is given by

$$I = AA^* = I_o \sum_{jk} f_j(\theta, E) f_k^*(\theta, E) e^{i\underline{S}.(\underline{r}_j - \underline{r}_k)}$$

This equation predicts a series of delta functions located at the Bragg conditions. Comparison with experimental LEED spectra not surprisingly shows poor correlation. Examination of the azimuthal dependence of experimental spectra reveals a noticeable change which is not accounted for by kinematic theory.

The attenuation of elastically scattered beams is simulated by the addition of β, the constant imaginary potential, to the Schrödinger equation. This absorption has the effect of reducing the delta function intensities and broadening peaks.

If elastic scattering is weak in comparison with absorption, kinematic theory should predict I-V spectra reasonably well. This appears to be the case for xenon (24) but for transition metals, where scattering from ion-cores is not weak, kinematic theory is not a good match. It is the failure to include multiple scattering which is the cause of this.

2.4.3 Dynamical theory

There have been two basic approaches to the multiple scattering problem in LEED. These are:

(a) The Band Structure Approach.

(b) The Multiple Scattering Approach.

It must be emphasised here that the distinction is not really clear and the apparent classification has grown up merely on historical grounds, as will be obvious from the following sections.

(a) The Band Structure Method.- The earliest attempts to solve the problem using this technique were made by Bethe (25) and Morse (26) and later by Boudreaux and Heine (27). The basic idea of this method is to consider the crystal as an array of scatterers; the wavefunctions of electrons in bulk crystals are known (Bloch waves) as are the wavefunctions of electrons in vacuo (plane waves), so a smooth matching of these wavefunctions at the interface should be possible.

In this model, Bragg peaks are predicted by the energies of the band gaps. Usually, more than one Bloch wave is excited in the crystal by the incident beam and any one of these Bloch waves may undergo Bragg reflection and give rise to the multiple scattering features found in experimental LEED spectra. Secondary Bragg peaks are formed when an excited Bloch wave comes close in the band structure diagram to another Bloch wave by a form of coupling through which a beam may show a peak where another beam peaks. The surface band structure must be calculated; this is more difficult than the bulk band structure calculation because of the need to include evanescent waves.

There are two methods of calculating Bloch waves which have been widely used. One is the layer method as used by Marcus and Jepsen (28, 42) and the other is the pseudopotential method.

The pseudopotential method is based on the following argument that LEED reflectivities can be found without knowing the wave-functions inside the ion-cores. Only the waves outside the ion-cores need to be calculated since electrons are never actually observed within the ion-cores. Therefore a potential can be chosen for the ion-cores which is manageable from the point of view of the calculation with the constraint only that the situation outside the ion-cores remains well represented. This chosen potential is known as the pseudopotential and has been widely used by, for example, Capart (29), Strozier and Jones (30) and Pendry and Capart (31).

The layer method is a way of considering the crystal whereby wave amplitudes between pairs of layers differ only by a constant factor from those between the previous pair of layers and involves numerical techniques of generating Bloch waves from an eigenvalue equation. The crystal is considered to be composed of a series of layers parallel to the surface, each layer being composed of many ion-cores, and being periodic in directions parallel to the surface. Each layer deeper inside the crystal is displaced relative to its neighbour by a certain amount.

The layer method appears to be a rather more simple and speedy calculation. The pseudopotential scheme is reasonable when symmetry conditions of normal incidence can simplify and reduce the size of the matrices involved. The layer method especially is equivalent to multiple scattering since it uses multiple scattering techniques. It is a prime example of the unreal division into band structure and multiple scattering approaches.

(b) The Multiple Scattering Approach.- As in (a), since an incident low energy electron is likely to undergo inelastic collisions, these must be included in any cross-section by considering the wave function of the incident electron to be distorted by the electron-electron interactions as well as undergoing multiple elastic scattering by ion-cores. Much work has gone into this theory, including that by Laramore and Duke (32) and Duke and Tucker (33).

A model based on isotropic (s-wave) scattering was used by McRae (34) based on the earlier work of Lax (35). In this model, ion-cores are approximated as s-wave scatterers and much of the early work was carried out using a single s-wave phase shift. This tended to give spectra in which scattered intensities were usually too weak and multiple scattering was not sufficiently represented. Holland et al. (36) suggested that the s-wave phase shift would lead to stronger scattering if it were made complex, since this would effectively mean that ion-cores would become radiators as well as scatterers. Although this modification provides some improvement, serious discrepancies still remain between theory and experiment.

Beeby (37) formulated a scheme of multiple scattering using more phase shifts. Tait et al. (38) and Tong and Rhodin (39) have applied Beeby's multiple scattering approach and reduced it to a third order perturbation.

Pendry (40) has developed a scheme by which backscattered contributions are included to third order by a perturbation method. This approach is called the Renormalised Forward Scattering (RFS)

method. It involves solving exactly the forward scattering part of the scattering expansion and, assuming that backscattering is weak, neglecting it altogether. It has proved reliable above ~ 10 eV for a number of metal surface calculations; it works for strong back-scattering cases if damping is strong.

Holland and Zimmer (41) have devised a perturbation method known as the Reverse Scattering (RS) method. This method can cope with situations where RFS fails, *e.g.* closely spaced layers and co-planar sublayers.

The dynamical calculations applied by Demuth *et al.* (22, 42) have proved highly successful, especially for the low index faces of nickel, and their method will be briefly discussed here. This is basically a band structure approach incorporating the Korringa-Kohn-Rostoker (43) (KKR) method which implements the requirement of Bloch periodicity by using a Green's function which can be thought of as representing the propagation of waves in a uniform potential between the atoms and incorporates the ideas of multiple scattering by a spherical wave representation. Following the method of Kambe (44), spherical waves are converted to plane waves at the boundary of a layer, and thereby multiple scattering information contained in a crystal wave-function is transferred from one layer to another. At the crystal-vacuum boundary, the wave equations are matched. A "no-reflection" boundary condition stipulates that no incident electrons having sufficient energy to get over the potential barrier V_o are reflected, and those electrons with too small an energy are completely absorbed. From this description, it is obvious that many of the separate methods have been combined - the layer method, wave-matching and multiple scattering.

It is clear from the preceding sections that the most successful correlations of theory with experiment have been obtained with a tremendous amount of computing effort and time. The number of phase shifts needed to provide an accurate description of scattering properties increases as the energy is increased. At higher energies, the computing time is also lengthened by the fact that the number of beams involved is greater and so all the interactions between beams must be included.

Kinematic theories are substantially easier and faster to calculate and it would be a major simplification if single scattering features in LEED spectra could be extracted from the tangle of multiple scattering information.

Several suggestions have been made as methods of extracting the kinematic features from experimental data. These will now be discussed.

2.4.4 The extraction of kinematic information by data reduction

The principal three methods which have been tried are

(a) Fourier Transform Methods.

(b) Energy Averaging.

(c) Constant Momentum Transfer Averaging.

These techniques, together with a discussion of the problems involved, are described by Woodruff (45), but a brief description will be mentioned here.

The major problem in all three techniques is one which can be described as a phase problem. In the case of X-ray diffraction, the atomic scattering factors f_j are real, and the phase of the geometrical structure factor is influenced only by the positions of scatterers. In the LEED situation, the scattering factors are complex and modified by multiple scattering effects. This means that peak intensity positions are not solely dictated by the positions of scatterers. The case of an adsorbate on a surface introduces even more severe phase problems since the f_j are different for different elements.

(a) Fourier Transform Methods.- An application of Fourier transform methods as used in X-ray diffraction has been made by Clarke et al. (46) and Buchholtz et al. (47). In principle, this method gives a direct means of structural analysis rather than a comparative one, but has not been successful. This failure is due mainly to the fact that Fourier transform methods assume that atomic scattering factors are real and have a constant phase factor. It is not certain whether Fourier transforms actually remove multiple scattering effects and some other method of doing this and removing the phase

problem could, perhaps, be used in conjunction with the transform method. Fourier transform techniques seem, so far, to be totally inapplicable to adsorbate structures for the phase problem mentioned above and some method of reducing this problem (48) must certainly be incorporated before any reliable analyses can be performed.

(b) Energy Averaging.- (Tucker and Duke (49)). The fundamental idea behind the energy averaging method is the thought that, in the limit of strong inelastic damping, multiple scattering between an overlayer and the substrate redistributes the kinematic intensity (as a function of incident beam energy) within a given scattered beam rather than from one beam to another. Energy averaging should therefore be able to supply information about adsorbate structures, but has not proved fruitful to date. All information about the registry of the adsorbate relative to the substrate is thrown away by this type of averaging.

(c) Constant Momentum Transfer Averaging (CMTA).- This is a technique which has been proposed by Lagally, Ngoc and Webb (50). The basic idea is that single scattering intensities are dependent only on the diffraction vector $\underline{S}$, whereas multiple scattering contributes intensities dependent explicitly on $\underline{k}$ and $\underline{k}'$. Therefore, if data taken over a range of $\underline{k}$ and $\underline{k}'$ but of fixed $\underline{S}$ are averaged, the kinematic part should remain unchanged and the multiple scattering features be eliminated. Some analyses have revealed extremely kinematic spectra (Ni(111) (50), Ag(111) (50), Cu(111) (51)) and several more analyses of other surfaces have resulted in less kinematic spectra (52). A more detailed description of CMTA is presented in Chapter Seven, together with the results from analyses carried out on the Ni(100) and Ni(110) surfaces.

CHAPTER TWO
REFERENCES

1. J.C. Riviere, Cont. Phys., 14 (1973) 513.
2. C.C. Chang, Surface Sci., 25 (1971) 53.
3. C.J. Davisson & L.H. Germer, Phys. Rev., 30 (1927) 705.
4. H.E. Farnsworth, Phys. Rev., 34 (1929) 679.
5. W. Ehrenberg, Phil. Mag., 18 (1934) 878.
6. E.J. Scheibner, L.H. Germer & C.D. Hartman, Rev. Sci. Instr., 31 (1960) 112.
7. J.J. Lander, J. Morrison & F. Unterwald, Rev. Sci. Instr., 33, (1962) 782.
8. R.L. Park & H.E. Farnsworth, Rev. Sci. Instr., 35 (1964) 1592.
9. L. de Bersuder, Rev. Sci. Instr., 45 (1974) 1569.
10. T.E. Felter & P.J. Estrup, Rev. Sci. Instr., 47 (1976) 158.
11. P.C. Stair, T.J. Kaminska, L.L. Kesmodel & G.A. Somorjai, Phys. Rev. B, 11 (1975) 623.
12. D.C. Frost, K.R. Mitchell, F.R. Shepherd & P.R. Watson, J. Vac. Sci. & Technol., 13 (1976) 1196.
13. P. Hellmann, E. Land, K. Heinz & K. Muller, Appl. Phys., 9 (1976) 247.
14. R.D. Heidenreich, ' Fundamentals of transmission electron microscopy', Wiley, New York (1964).
15. R.J. Reid, Surface Sci., 29 (1972) 623.
16. J.B. Pendry, 'Low energy electron diffraction', Academic Press, London (1974) 236.
17. E.A. Wood, J. Appl. Phys., 35 (1964) 1306.
18. International Tables for X-ray Crystallography, Kynoch Press, Birmingham (1965).
19. D.W. Jepsen, P.M. Marcus & F. Jona, Phys. Rev. Lett., 26 (1971) 1365.
20. D.W. Jepsen, P.M. Marcus & F. Jona, Phys. Rev. B, 5 (1972) 3933.
21. J.B. Pendry, Institute of Physics Meeting, Imperial College (May, 1974).

CHAPTER TWO
REFERENCES

1. J.C. Riviere, Cont. Phys., 14 (1973) 513.
2. C.C. Chang, Surface Sci., 25 (1971) 53.
3. C.J. Davisson & L.H. Germer, Phys. Rev., 30 (1927) 705.
4. H.E. Farnsworth, Phys. Rev., 34 (1929) 679.
5. W. Ehrenberg, Phil. Mag., 18 (1934) 878.
6. E.J. Scheibner, L.H. Germer & C.D. Hartman, Rev. Sci. Instr., 31 (1960) 112.
7. J.J. Lander, J. Morrison & F. Unterwald, Rev. Sci. Instr., 33, (1962) 782.
8. R.L. Park & H.E. Farnsworth, Rev. Sci. Instr., 35 (1964) 1592.
9. L. de Bersuder, Rev. Sci. Instr., 45 (1974) 1569.
10. T.E. Felter & P.J. Estrup, Rev. Sci. Instr., 47 (1976) 158.
11. P.C. Stair, T.J. Kaminska, L.L. Kesmodel & G.A. Somorjai, Phys. Rev. B, 11 (1975) 623.
12. D.C. Frost, K.R. Mitchell, F.R. Shepherd & P.R. Watson, J. Vac. Sci. & Technol., 13 (1976) 1196.
13. P. Hellmann, E. Land, K. Heinz & K. Muller, Appl. Phys., 9 (1976) 247.
14. R.D. Heidenreich, ' Fundamentals of transmission electron microscopy', Wiley, New York (1964).
15. R.J. Reid, Surface Sci., 29 (1972) 623.
16. J.B. Pendry, 'Low energy electron diffraction', Academic Press, London (1974) 236.
17. E.A. Wood, J. Appl. Phys., 35 (1964) 1306.
18. International Tables for X-ray Crystallography, Kynoch Press, Birmingham (1965).
19. D.W. Jepsen, P.M. Marcus & F. Jona, Phys. Rev. Lett., 26 (1971) 1365.
20. D.W. Jepsen, P.M. Marcus & F. Jona, Phys. Rev. B, 5 (1972) 3933.
21. J.B. Pendry, Institute of Physics Meeting, Imperial College (May, 1974).

22. J.C. Slater, 'Insulators, semiconductors and metals', McGraw Hill, New York (1967).

23. P.M. Marcus, J.E. Demuth & D.W. Jepsen, Surface Sci., 53 (1975) 501.

24. A. Ignatjev , J.B. Pendry & T.N. Rhodin, Phys. Rev. Lett., 26 (1971) 189.

25. H. Bethe, Annalen der Physik, 87 (1928) 55.

26. P.M. Morse, Phys. Rev., 35 (1930) 1310.

27. D.S. Boudreaux & V. Heine, Surface Sci., 8 (1967) 426.

28. P.M. Marcus & D.W. Jepsen, Phys. Rev. Lett., 20 (1968) 925.

29. G. Capart, Surface Sci., 26 (1971) 429.

30. J.A. Strozier & R.O. Jones, Phys. Rev. B, 3 (1971) 3228.

31. J.B. Pendry & G. Capart, J. Phys. C, 2 (1969) 841.

32. G.E. Laramore & C.B. Duke, Phys. Rev. B, 2 (1970) 4765.

33. C.B. Duke & C.W. Tucker, Surface Sci., 15 (1969) 231.

34. E.G. McRae, J. Chem. Phys., 45 (1966) 3258.

35. M. Lax, Rev. Mod. Phys., 23 (1951) 287; Phys. Rev., 85 (1952) 621.

36. B.W. Holland, R.W. Hannum, A.M. Gibbons & D.P. Woodruff, Surface Sci., 25 (1971) 576.

37. J.L. Beeby, J. Phys. C, 1 (1968) 82.

38. R.H. Tait, S.Y. Tong & T.N. Rhodin, Phys. Rev. Lett., 28 (1972) 553.

39. S.Y. Tong & T.N. Rhodin, Phys. Rev. Lett., 26 (1971) 711.

40. J.B. Pendry, Phys. Rev. Lett., 27 (1971) 856; J. Phys. C, 4 (1971) 3095.

41. B.W. Holland & R.S. Zimmer, J. Phys. C, 8 (1975) 2395.

42. J.E. Demuth, P.M. Marcus & D.W. Jepsen, Phys. Rev. Lett., 31 (1973) 540.

43. D.W. Jepsen, P.M. Marcus & F. Jona, Phys. Rev., 135 (1972) 3933.

44. K. Kambe, Z. Naturf., 22a (1967) 322, 422; Z. Naturf., 23a (1968) 1280.

45. D.P. Woodruff, Discussions Faraday Soc., 60 (1976) 218.

46. T.A. Clarke, R. Mason & M. Tescari, Proc. Roy. Soc. A, 331 (1972) 321.

47. J.C. Buchholtz, M.G. Lagally & M.B. Webb, Surface Sci., 41 (1974) 248.

48. D.L. Adams & U. Landman, Phys. Rev. Lett., 33 (1974) 585.

49. C.W. Tucker & C.B. Duke, Surface Sci., 23 (1970) 411; Surface Sci., 29 (1972) 237.

50. M.G. Lagally, T.C. Ngoc & M.B. Webb, Phys. Rev. Lett., 26 (1971) 1557; J. Vac. Sci. & Technol., 9 (1972) 546.

51. L. McDonnell, D.P. Woodruff & K.A.R. Mitchell, Surface Sci., 45 (1974) 1.

52. A. Kahn, E. So, P. Mark, C.B. Duke & R.J. Meyer, to be published in J. Vac. Sci. & Technol.

CHAPTER THREE

THE EXPERIMENTAL ARRANGEMENT AND PROCEDURES

3.1 The Facilities of the Present LEED System

The LEED studies to be described shortly were carried out in a combined Faraday cup/display system, slightly modified from that previously described by McDonnell (1) and White (2) (Plate 3.1). This system combined the advantages of a visual display system with the direct measuring capabilities of a Faraday cup, using both a.c. and d.c. techniques, dispensing with the inherent difficulties of a spot-photometer. UHV conditions were maintained in a stainless-steel chamber and gas analysis was possible by means of two mass spectrometers. The specimen could be cleaned by cycles of heating and argon ion bombarding and surface cleanliness monitored by means of an AES facility. Cooling of the sample to $\sim 150^{o}$ K was possible. A separately pumped gas-handling line allowed the admission to the main chamber of either argon (for cleaning purposes) or any other specified gas for adsorption studies. The equipment was on-line to a GEC 4080 computer which enabled I-V spectra to be immediately stored for future analysis, and was of great use in the acquisition of the specular beam data which were taken for averaging purposes. This system will now be described more fully.

3.1.1 The UHV chamber, gas-handling line and pumping system

A schematic diagram of the system is shown in Fig. 3.1.

Four types of pump were available to achieve and maintain UHV conditions in the main chamber. These were:-

(1) A liquid nitrogen cooled sorption pump, used to pump down the system from atmospheric pressure to 10^{-3} τ.

(2) A 3" diameter Edwards EO2 diffusion pump (backed by an Edwards ED75 rotary pump), situated to enable independent pumping of the gas-handling line, used to take the system to 5×10^{-6} τ.

(3) A 120 ls^{-1} Ferranti ion pump which, after system bakeout, could maintain a chamber pressure of $\sim 2 \times 10^{-10}$ τ (as measured by a Bayard Alpert gauge) with the help of

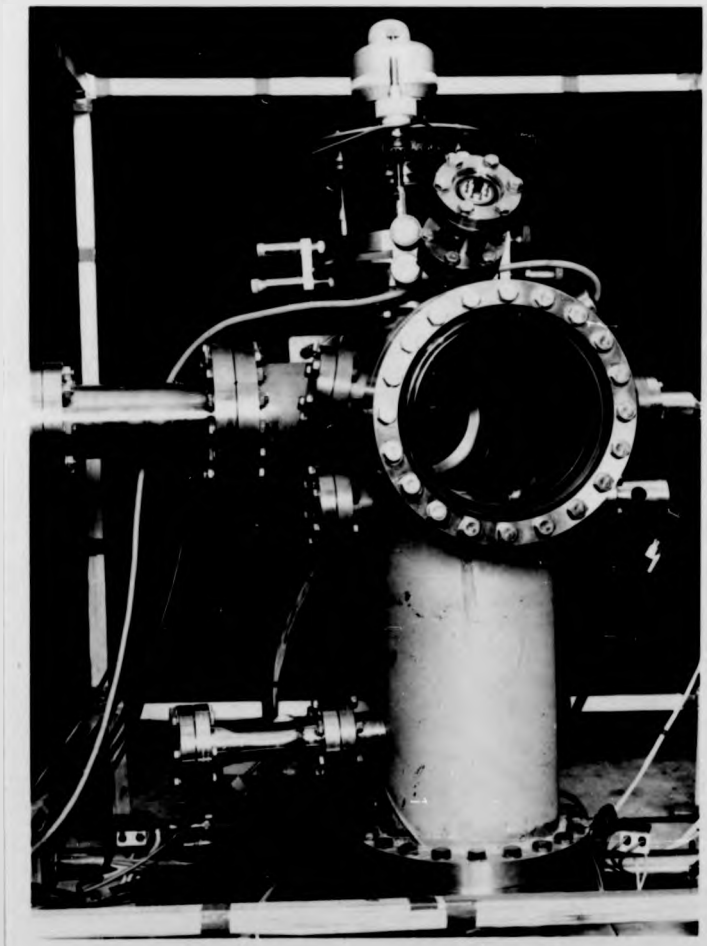

EXPERIMENTAL CHAMBER
(FRONT VIEW)

PLATE 3·1(a)

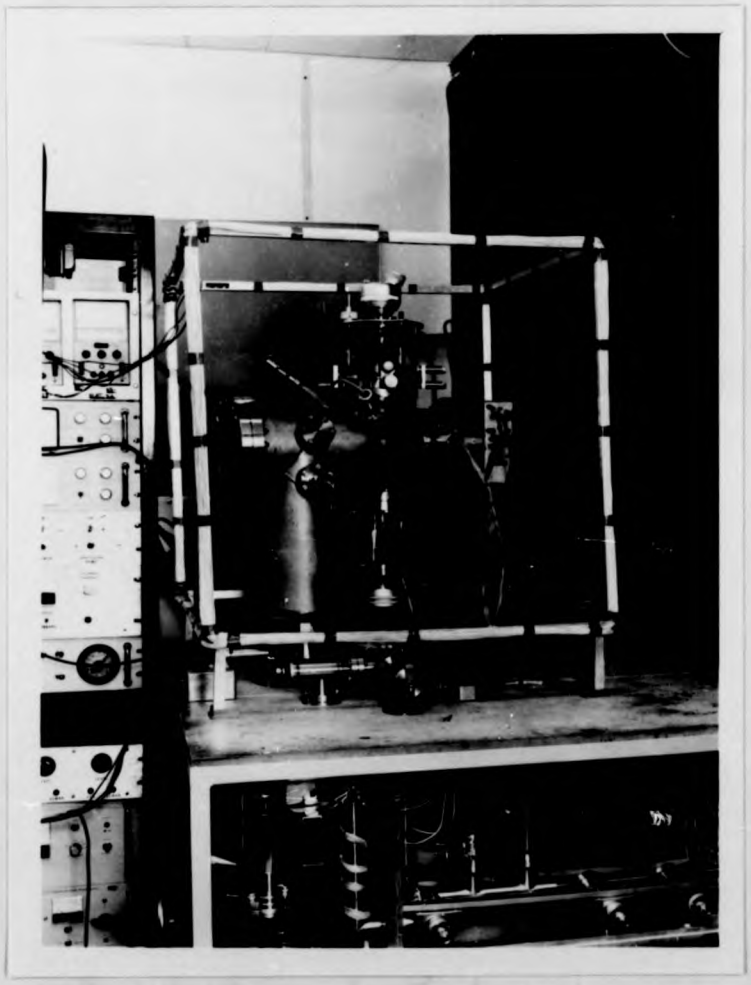

EXPERIMENTAL CHAMBER
(SIDE VIEW)

PLATE 3·1(b)

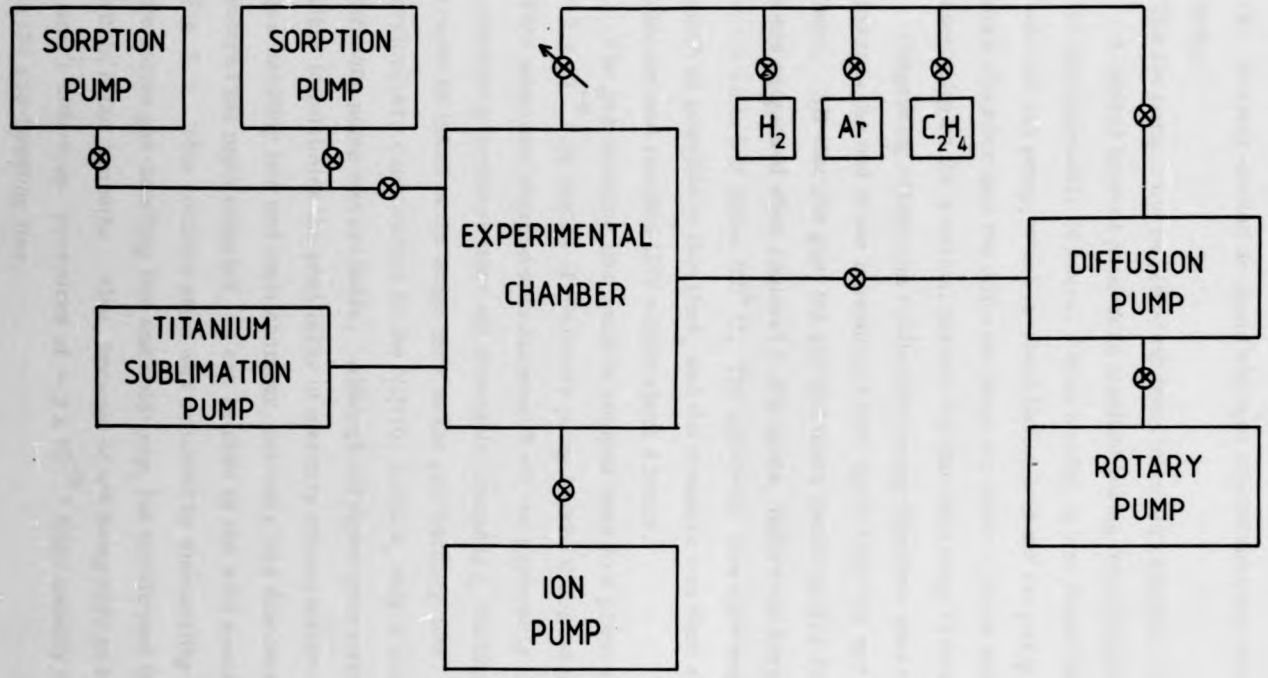

Fig. 3.1

Schematic diagram of the experimental UHV system

(4) A water-cooled or liquid nitrogen-cooled titanium sublimation pump.

The ion pump could be valved off from the main chamber if desired.

A typical bakeout procedure involved baking the chamber at 220° C for approximately 24 hours. Occasionally, it was found necessary to bake the ion pump, which involved baking both the ion pump and the main chamber into the diffusion pump for about 8 hours and then continuing as for a normal bakeout for the remaining 16 hours.

Outgassing of titanium sublimation pump filaments was carried out towards the end of the bakeout and then again after the end of the bake. All electron gun, ion gun and mass spectrometer filaments were outgassed after removal of the ovens, before the temperature of the walls fell below 100° C. The specimen was also outgassed as much as possible at this time, and the pressure was then allowed to recover and reached UHV within about 4 hours.

The gas-handling line could be pumped down to a pressure of $\sim 2 \times 10^{-9}$ T by means of the rotary pump backed diffusion pump. This pump was charged with Santovac 5 oil, an extremely low vapour pressure polyphenyl ether oil (Monsanto Company), enabling the cold trap to be baked at the same time as the gas-handling line. For some preliminary experiments on the Ni(110) surface, only a mercury diffusion pump was available. Although stringent precautions were taken to minimise the possibility of mercury contamination of the gas-handling line and main chamber, mercury was discovered to have entered the main chamber, as can be seen by the AES spectrum of Fig. 3.2. This contamination was removed by dismantling and cleaning the entire gas-handling line and cold-trap, but manifested itself again within about 2 months. Also, because of not being able to bake the pump's cold-trap, pressures of $\sim 2 \times 10^{-8}$ T were usually obtained in the gas-handling line.

3.1.2 Mass spectral analysis

The experimental chamber was provided with two mass spectrometers, namely a Micromass 2 and a Q7 (VG Ltd.). The Micromass

(4) A water-cooled or liquid nitrogen-cooled titanium sublimation pump.

The ion pump could be valved off from the main chamber if desired.

A typical bakeout procedure involved baking the chamber at 220° C for approximately 24 hours. Occasionally, it was found necessary to bake the ion pump, which involved baking both the ion pump and the main chamber into the diffusion pump for about 8 hours and then continuing as for a normal bakeout for the remaining 16 hours.

Outgassing of titanium sublimation pump filaments was carried out towards the end of the bakeout and then again after the end of the bake. All electron gun, ion gun and mass spectrometer filaments were outgassed after removal of the ovens, before the temperature of the walls fell below 100° C. The specimen was also outgassed as much as possible at this time, and the pressure was then allowed to recover and reached UHV within about 4 hours.

The gas-handling line could be pumped down to a pressure of $\sim 2 \times 10^{-9}$ τ by means of the rotary pump backed diffusion pump. This pump was charged with Santovac 5 oil, an extremely low vapour pressure polyphenyl ether oil (Monsanto Company), enabling the cold trap to be baked at the same time as the gas-handling line. For some preliminary experiments on the Ni(110) surface, only a mercury diffusion pump was available. Although stringent precautions were taken to minimise the possibility of mercury contamination of the gas-handling line and main chamber, mercury was discovered to have entered the main chamber, as can be seen by the AES spectrum of Fig. 3.2. This contamination was removed by dismantling and cleaning the entire gas-handling line and cold-trap, but manifested itself again within about 2 months. Also, because of not being able to bake the pump's cold-trap, pressures of $\sim 2 \times 10^{-8}$ τ were usually obtained in the gas-handling line.

3.1.2 Mass spectral analysis

The experimental chamber was provided with two mass spectrometers, namely a Micromass 2 and a Q7 (VG Ltd.). The Micromass

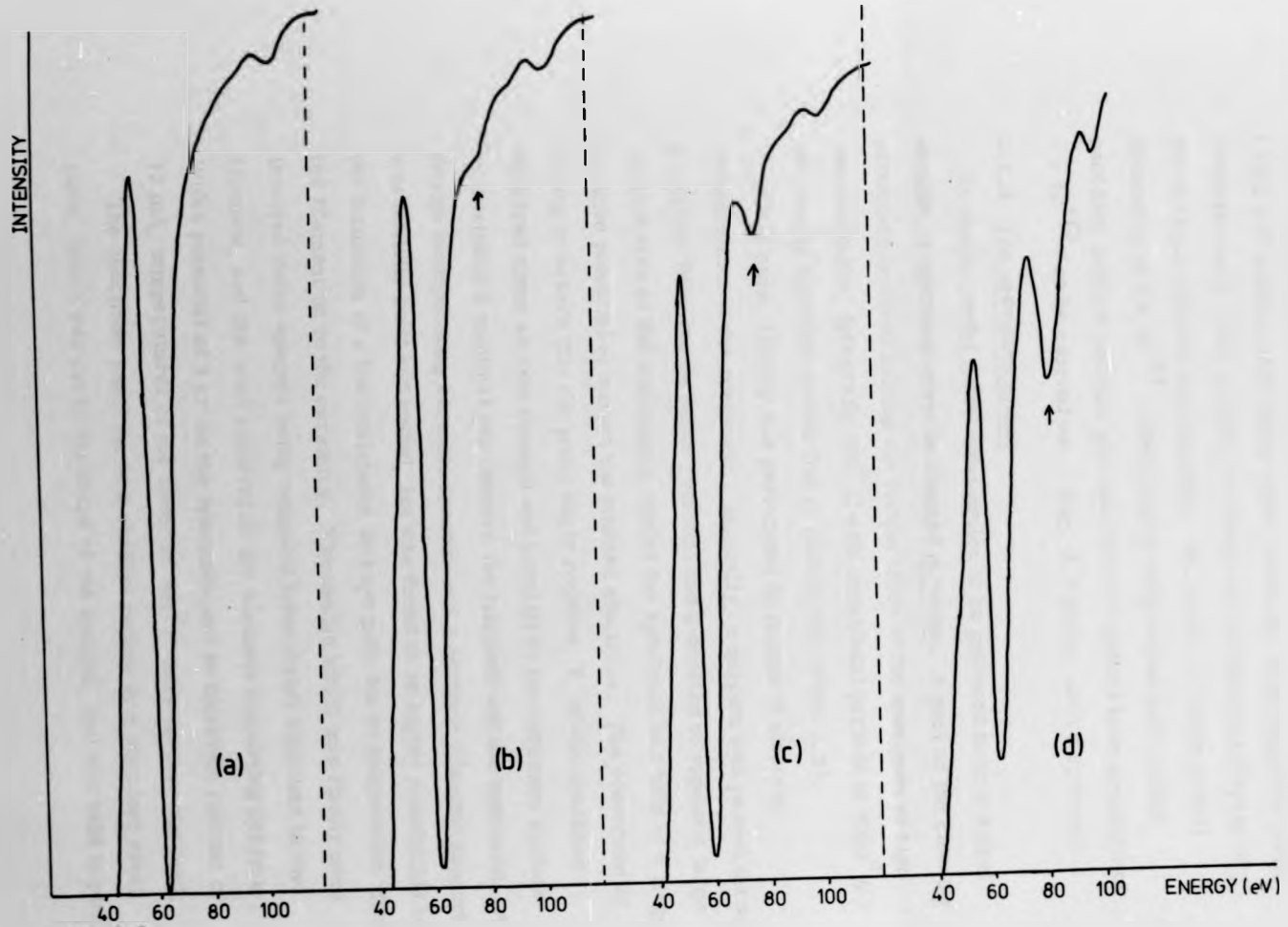

Fig. 3.2
AES spectra revealing increasing mercury contamination

2 is a magnetic spectrometer and was useful for gas analysis in the pressure range 10^{-3} τ and lower. The Q7 quadrupole spectrometer was used at pressures lower than 10^{-6} τ and was of great value when LEED I-V spectra were being taken, since any stray magnetic fields would seriously alter spectra, or where an oscilloscope display of residual gas spectra was required. Its ability to detect partial pressures of 5×10^{-14} τ when used in conjunction with a chart recorder enabled residual gas analysis at a typical base pressure of 1×10^{-10} τ to be carried out. Fig. 3.3 shows such a spectrum.

3.1.3 The specimen mount

To enable useful LEED information to be gathered from a nickel sample, a specimen must be cleaned in vacuo. A part of the cleaning procedure involved raising the temperature of the specimen to high temperatures, (generally 800^{o} C with occasional periods at 1000^{o} C) and so any specimen holder had to permit this (Plate 3.2).

In this case, heating was performed by means of electron bombardment of the specimen. Basically, a current was passed through a tungsten filament (at earth potential and contorted to expose a large surface area to the specimen), whilst the specimen was held at a large positive potential to attract the emitted electrons. The constraint of having to ensure that the polar angle rotation, θ, of the specimen occurred about an axis through and parallel to the specimen surface necessitated a minimal gap between the filament and the specimen. A design incorporating ceramic spacers and a ceramic filament support was initially built and tested, but was found to be highly susceptible to the formation of a low resistance leakage path due to evaporation from the filament on to the ceramics. The design which was finally used involved these spacers being removed from direct exposure to the filament, and the total removal of the filament supporting ceramic. With a potential of 1 kV on the specimen and an emission current of 12 mA, temperatures of the order of 800^{o} C were quickly obtained.

The specimen itself sat in a shallow recess in a stainless steel plate, which was cut to the shape of the sample, and was held in place

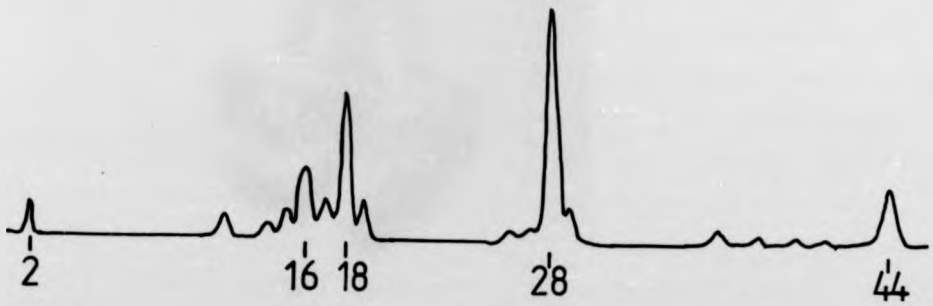

Fig. 3.3

A typical mass spectrum obtained at a pressure of 1×10^{-10} τ

SPECIMEN HOLDER

PLATE 3·2

by a thin nickel ring, spot-welded to the stainless steel (Fig. 3.4). This assembly was, in turn, spot-welded to a pair of stainless steel arms and fastened to plates mounted on ceramic spacers located out of line of sight of the filament. The temperature of the specimen could be measured by a chromel-alumel thermocouple in contact with the back of the sample.

The specimen holder also incorporated a cooling facility by passing liquid nitrogen through $\frac{1}{4}$" diameter copper tubing coiled around a copper cylinder, which was connected via two crimped copper leads to the front arms of the holder. The problem of requiring the specimen to be electrically isolated but still in good thermal contact with the cold copper block was tackled by using a 1/16" thick slice of sapphire cut from a 3/8" diameter rod to act as a spacer between the copper cylinder and a copper plate to which the crimped leads were attached. Sapphire has the property of being a good thermal conductor (conductivity $\sim 10^4$ W $m^{-1}K^{-1}$) between about 10^o K and 200^o K, whilst being, at the same time, a good electrical insulator (12). Diamond possesses good themal conductivity over a larger range but was too expensive to use. The minimum temperature attainable by this rather crude arrangement was 150^o K and a typical cooling curve is shown in Fig. 3.5.

Care was taken to minimise the mass of the holder which was in thermal contact with, and at the same potential as the specimen in order to heat as little as possible besides the specimen and reduce the mass to be cooled. Consequently, the front supporting arms, made from stainless steel sheet, were just thick enough to be rigid and had holes drilled in them, both to reduce the thermal mass and to provide easy access for filament replacement.

The entire holder was mounted on a dual motion rotary drive (VG RD2) which, in principle, allowed a rotation of 360^o about the vertical axis (for θ) and 180^o rotation about an axis perpendicular to the specimen surface (for φ). The presence of the cooling stage limited the θ-rotation to about 270^o, but this was more than adequate

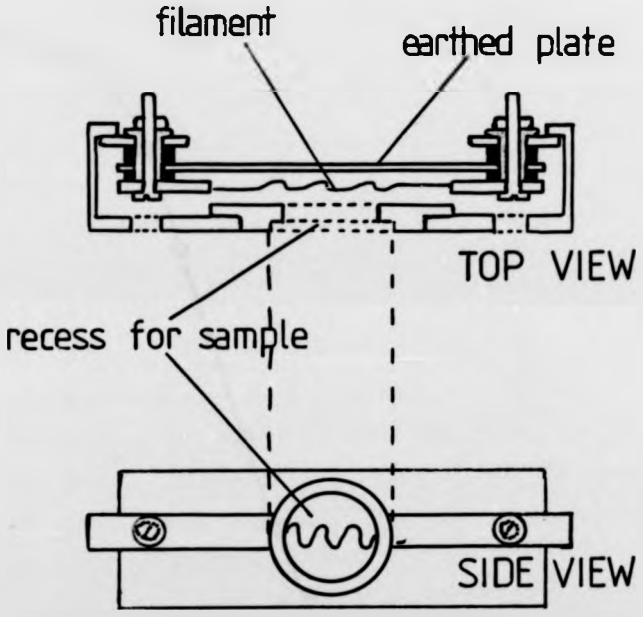

SCHEMATIC DIAGRAM
OF SPECIMEN HOLDER

Fig. 3.4

Top and side views of the stainless steel specimen holder

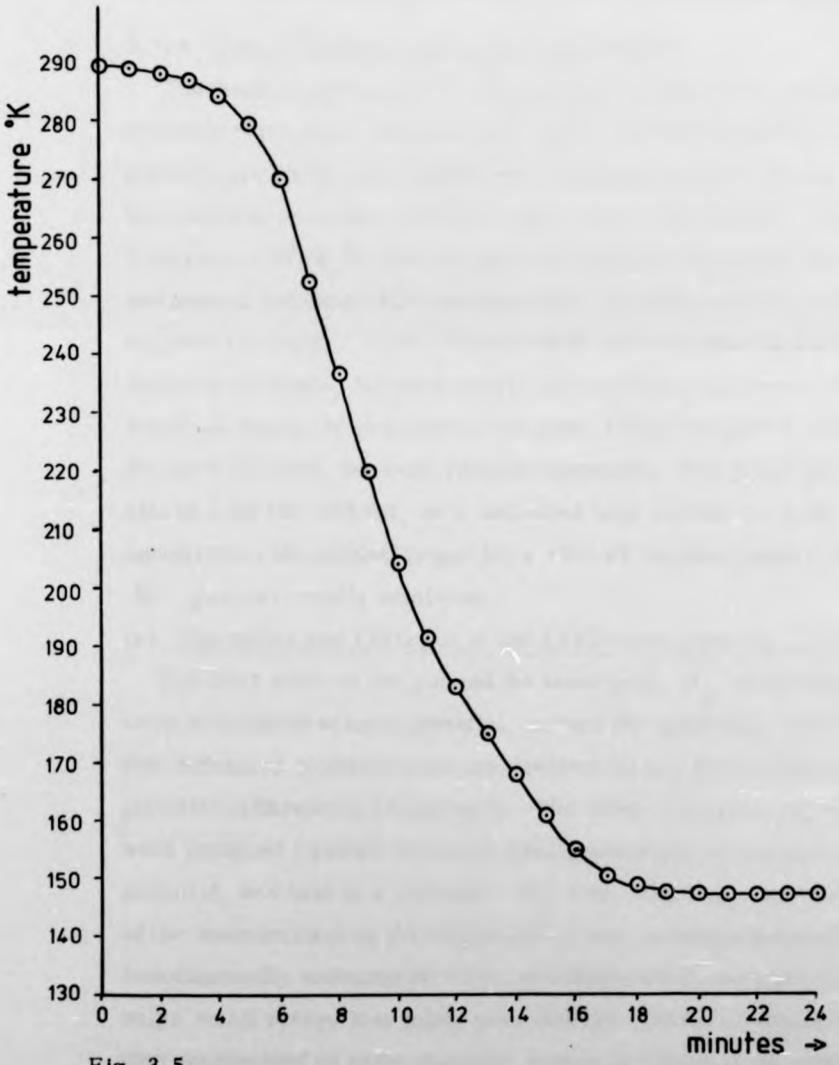

Fig. 3.5

A typical specimen cooling curve obtained by liquid nitrogen cooling

for the requirements of the experiments. A manipulator enabled the bellows and flange on which the RD2 was mounted to be tilted to give a specimen movement of $\pm 5^{o}$ and allowed horizontal translations of ± 0.5" and vertical translations of ± 1" from the mean position.

3.1.4 The LEED/Auger optics and electron guns

The display system used in this work was a standard, commercially available three grid optics with phosphor screen (VG Ltd.). A LEG2 electron gun fitted with a lanthanum hexaboride coated rhenium filament was mounted in a fixed position in the centre of the grids. A Superior Electronics SE 3K 5U electron gun was used as the source for glancing and normal incidence AES and was used with both oxide cathodes and tungsten filaments. Oxide cathodes were found to give very good emission currents, but were readily poisoned on exposure to air and would not regularly reactivate. Tungsten filaments gave a lower emission current, but were reliably operative. The LEG2 gun could also be used for AES but, as it delivered less current (~ 1 μA measured at the earthed target for a 1500 eV incident beam), the SE 3K 5U gun was usually employed.

(a) The optics and LEG2 gun in the LEED mode (see Fig. 3.6)

The final anode of the gun and the inner grid, G_4, of the optics were maintained at earth potential, as was the specimen, to ensure that diffracted electrons were not deviated by any field which a potential difference would produce. The other two grids, G_2 and G_3, were strapped together to reduce field penetration by the screen potential, and held at a potential $-(E_I - \epsilon)$, where E_I was the energy of the beam incident on the target and ϵ was a voltage selected so that both elastically scattered electrons and those which had undergone only a small energy loss might pass through. These electrons were then accelerated on to the phosphor screen by virtue of its positive bias of 5 kV.

All gun anode potentials were referred to the filament which was biased negatively at the beam energy. This necessitated the use of a floatable filament supply, which was also fully stabilized. The

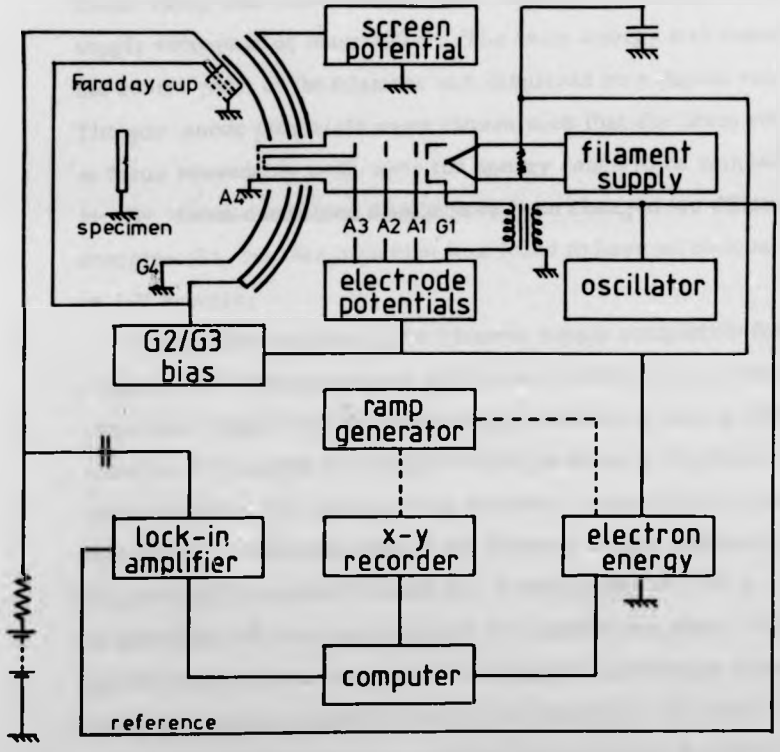

Fig. 3.6

Schematic diagram of the optics and electronics in the LEED mode.

equipment used gave a variable d.c output of 0-10 A and 0-12 V (KSM Ltd.). The other gun and optics potentials were obtained from two 300 V d.c. supplies and a ± 30 V d.c. supply (APT Ltd.). The negative potential which was applied to the filament and provided the beam energy was taken from a programmable 0 to ± 3 kV supply (J & P. Ltd.). This supply was backed off by a battery, since a fast linear ramp was only obtained when ramping commenced from a supply voltage of at least 100 V. The beam energy was measured at the centre point of the filament and displayed on a digital voltmeter. The gun anode potentials were chosen such that the beam remained in focus reasonably well over the energy range to be ramped. Ideally, focus conditions should have been changed for different beam energies (3), but this omission was found to have no noticeable effect on I-V spectra.

The problem of obtaining a filament supply completely free from ripple is not easily overcome if relatively short time constants are required. Ripple on the beam energy will tend to have a smoothing effect on I-V curves and ripple on the gun focus will produce a varying spot diameter. To alleviate this problem, a smoothing capacitor, C, was placed between one side of the filament supply and earth. Empirically, it was still found that a ramp speed of 3 eV s^{-1} could not be exceeded without distorting the I-V spectra obtained. Faster ramp speeds tend to move the position of features and reduce intensities and, at the same time, cause an overall broadening of the peaks.

The effective shape of an analyser transmission function is distorted if the detection system has a time constant. In general, the shorter the time constant or the slower the sweep speed, the more accurate the spectra obtained (4). In practice, a fairly good approximation is obtained when

$$\tau \leq \frac{1}{5} \frac{\Delta E}{S}$$

where τ is the time constant, ΔE is the full width at half maximum and S is the ramp speed.

For the a.c. detection system, using the Faraday cup, the incident beam was modulated by superimposing a 1 kHz signal on the G_1 voltage, which was set so that the beam current was caused to oscillate between total cut-off and a maximum. A lock-in amplifier was used in the usual way to monitor the "in-phase" signal.

A Keithley picoammeter was available for d.c. measurements, but, in view of the fact that slower ramping speeds were necessary when using this instrument, it was used mainly for absolute intensity measurements and for corroboration of a.c. detected data.

(b) The optics in the AES mode (Fig. 3.7)

As an Auger electron detector, the three grid optics was biased as follows:-

G_4 was again at earth potential;

G_2 and G_3 were the retard grids and were ramped;

the screen, acting as collector, was held at a small positive potential to reduce secondary emission.

Using an a.c. detection system, a modulation of frequency ω was superimposed, (using an isolating transformer), on the retard voltage and the lock-in-amplifier was tuned in to either ω or 2ω to give N(E) or N'(E), respectively. The collection angle of the screen was π steradians. In order to neutralize the capacitive coupling between the retard grids and the collector, a variable capacitor was placed between the low side of the transformer and the lock-in-amplifier. In this way, it was possible to neutralize the capacitance so that a modulation of less than 2 mV peak to peak was superimposed on the collector signal.

The incident beam was provided by an SE 3K 5U electron gun, which gave $\sim 5\mu A$ at the earthed target for an energy of 1500 eV. This gun could be used for glancing incidence ($\sim 15^{o}$) AES, but was rather difficult to align with the target initially. In order to overcome this problem, a scanning system was used. Briefly, rasters were applied to the X and Y deflection plates of the gun. The current collected at the target was fed, via a voltage amplifier, into the Z intensity modulation input of an oscilloscope. The X and Y plates of the oscilloscope were also ramped in the frequency ratio of 1000:1 so that a picture

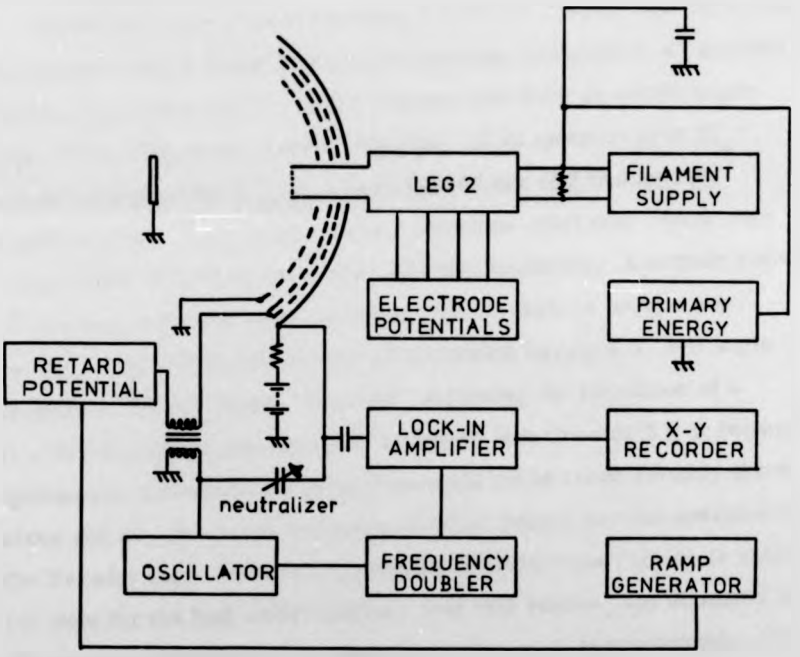

Fig. 3.7

Schematic diagram of the optics and electronics in the AES mode.

of the specimen was built up. By reducing the extent of the ramps applied to the deflection plates of the gun, a specific point on the sample could be "homed on". From the pictures obtained it was found that, for a 1500 eV beam, the diameter of the spot at the specimen was less than 0.5 mm. The retard voltage applied to G_2/G_3 was supplied by a second programmable power supply.

3.1.5 The Faraday cup

The Faraday cup used in obtaining LEED I-V spectra was basically a miniature planar three grid optics assembly, mounted in an earthed nichrome cylinder which was the Wehnelt can from an electron gun (Fig. 3.8). The grids, which consisted of an aperture grid (G_4) and the retard grids (G_2, G_3) were made from 96% transparent tungsten mesh. The collector was a stainless steel disc coated with carbon black to reduce secondary electron emission. A certain amount of data was collected from the clean Ni(110) surface using a cup aperture which subtended a cone of collection having a 3^{o} half angle relative to the specimen. However, following the formation of a (1 x 2) structure on adsorption of hydrogen (see Chapter 5), it became obvious that non-specular beam data could not be taken reliably above about 100 eV, due to the intrusion of other beams into the aperture of the Faraday cup. This was especially important when trying to obtain I-V data for the half-order beams. For this reason, the diameter of the entrance aperture was reduced by a factor of approximately $\sqrt{2}$, hence doubling the energy range reliably available. The clean Ni(110) I-V spectra previously obtained were repeated using the reduced aperture, and proved to be identical up to 100 eV but could then be taken reliably to well over 200 eV.

The Faraday cup was mounted on tubular stainless steel supports, through which all the electrical connections were made. By virtue of its being mounted on a single motion rotary drive (RD1 V.G. Ltd.), the cup was rotatable about the axis which passed through and was parallel to the surface of the specimen. The plane of rotation was the same as that of the (00) beam of the diffraction pattern.

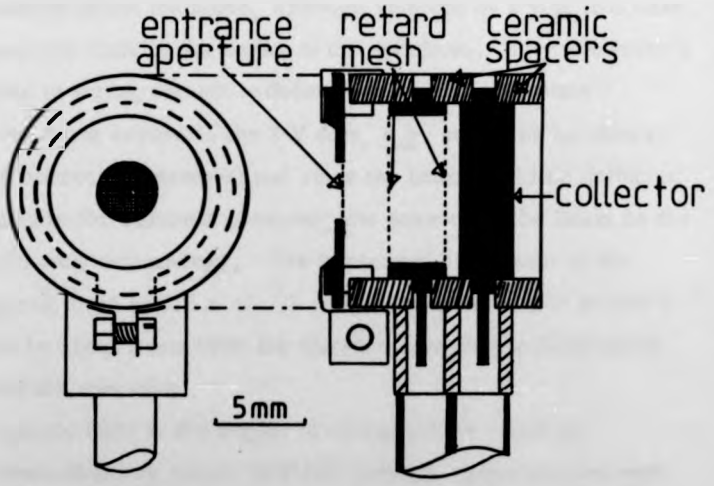

Fig. 3.8

Schematic diagram of the reduced aperture Faraday cup

In view of minor errors in the construction of the chamber and a noticeable distortion after many bakeouts, the axes of the Faraday cup flange and specimen flange were slightly misaligned. The forward displacement of the specimen from its axis of rotation also added to this error. To correct this, a bellows was included which, with the help of three adjustable supporting pillars, allowed precise alignment of the two axes of rotation.

3.1.6 Magnetic field neutralization

Since electrons are deflected by magnetic and electric fields, care had to be taken to ensure that such fields were eliminated, or at least minimised, in the experimental chamber. The absence of stray electric fields was ensured by comparing I-V spectra taken both with and without potentials applied to the three grid optics and screen.

The presence of the ion pump, although shielded by a soft iron case, caused a magnetic field in the region of the specimen. Even the earth's magnetic field is strong enough to deflect low energy electrons sufficiently to cause errors in the I-V data, e.g. angles of incidence would not be correctly measured and since the beam would be deflected different amounts for different energies, the position of the beam on the surface would vary with energy. The horizontal component of the earth's magnetic field is 1.8×10^{-5} T and this is sufficient to deflect a 100 eV beam by about 2 mm over the distance between the final anode of the gun and the specimen.

This magnetic field in the region of the specimen could be effectively neutralized by means of three mutually perpendicular sets of square Helmholtz coils powered by three stabilized d.c. power supplies (Farnell Ltd.). Initial neutralization was carried out by adjusting the Helmholtz coils' field until the specular beam viewed on the screen remained stationary as the incident beam energy was varied down to about 20 eV. Then, fine adjustments were made until the I-V spectra taken for the specular beam at equivalent angles on either side of normal incidence were identical. Final adjustments were made to ensure that symmetrically equivalent beams possessed identical I-V characteristics at normal incidence.

In view of minor errors in the construction of the chamber and a noticeable distortion after many bakeouts, the axes of the Faraday cup flange and specimen flange were slightly misaligned. The forward displacement of the specimen from its axis of rotation also added to this error. To correct this, a bellows was included which, with the help of three adjustable supporting pillars, allowed precise alignment of the two axes of rotation.

3.1.6 Magnetic field neutralization

Since electrons are deflected by magnetic and electric fields, care had to be taken to ensure that such fields were eliminated, or at least minimised, in the experimental chamber. The absence of stray electric fields was ensured by comparing I-V spectra taken both with and without potentials applied to the three grid optics and screen.

The presence of the ion pump, although shielded by a soft iron case, caused a magnetic field in the region of the specimen. Even the earth's magnetic field is strong enough to deflect low energy electrons sufficiently to cause errors in the I-V data, e.g. angles of incidence would not be correctly measured and since the beam would be deflected different amounts for different energies, the position of the beam on the surface would vary with energy. The horizontal component of the earth's magnetic field is 1.8×10^{-5} T and this is sufficient to deflect a 100 eV beam by about 2 mm over the distance between the final anode of the gun and the specimen.

This magnetic field in the region of the specimen could be effectively neutralized by means of three mutually perpendicular sets of square Helmholtz coils powered by three stabilized d.c. power supplies (Farnell Ltd.). Initial neutralization was carried out by adjusting the Helmholtz coils' field until the specular beam viewed on the screen remained stationary as the incident beam energy was varied down to about 20 eV. Then, fine adjustments were made until the I-V spectra taken for the specular beam at equivalent angles on either side of normal incidence were identical. Final adjustments were made to ensure that symmetrically equivalent beams possessed identical I-V characteristics at normal incidence.

3.2 Specimen Preparation and Cleaning

3.2.1 Ex vacuo preparation

The two nickel surfaces investigated in this work were prepared from a 10 mm diameter, 4 N pure single crystal boule (Metals Research Ltd.). The crystal was oriented to within $\pm \frac{1}{2}^{o}$ of the desired plane by means of X-ray diffraction, and then 1 mm slices were spark-machined. Following mechanical polishing with 6μ, 1μ and 0.25μ diamond paste, each sample was electropolished in an ortho-phosphoric acid solution (5). The orientation was again checked by X-ray diffraction. Before mounting on the specimen stage, each sample was vapour degreased in a trichloroethylene vapour bath. The whole assembly was then degreased and installed in the chamber.

3.2.2 In situ cleaning

As mentioned in Section 3.2.1, the specimens were outgassed as much as possible after bakeout, whilst the chamber was still hot. A typical AES spectrum taken from such a specimen is shown in Fig. 3.9. As would be expected, there was a large sulphur peak and phosphorus was also present. There was also a carbon peak present on the spectrum obtained from the (110) surface, but this was not evident on the spectrum from the (100) surface, and it was assumed that segregation competition between sulphur and carbon resulted, upon cooling, in the sulphur occupying the topmost layer. When the sample had been bombarded for approximately half an hour by 500 eV argon ions, the AES spectra showed no sulphur but a definite carbon peak was present for both samples.

The behaviour of impurities on polycrystalline and single crystal nickel surfaces has been discussed in a number of papers (6, 7, 8). To obtain a clean surface, various combinations of heating, bombarding and exposure to oxygen have been used, but no standard cleaning formula is applicable. The procedure employed seems to vary from sample to sample and may be dependent on the initial sample impurities or the heating conditions.

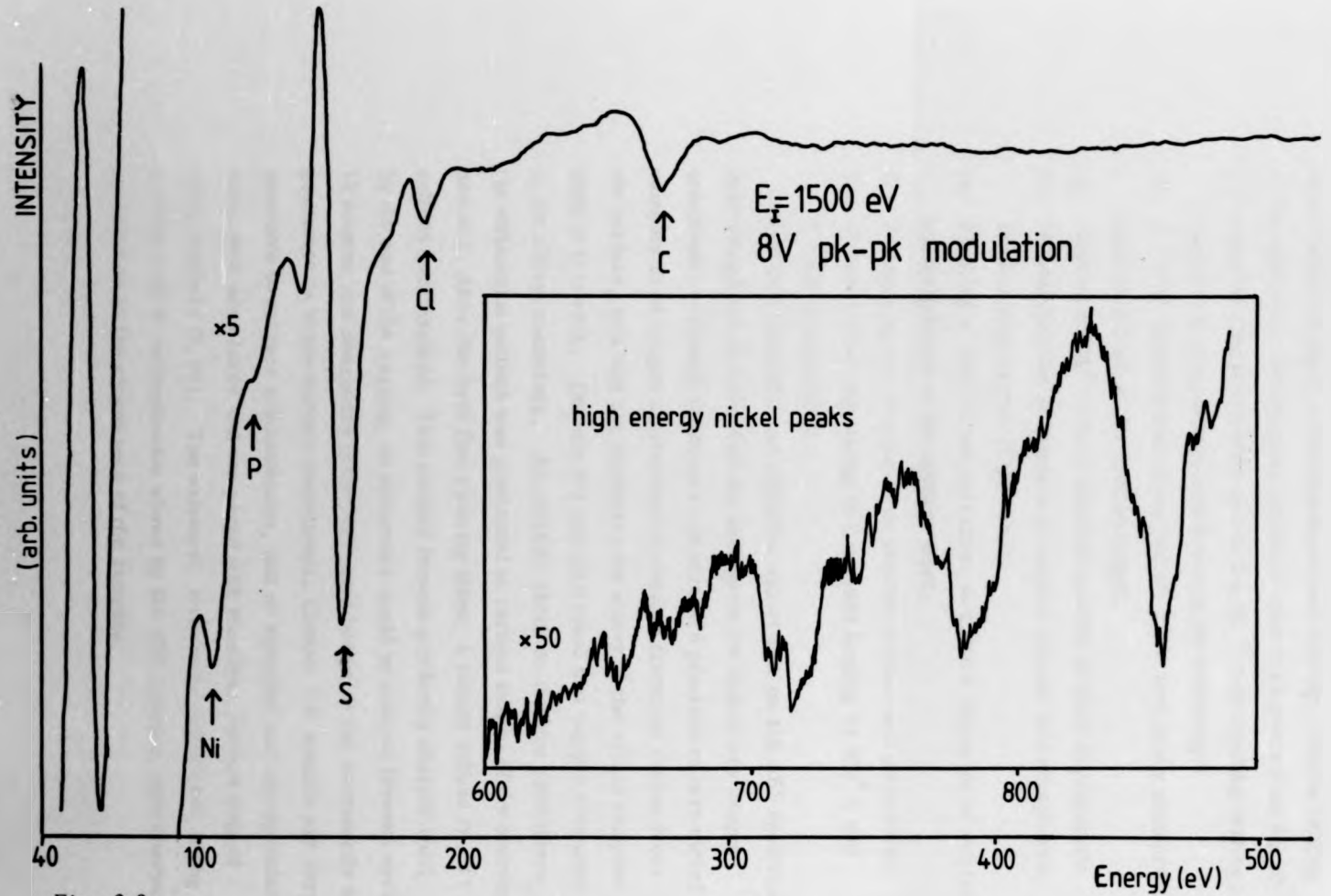

Fig. 3.9

A typical AES spectrum obtained immediately after bake-out.

The method of cleaning employed in the present work involved many cycles of argon ion bombardment and heating. During heating of the specimen, the chamber pressure rose to no more than 8×10^{-10} τ and returned almost instantly to 1 or 2×10^{-10} τ on ceasing heating.

A typical cleaning programme involved the following:-

(1) A 4 hour bombardment using 500 eV argon ions and a measured current of 2 μA at the earthed target;

(2) Heating at 800° C for 5 minutes to cause sulphur segregation;

(3) Bombarding for 20 minutes to remove sulphur and phosphorus, leaving only carbon (Fig. 3.10).

(4) Flashing to 1000° C several times to cause a depletion of sulphur and phosphorus in the surface layer;

(5) Bombarding for 20 minutes to remove sulphur and phosphorus;

(6) Fifteen cycles consisting of 5 minutes heating at 800° C and ½ hour bombardment.

After this treatment, no impurity was visible on the AES spectrum, even though the samples had not undergone the customary oxygen treatment. Although it seems to be standard practice to burn nickel samples in an oxygen atmosphere to remove traces of carbon from the surface, this was not necessary for either of the nickel samples used in this work. Demuth (9) has also found that oxygen treatment is not always necessary. As a further check on surface cleanliness, the diffraction pattern was monitored at various stages of the cleaning process. After the first five cleaning steps, a rather diffuse (1 x 1) pattern was obtained. This pattern became gradually sharper until, by the end of the cycling, no difference could be noticed between cycles. Of course, the sharpness of the diffracted beams is not necessarily a guarantee as to the surface cleanliness. Certain I-V spectra are very sensitive to surface contamination, and so specular and non-specular beam data were taken and compared with the clean surface data of other workers (9, 10). The extremely favourable agreement, along with the lack of contamination shown by the AES spectra, was convincing evidence as to the cleanliness of the samples.

Fig. 3.10

Overleaf is shown the AES spectrum obtained from a nickel sample after an initial heat treatment and subsequent argon ion bombardment.

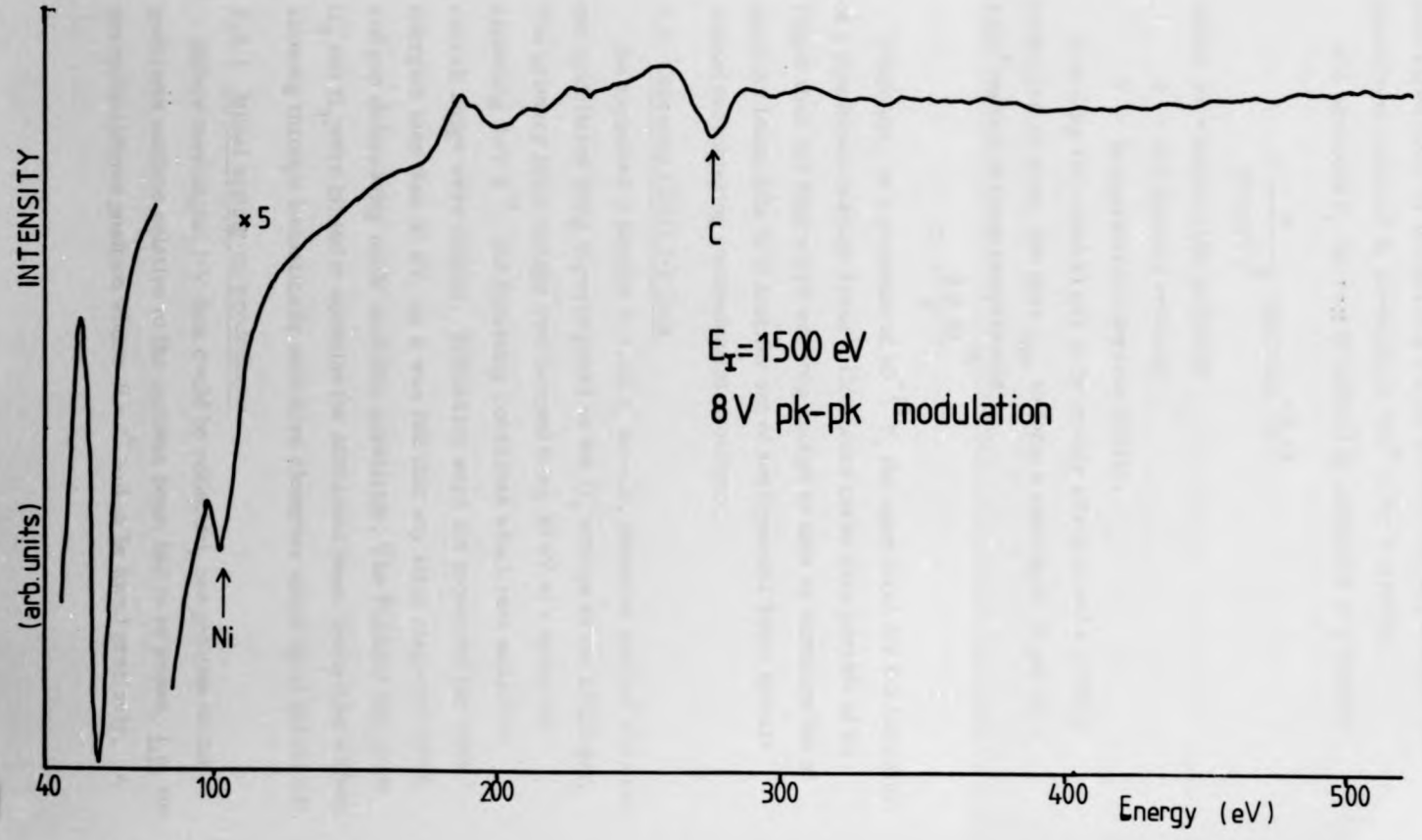
INTENSITY
(arb. units)
×5
Ni
C
E_I=1500 eV
8 V pk-pk modulation
40
100
200
300
400
500
Energy (eV)

Once this state was achieved, the samples were cleaned before each experiment by bombarding for 20 minutes and any damage thus caused was removed by annealing at 800^{o} C for 3 minutes.

At a pressure P, the rate of arrival of molecules at a surface

$$= \frac{P}{(2\pi kmT)^{\frac{1}{2}}} \text{ mols cm}^{-2}\text{s}^{-1}$$

where m = mass of the molecule

k = Boltzmann's constant

T = temperature in degrees Kelvin.

Assuming the residual gas to be mainly nitrogen and a sticking coefficient of unity, the time t_m, to form a monolayer of gas on a $1\,\text{cm}^2$ surface at room temperature

$$\simeq \frac{2 \times 10^{-6}}{P}$$

Therefore, at a pressure of 10^{-10} τ, the time taken for the formation of a monolayer is about 5 hours. Data were taken over periods of no longer than one hour which was long enough to take an extensive set of specular beam data or a smaller set of non-specular beam spectra without encountering contamination problems.

3.3 Obtaining LEED I-V Data

As explained in Section 3.1.4(a), an a.c. detection method was used, the modulation being superimposed on the G_1 voltage of the LEG2 gun. The primary beam energy was ramped from 30 eV at a speed not exceeding $3\,\text{eV s}^{-1}$, and focussing conditions which best suited the overall range were chosen. Intensities were not measured for beam energies less than 30 eV, as it was felt that any stray magnetic fields and gun defocussing made such data unreliable. The Faraday cup grids, G_2 and G_3, were biased to optimise the diffracted beam intensities without allowing through inelastically scattered electrons which spoil resolution.

3.3.1 Initial setting-up procedures

Before meaningful I-V data could be collected, the position of the specimen surface relative to the incident beam had to be known, i.e. the normal incidence position where $\theta = 0^{o}$ had to be found precisely. A

rough idea of this position could be ascertained initially by viewing the diffraction pattern. A comparison was then made of (00) beam spectra taken for a range of θ values on each side of the proposed normal incidence position. This enabled the precise position of normal incidence to be located. A further check was then made by comparing the I-V curves of symmetrically equivalent non-specular beams at normal incidence.

Having located the position of normal incidence, θ for the (00) beam from 8^{o} upwards could be obtained to within an accuracy of $\pm \frac{1}{2}^{o}$. The angle of incidence was always measured after a rotation in a fixed sense to minimise errors due to play in the drive mechanism. Specular beam data collected on both sides of normal incidence over a range of 8^{o} to 30^{o} were compared in order to ensure that the slight forward displacement of the sample from its axis of rotation had no serious effect on results.

The azimuthal angle, φ, was found by means of photographs and, for the high symmetry azimuths, by ensuring that beams such as, say, the 10 and $\bar{1}0$ lay in the same plane of rotation as the Faraday cup.

3.3.2 Collecting specular beam data

(a) Manually

Specular beam I-V spectra could be collected for angles of incidence of 8^{o} and greater, but when larger angles were reached, intensities were much reduced and the beam was no longer visible on the screen. For this work, a maximum value of $\theta = 32^{o}$ was taken. Spectra for a value of θ smaller than 8^{o} could not be obtained because the Faraday cup could not move in closer to A_4 of the gun. Since the specular beam remains stationary as the primary beam energy is changed, the Faraday cup was merely positioned to catch the (00) beam for a known angle of incidence and the I-V spectrum was plotted directly on an X-Y recorder.

(b) Computer-aided

The on-line GEC 4080 computer provided an extremely useful facility for the acquisition and analysis of diffraction beam data. In this

work, it was only used for the collection of specular beam intensities, mainly with respect to the data averaging discussed in Chapter Seven.

The computer ramped the beam energy via a DAC and stored the intensity measured at a selected time interval (usually 200 ms) via an ADC. The information thus obtained by the computer was simultaneously displayed on the X-Y recorder.

3.3.3 Non-specular beam data

Since the position of non-specular beams is energy-dependent, I-V spectra were much less easily obtainable. Spectra could only be obtained for these beams when they were in the azimuth which placed them in the plane of rotation of the Faraday cup. The technique used was the usual one employed for Faraday cup systems (13), whereby the beam energy was ramped through a small range and the intensity of the beam as it passes through the cup was plotted. Then the cup was moved through $\sim \frac{1}{2}^{o}$ intervals and the energy again ramped thus building up an envelope from the intensity of the beam at each particular energy. Extreme care was taken to ensure that only the beam under investigation was measured and so only a limited energy range was scanned each time. It was found that a ramp speed of not greater than $2 eV\, s^{-1}$ was necessary to be certain of not losing some of the narrower features. The Faraday cup had to be moved in small steps for the same reason, the increments getting smaller as higher energies were reached.

No non-specular beam spectra were obtained using the computer, since a large proportion of time was taken in moving the Faraday cup and, unless a major programme had been undertaken to computerise this movement, no great saving in time would have ensued.

3.3.4 The normalization of I-V data

The LEG2 gun did not give a constant beam current throughout the energy range used and so any I-V spectrum had true peak shapes and intensities modified by this current/energy characteristic of the gun. In order to compare experimental data with theoretically calculated spectra (11), all curves were normalized to a constant incident current. The Faraday cup was used to measure the current/energy

characteristics of the gun and the resulting "normalizing" curve is shown in Fig. 3.11.

All I-V spectra presented in this work have been normalized. In the case of the specular beam results, normalization was easily carried out by computer, since these results were already stored; all non-specular beam data had first to be digitised by hand and entered into the computer before normalization could be carried out.

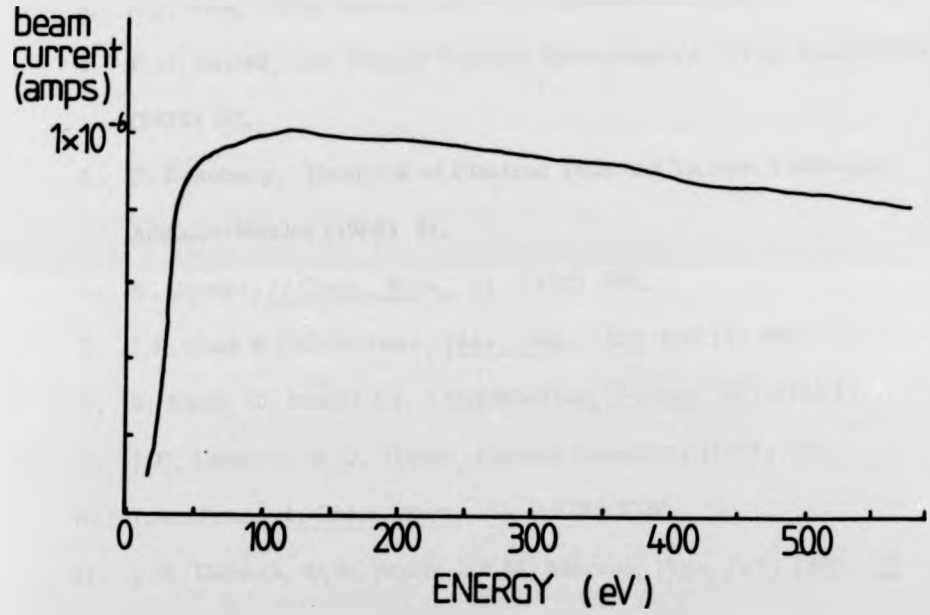

LEG 2 BEAM CURRENT
NORMALIZATION CURVE

Fig. 3.11

Graph showing the variation of beam current with energy for a LEG 2 electron gun.

CHAPTER THREE
REFERENCES

1. L. McDonnell, Ph.D. Thesis, University of Warwick (1974).
2. S.J. White, Ph.D. Thesis, University of Warwick (1977).
3. R.J. Reid, Ph.D. Thesis, University of Warwick (1971).
4. K.D. Sevier, Low Energy Electron Spectrometry, Wiley Interscience (1972) 30.
5. F. Rosebury, Handbook of Electron Tube and Vacuum Techniques, Addison-Wesley (1965) 21.
6. R. Gomer, J. Chem. Phys., 21 (1953) 293.
7. J.P. Coad & J.C. Riviere, Phys. Lett., 35A (1971) 185.
8. S. Mroz, C. Koziol & J. Kolaczkiewicz, Vacuum, 26 (1976) 61.
9. J.E. Demuth, Ph.D. Thesis, Cornell University (1973) 30.
10. J.C. Tracy, J. Chem. Phys., 53 (1972) 2736.
11. J.E. Demuth, D.W. Jepsen & P.M. Marcus, Phys. Rev. Lett., 31 (1973) 540.
12. R. Berman, Contemp. Phys., 14 (1973) 107.
13. R.L. Park & H.E. Farnsworth, Rev. Sci. Instr., 35 (1964) 1592.

CHAPTER FOUR
QUALITATIVE ADSORPTION STUDIES

4.1 Introduction

In this chapter there will be a general discussion of the conditions in which adsorption studies were undertaken, including the precautions necessary to ensure that the effects of the electron beam are known. The adsorption systems studied were hydrogen, ethylene and carbon on the (100) and (110) surfaces of nickel. Extensive sets of LEED I-V data were taken for the Ni(110)(1 x 2)H and Ni(100) (2 x 2)C systems and will be discussed in detail in Chapters Five and Six, but in qualitative terms in this chapter.

In recent years there have been several studies of the interaction of olefins with transition metal surfaces. The adsorption of ethylene on nickel has probably received more attention than any other hydrocarbon-metal system, with the exception of hydrocarbon-platinum (1-4). The hydrocarbon-rhenium(5)/iridium (6) systems have also been studied. Erkelens and Liefkens (7) and Morrow and Sheppard (8) have employed infra-red spectroscopy on polycrystalline samples, while Whalley et al. (9) have used field emission techniques and Selwood (10) and Martin et al. (11) have used magnetic techniques. LEED and thermal desorption studies have been made on single crystal surfaces by Dalmai-Imelik and Bertolini (12) and by Ertl (13). More recently, Demuth and Eastman (14) and Horn et al. (15) have reported UPS studies on this system and Demuth (16) has studied the related system C_2H_2 on Ni(111), also by UPS. AES and modulated molecular beam techniques have been used by Zuhr and Hudson (17). There is general agreement amongst recent studies that strong, dissociative chemisorption takes place on the various single crystal faces of nickel. What is not certain is the temperature at which the dissociation takes place, the completeness of the dehydrogenation, and the eventual fate of the liberated hydrogen.

4.2 Adsorption Conditions and Electron Beam Effects

Since the main purpose of this work was to collect a reliable set of I-V spectra for any of the adsorption systems, one of the major experimental considerations had to be a characterization of the conditions of adsorption, temperature and the effect of the incident electron beam (18, 19). These problems were investigated in detail for the Ni(110) (1 x 2)H system, and also for the adsorption of C_2H_4 on Ni(100) where beam effects were felt to be a very important consideration (15).

4.2.1 The Ni(110)-hydrogen adsorption system

The three main problems investigated through a study of the I-V spectra were:-

(1) How does the electron beam affect hydrogen adsorption ?

(2) Is the restoration of the I-V spectrum to the "clean" spectrum on termination of hydrogen admittance due to electron stimulated desorption (ESD), or is it a function of time alone ?

(3) Is hydrogen adsorbed as an atom or as a molecule ?

Adsorption was carried out at 150^{o} K dynamically by allowing a continual flow of hydrogen through the chamber, since it was found that during static adsorption the LEED pattern could easily be seen to deteriorate. Exposure at a pressure of 1×10^{-8} τ (corrected to the equivalent nitrogen pressure) was found to be the optimum to give an immediate sharp (1 x 2) pattern and an alteration in the I-V spectra.

To investigate electron beam effects and exposure/pressure dependence, it was decided to monitor the (00) beam I-V spectrum at a fixed angle of incidence so that possible errors due to inexact repositioning of the specimen would be avoided, and a rapid monitoring of the various effects could be made. The specular beam was chosen since the acquisition of its I-V spectrum is far quicker than for a non-specular beam.

After cooling the specimen to 150^{o} K, the I-V spectrum for the clean surface (00) beam at an angle of incidence $\theta = 8^{o}$ was taken.

With the electron beam on and ion gauge on, hydrogen was admitted dynamically and successive I-V spectra were taken at two minute intervals. The experiment was repeated, but this time with the electron beam switched off between spectra and then again with both the ion gauge and beam off as much as possible. In each experiment, the hydrogen admittance was terminated and spectra were taken for another 30 minutes at 2 minute intervals at 2×10^{-10} T.

(a) Ion gauge on and electron beam on:-

On exposure to hydrogen, the clean surface spectrum showed an immediate overall decrease in intensity and a (1 x 2) pattern was observed. The intensity peak at 133 eV shifted to 123 eV, with a shoulder appearing at 133 eV (Fig. 4.1(a)). The slight hump at 165 eV increased substantially to a definite peak at 163 eV and the peak at 210 eV increased in intensity relative to the others. These changes remained constant throughout the 30 minutes of exposure.

On termination of exposure, there was no change in the spectrum for ~240 seconds, but there followed a gradual decrease in intensity of the 41 eV peak until, after ~ 30 minutes, it was almost completely extinguished. The 92 eV peak also gradually increased relative to the 123 eV peak.

(b) Ion gauge on and electron beam off:-

On exposure to hydrogen, (Fig. 4.1(b)), there was an immediate reduction in the overall intensity of the spectrum, but the 133 eV peak was only slightly shifted and broadened to ~ 128 eV, having no shoulder. No peak appeared at 163 eV and the 90 eV peak was depressed relative to the one at 40 eV. If the beam were left on between scans, the 90 eV peak grew in intensity but decreased when the beam was switched off. A (1 x 2) pattern formed more slowly than in (a) via a streaking in the <100> direction and was generally less sharp.

On termination of exposure, the 90 eV peak immediately grew relative to the 40 eV peak and gradually grew larger than the 130 eV peak. The peak at 40 eV was not suppressed as in the "beam-on" case.

Fig. 4.1

The following three figures show the effects of various adsorption/desorption conditions on a specular beam I-V profile during and after exposure of the Ni(110) surface to hydrogen at 150^{o} K.

BEAM ON / GAUGE ON

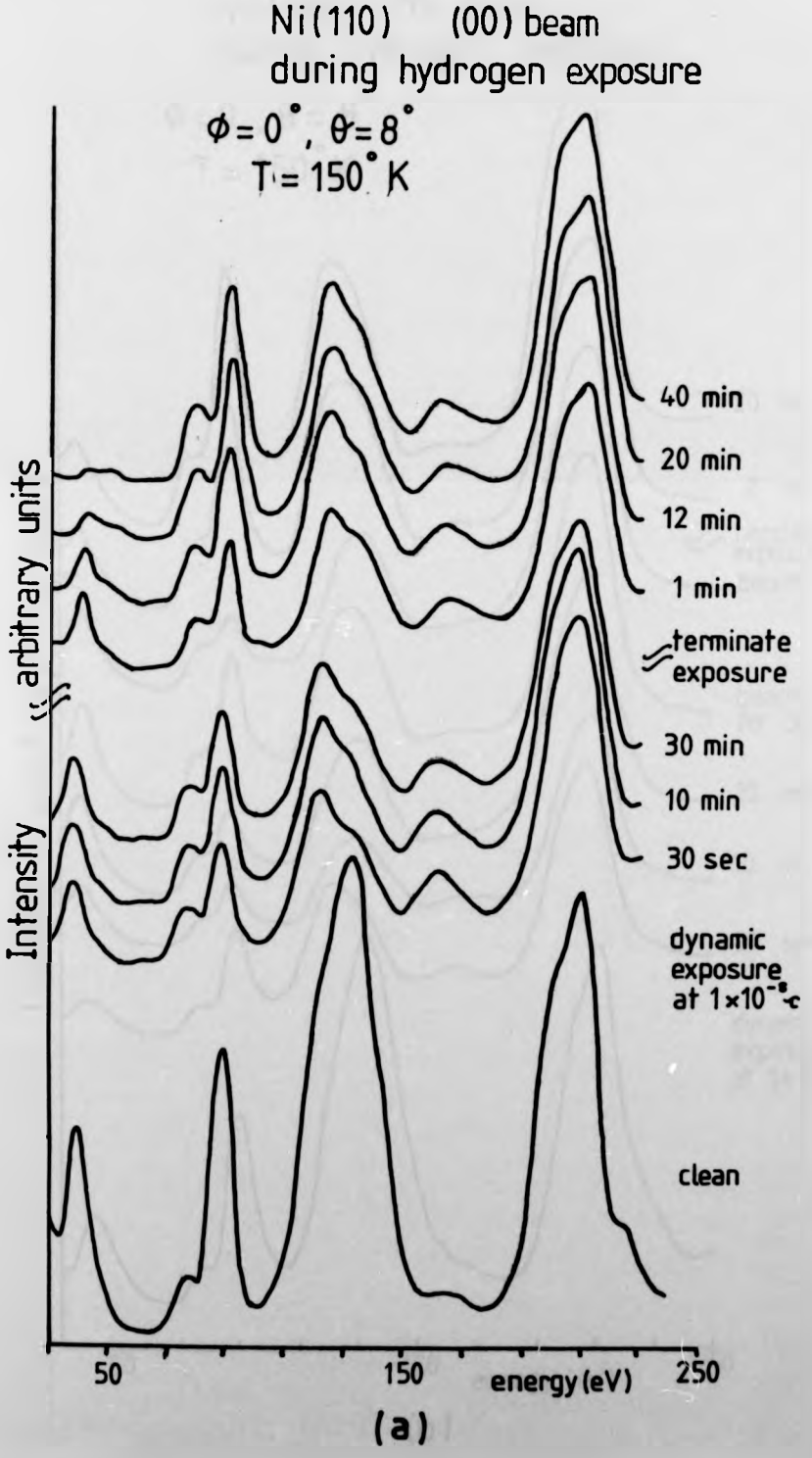

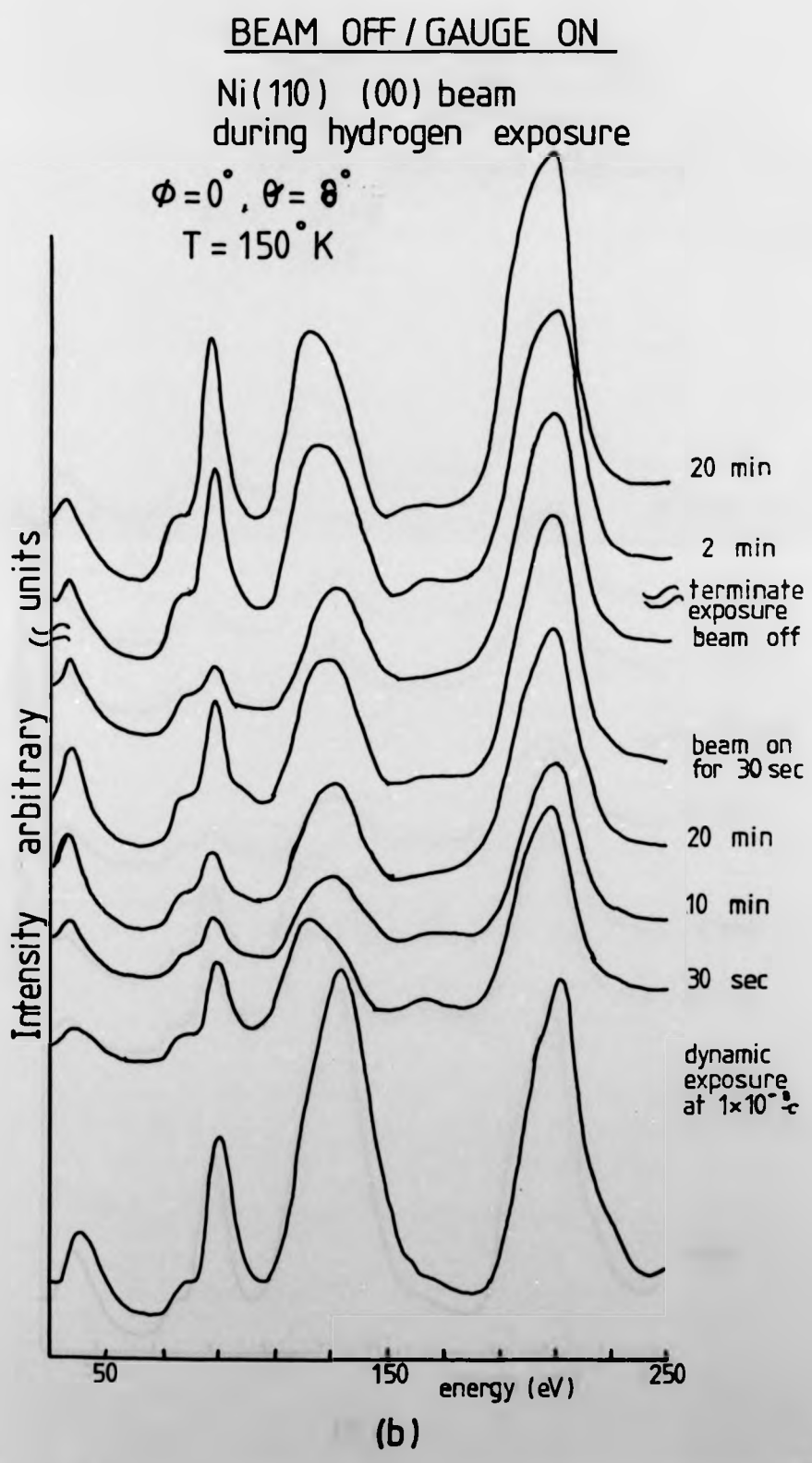
BEAM OFF / GAUGE ON
Ni(110) (00) beam
during hydrogen exposure
Φ = 0°, θ = 8°
T = 150°K
Intensity arbitrary units
20 min
2 min
terminate exposure beam off
beam on for 30 sec
20 min
10 min
30 sec
dynamic exposure at 1×10⁻⁸
50
150
250
energy (eV)
(b)

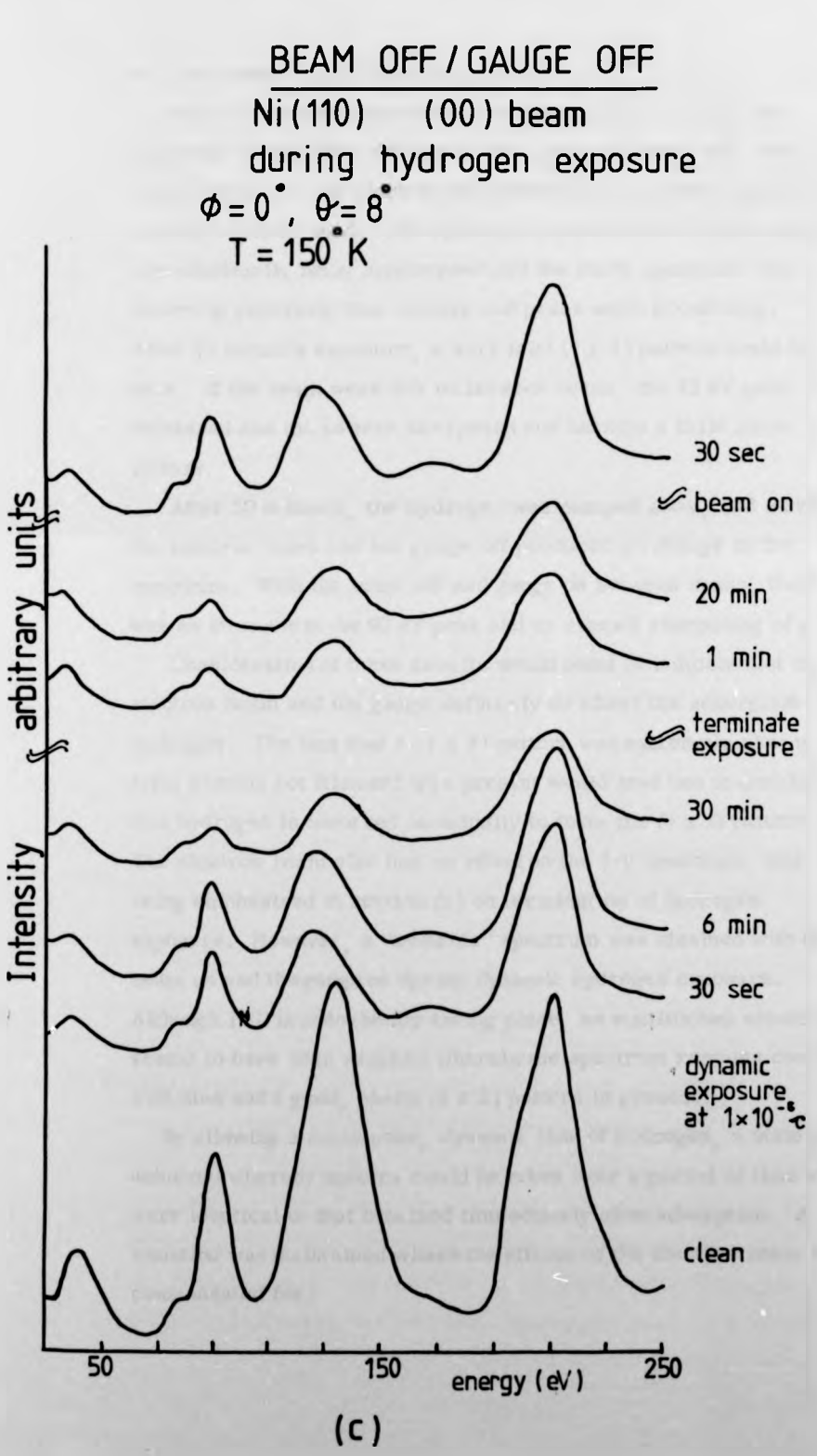
BEAM OFF / GAUGE OFF
Ni(110) (00) beam
during hydrogen exposure
$\phi = 0^\circ$, $\theta = 8^\circ$
$T = 150^\circ K$
30 sec
beam on
20 min
1 min
terminate exposure
30 min
6 min
30 sec
dynamic exposure at 1×10^{-6} c
clean
Intensity
arbitrary units
50
150
250
energy (eV)

(c)

(c) Ion gauge off and electron beam off:-

After 90 seconds exposure to hydrogen, (Fig. 4.1(c)), the spectrum looked very similar to the "gauge on/beam off" scan. After 6 minutes, the pattern was observed but no extra spots or streaks could be seen. The spectrum showed that the 92 eV peak was continually being suppressed and the whole spectrum was becoming generally less intense and peaks were broadening. After 15 minutes exposure, a very faint (1 x 2) pattern could be seen. If the beam were left on between scans, the 92 eV peak increased and the pattern sharpened and became a little more intense.

After 50 minutes, the hydrogen was pumped away, and leaving the electron beam and ion gauge off produced no change in the spectrum. With the beam off and gauge on between scans, there was an increase in the 90 eV peak and an overall sharpening of peaks.

Consideration of these results would seem to indicate that the electron beam and ion gauge definitely do affect the adsorption of hydrogen. The fact that a (1 x 2) pattern was extremely slow to form when no hot filament was present would lead one to conclude that hydrogen is adsorbed atomically to form the (1 x 2) pattern. The electron beam also has an effect on the I-V spectrum, this being emphasised in section (a) on termination of hydrogen exposure. However, a "reliable" spectrum was obtained with the beam on and the gauge on during dynamic hydrogen exposure. Although ESD is undoubtedly taking place, an equilibrium situation seems to have been reached whereby the spectrum remains constant with time and a good, sharp (1 x 2) pattern is present.

By allowing a continuous, dynamic flow of hydrogen, a state was achieved whereby spectra could be taken over a period of time which were identical to that obtained immediately after adsorption. A situation was maintained where the effects of the electron beam were compensated for.

It is interesting to note that when, in the early part of this work, mercury contamination of the specimen occurred, it was not possible to form any ordered overlayer, and only a (1 x 1) pattern was visible.

4.2.2 The nickel-ethylene system

One of the first considerations of an experiment attempting ethylene adsorption must be the question of how it is possible to know whether C_2H_4 is the actual species adsorbed, or whether dehydrogenation to C_2H_2 or even to carbon has occurred. An obvious precaution is to adsorb the gas with all hot filaments turned off and subsequently use a low beam current to monitor the LEED pattern and I-V spectra. Unfortunately, the latter condition cannot be met very successfully, since an incident beam current of $\sim 1\ \mu A$ is necessary to provide a pattern which is visible on the screen and a reasonable signal in the Faraday cup. However, unless the beam has an immediate devastating effect before the pattern and beam intensities can be examined, it should be possible to be aware at least of its effect.

Despite a variety of conditions of exposure of the cooled or room temperature Ni(110) surface to C_2H_4, no extra diffraction features were formed (or at least were not detectable), and the integral order beam I-V data were modified only by a general broadening of peaks and an overall decrease in peak intensities.

The Ni(100) surface did, however, show extra diffraction features. After exposures of ~ 5 L at 5×10^{-8} T at 150° K, $(\pm \frac{1}{2}, \pm \frac{1}{2})$ spots characteristic of the $(\sqrt{2} \times \sqrt{2})$ R 45° structure were observed. These extra beams were extremely diffuse, merging indistinctly into the greatly increased background intensity. It was impossible to take any I-V spectra for these extra spots at this temperature, since their position could not be precisely located. On allowing the sample to warm to 293° K, the extra spots became somewhat less diffuse, but by no means sharp. On warming a similarly exposed sample to $\sim 400^{\circ}$ K, Horn et al. (15) report a conversion to a (2 x 2)-C overlayer

It is interesting to note that when, in the early part of this work, mercury contamination of the specimen occurred, it was not possible to form any ordered overlayer, and only a (1 x 1) pattern was visible.

4.2.2 The nickel-ethylene system

One of the first considerations of an experiment attempting ethylene adsorption must be the question of how it is possible to know whether C_2H_4 is the actual species adsorbed, or whether dehydrogenation to C_2H_2 or even to carbon has occurred. An obvious precaution is to adsorb the gas with all hot filaments turned off and subsequently use a low beam current to monitor the LEED pattern and I-V spectra. Unfortunately, the latter condition cannot be met very successfully, since an incident beam current of $\sim 1\ \mu A$ is necessary to provide a pattern which is visible on the screen and a reasonable signal in the Faraday cup. However, unless the beam has an immediate devastating effect before the pattern and beam intensities can be examined, it should be possible to be aware at least of its effect.

Despite a variety of conditions of exposure of the cooled or room temperature Ni(110) surface to C_2H_4, no extra diffraction features were formed (or at least were not detectable), and the integral order beam I-V data were modified only by a general broadening of peaks and an overall decrease in peak intensities.

The Ni(100) surface did, however, show extra diffraction features. After exposures of ~ 5 L at 5×10^{-8} T at 150° K, $(\pm \frac{1}{2}, \pm \frac{1}{2})$ spots characteristic of the $(\sqrt{2} \times \sqrt{2})$ R 45° structure were observed. These extra beams were extremely diffuse, merging indistinctly into the greatly increased background intensity. It was impossible to take any I-V spectra for these extra spots at this temperature, since their position could not be precisely located. On allowing the sample to warm to 293° K, the extra spots became somewhat less diffuse, but by no means sharp. On warming a similarly exposed sample to $\sim 400^{\circ}$ K, Horn et al. (15) report a conversion to a (2 x 2)-C overlayer

and this was also observed in this present work. Casalone et al. (20) report the formation of a $(\sqrt{2} \times \sqrt{2})$ R 45° pattern upon exposure at room temperature, and find that the clarity is maximised after 5 L exposure. Upon prolonged exposures they report a p(2 x 2) pattern with extinctions in the $([\frac{2n+1}{2}], 0)$, $(0, [\frac{2n+1}{2}])$ positions, characteristic of a carbon overlayer. In the present work, the p(2 x 2) structure was never observed to form merely on exposure of either the cooled or room temperature specimen to C_2H_4, even though exposures as large as 400 L were tried. The p(2 x 2) structure was formed only when the sample temperature was taken to ~400° K, or when the electron beam had been incident on the surface for long periods. The adsorbate is then thought to be carbon. Both Horn and Casalone report that the LEED structure ($(\sqrt{2} \times \sqrt{2})$R 45°) is strongly sensitive to beam effects and this was definitely found to be the case in this current work. For example, it has been mentioned above that the $(\sqrt{2} \times \sqrt{2})$ R 45° pattern, formed at 150° K, sharpened somewhat on allowing the specimen to warm up to room temperature; however, it must be pointed out that this was done with the electron beam switched on. Repeating the experiment with the beam off gave rise to half order spots only very slightly more distinct than those at 150° K. Heating the sample rapidly by electron bombardment to room temperature, thus greatly reducing the time of exposure to the beam, also resulted in half order spots which were only marginally more distinct than at 150° K. After the electron beam had been incident on the surface for 10 minutes following warming of the sample to room temperature after 40 L exposure to C_2H_4, a faint p(2 x 2) pattern became apparent and grew clearer and more intense with continued exposure to the electron beam (Plate 4.1). Repeating this exposure and warming procedure, with the electron beam off as much as possible, gave rise only to the slight sharpening of the blurred $(\pm \frac{1}{2}, \pm \frac{1}{2})$ spots of the $(\sqrt{2} \times \sqrt{2})$R 45° pattern previously mentioned.

Ni (100)

5 L C_2H_4, $\Phi = 45^\circ$, 127 eV

40 L C_2H_4, $\Phi = 45^\circ$, 127 eV

150° K

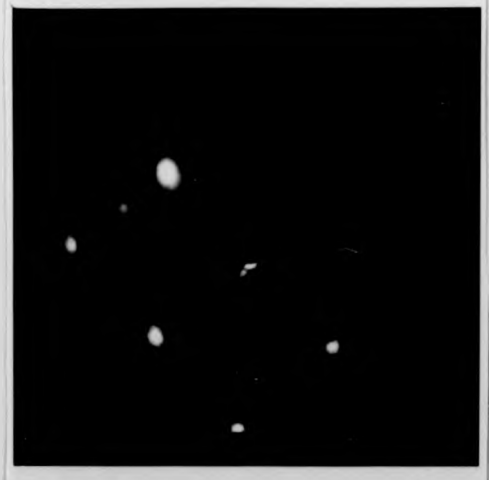

40 L C_2H_4 + 10 mins. electron beam at 150° K, $\Phi = 45^\circ$, 127 eV

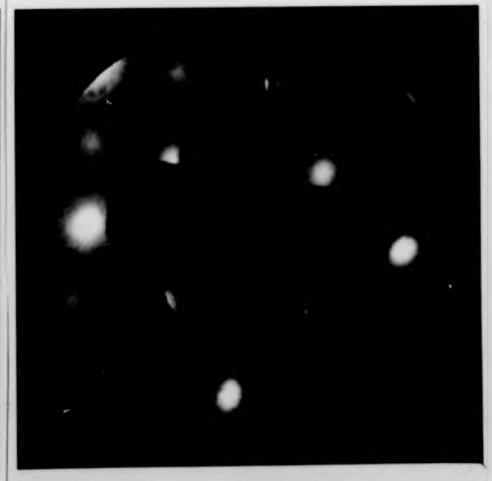

120 L C_2H_4 + 5 mins. electron beam at 290° K, $\Phi = 0^\circ$, 59 eV

PLATE 4·1

Mass spectra were taken at various stages during all adsorption experiments (Fig. 4.2(a)). The position of the C_2H_4 peak at mass number 28 made contamination by either CO or N_2 rather difficult to detect; however, the presence of peaks at mass numbers 16, 17 and 27, and their absence at 14 and 44, was, at least, an indication of the presence of C_2H_4 as opposed to totally CO or nitrogen. When C_2H_4 exposures were terminated, the pressure returned to the 10^{-10} τ region within $1\frac{1}{2}$ minutes and a spectrum similar to the UHV spectrum of Fig. 3.3 was obtained, with a very slightly increased 28 peak. On allowing the specimen to warm to room temperature by radiation and conduction alone, only the mass 28 peak was observed to grow (Fig. 4.2(b)); however, rapid heating by electron bombardment revealed a large peak at mass 2 (molecular hydrogen) at a temperature of $\sim 350^{\circ}$ K (Fig. 4.2(c)). This could well indicate dehydrogenation of the ethylene, perhaps to acetylene. When the sample was heated up to a temperature of 600° K, no further hydrogen was seen to evolve, even though more dehydrogenation might be expected to occur.

The proposition that the electron beam has a strong effect on the state of the adsorbed hydrocarbon is strengthened by the inability to obtain reliably consistent I-V spectra for any of the beams. A dynamic exposure resulted in a greatly increased background and a large reduction in integral order beam intensities; therefore, static exposures, typically of 5-40 L, were used. After 5 L exposure at 150° K, the (10) beam spectrum of Fig. 4.3(a) was obtained. Then, after 40 L exposure and warming to room temperature (electron beam on), the (10) beam spectrum of Fig. 4.3(c) was obtained. A faint p(2 x 2) pattern was, at that time, apparent. For comparison, the (10) beam spectrum, obtained from the Ni(100) (2 x 2)C-p4g structure and the clean surface (10) beam spectrum are shown. (00) beam spectra taken after 5 L C_2H_4 exposure at 150° K show very little change from clean surface data, apart from

Fig. 4.2

Mass spectra taken

(a) during exposure to ethylene,

(b) on allowing the specimen to warm to room temperature after exposure to ethylene at 150° K,

(c) at a temperature of $\sim 350^{\circ}$ K after exposure to ethylene at 150° K.

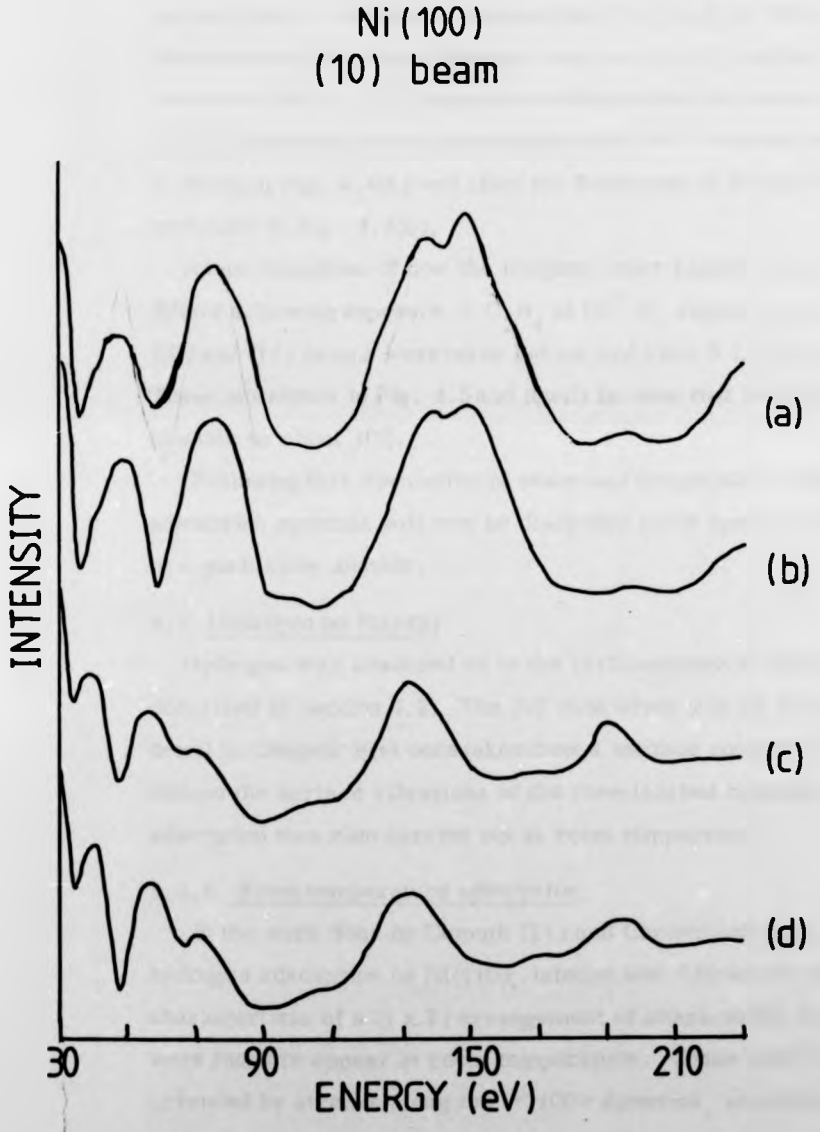

Fig. 4.3

Ni(100) (10) beam I-V spectra taken

(a) after 5 L C_2H_4 exposure at 150° K,

(b) from a clean surface,

(c) after 40 L C_2H_4 exposure and warming to room temperature with the electron beam on,

(d) from the Ni(100)(2x2)C-p4g surface.

an overall drop in intensity and suppression of the peak at ~ 225 eV. However, on further exposure to a total of 40 L C_2H_4 and warming the specimen to room temperature with the beam on, the spectra became more like those obtained from the p(2 x 2) carbon structure and a (2 x 2) pattern was observed to be gradually forming. An AES spectrum taken immediately after 40 L exposure at 150° K is shown in Fig. 4.4(a) and after the formation of the p(2 x 2) structure in Fig. 4.4(b).

As an indication of how the integral order beams become more diffuse following exposure to C_2H_4 at 150° K, angular profiles of the (00) and (11) beams were taken before and after 5 L exposure. These are shown in Fig. 4.5 and it will be seen that both beams are broader by about 10%.

Following this discussion of beam and temperature effects, the adsorption systems will now be discussed more specifically, although in a qualitative manner.

4.3 Hydrogen on Ni(110)

Hydrogen was adsorbed on to the (110) surface of nickel as described in Section 4.2. The I-V data which will be discussed in detail in Chapter Five were taken from a surface cooled to 150° K to reduce the surface vibrations of the chemisorbed hydrogen. Some adsorption was also carried out at room temperature.

4.3.1 Room temperature adsorption

In the work done by Demuth (21) and Christmann et al. (22) on hydrogen adsorption on Ni(110), intense new diffraction spots characteristic of a (1 x 2) arrangement of atoms on the surface were found to appear at room temperature. These spots were preceded by streaks along the < 100> direction, and the streaks were observed to sharpen with increased hydrogen exposure. Demuth found that these extra features gradually disappeared after termination of the hydrogen pressure. Taylor and Estrup (23) found that room temperature exposure of 0.2 L led to faint streaks which sharpened to a (1 x 2) pattern with continued exposure.

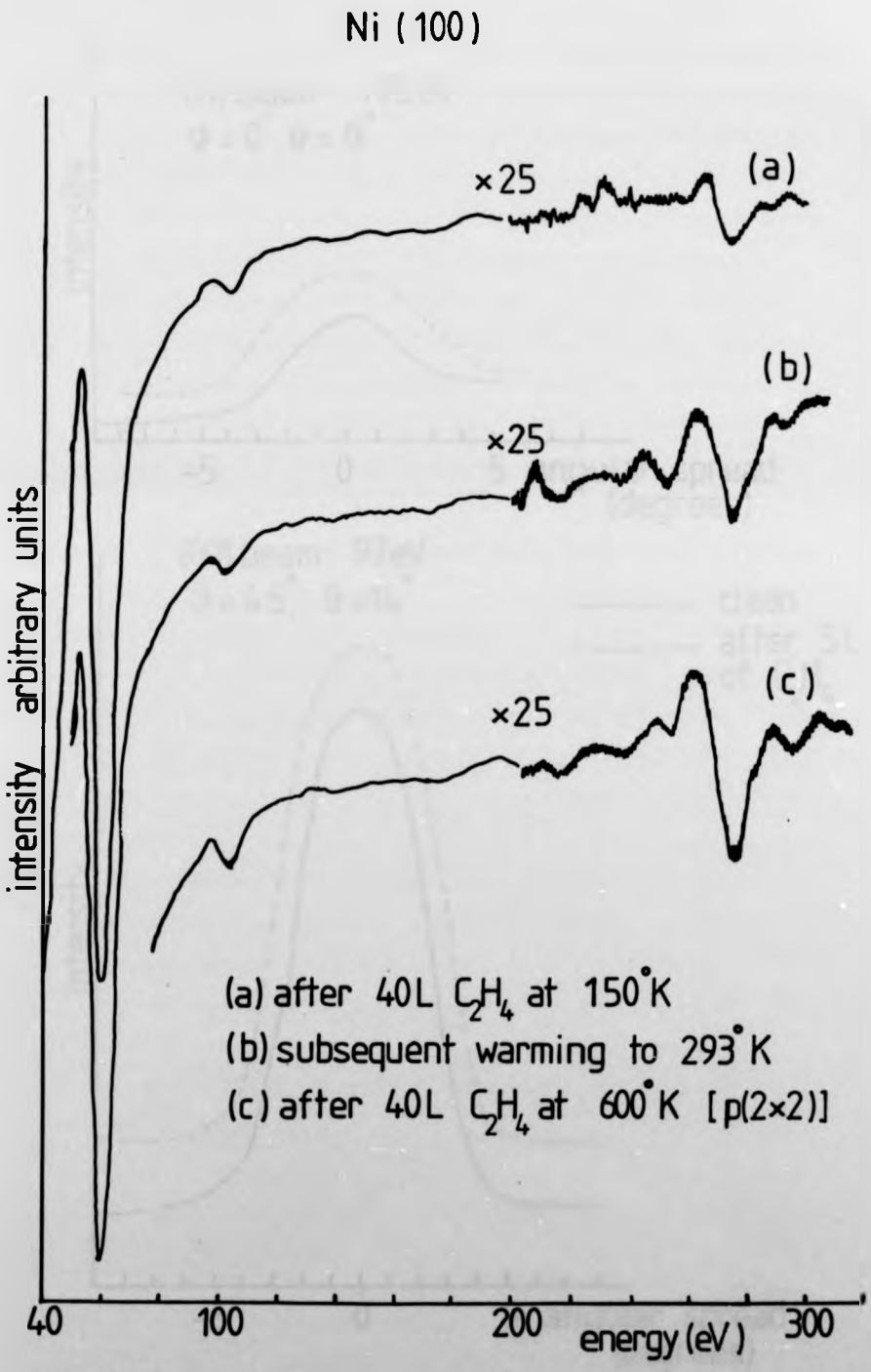

Fig. 4.4

AES spectra taken after the adsorption of ethylene on Ni(100)

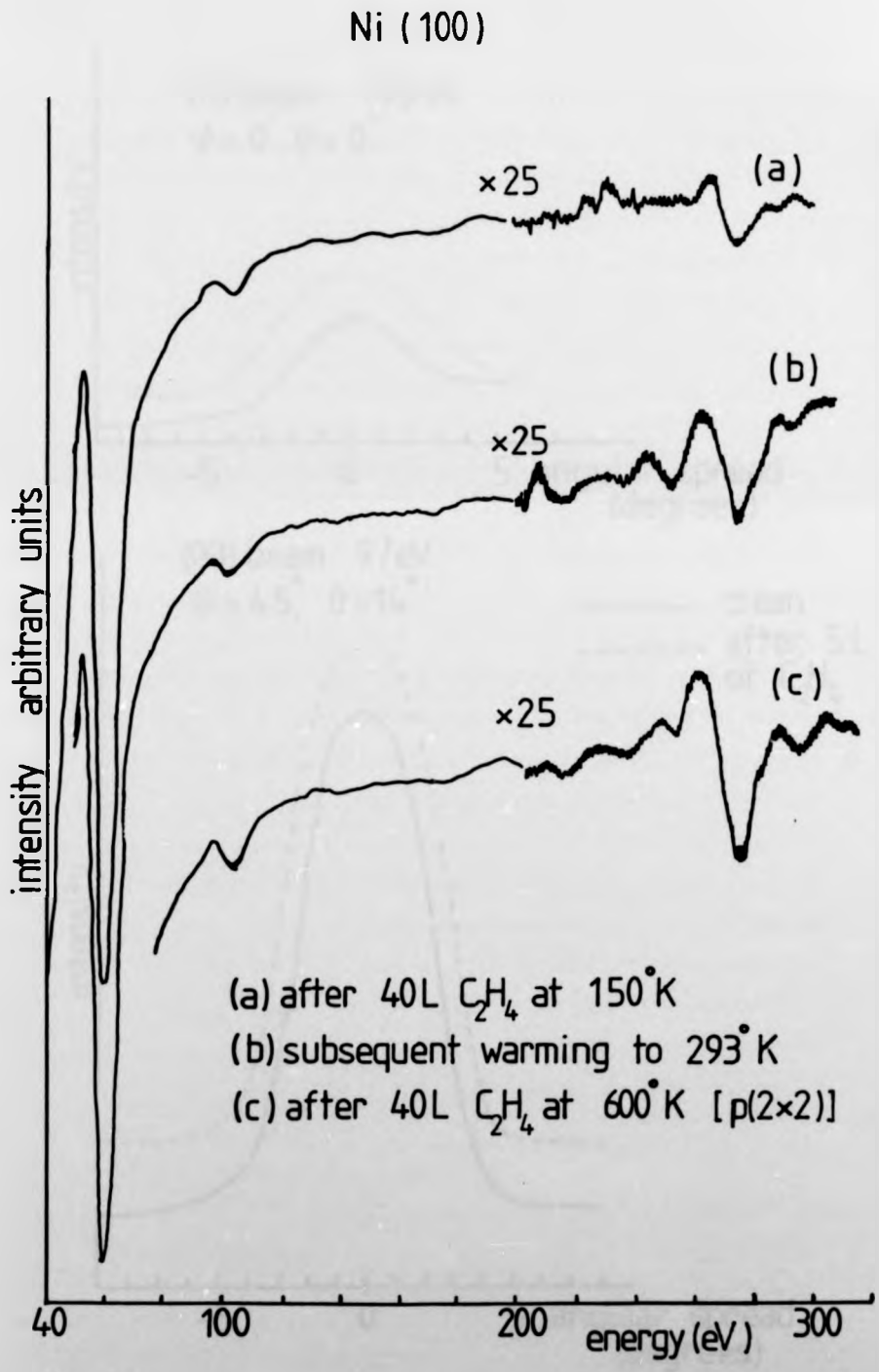

Fig. 4.4

AES spectra taken after the adsorption of ethylene on Ni(100)

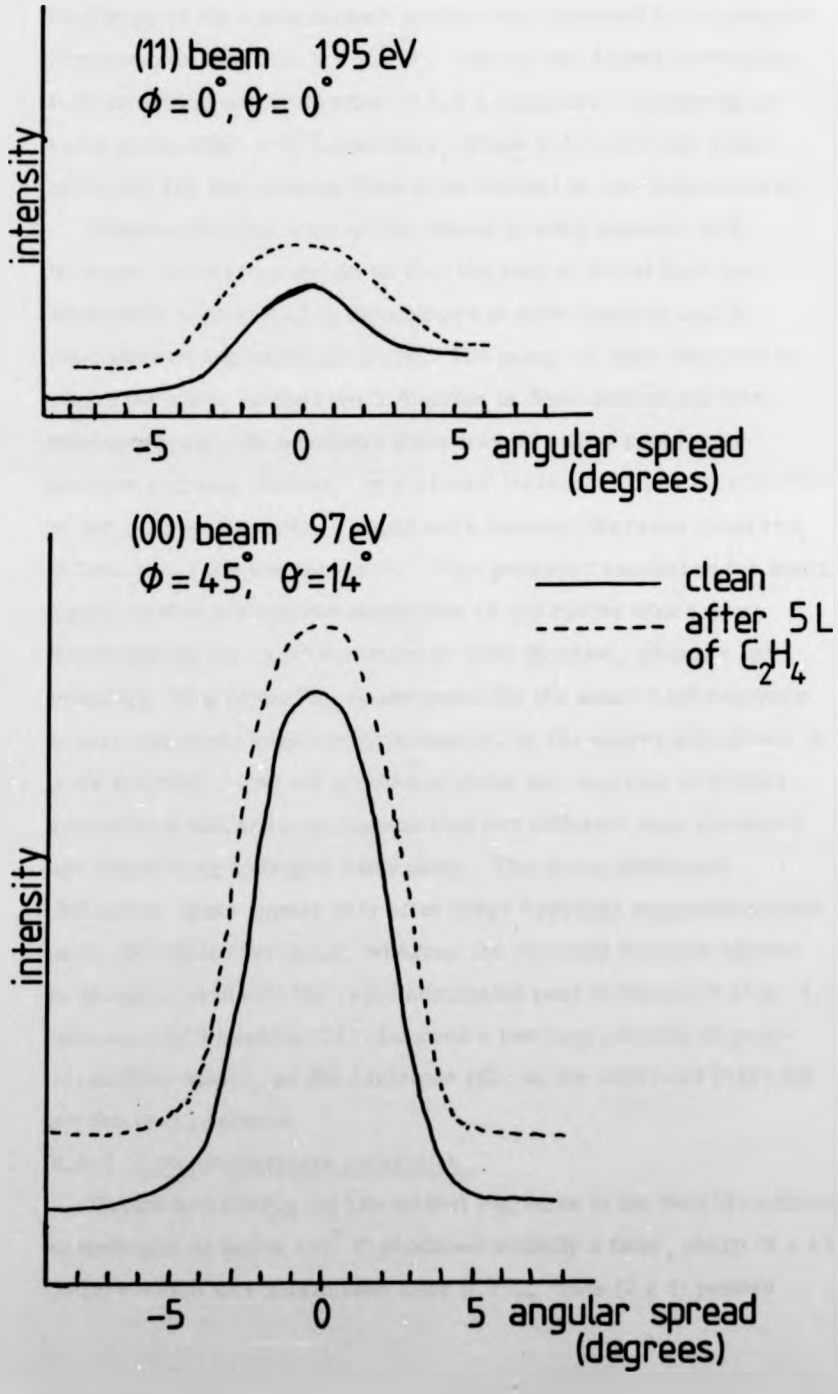

Fig. 4.5

Angular profiles of the clean (00) and (11) beams of Ni(100) compared with the same beams after exposure to 5 L C_2H_4 at 150° K.

In the various adsorption conditions investigated in this work, no change in the clean surface pattern was observed for exposures at pressures less than 5×10^{-9} T. At this and higher pressures, faint streaking occurred after ~0.5 L exposure, sharpening to extra spots after ~10 L exposure, (Plate 4.2), although these spots are far less intense than those formed at low temperatures.

Demuth (21) has studied the change in work function with hydrogen adsorption and found that the rate of initial hydrogen adsorption is indicated by the changes in work function and is dependent on exposure pressure. The pump-off time required to obtain the clean surface work function is dependent on the total exposure time. He found that there was an initial rapid work function increase followed by a slower increase. Upon termination of the hydrogen supply, a rapid work function decrease occurred, followed by a slower decrease. High pressure exposures for short times yielded adsorption-desorption (A-D) cycles which were dominated by the rapid variation in work function, whereas low pressure, long period exposure (even for the same total exposure in torr-seconds) gave cycles dominated by the slower variations in work function. The occurrence of these two separate A-D time constants would seem to suggest that two different rate constants are controlling hydrogen adsorption. The sharp additional diffraction spots appear only after large hydrogen exposures where pump-off cycles are large, whereas the streaked features appear to be associated with the rapid adsorption part of the cycle (Fig. 4.6). Delchar and Tompkins (24) observed a two step process on polycrystalline nickel, as did Lichtman (25) on the (100) and (110) but not the (111) surface.

4.3.2 Low temperature adsorption

Taylor and Estrup (23) found that exposure of the Ni(110) surface to hydrogen at below 170° K produced initially a faint, sharp (2 x 1) pattern which was maximised after 0.7 L. This (2 x 1) pattern

Ni (110) 290°K

CLEAN 118 eV

$\phi = 90^{\circ}$

0·5 L hydrogen

$\phi = 90^{\circ}$

134 eV

10 L hydrogen

$\phi = 0^{\circ}$

166 eV

PLATE 4·2

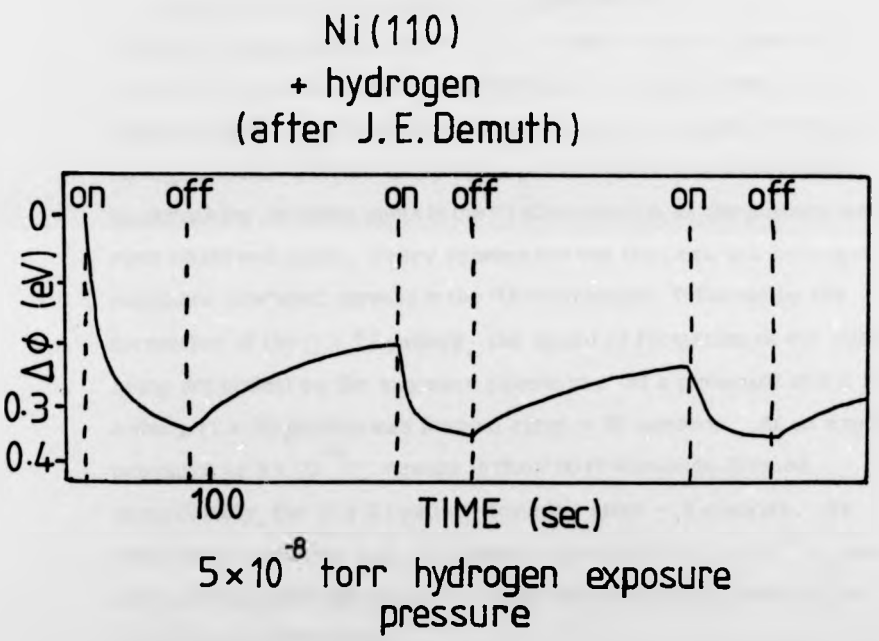

Fig. 4.6

Adsorption/desorption cycles for the Ni(110) + hydrogen system (21)

remained sharp but grew fainter until 2 L, when extinction occurred. Concurrent with the decay of the (2 x 1) pattern, they observed a (1 x 2) pattern which was sharp after 0.7 L and increased in intensity until saturation near 2 L. By raising the pressure above 6.2×10^{-9} τ, the sharp (1 x 2) pattern could be obtained in a few seconds.

In the present work, after 0.5 L exposure at 5×10^{-9} τ, streaking was observed in the $< 1\bar{1}0 >$ and $< 001 >$ directions, followed by the formation of very faint (2 x 1) spots after 0.7 L. Unfortunately, this was only observed on one occasion and was not photographed. Despite many attempts to repeat this experiment, no streaking or extra spots in the $<1\bar{1}0>$ direction of the pattern were ever observed again. Every subsequent low temperature hydrogen exposure produced streaks in the $<001>$ direction, followed by the formation of the (1 x 2) pattern, the speed of formation of the latter being dependent on the exposure pressure. At a pressure of 1×10^{-8} τ, a sharp (1 x 2) pattern was formed after ~ 30 seconds. At an exposure pressure of 5×10^{-9} τ, streaks in the $< 001>$ direction formed immediately, the (1 x 2) pattern forming after ~ 2 minutes. As mentioned in Section 4.2, an exposure pressure of 1×10^{-8} τ was used during the collection of I-V data for the detailed study of the Ni(110) (1 x 2) H system.

After each adsorption experiment, the surface was allowed to warm from 150° K to 293° K either slowly by ceasing cooling, or rapidly by electron bombardment. In both cases, hydrogen at mass 2 was detected by the mass spectrometer. The maximum hydrogen partial pressure always occurred when the temperature of the specimen was between 150° K and 200° K, decreasing to a steady value for higher temperatures. (For the room temperature adsorption system, only a slight hydrogen peak could be detected while heating the specimen to 773° K). It is impossible to be sure whether the hydrogen was desorbed from the specimen or from the cooling coils, but it seems likely to suppose that desorption occurred from all cooled parts of the specimen mount on heating.

4.4 Hydrogen on Ni(100)

Despite many conditions of exposure of the Ni(100) surface to hydrogen, no new diffraction features have been observed in this work. Exposures were given at a large variety of pressure for different lengths of time at both 150^{o} K and 293^{o} K. In case such weak diffraction features had been formed that were undetectable by eye or by camera, the Faraday cup was scanned near the positions where extra diffraction spots might be expected to occur, but no variation in intensity was found.

During dynamic hydrogen exposure at 1×10^{-8} T at 150^{o} K, the (00) beam I-V spectra showed slight changes (Fig. 4.7). The peaks at 58 eV and 130 eV were slightly depressed and even when exposure was terminated, these peaks did not return even gradually to their former intensities relative to the other peaks. Only after flashing to 600^{o} K, where hydrogen at mass 2 was observed to evolve, and then cooling the specimen to room temperature, did the 58 eV and 130 eV peaks return to their former intensities. Christmann et al. (26) found a general decrease in intensity of the I-V profile for the (00) beam upon hydrogen adsorption and suggested that the decrease of the intensities of the Bragg peaks, together with the observed increase of the background intensity, should be ascribed to the formation of (at room temperature) a disordered adsorbed layer, but that an ordered layer might well be found for lower temperature adsorption.

Very recent work by Andersson (27) reports the formation of a quasi-ordered hydrogen structure for adsorption at 200^{o} K. This structure was observed after about 0.5 L hydrogen exposure. The LEED pattern, which is discernible in the primary electron energy range 35-50 eV, is very faint, and the adsorbate induced beams are centred at the (3/2, 1/2) positions and are elongated and curved around the (10) beams. This would seem to indicate that the ordering is partially of uniform character, the LEED pattern being described

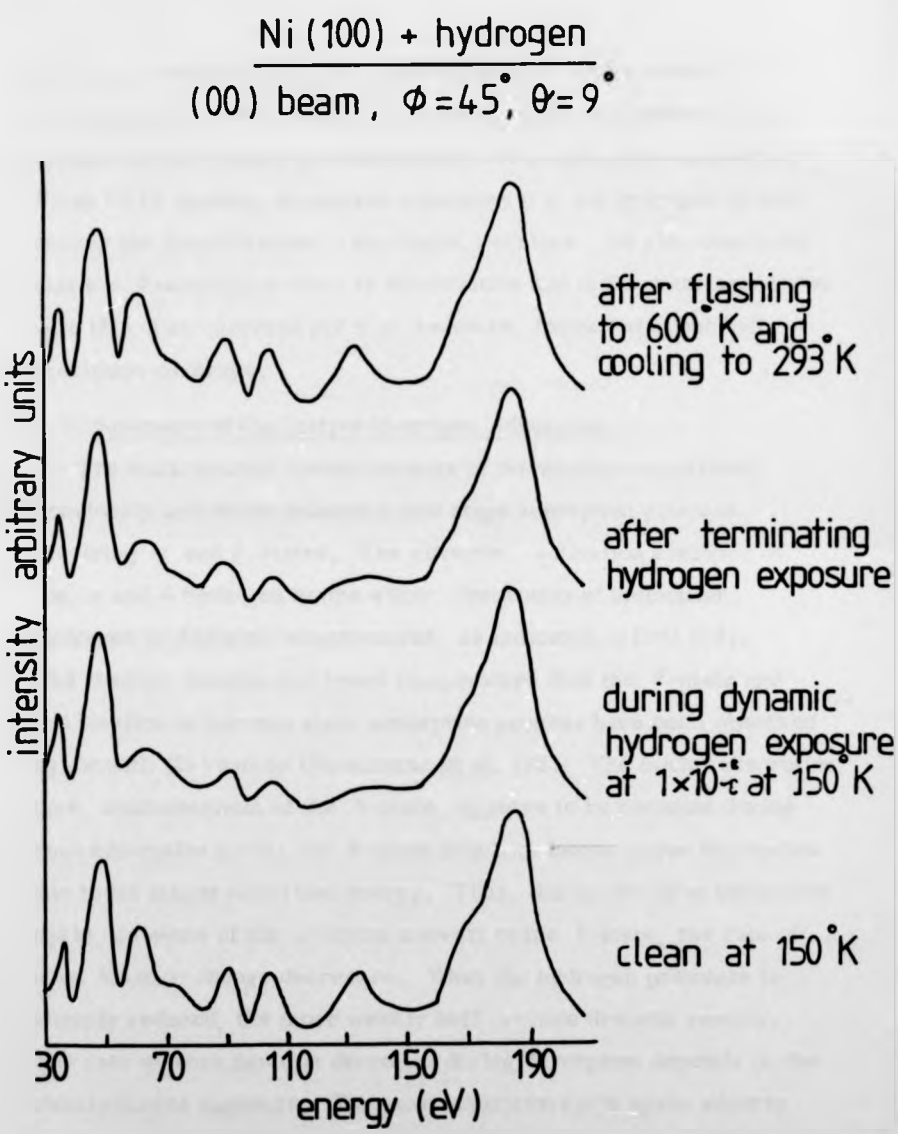

Fig. 4.7

Ni(100) specular beam spectra taken before, during and after exposure to hydrogen at 150° K

as a quasi-ordered p(2 x 2). The diffraction beams decrease in intensity until, after about 5 L exposure, the extra beams are not visible and the pattern is characteristic of a disordered adsorbate. From EELS studies, Andersson concludes that the hydrogen atoms occupy the fourfold sites on the Ni(100) surface. He also concludes that the β-adsorption state is dissociative and is the state associated with this quasi-ordered p(2 x 2) structure, formed at about half maximum coverage.

4.5 Summary of Qualitative Hydrogen Adsorption

The work function measurements of the workers mentioned previously and below indicate a two stage adsorption process involving α and β states. The different activation energies of the α and β hydrogen states allow desorption of molecular hydrogen at different temperatures, as indicated by Ertl (13). The α-state desorbs at a lower temperature than the β-state and the kinetics of this two state adsorption process have been observed by Demuth (21) and by Christmann et al. (22). The initial adsorption rate, characteristic of the α-state, appears to be constant during each adsorption cycle; the β-state requires longer times to populate due to its larger activation energy. Thus, during the first adsorption cycle, as some of the α-states convert to the β-state, the rate of work function change decreases. When the hydrogen pressure is sharply reduced, the more weakly held α-state desorbs readily. The rate of work function decrease during desorption depends on the total hydrogen exposure. The next adsorption cycle again adsorbs hydrogen very rapidly since some hydrogen still exists in the β-state. The α-state fills almost linearly with time until more of the β-state hydrogen is present, thereby decreasing the uptake rate.

The degradation of the specular beam intensity of Ni(110) and permanent alterations in spectra for Ni(100) during hydrogen exposure strongly suggest that β-hydrogen is absorbed into the bulk. Irreversability has been observed in magnetization work by Bauer et al. (28) and in resistivity measurements by Brocker and

Wedler (29). Correlation of electron impact and flash filament desorption data by Gilbreath and Wilson (30) on polycrystalline nickel indicates that the H^+ ion signal terminates at the temperature which coincides with the flash filament desorption states. Thus, absorbed atomic hydrogen at higher temperatures may diffuse to the surface, combine, and desorbas molecular hydrogen. The absorbed, or β-state, of atomic hydrogen then produces the higher temperature molecular hydrogen desorption peaks. The two reported hydrogen states may well, therefore, correspond to adsorbed hydrogen (the α-state) and absorbed hydrogen (the β-state). Molecular orbital calculations by Toya (31) indicate two types of hydrogen adsorbate. One type is simply adsorbed on top of the surface, whilst the other is dissolved in the metal and corresponds to a proton dissolved in the electron gas of the solid.

4.6 Discussion of Ethylene Adsorption

Simple considerations of molecular models suggest that ethylene cannot adsorb molecularly, especially if the interaction is between the π-electrons of ethylene and the d-electrons of nickel, because the H-H distance is always too short (less than 0.95 Å). This kind of bond, implying that the ethylene lies flat on the surface, was recently confirmed by the SCF-X α calculations of Rosch and Rhodin (32). Recent UPS studies by Demuth and Eastman (33) on Ni(111) and polycrystalline nickel indicate that ethylene physisorbed at liquid nitrogen temperature dehydrogenates to acetylene at a temperature of 230° K, while the two hydrocarbons at room temperature show the same UPS spectrum. In the case of C_2H_4 adsorption on Ni(100), the dehydrogenation of C_2H_4 to C_2H_2 could explain the reportedly slower formation of the $(\sqrt{2} \times \sqrt{2})$ R 45° pattern than for C_2H_2 adsorption. They report a smaller amount of carbon, as monitored by AES, for the $(\sqrt{2} \times \sqrt{2})$ R 45° pattern formed by C_2H_4 exposure. This could be due in some way to the presence of hydrogen on the surface, blocking some sites for further adsorption. Once a p(2 x 2) pattern

is formed, subsequent heating causes no further change in pattern but improves the features. Casalone et al. (20) report that after 10 L exposure at C_2H_4 at room temperature ($\sqrt{2} \times \sqrt{2}$) R 45° structure), the ratio of the carbon 272 eV peak to the L_3VV 850 eV nickel peak is 0.25. After 25 L exposure, a p(2 x 2) structure gives the peak ratio of 0.40. The qualitative AES spectra shown in Fig.4.4 clearly show the same trend. If the same species were present on the surface in both cases, a ($\sqrt{2} \times \sqrt{2}$) R 45° pattern, with larger density, ought to follow the p(2 x 2) pattern. A possible explanation could be that the dehydrogenation of the adsorbed species leaves some sort of carbonaceous residue on the surface, and it is this carbon which gives rise to the p(2 x 2) pattern and the C_2H_4 or C_2H_2 to the ($\sqrt{2} \times \sqrt{2}$) R 45° pattern.

The carbon structures discussed below were found to be far more stable and not detectably affected by the electron beam. A qualitative description of their formation follows.

4.7 Formation of a Carbon Structure

4.7.1 Experimental arrangements

Carbon adsorption was achieved by admitting ethylene to the chamber while the specimens were at a temperature greater than 600° K. A variety of exposures was tried and the dosage which eventually proved to give, reliably, the sharpest diffraction features and, in the case of the (100) surface, consistent I-V data, was 40 L at 1 x 10^{-8} τ, statically. During this exposure, the specimens cooled by radiation from 600° K to 450° K. AES spectra taken on cooling revealed a significant carbon peak, the carbon 272 eV to nickel 61 eV peak to peak ratio being approximately 1½ times as large as that shown in Fig.4.4 from the p(2 x 2) "ethylene" structure. For both the (100) and (110) surfaces, new diffraction features were not readily apparent until the samples had cooled below ~ 350° K. On subsequent heating of each sample, no hydrogen was detected to have desorbed in either case. During the adsorptions, however, the mass spectra showed a large H_2 peak, larger than that usually associated with the admittance of C_2H_4 to the chamber.

4.7.2 Carbon on the Ni(110) surface

Although exposure of the Ni(110) surface to C_2H_4 at 150° K or room temperature, followed by heating to temperatures of ~600° K produced no extra diffraction features, exposure of the hot specimen as detailed in 4.7.1 resulted in the formation of the Ni(110) (4 x 5)C structure (Plate 4.3). This structure can be obtained after an exposure of ~ 40 L at any temperature between 500° K and 700° K (specimen cooling during exposure), but is optimised with an initial temperature of 600° K. Schouten et al. (34, 35) in a combined LEED, AES, ellipsometry study of methane on Ni(110), report that for an exposure of 1 torr minute in the temperature range 623° K -673° K, a carbon coverage of approximately half a monolayer (ratio of carbon 272 eV to nickel 848 eV peak to peak heights = 1.2) was indicated after cooling the crystal. Their observed LEED pattern was identical to that found after the adsorption of olefins by Ertl (13) and acetylene by Imelik (36) and also to that observed in the present work, namely the Ni(110) (4 x 5)C. On heating the sample above 650° K for 3 minutes or longer, the (4 x 5) pattern disappeared, leaving the Ni(110) (1 x 1) structure. Presumably, the deposited carbon diffuses into the bulk during this heating. At no stage were any signs of the formation of a graphitic overlayer apparent.

Table 4.1 summarises the LEED data reported in the literature for the adsorption of saturated and unsaturated hydrocarbons on Ni(110). The data were mostly obtained at pressures of 10^{-6} τ - 10^{-7} τ in the presence of electron beams. At room temperature, disordered adsorption has always been seen to occur; at temperatures above ~ 423 K, a (4 x 5) structure is obtained and above ~623° K this reverts to a (1 x 1) pattern, accompanied, eventually, by graphite rings. Maire et al. (37) found an ordered p(2 x 2) pattern after an exposure of 600 L at room temperature, and a (4 x 3) pattern on heating the (2 x 2) structure at base pressure above 423° K.

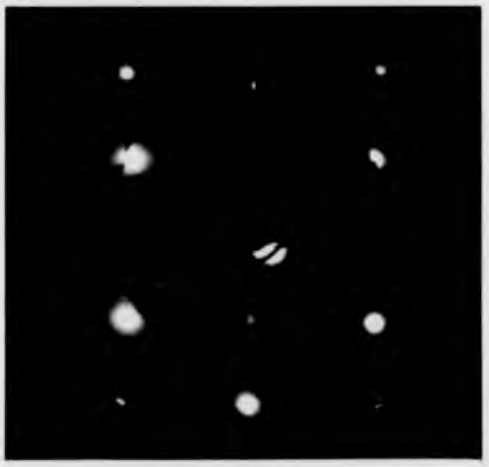

Ni(110) 122 eV

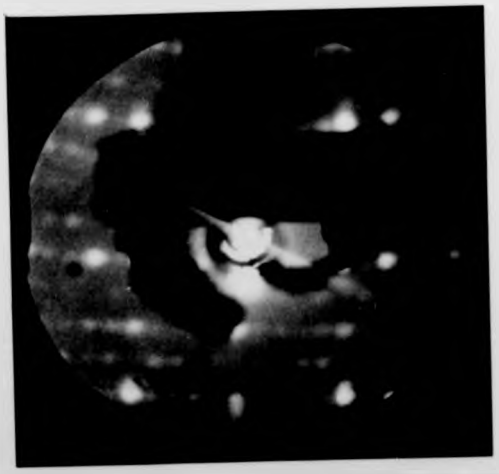

Ni(110)(4×5)C 96 eV

PLATE 4·3

LEED Patterns of Hydrocarbons on Ni(110)

(after Schouten et al. (34))

C_nH_m	20° C	>150° C	>350° C	Ref.
C_2H_2	Disorder	(4x5)(2x1)	(1x1)+graphite	(38)
C_2H_4	Disorder	(4x5)	(1x1)+graphite	(13)
C_2H_4, C_3H_6, C_4H_8	Disorder	(4x5)		(36)
$CH_4 C_2H_6, C_5H_{12}$	Disorder (2 x 2)	(4x3)(4x5)	(1x1)+graphite	(37)
CH_4	-	(2x3)+streaks	(4x5)(1x1)	(34)
C_2H_4	Disorder	(4x5)	(4x5)(1x1)	present work

Table 4.1

Pitkethly (38) reports the reversible formation of a (2 x 1) structure from the (4 x 5) pattern. He suggests that the formation of streaks and extra spots could conceivably be associated with the formation of domains, elongated along the direction of the troughs in the (110) surface, with disorder perpendicular to the troughs; a suggestion of a coverage of 0.4 is made for the (4 x 5) structure.

It can be noted that the (4 x 5) structure is only formed in the temperature range where carbon diffuses into the bulk, it may, perhaps, represent a nickel carbide phase extending over more than one layer. In view of the geometrical arrangement in bulk Ni_3C described by Nagakura (39), reconstruction of Ni(110) upon formation of a surface carbide seems highly probable. A detailed study of LEED I-V data from such a surface would be interesting, but unfortunately, owing to the proximity of the diffraction spots, it is impossible to take data with any degree of certainty of measuring the intensity of one spot alone; if any data could be collected, they could not be tackled easily by any theoretical calculations.

4.7.3 Carbon on the Ni(100) surface

After exposure of the Ni(100) surface to C_2H_4 for 40 L between 600° K and 450° K, the formation of what seemed to be a p(2 x 2) pattern occurred; the diffraction features became much clearer and the background less intense on cooling below $\sim 350^{\circ}$ K. A notable feature of this p(2 x 2) structure is that, at low energies, i.e. where the (11) beam is just visible on the screen, it could quite easily be mistaken for the $(\sqrt{2} \times \sqrt{2})$ R 45° pattern. On increasing the incident beam energy, however, it is obvious that there is, in fact, a (2 x 2) pattern present but that the $(\frac{2n+1}{2}, 0)$ $(0, \frac{2n+1}{2})$ spots are missing at normal incidence. This provides a valuable clue as to the possible structures of the overlayer and, since the acquisition of the I-V curves for several beams proved possible, these results will be discussed in detail in Chapter Six. On heating at temperatures of $\sim 800^{\circ}$ K, the formation of a (1 x 1) pattern occurred.

Since this chapter deals with the qualitative aspects of adsorption, it is, perhaps, desirable to emphasise here the conclusions arrived at concerning the carbon adsorption conditions and beam effects as revealed mainly by the I-V spectra. These can be most clearly detailed as follows:-

(1) A p(2 x 2) pattern was observed to form on the Ni(100) surface after an exposure to C_2H_4 of 40 L ± 20% with the specimen temperature cooling from 600°K. This pattern formed consistently for such an exposure, whether for a long time at a low pressure or vice versa, irrespective of whether the exposure was static or dynamic. However, from previous experience gained from adsorption of other gases, an exposure pressure of greater than 5×10^{-9} τ was felt to be necessary, since for lower pressures it is rather doubtful that one can be sure that the increase in pressure is not due, in part, to the valving or switching off of the ion pump. On the present system, switching or valving off the ion pump causes the base pressure of 1 or 2×10^{-10} τ to rise to 7 or 8×10^{-10} τ after about 2 minutes, the major contaminant being argon. An exposure pressure of 1×10^{-8} τ was found to be good as far as lack of contamination was concerned; also, since a variety of exposures was tested, the relatively long time required for 1 L exposure at this pressure (100 seconds) made the exposures more accurately obtainable. The diffusion pump which was used to pump away the C_2H_4 was far more efficient when coping with a pressure of 1×10^{-8} τ than with pressures in the 10^{-7} τ or 10^{-6} τ regions, and a base pressure of 2×10^{-10} τ could be reached from 1×10^{-8} τ C_2H_4 by use of this pump and then the ion pump within about 2 minutes.

(2) The presence of the electron beam or any hot filament was not found to have any detectable effect on the adsorption of carbon. An exposure of 40 L was still needed to produce the p(2 x 2) pattern, regardless of whether the beam or filaments were on or off.

(3) I-V spectra were taken at intervals after the specimen had cooled to room temperature (beam off during cooling) and were not found to change with time, even with the beam on between scans. The electron beam had no noticeable effect on the spectra, even after periods of incidence as long as $1\frac{1}{2}$ hours.

4.8 Summary

In this chapter, an attempt has been made to describe the conditions in which the adsorption of hydrogen, ethylene and carbon on the Ni(110) and (100) faces was carried out. Although there has been no quantitative study of electron stimulated adsorption or desorption, these effects have been allowed for and a qualitative interpretation of their effect on the systems studied has been made.

Demuth (21) obtained a p(2 x 2) carbon structure upon adsorption and subsequent cracking of CO on Ni(100). The "missing spots" were not reported, but were seen by Isett and Blakely (40) upon segregation of carbon to the Ni(100) surface. Hence it is clear that the "missing spot" structure is characteristic of carbon adsorption rather than of ethylene adsorption.

The I-V spectra presented and discussed in the following chapters can now, more certainly, be considered reliable data from the systems under examination.

CHAPTER FOUR

REFERENCES

1. P.C. Stair & G.A. Somorjai, Chem. Phys. Lett., 41 (1976) 391.
2. L.L. Kesmodel, R.C. Baetzold & G.A. Somorjai, Surface Sci., 66 (1977) 299.
3. L.L. Kesmodel, L.H. Dubois & G.A. Somorjai, Chem. Phys. Lett., 56 (1978) 267.
4. T.E. Fischer & S.R. Kelemen, Surface Sci., 69 (1977) 485.
5. G. Broden, T. Rhodin & W. Capehart, Surface Sci., 61 (1976) 143.
6. R. Ducros, M. Housely, M. Alnot & A. Cassuto, Surface Sci., 71 (1978) 433.
7. J. Erkelens & Th.J. Liefkens, J. Catalysis, 8 (1967) 36.
8. B.A. Morrow & N. Sheppard, Proc. Roy. Soc. (London), A3111 (1969) 391.
9. L. Whalley, B.J. Davis & R.L. Moss, Trans. Faraday Soc., 66 (1970) 3143.
10. P.W. Selwood, in: Adsorption and Collective Paramagnetism. Academic Press, New York (1969).
11. G.A. Martin, G. Dalmai-Imelik & B. Imelik, in:Adsorption-Desorption Phenomena, ed. F. Ricca. Academic Press, New York (1972) 433.
12. G. Dalmai-Imelik & J.C. Bertolini, Compt. Rend.(Paris), C270 (1970) 1079.
13. G. Ertl, in:Molecular Processes on Solid Surfaces, eds. E. Drauglis, R.D. Gretz & R.I. Jaffe. McGraw-Hill, (1969) 155.
14. J.E. Demuth & D.E. Eastman, Phys. Rev. Lett., 13 (1976) 1523; J.E. Demuth, Chem. Phys. Lett., 45 (1977) 12.
15. K. Horn, A.M. Bradshaw & K. Jacobi, J. Vac. Sci. & Technol., 15 (1978) 575.
16. J.E. Demuth, Surface Sci., 69 (1977) 365.
17. R.A. Zuhr &J.B. Hudson, Surface Sci., 66 (1977) 405.
18. D. Menzel, Surface Sci., 47 (1975) 370.

19. R. Jaeger & D. Menzel, Surface Sci., 63 (1977) 232.

20. G. Casalone, M.G. Cattania, M. Simonetta & M. Tescari, Surface Sci., 62 (1977) 321.

21. J.E. Demuth, Ph.D. Thesis, Cornell University, (1973).

22. K. Christmann, O. Schober, G. Ertl & M. Neumann, J. Chem. Phys., 60 (1974) 4528.

23. T.N. Taylor & P.J. Estrup, J. Vac. Sci. & Technol., 11 (1974) 244.

24. T.A. Delchar & F.C. Tompkins, Surface Sci., 8 (1967) 165.

25. D. Lichtman, Surface Sci., 9 (1968) 325.

26. K. Christmann, G. Ertl & O. Schober, Surface Sci., 40 (1973) 61.

27. S. Andersson, Chem. Phys. Lett., 55 (1978) 185.

28. E. Bauer, Surface Sci., 5 (1966) 152.

29. F.T. Bröcker & G. Wedler, Disc. Faraday Soc., 41 (1966) 87.

30. W.P. Gilbreath & D.E. Wilson, J. Vac. Sci., 8 (1971) 45.

31. T. Toya, J. Res. Inst. Catalysis, Hokkaideo Univ., 6 (1958) 308; 8 (1960) 209; 10 (1962) 236.

32. N. Rosch & T.N. Rhodin, Faraday Discussion, 58 (1974) 28.

33. J.E. Demuth & D.E. Eastman, Phys. Rev. Lett., 32 (1974) 1123.

34. F.C. Schouten, E.W. Kaleweld & G.A. Bootsma, Surface Sci., 63 (1977) 460.

35. F.C. Schouten, E. Te Brake, O.L.J. Gizeman & G.A. Bootsma, Surface Sci., 74 (1978) 1.

36. G. Imelik, discussion remark in ref. 37.

37. G. Maire, J.R. Anderson & B.B. Johnson, Proc. Roy. Soc., (London), A320 (1976) 227.

38. R.C. Pitkethly, in: Chemisorption and Catalysis, ed. P. Hepple. Elsevier, Amsterdam (1971) 98.

39. S. Nagakura, J. Phys. Soc. Japan, 12 (1957) 482; 13 (1958) 1005.

40. L.C. Isett & J.M. Blakely, Surface Sci., 47 (1975) 645.

CHAPTER FIVE

THE CLEAN Ni(110) AND Ni(110)(1x2)H SURFACES

5.1 Introduction

In this chapter, extensive I-V data are presented for the Ni(110)(1x2)H structure and possible models for this system are discussed. Firstly, however, I-V spectra for the clean Ni(110) surface are shown and compared with the results of other workers to provide confidence in the reliability of the subsequent hydrogen adsorption data. All results presented here were obtained using the procedures described in Chapters Three and Four.

5.2 The Clean Ni(110) Surface

5.2.1 Experimental observations

Both before and after the acquisition of LEED I-V spectra, surface cleanlinesss was always monitored by means of AES. A typical clean surface AES spectrum is shown in Fig. 5.1. The arrows indicate diffraction features, or temperature dependent peaks, which, in the early 1970's, caused much confusion as their transient nature led to the belief that they were due to ill-defined impurities, although work function measurements rendered this unlikely. These diffraction features are dependent on the temperature of the specimen, their intensity decreasing with increasing temperature (1), and they also appear to be sensitive to the degree of surface order and disordered contamination ; however, they do seem to be insensitive to the presence of well-ordered adsorbates and to the surface crystallography. These diffraction peaks have been reported widely, notably by Becker and Hagstrum (2), Netzer and Prutton (3) and McDonnell et al. (4). Their presence here is noted as an indication of the order of the surface.

A clean surface LEED pattern is shown in Plate 5.1. The convention for beam and azimuthal indexing is given in Fig. 5.2.

Some I-V spectra were taken with the specimen at room temperature and compared with those taken at 150° K. Apart from an overall reduction in peak intensity of ~ 20% for the warmer specimen, no

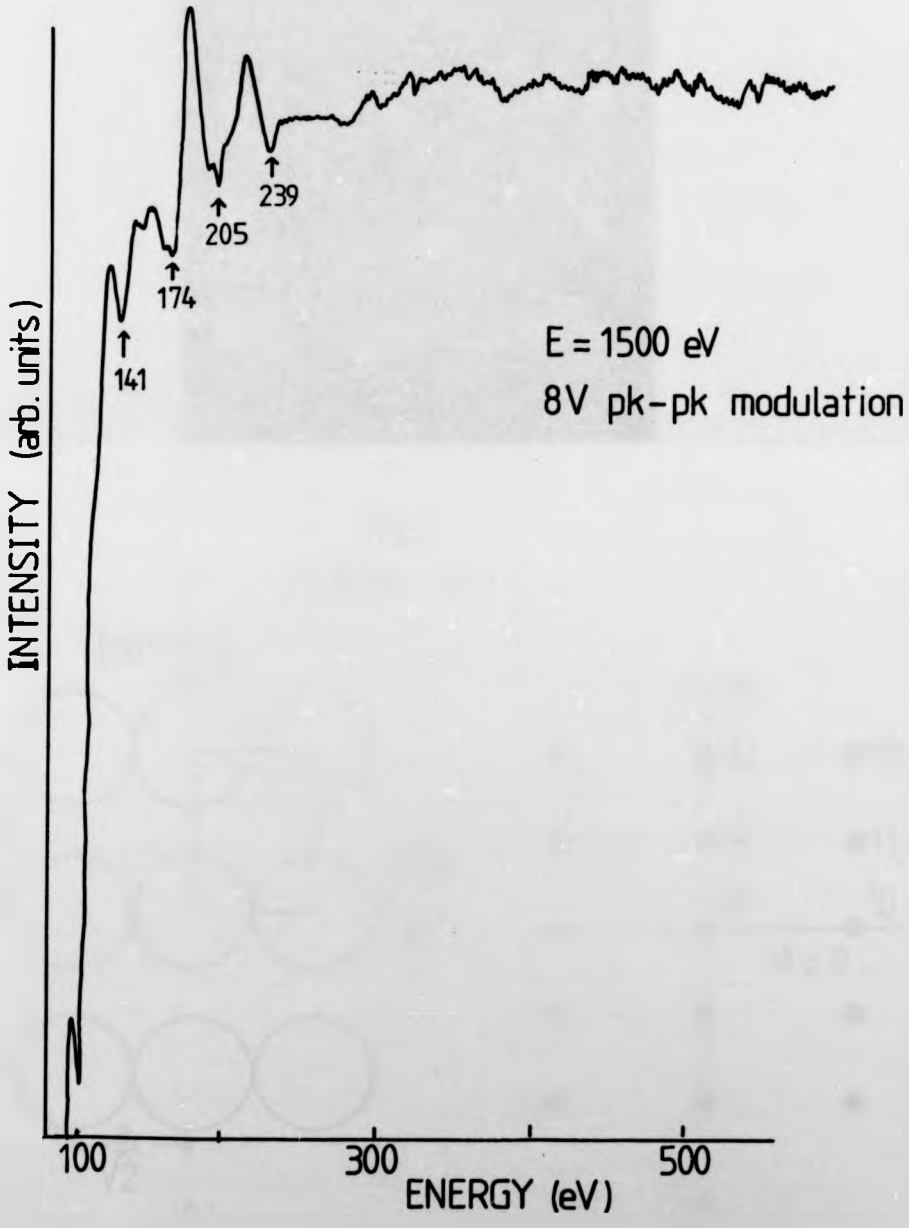

Fig. 5.1

AES spectrum from clean Ni(110). The arrows indicate diffraction peaks.

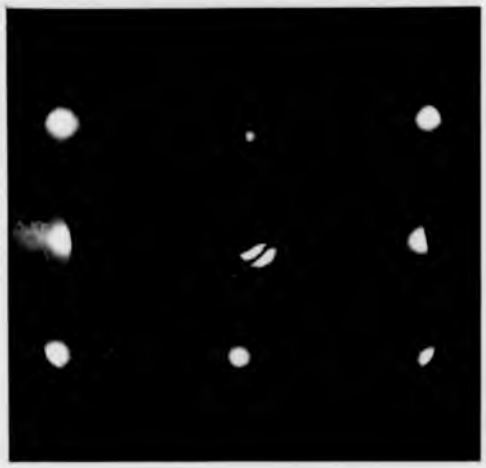

90 eV

PLATE 5·1

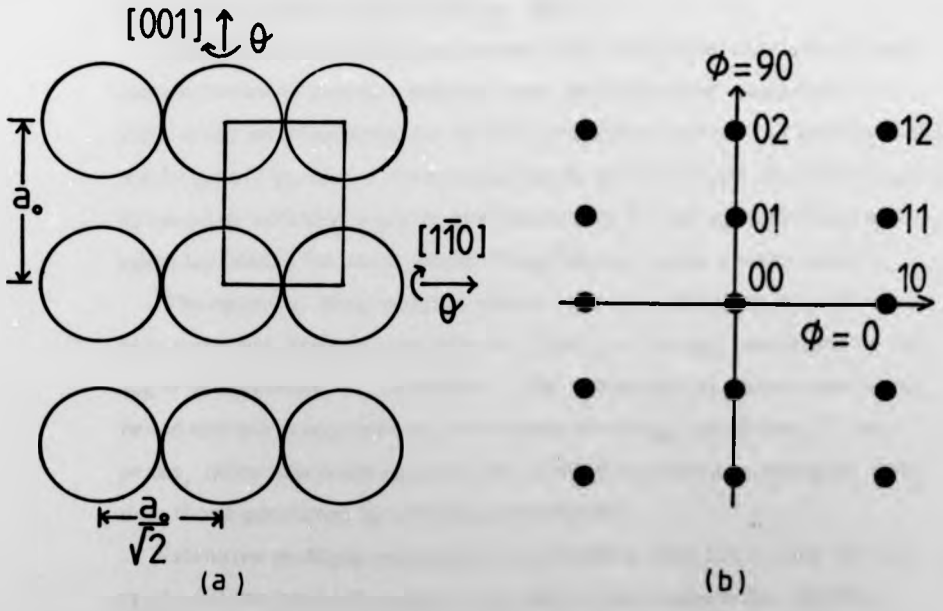

Fig. 5.2

Conventions for

(a) azimuthal indexing (real space)

(b) beam indexing (diffraction pattern)

further differences are noticeable. Thermal diffuse scattering due to single and multiple phonon scattering at finite crystal temperatures reduces the elastic diffraction intensity and effectively distributes part of the total diffracted beam over k-space and so over real space. Taking I-V spectra at 150^{o} K and using a small Faraday cup aperture reduces the thermal diffuse scattering component (see Chapter Two).

The I-V spectra for the specular and some non-specular beams, obtained from a cooled, clean specimen, are presented in Fig. 5.3.

The number S by the side of each spectrum is a scaling factor. The intensity relative to the incident current of only the first spectrum for each beam is marked and all spectra are scaled in such a way that the maximum peak of each is the same height. S is the digitized value of this peak in arbitrary units. Comparisons of intensities can only be made using S alone within a set of data. This system is used for I-V spectra subsequently presented.

5.2.2 Discussion of clean surface data

Comparison of these experimental data with other data shows good correspondence between relative peak positions and intensities, in view of the uncertainties due to different experimental and instrumental techniques (Fig. 5.4). Comparing the work of Demuth (5) reveals good agreement with this work in peak structure for the specular and non-specular beams but some slight disagreement in the energy scale.

The specular beam spectra show a strong modulation in peak structure and intensity near the n = 2 and n = 3 Bragg conditions as the angle of incidence, θ, is varied. The non-specular beams also show broad and non-symmetrical peaks near the Bragg conditions. Other peaks, quite markedly pronounced, are also present at energies other than those predicted by the Bragg conditions.

Extensive multiple scattering calculations have been made by Tait et al. (6) for several angles of incidence and azimuth for Ni(110). Their method, known as the "t-matrix" method, is mentioned earlier in Chapter Two.

Fig. 5.3

The following figures show the I-V spectra obtained from a clean Ni(110) surface at 150^{o}K. Specular beam data for each value of θ are presented to scale within an azimuth, φ, whereas non-specular beam data employ the scaling factor S, defined in Section 5.2.1. Data are presented for the specular beam ($\varphi = 0^{o}, 90^{o}$) and for the (01), ($0\bar{1}$), (11), (10), (02), ($0\bar{2}$) and ($0\bar{3}$) beams.

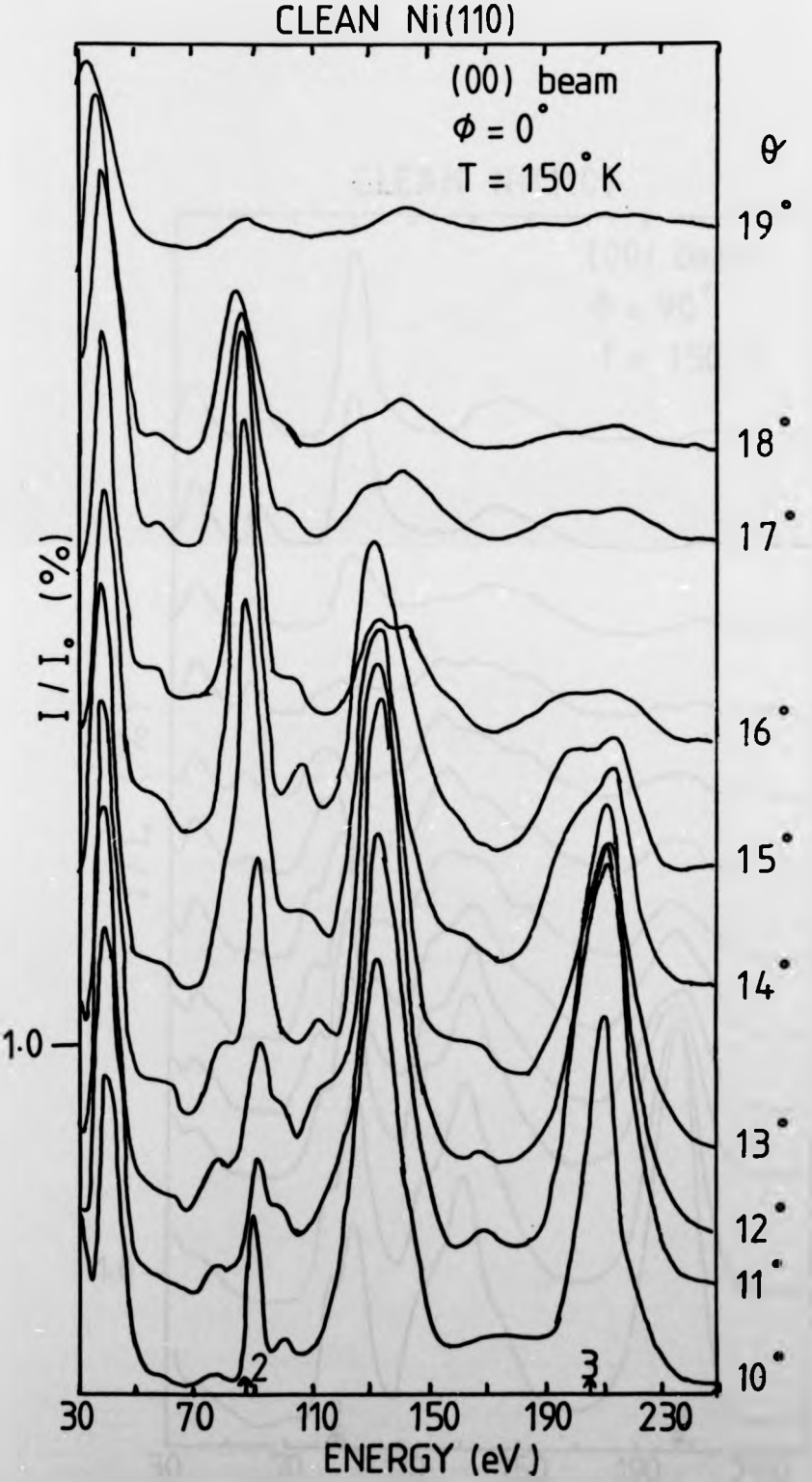
CLEAN Ni(110)
(00) beam
$\phi = 0^\circ$
T = 150° K
θ
19°
18°
17°
16°
15°
14°
13°
12°
11°
10°
I / I$_o$ (%)
1·0
2
3
30
70
110
150
190
230
ENERGY (eV)

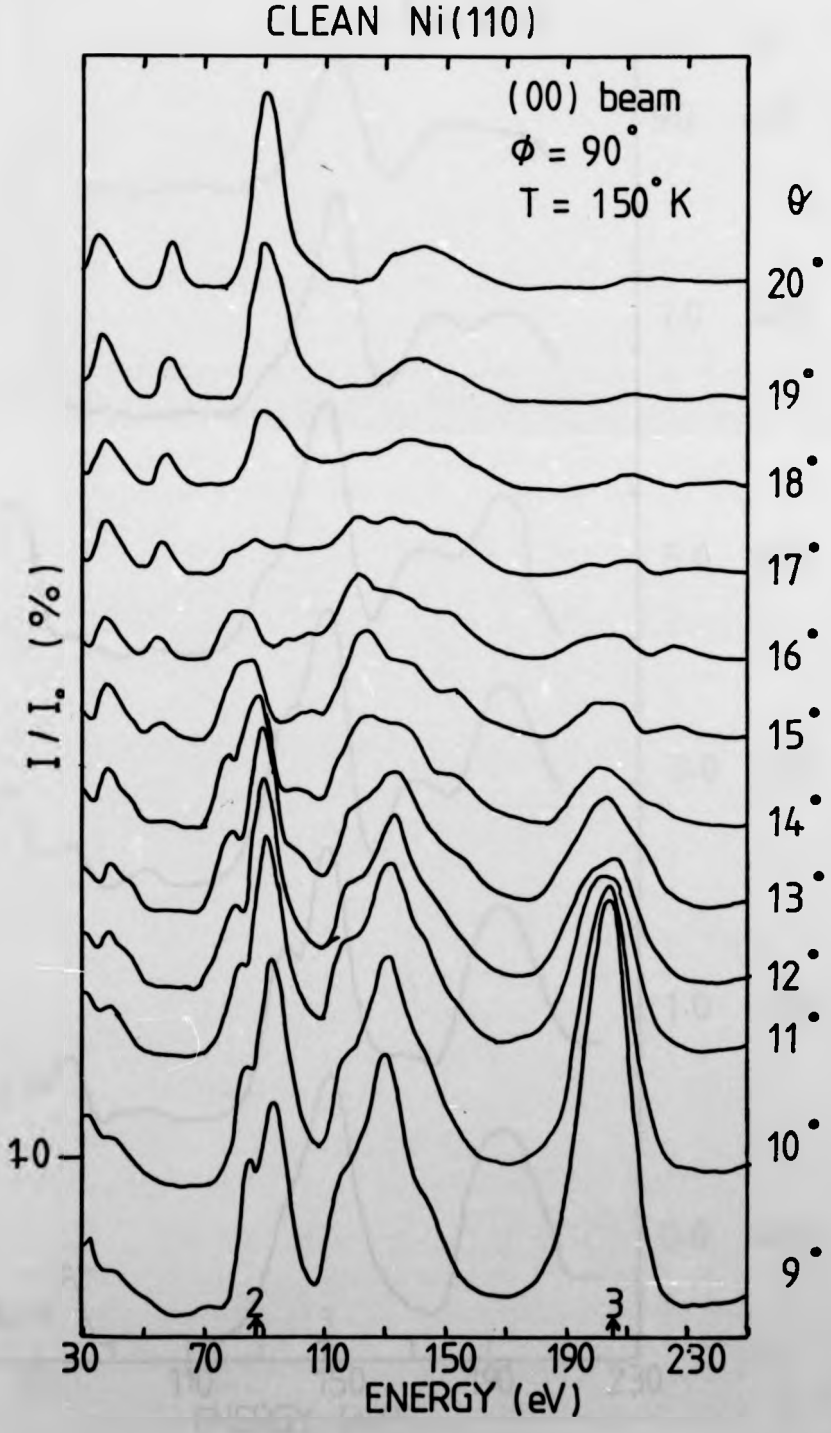
CLEAN Ni(110)
(00) beam
Φ = 90°
T = 150°K
θ
20°
19°
18°
17°
16°
15°
14°
13°
12°
11°
10°
9°
I/I₀ (%)
10
2
3
30
70
110
150
190
230
ENERGY (eV)

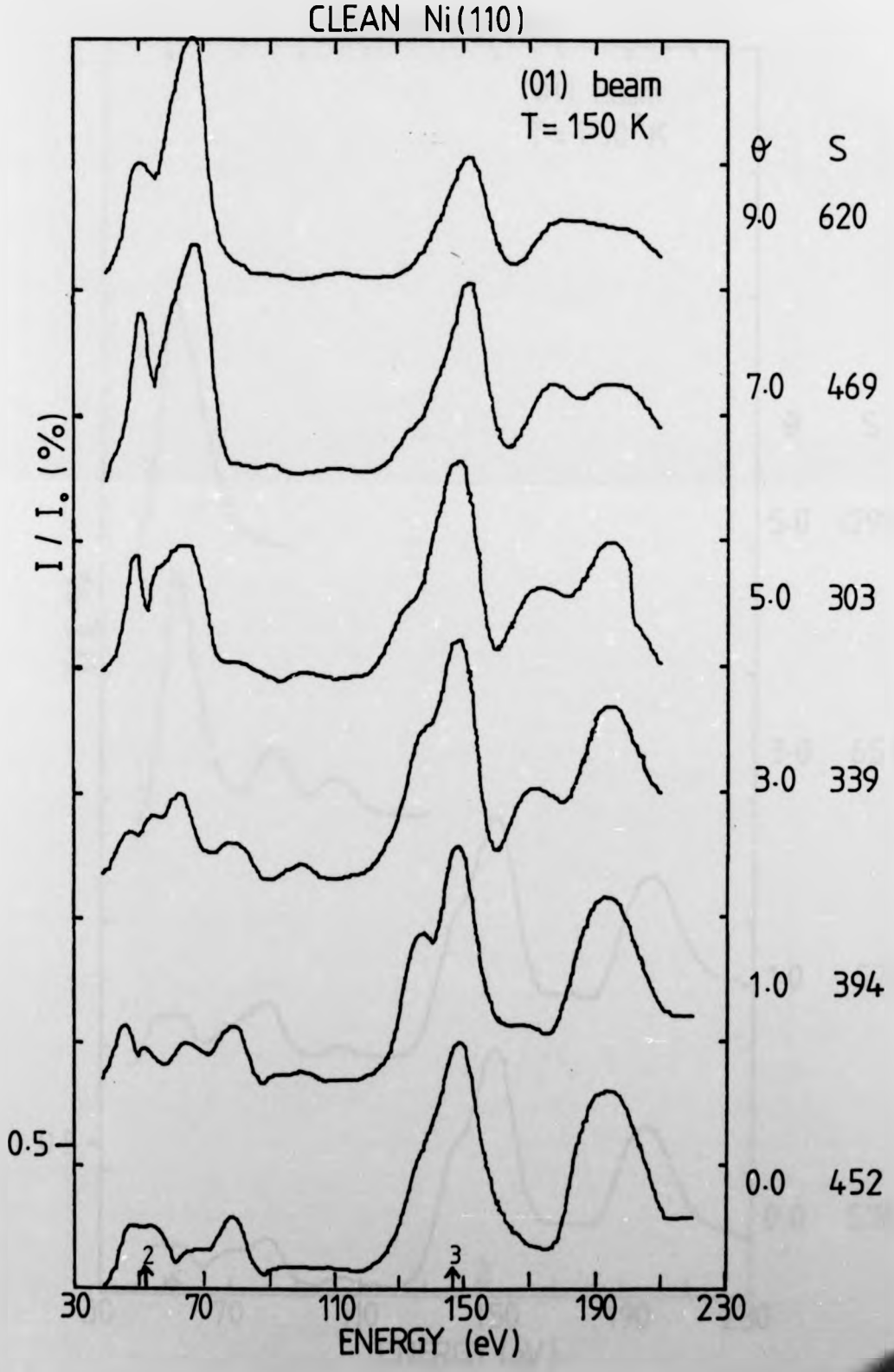
CLEAN Ni(110)
(01) beam
T= 150 K
θ S
9·0 620
7·0 469
5·0 303
3·0 339
1·0 394
0·0 452
I / I₀ (%)
0·5
2
3
30
70
110
150
190
230
ENERGY (eV)

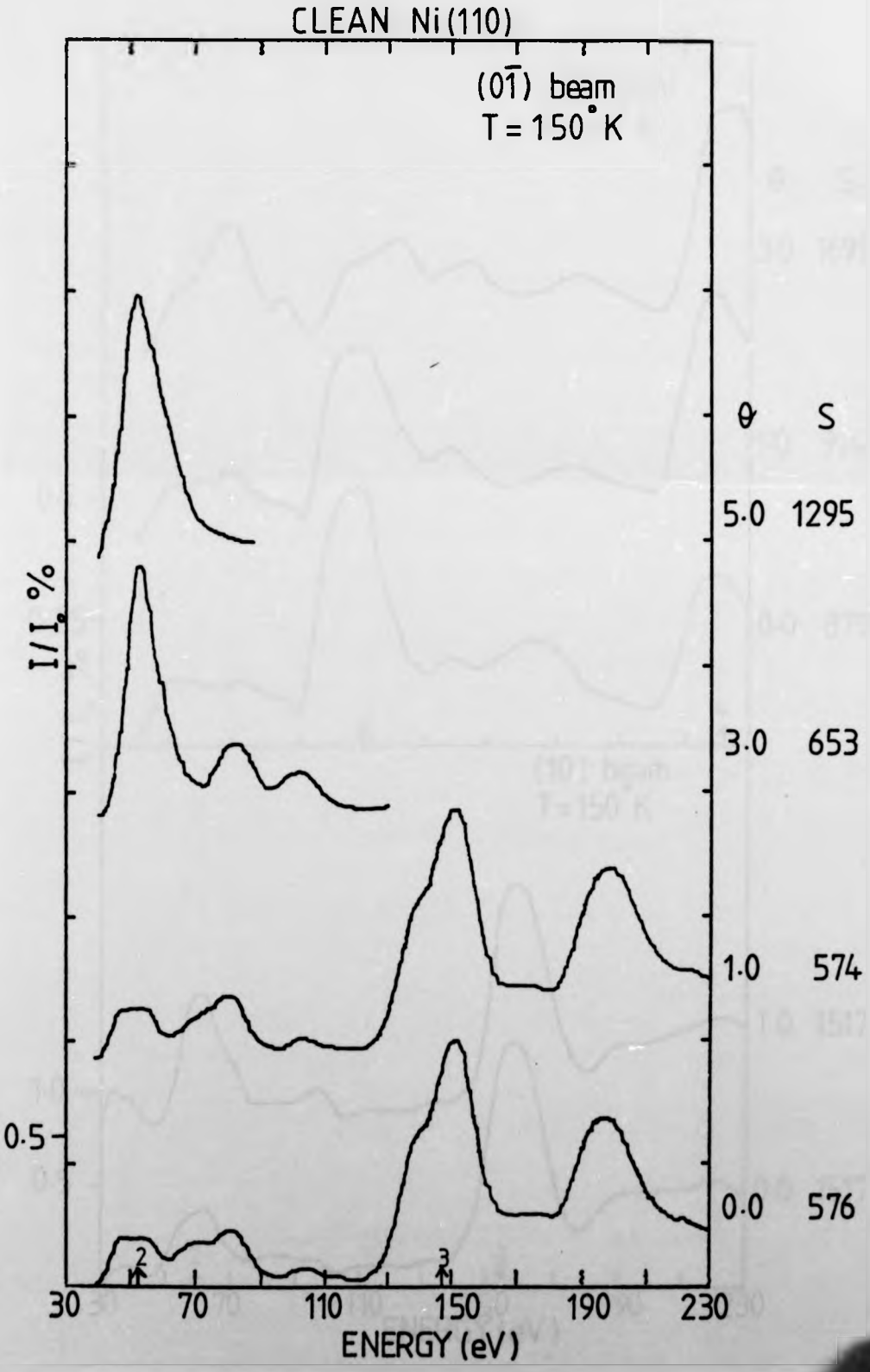
CLEAN Ni(110)
(0$\bar{1}$) beam
T = 150° K
θ S
5·0 1295
3·0 653
1·0 574
0·0 576
I/I$_0$ %
0·5
2
3
30
70
110
150
190
230
ENERGY (eV)

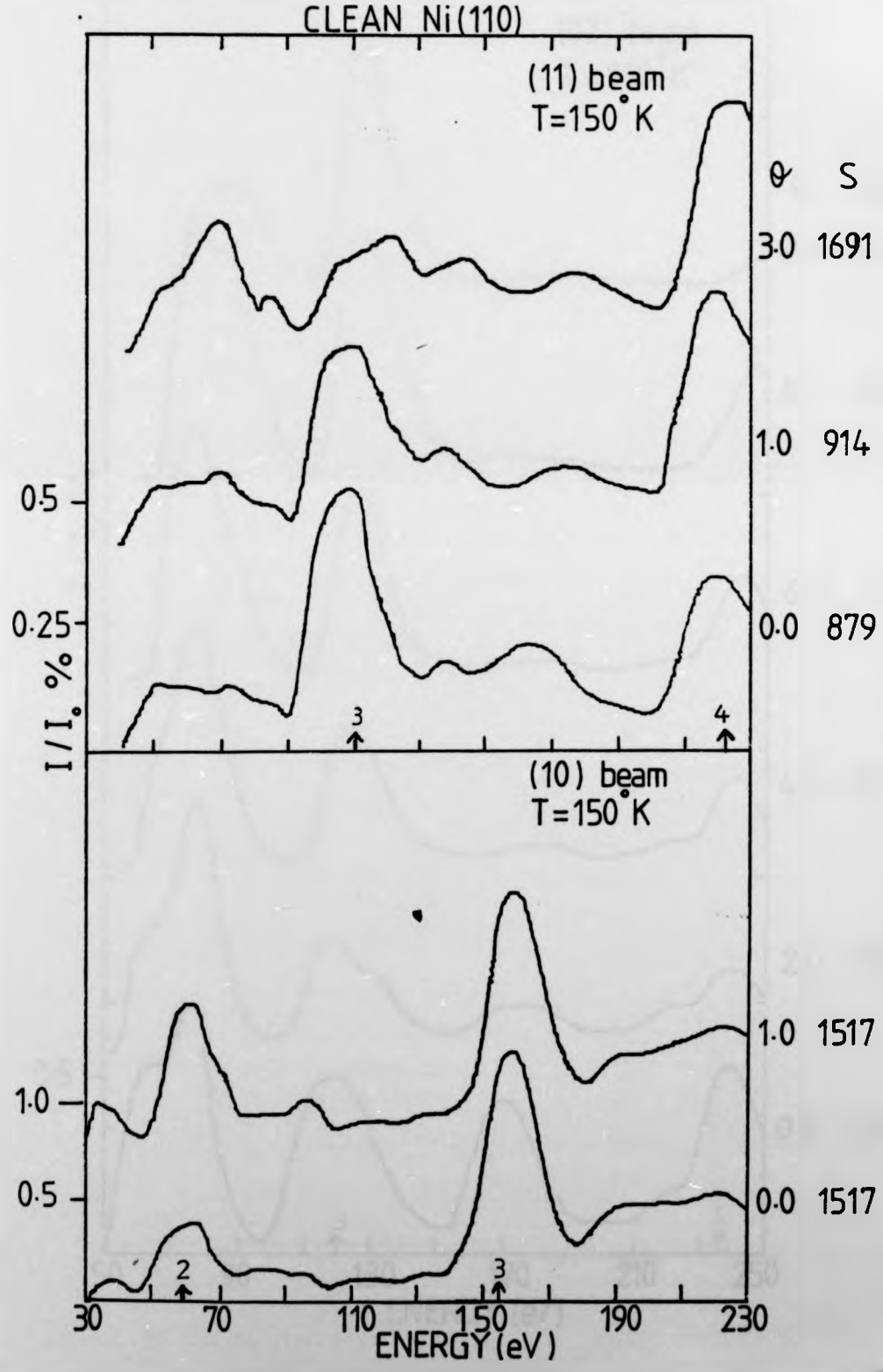
CLEAN Ni(110)
(11) beam
T=150°K
θ S
3·0 1691
1·0 914
0·0 879
0·5
0·25
I/I₀ %
3
4
(10) beam
T=150°K
1·0 1517
0·0 1517
1·0
0·5
2
3
30
70
110
150
190
230
ENERGY (eV)

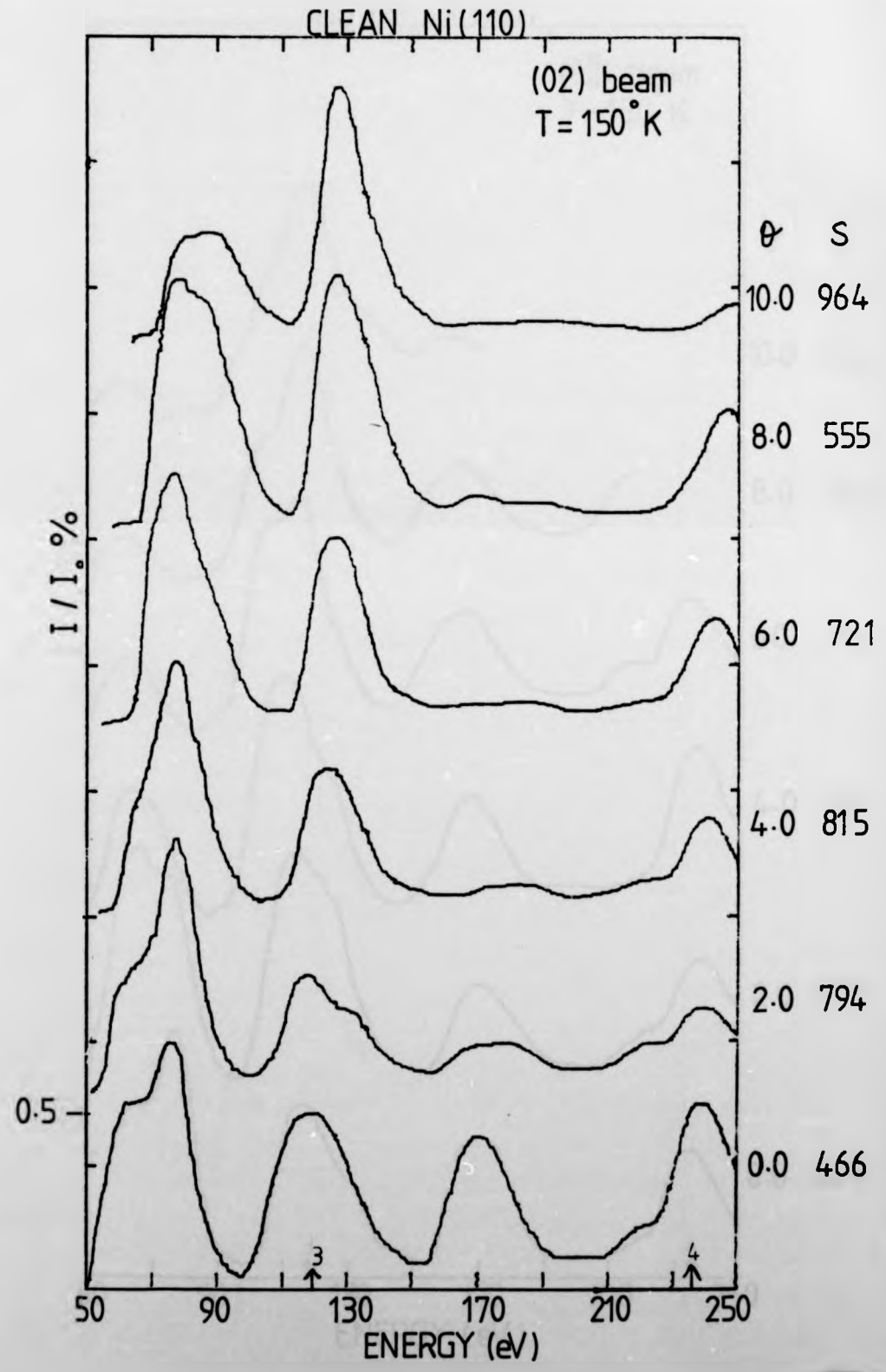
CLEAN Ni(110)
(02) beam
T = 150°K
θ S
10.0 964
8.0 555
6.0 721
4.0 815
2.0 794
0.0 466
I / I₀ %
0.5
3
4
50
90
130
170
210
250
ENERGY (eV)

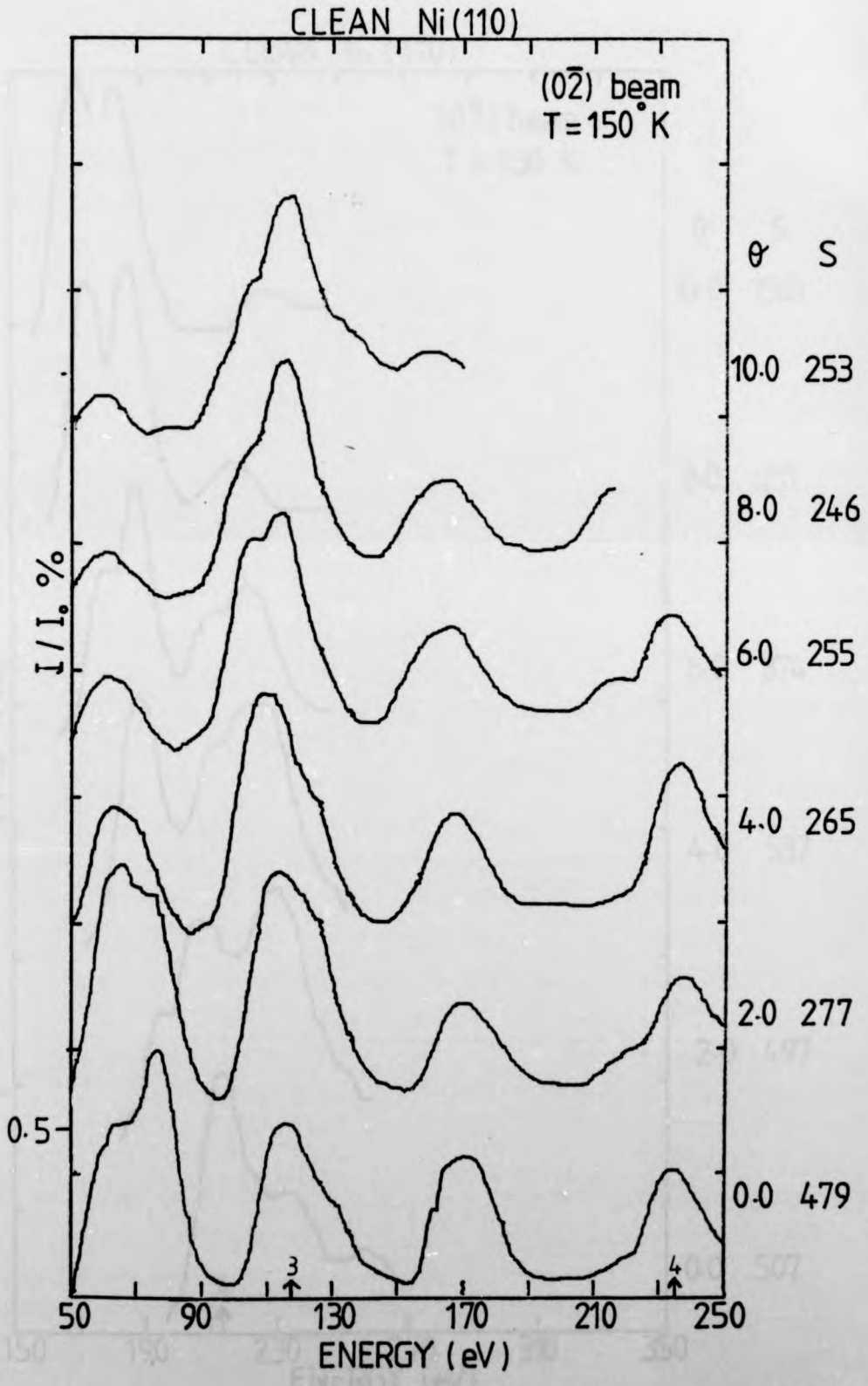
CLEAN Ni(110)
(0$\bar{2}$) beam
T = 150° K
θ S
10·0 253
8·0 246
6·0 255
4·0 265
2·0 277
0·0 479
I / I₀ %
0·5
3
4
50
90
130
170
210
250
ENERGY (eV)

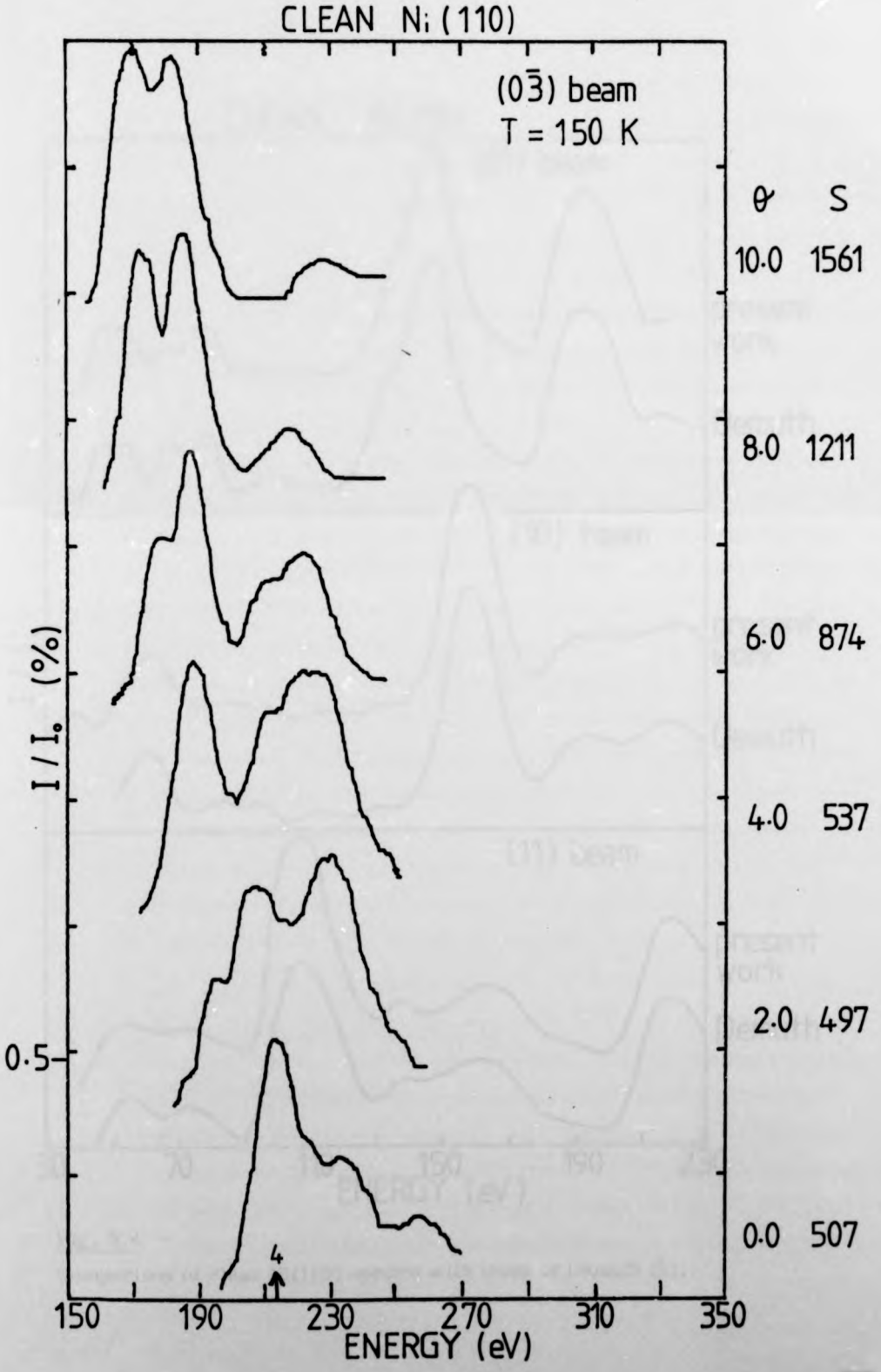
CLEAN Ni (110)
(0$\bar{3}$) beam
T = 150 K
θ S
10.0 1561
8.0 1211
6.0 874
4.0 537
2.0 497
0.0 507
I / I₀ (%)
0.5
4
150
190
230
270
310
350
ENERGY (eV)

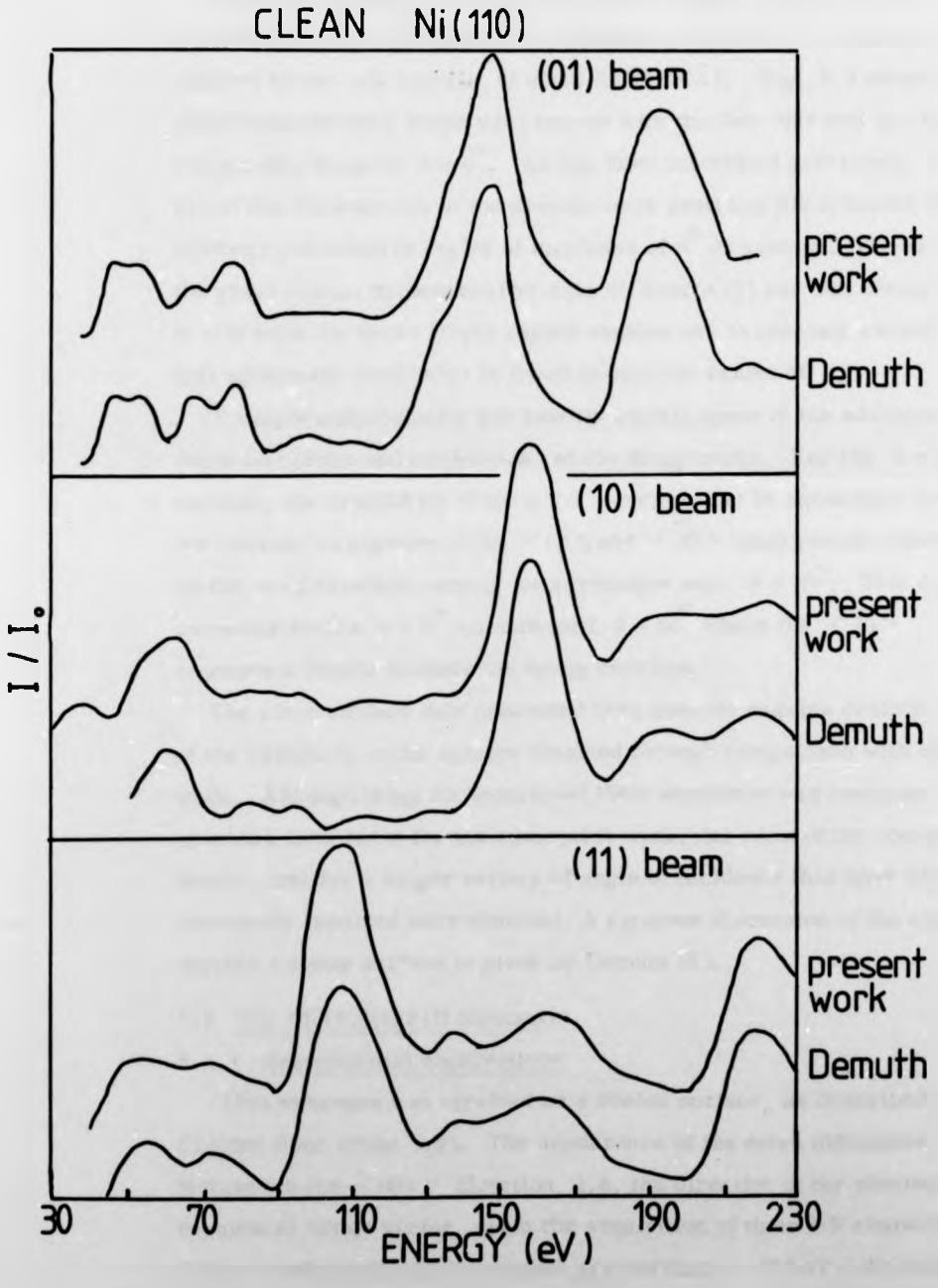

Fig. 5.4

Comparison of clean Ni(110) spectra with those of Demuth (5).

Using full dynamical calculations, Demuth et al. (7) have made a convincing case for the belief that the Ni(110) surface has a contraction, relative to the bulk spacing, of about 5% (0.06 Å). Fig. 5.5 shows a comparison of their theoretical curves with the data obtained by Demuth for the (00) beam at $\theta = 4^{o}$. As has been mentioned previously, the use of the Faraday cup in the present work restricts the specular beam intensity collection to angles of incidence of 8^{o} or greater. However, the great similarity between the data of Demuth (5) and that obtained in this work for these larger angles enables one to conclude reasonably that agreement would also be found at smaller values of θ.

A simple consideration can loosely explain some of the additional secondary peaks and modulation of the Bragg peaks. For the $\varphi = 90^{o}$ azimuth, the modulation of the n = 2 envelope can be associated with the internal emergence of the $<12>$, and $<\bar{2}0>$ emergences converge on the n = 2 envelope causing its attenuation near $\theta = 10^{o}$. This does not occur for the $\varphi = 0^{o}$ azimuth until $\theta = 16^{o}$ where the $<\bar{2}0>$ emergence finally crosses the Bragg envelope.

The clean surface data presented here provide suitable evidence of the reliability of the spectra obtained through comparison with other work. Although being far from novel, their acquisition was necessary to provide a firm basis for the adsorption work; for some of the non-specular beams, data for a larger variety of angle of incidence than have been previously reported were obtained. A rigorous discussion of the clean surface spectra for this surface is given by Demuth (5).

5.3 The Ni(110)(1x2)H Structure

5.3.1 Experimental observations

This structure was obtained on a cooled surface, as described in Chapter Four (Plate 5.2). The appearance of the extra diffraction features in the $<001>$ direction, i.e. the direction of the shortest reciprocal lattice vector, made the acquisition of their I-V characteristics difficult and unreliable at energies greater than ~ 250 eV. An extensive set of data was taken for the specular and some non-specular beams and is presented in Fig. 5.6.

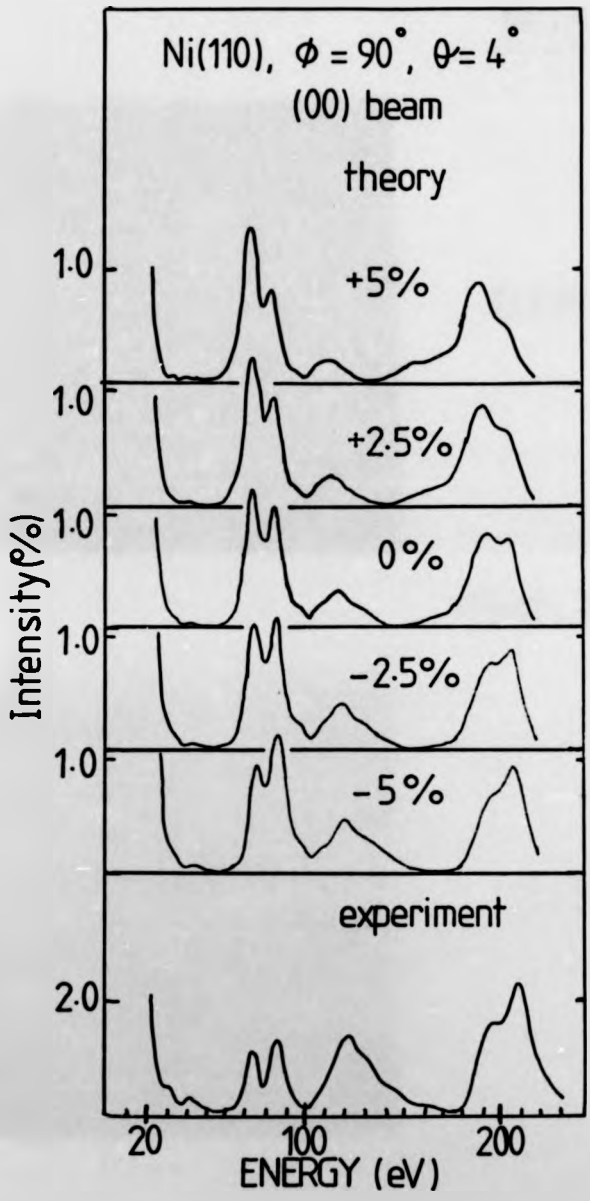

Fig. 5.5

A comparison of the theoretical spectra of Demuth et al. (7) with the experimental spectrum of Demuth (5).

Ni(110) 150° K

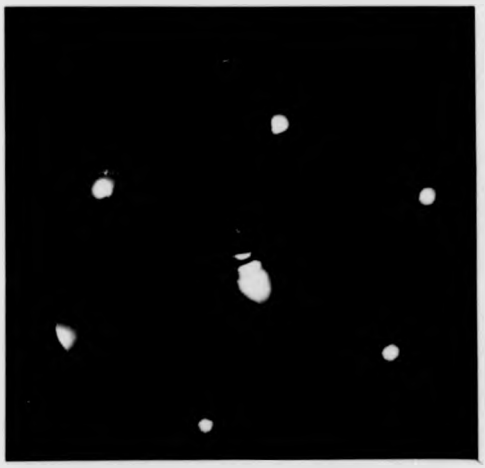

CLEAN

115eV , $\phi = 70^{\circ}$

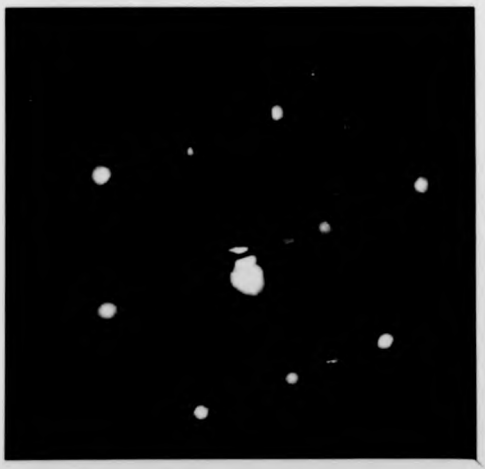

(1×2)H

PLATE 5·2

Fig. 5.6

In the following figures, I-V spectra obtained from the Ni(110)(1x2)H surface are presented.

Data are shown for the specular beam ($\varphi = 0^{o}$, 45^{o}) and the (01), $(0\bar{1})$, (11), (10), $(0\ \bar{3}/2)$, (0 3/2), $(0\bar{3})$, (0 1/2), (1 1/2), (02) and $(0\bar{2})$ beams.

Fig. 5.6

In the following figures, I-V spectra obtained from the Ni(110)(1x2)H surface are presented.

Data are shown for the specular beam ($\varphi = 0^{o}$, 45^{o}) and the (01), ($0\bar{1}$), (11), (10), (0 $\bar{3}$/2), (0 3/2), ($0\bar{3}$), (0 1/2), (1 1/2), (02) and ($0\bar{2}$) beams.

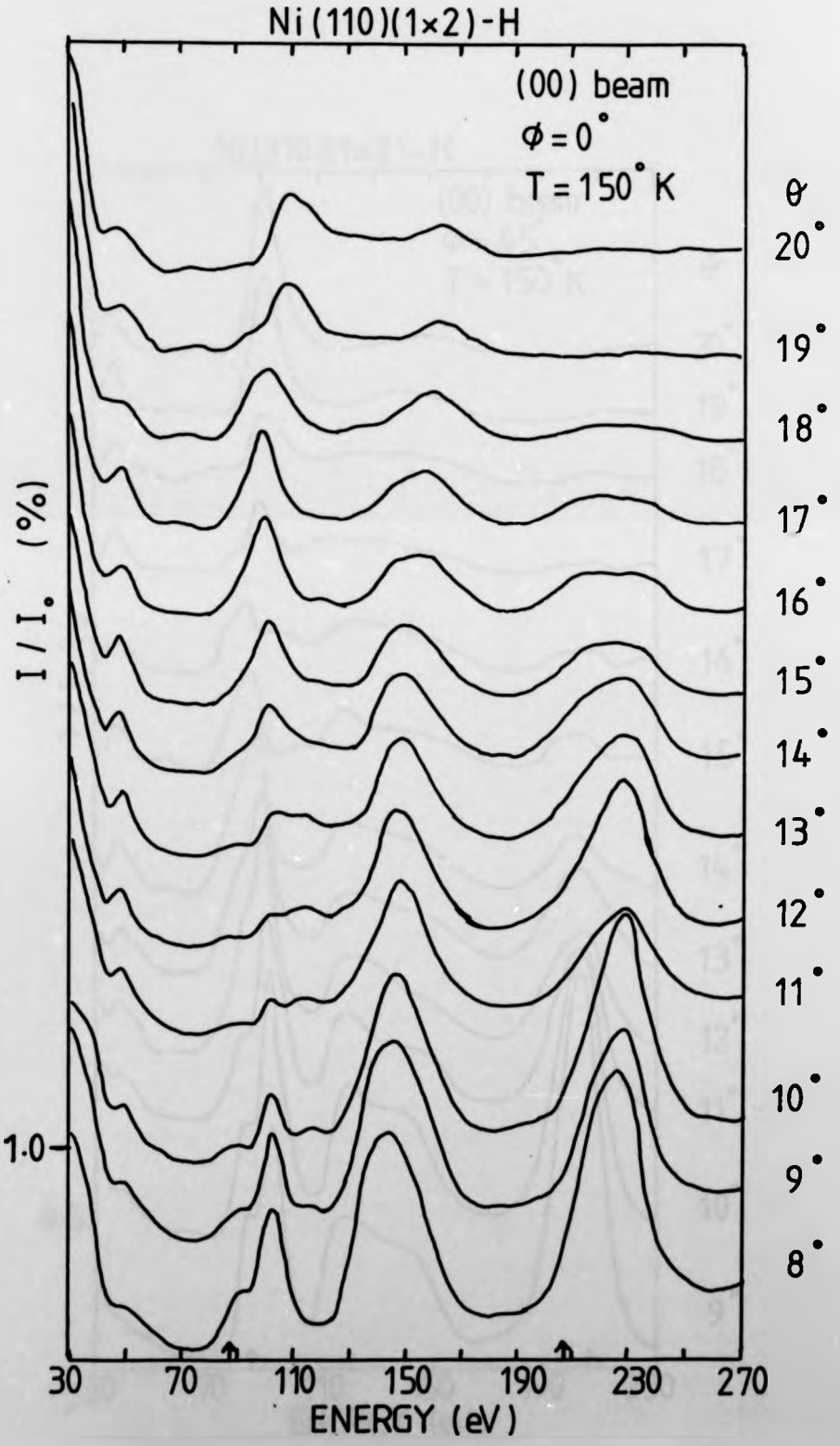
Ni(110)(1×2)-H
(00) beam
φ = 0°
T = 150° K
θ
20°
19°
18°
17°
16°
15°
14°
13°
12°
11°
10°
9°
8°
I / I₀ (%)
1·0
30
70
110
150
190
230
270
ENERGY (eV)

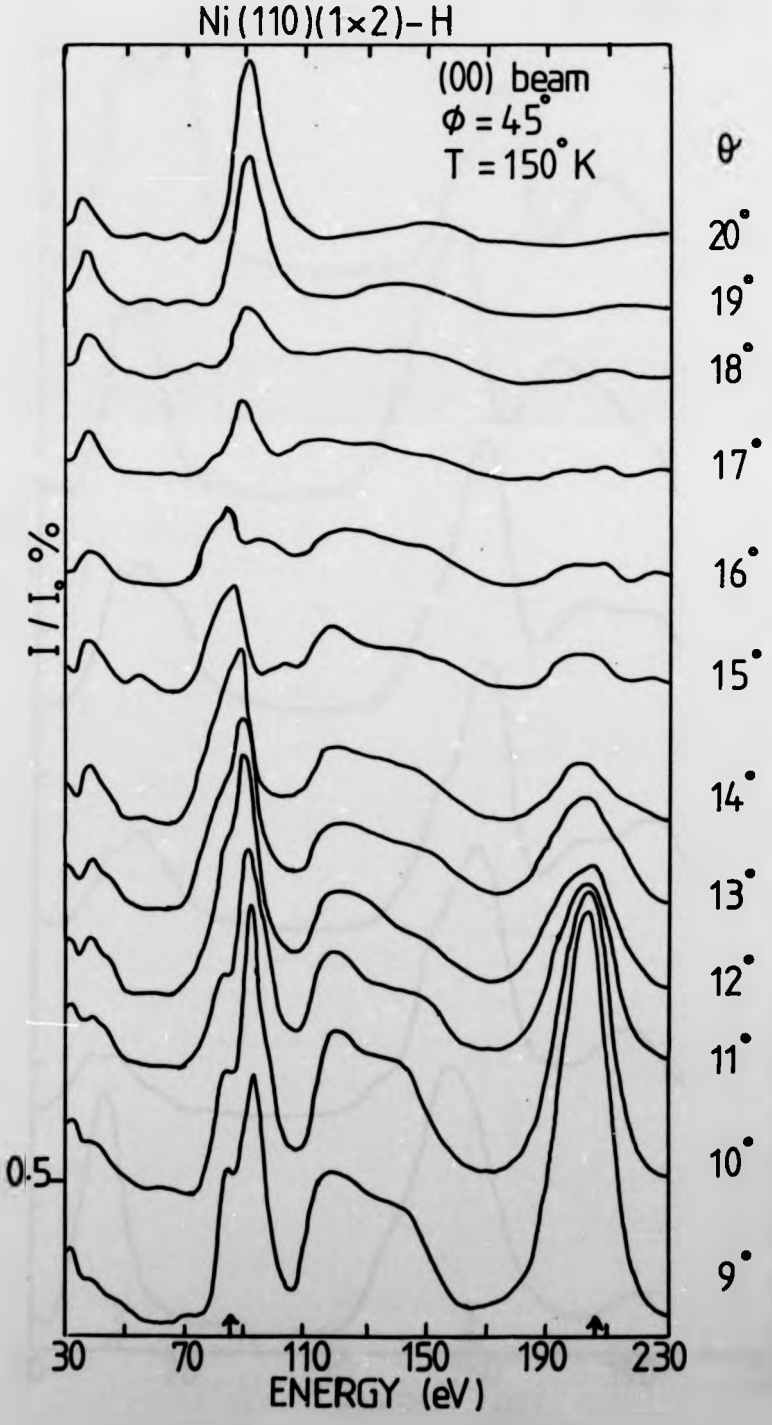
Ni(110)(1×2)-H
(00) beam
φ = 45°
T = 150°K
θ
20°
19°
18°
17°
16°
15°
14°
13°
12°
11°
10°
9°
I/I₀ %
0.5
30
70
110
150
190
230
ENERGY (eV)

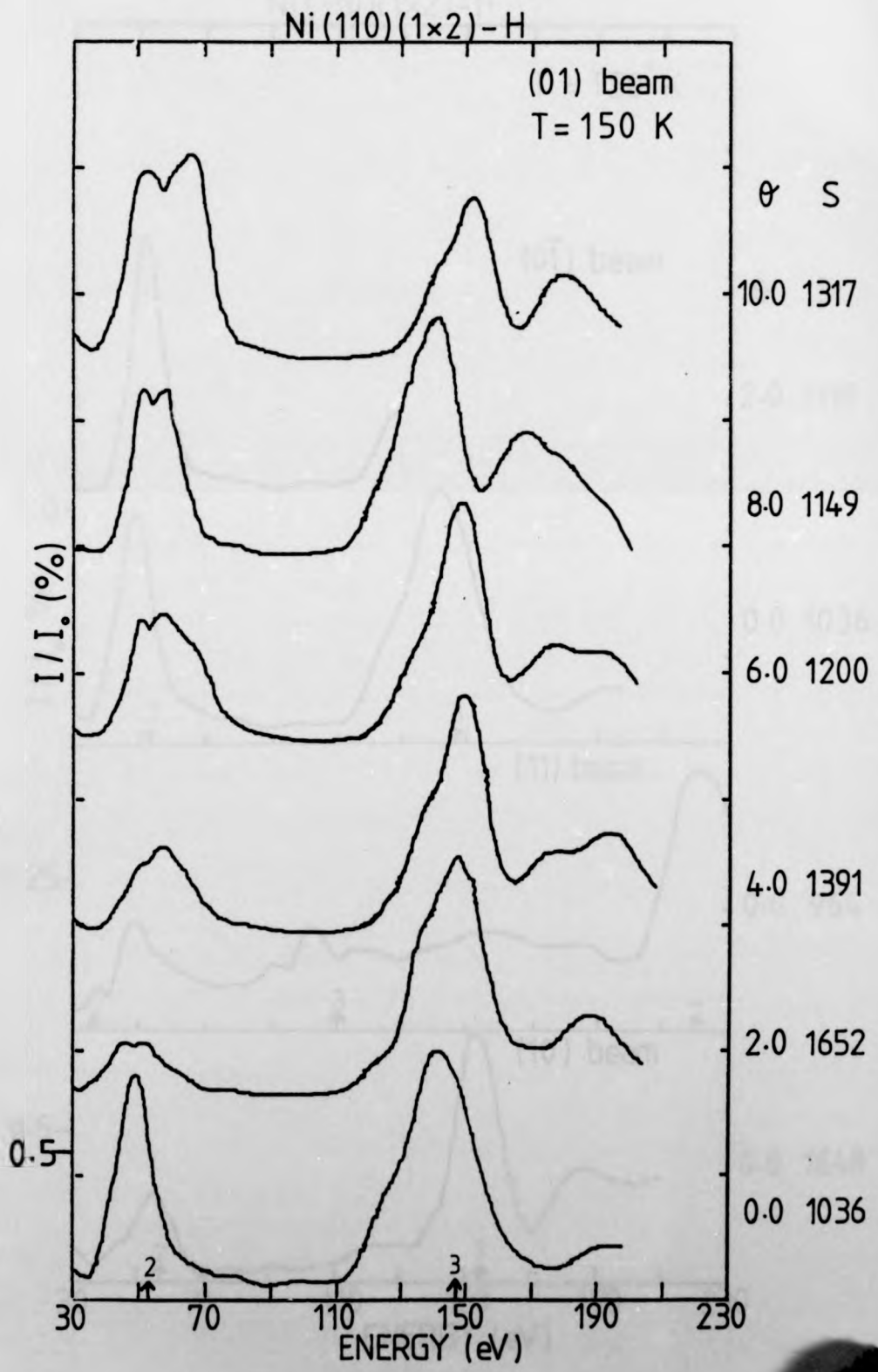
Ni(110)(1×2)-H
(01) beam
T = 150 K
θ S
10·0 1317
8·0 1149
6·0 1200
4·0 1391
2·0 1652
0·0 1036
I/I₀ (%)
0·5
2
3
30
70
110
150
190
230
ENERGY (eV)

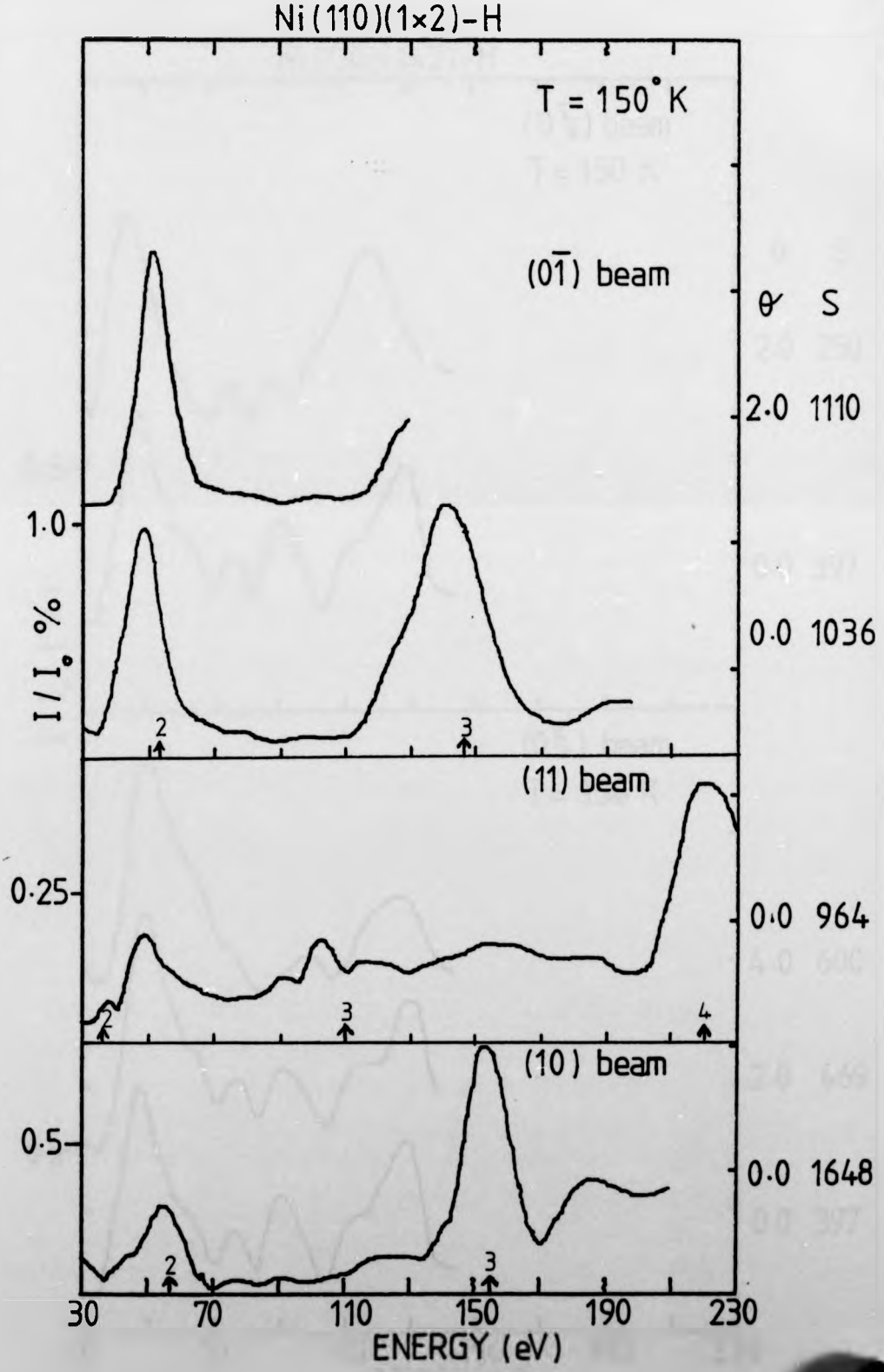
Ni(110)(1×2)-H
T = 150°K
(0$\bar{1}$) beam
θ S
2·0 1110
0·0 1036
1·0
I/I$_o$ %
2
3
(11) beam
0·25
0·0 964
2
3
4
(10) beam
0·5
0·0 1648
2
3
30
70
110
150
190
230
ENERGY (eV)

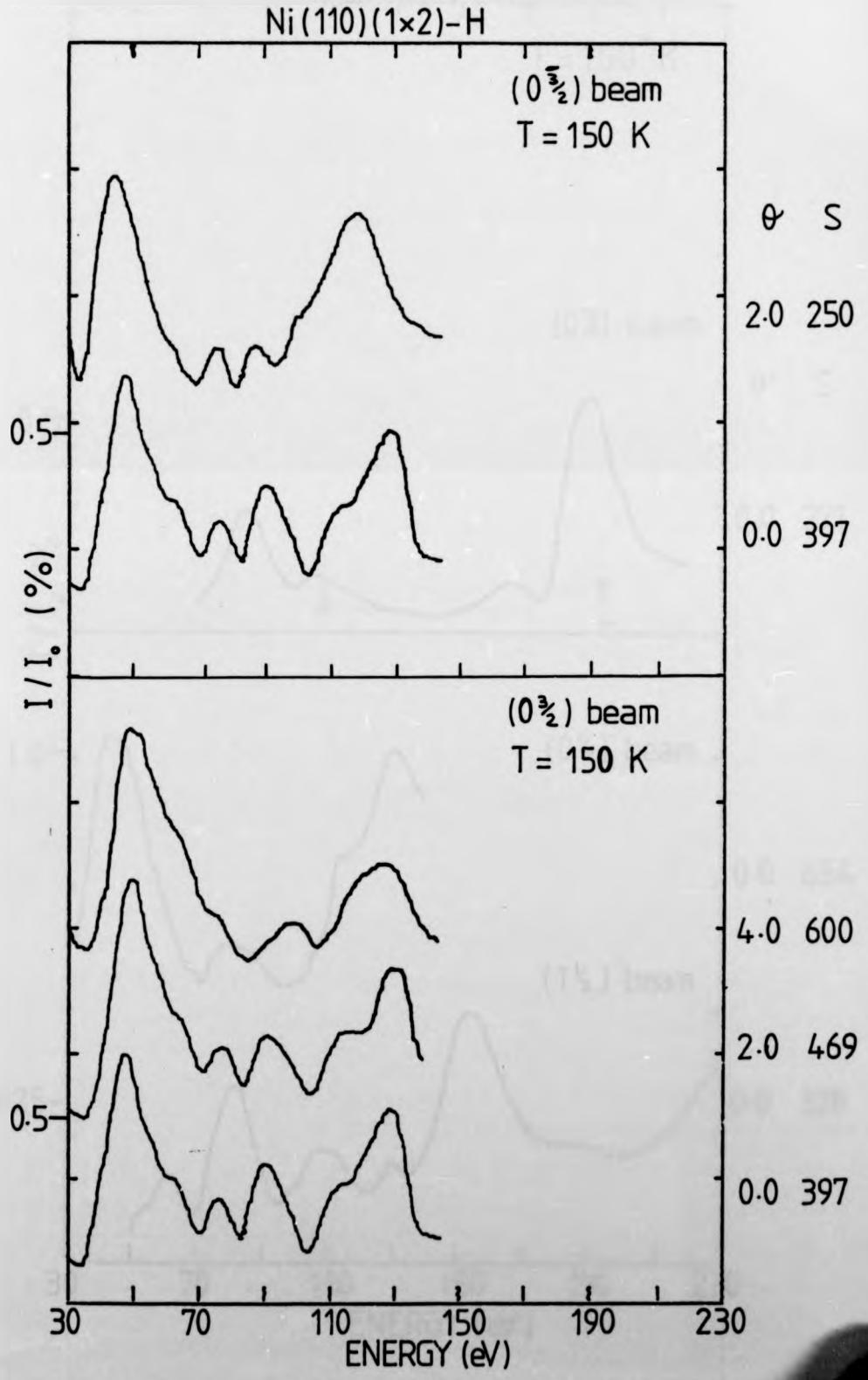
Ni(110)(1×2)-H
(0 3/2) beam
T = 150 K
θ S
2·0 250
0·0 397
0·5
I / I₀ (%)
(0 3/2) beam
T = 150 K
4·0 600
2·0 469
0·5
0·0 397
30
70
110
150
190
230
ENERGY (eV)

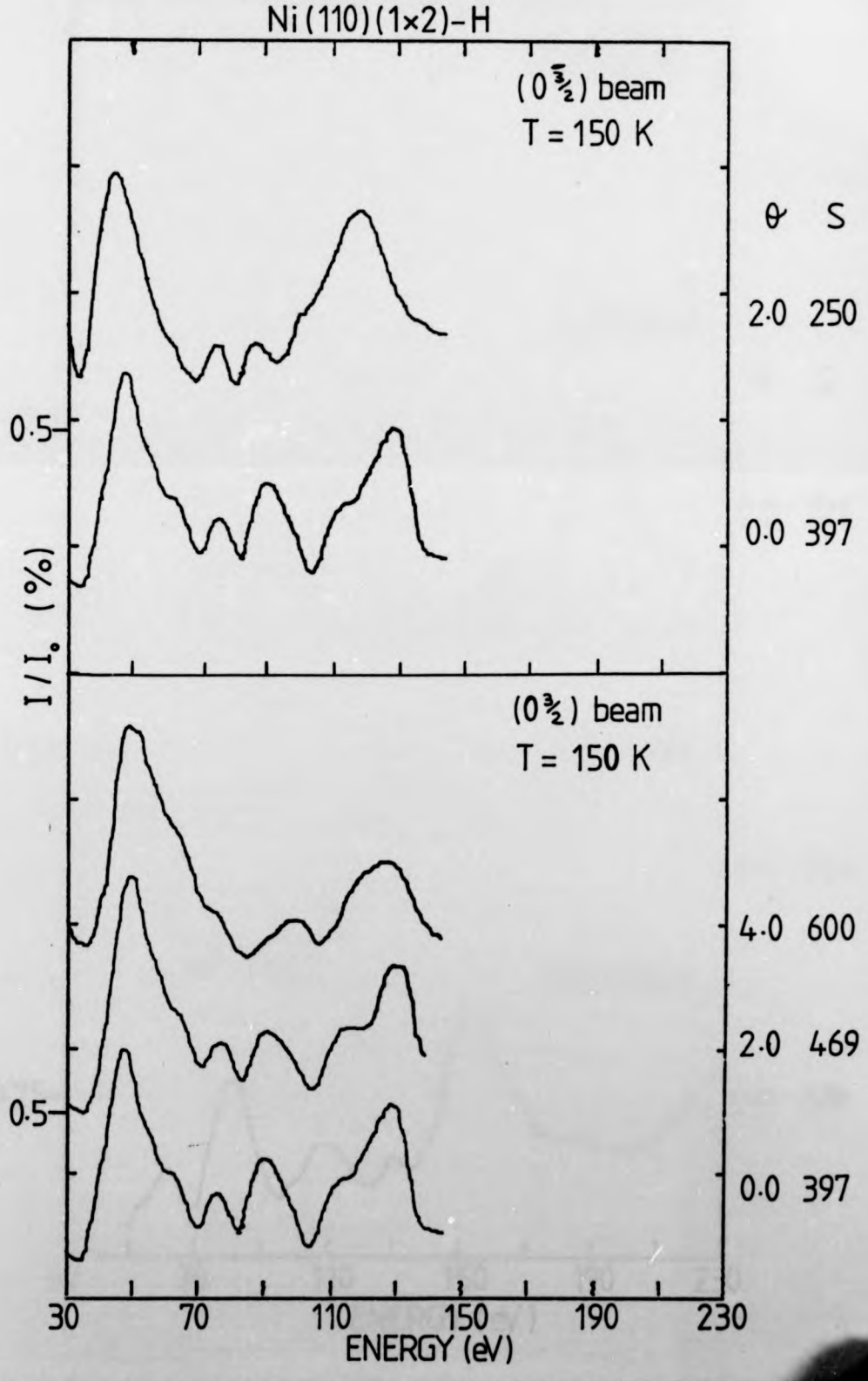
Ni(110)(1×2)-H
(0 3/2) beam
T = 150 K
θ S
2·0 250
0·0 397
0·5
I / I₀ (%)
(0 3/2) beam
T = 150 K
4·0 600
2·0 469
0·0 397
0·5
30 70 110 150 190 230
ENERGY (eV)

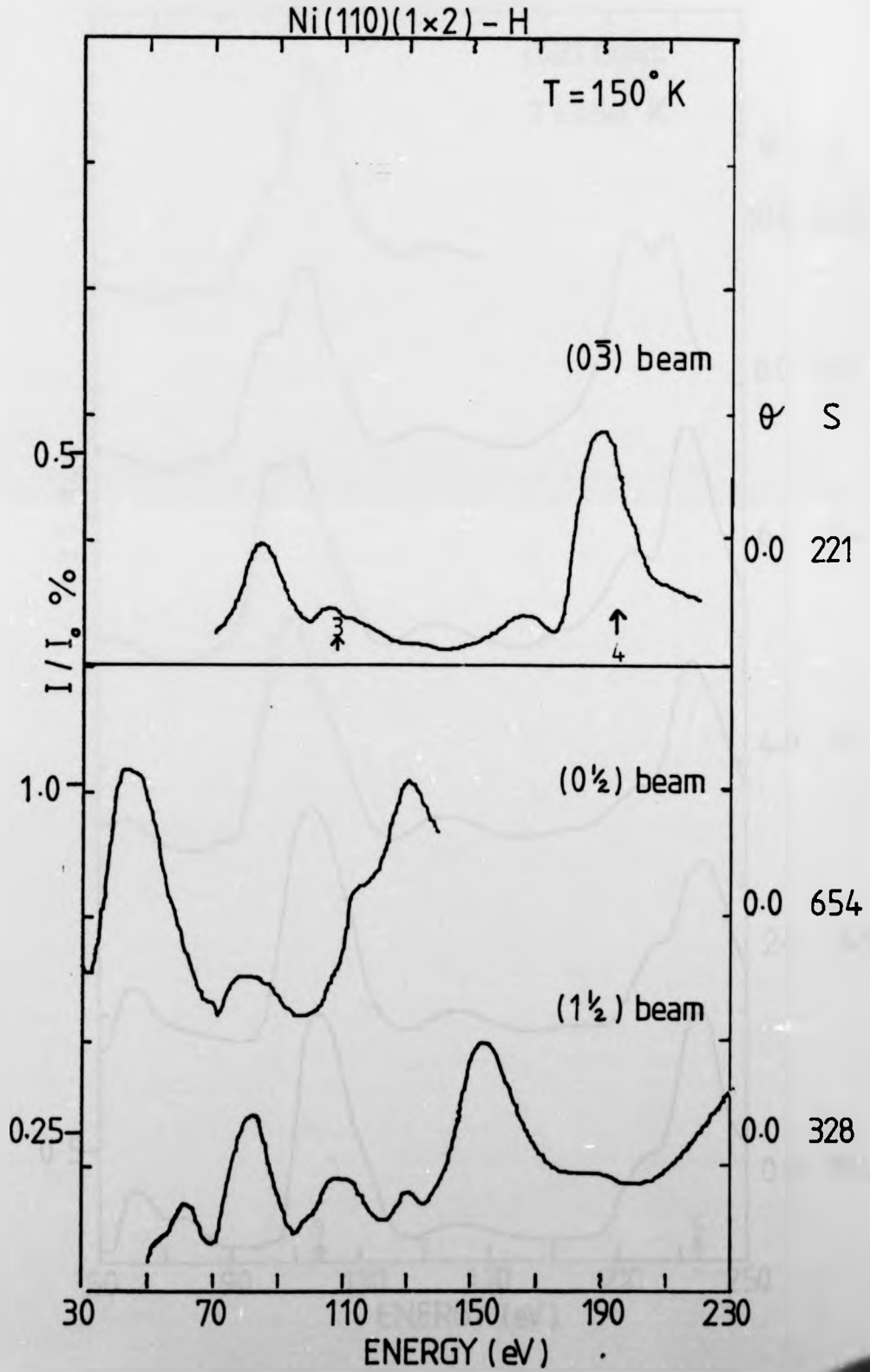
Ni(110)(1×2) – H
T = 150° K
(0$\bar{3}$) beam
θ S
0·0 221
0·5
I/I$_o$ %
3
4
(0½) beam
1·0
0·0 654
(1½) beam
0·25
0·0 328
30
70
110
150
190
230
ENERGY (eV)

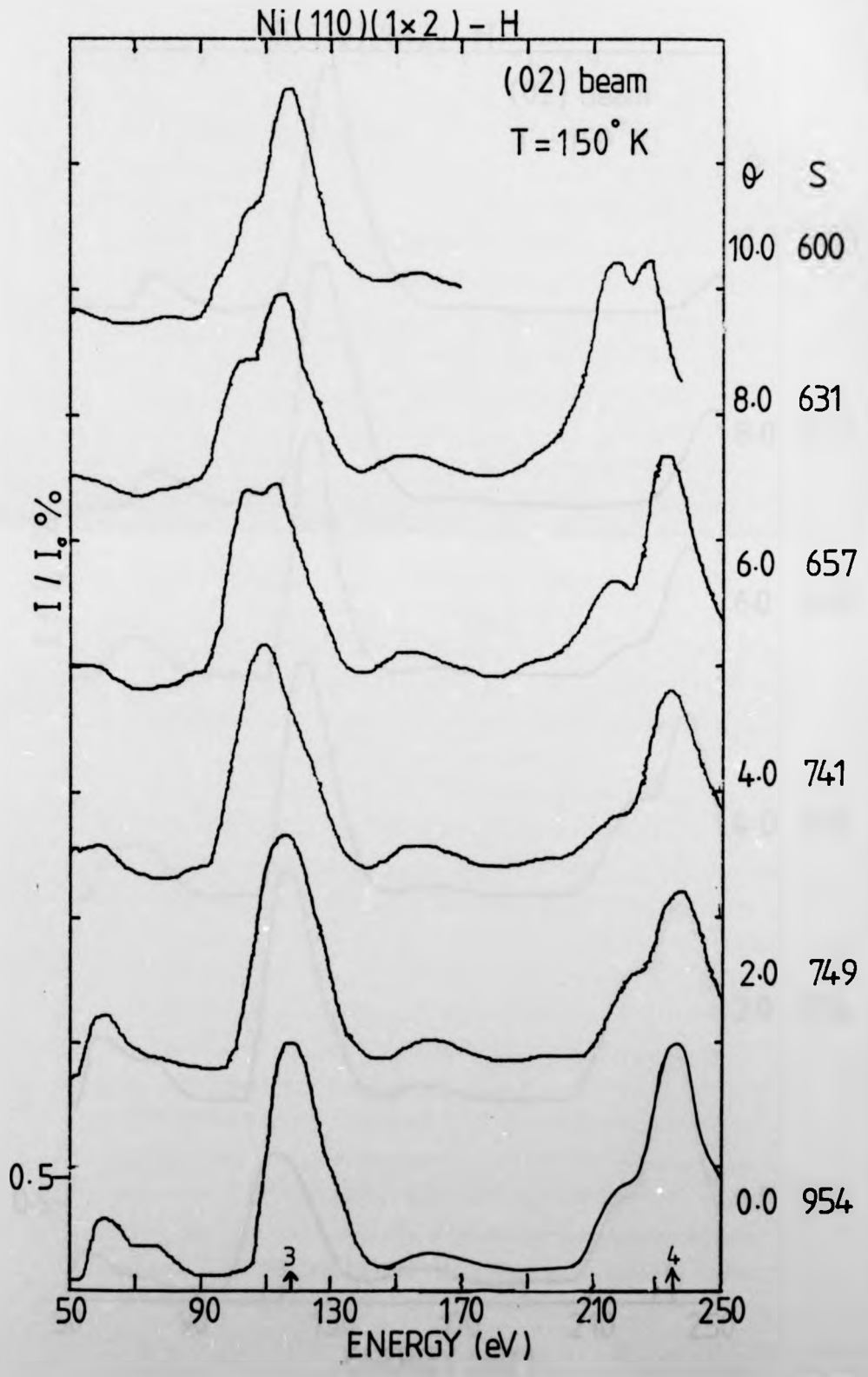
Ni(110)(1×2)-H
(02) beam
T=150° K
θ S
10.0 600
8.0 631
6.0 657
4.0 741
2.0 749
0.0 954
I/I₀ %
0.5
3
4
50
90
130
170
210
250
ENERGY (eV)

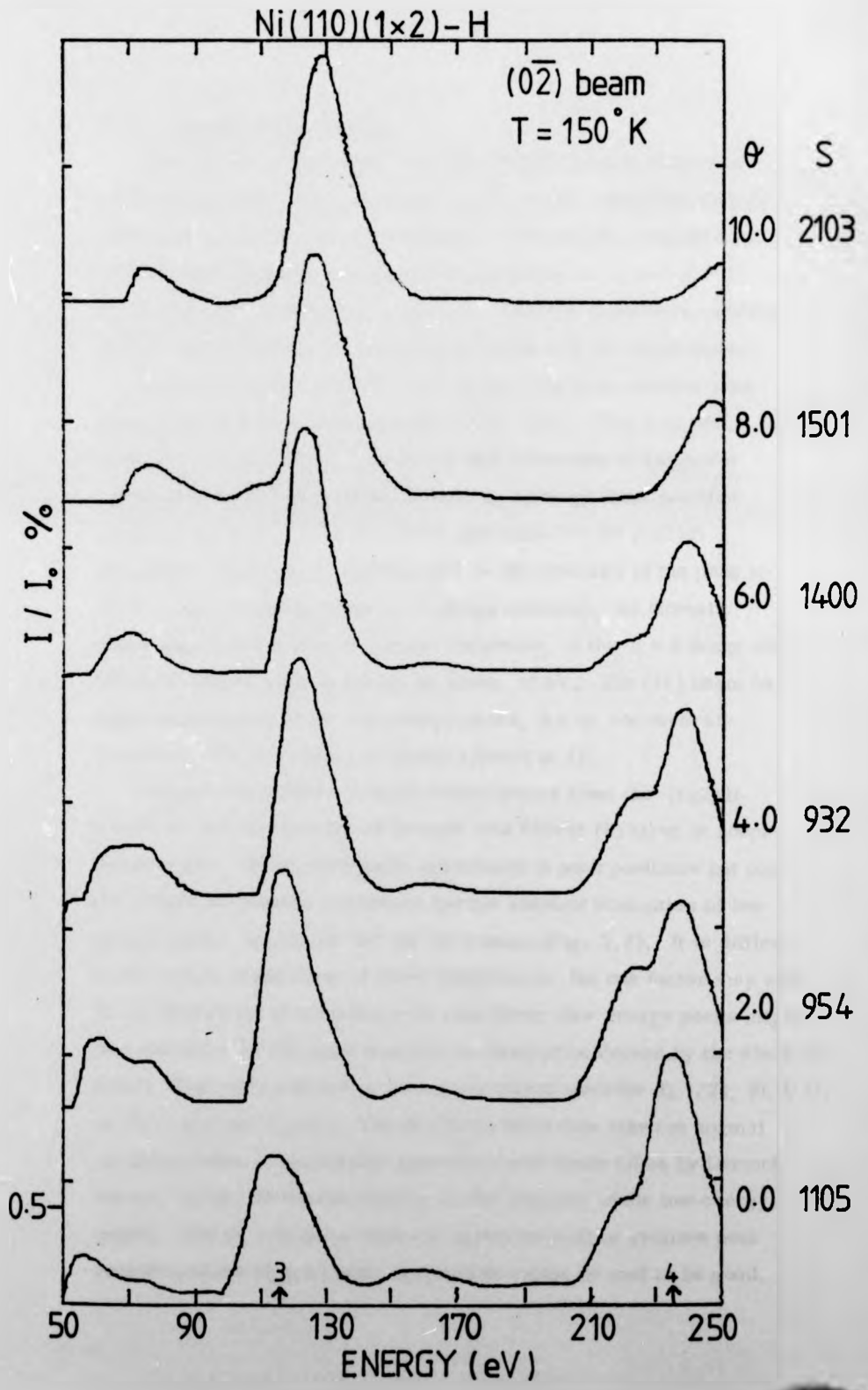
Ni(110)(1×2)-H
(0$\bar{2}$) beam
T = 150°K
θ
S
10·0 2103
8·0 1501
6·0 1400
4·0 932
2·0 954
0·0 1105
I / I₀ %
0·5
3
4
50
90
130
170
210
250
ENERGY (eV)

5.3.2 Discussion of results

Specular beam data show no great changes in peak shapes or positions with respect to the clean surface data, except for a slight shift of Bragg peaks to lower energies. Relative peak heights are altered, but a similar modulation of the Bragg n = 2 and n = 3 envelopes with variation of θ occurs. Absolute intensities relative to the clean surface are increased by about 50% for some beams.

Some non-specular beams show large changes in relative peak heights and shifts in peak positions (Fig. 5.7). The (02) beam, for example, suffers a great increase in the intensities of the peaks corresponding to Bragg peaks 3 and 4, although their position remains unaltered. The (01) beam spectrum for the (1x2) H structure undergoes a large increase in the intensity of the peak at 50 eV, corresponding to the n = 2 Bragg condition, its intensity becoming almost equal, at normal incidence, to the n = 3 Bragg peak which is shifted down in energy by about 10 eV. The (11) beam has some suppression of its low energy peaks, but is not severely modified. The (10) beam is barely altered at all.

Comparison of these integral order beams from the (1x2) H structure with the spectra of Demuth and Rhodin (8) taken at room temperature, shows reasonable agreement in peak positions but does not reveal too good an agreement for the absolute intensities of low energy peaks, especially for the (01) beam (Fig. 5.8). It is difficult to be certain of the cause of these differences, but one factor may well be the difference in the adsorption conditions: low energy peaks might be expected to be the most sensitive to desorption caused by the electron beam. The extra diffraction beams measured were the (0, 1/2), (0, 3/2), (0, $\bar{3}$/2) and the (1, 1/2). The (0, $\pm$3/2) beam data taken at normal incidence were in reasonable agreement with those taken by Demuth, except, again, for the discrepancy in the intensity of the low energy peaks. The (1, 1/2) beam does not agree too well on relative peak heights and the (0, 1/2) beam agreement cannot be said to be good.

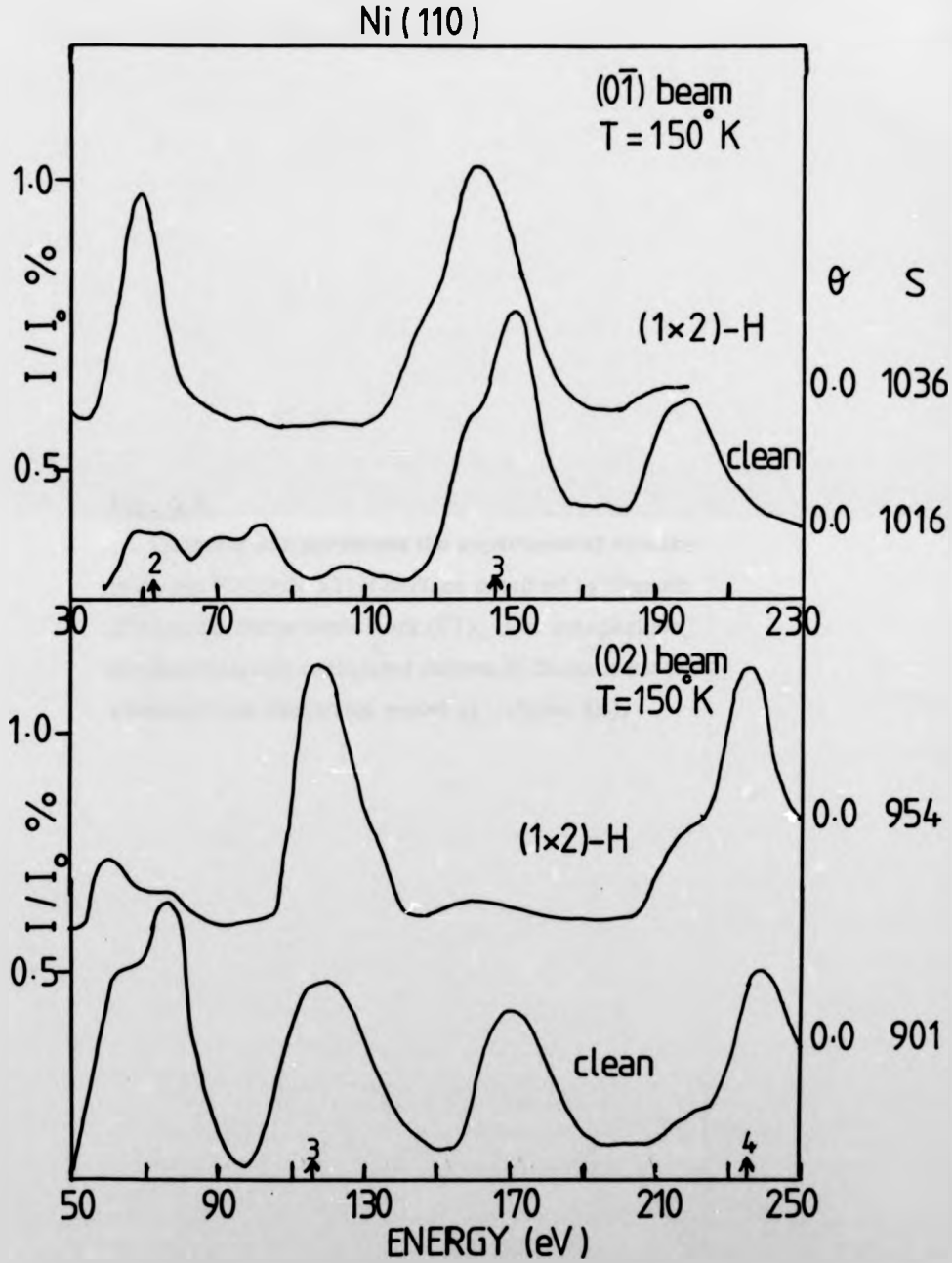

Fig. 5.7

A comparison between spectra from the clean Ni(110) and Ni(110)(1x2)H surfaces for the (0$\bar{1}$) and (02) beams at normal incidence.

Fig. 5.8

Overleaf are presented the experimental spectra from the Ni(110)(1x2)H surface obtained by Demuth (E1) and in the present work (E2). For comparison, the theoretically calculated curves of Demuth for the alternate row distortion model are shown (th).

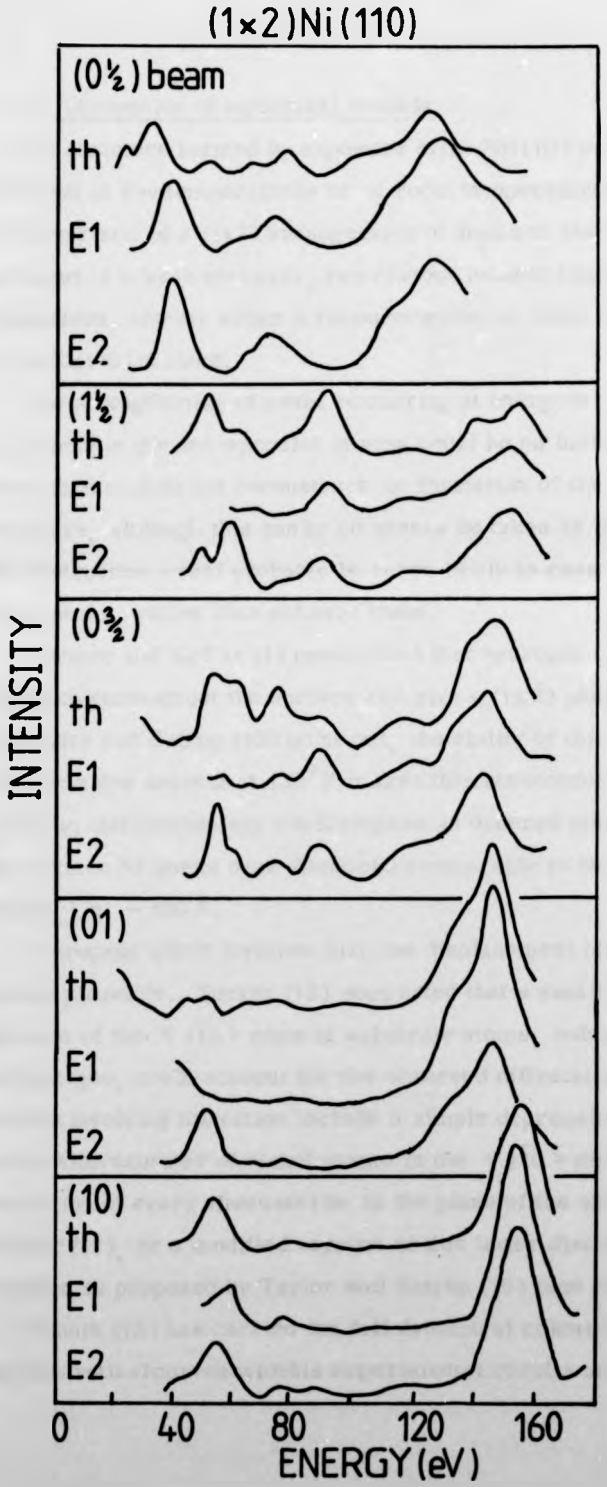
(1×2)Ni(110)
(0½) beam
th
E1
E2
(1½)
th
E1
E2
(0³⁄₂)
th
E1
E2
(01)
th
E1
E2
(10)
th
E1
E2
INTENSITY
0
40
80
120
160
ENERGY (eV)

5.3.3 Discussion of structural models

The structure formed by exposure of the Ni(110) surface to hydrogen at low temperatures or at room temperatures (9, 10) is characteristic of a (1x2) arrangement of atoms on the surface. Since hydrogen is a weak scatterer, two obvious models immediately present themselves, namely either a reconstruction or some type of distortion of the Ni(110) surface.

The strengthening of peaks occurring at energies satisfying Bragg conditions in the non-specular beams could be an indication that the (110) surface does not reconstruct on formation of the (1x2) H structure, although this can by no means be taken as absolute proof. Reconstruction would probably be more likely to cause a reduction in these peaks, rather than enhance them.

Germer and McRae (11) postulated that hydrogen causes the nickel atoms to reconstruct the surface and give a (1x2) pattern. However, as Taylor and Estrup (10) point out, the ability of this structure to form in a few seconds at 130^{o}K makes this reconstruction rather unlikely; this mechanism would require an ordered migration of half the surface Ni atoms over distances comparable to the coherence length, i.e. ~ 100 Å.

A process which involves only the displacement of substrate atoms seems plausible. Tucker (12) suggested that a small distortion in the location of the $< 1\bar{1}0 >$ rows of substrate atoms, induced by the presence of hydrogen, could account for the observed diffraction features. Models involving distortion include a simple depression or raising of every alternate row of nickel atoms in the $< 1\bar{1}0 >$ direction, a pairwise distortion of every alternate row in the plane of the surface suggested by Tucker (12), or a modified version of this latter distortion involving rotation as proposed by Taylor and Estrup (10) (see Fig. 5.9).

Demuth (13) has carried out full dynamical calculations and compared the theoretical curves with his experimental results at normal incidence.

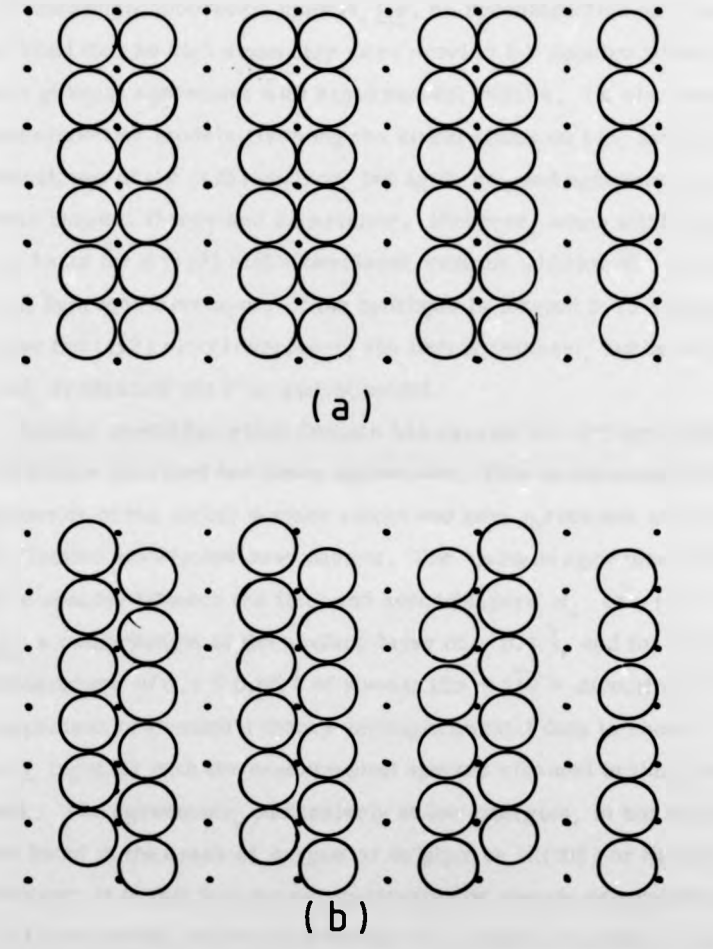

Fig. 5.9

Distortion models of the possible Ni(110)(1x2)H structure

(a) the Tucker model (12)

(b) the model proposed by Taylor and Estrup (10)

For the simple adsorption models, i.e. no reconstruction or distortion, he found that no high symmetry sites provide I-V spectra which are in even general agreement with experimental results. He also considered reconstruction models involving the nickel atoms on top, bridged and in the hollows of the (110) surface, but again no good agreement was found between theory and experiment. However, some slight agreement was found for a (1x2) nickel overlayer with the addition of a coincident (1x2) hydrogen overlayer; if the hydrogen is located 0.75 Å directly above the (1x2) nickel overlayer, the best agreement, but by no means good, is obtained for this type of model.

Another model for which Demuth has carried out full dynamical calculation provided far better agreement. This is the model involving distortion of the nickel surface atoms and best agreement is found for the Tucker model mentioned earlier. The optimum agreement occurs for a spacing between the first and second layers d_1 of $\sim 1.15 \pm 0.05$ Å i.e. a compression of the surface layer of ~ 0.1 Å, and for an alternate displacement of 0.1 ± 0.05 Å of rows in the $< 1\bar{1}0 >$ direction. The comparison of Demuth's theory and experimental data is shown in Figs. 5.8, 5.10, together with the experimental spectra obtained in this present work. The agreement, particularly at low energies, is not as good as that found in the cases of oxygen or sulphur on Ni(100) or Ni(110). However, it is felt that the reconstruction or simple adsorption models can be reasonably ruled out in favour of a distortion model, most favourably the Tucker model.

This apparent distortion of the lattice may be significant in that the attractive or repulsive forces involved could well account in some way for bulk hydrogen diffusion into metals. However, the proviso must be added that dynamical LEED calculations for the (1x2) hydrogen LEED structure on Ni(110) do not eliminate the possibility of hydrogen having been absorbed as well as adsorbed: the position of the hydrogen atoms has not been considered. Good correlation of theoretical and experimental

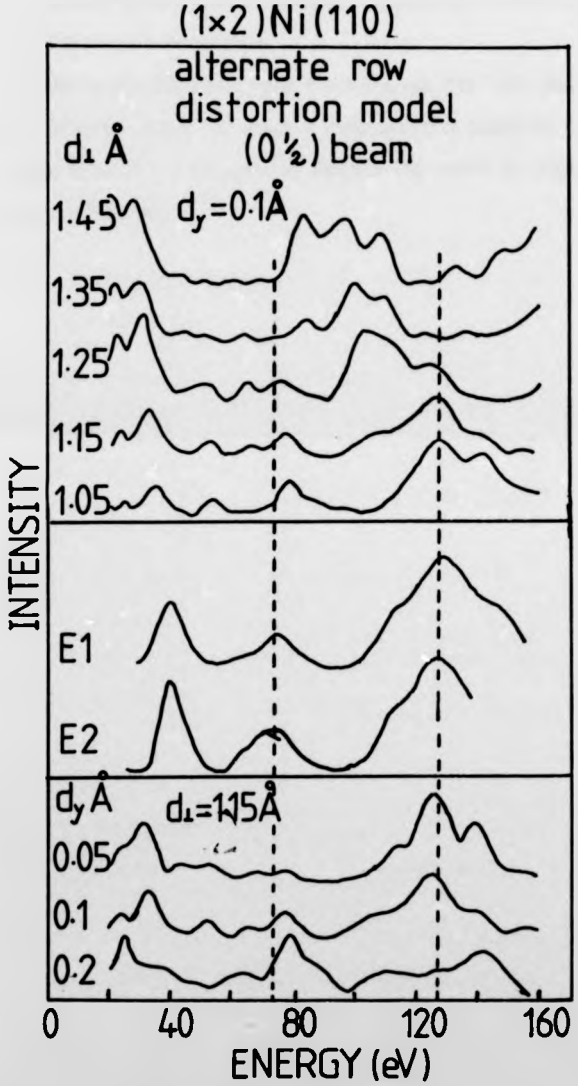

Fig. 5.10

A comparison of the theoretical spectrum and experimental work (E1) of Demuth (13) together with the spectrum obtained in the present work (E2) for the (0 1/2) beam, using the alternate row distortion model.

data over a much wider range of angles and a larger number of beams is needed before more certain conclusions as to the Ni(110)(1x2)H structure can be drawn.

The experimental work carried out for this thesis is intended to provide the basis for such a comparison between theory and experiment, since data for a number of beams for various angles of incidence have been collected.

CHAPTER FIVE

REFERENCES

1. M.A. Chesters & J. Pritchard, Surface Sci., 28 (1971) 460.
2. G.E. Becker & H.D. Hagstrum, J. Vac. Sci. & Technol., 11 (1974) 284.
3. F.P. Netzer & M. Prutton, Solid State Comm., 15 (1974) 341.
4. L. McDonnell, B.D. Powell & D.P. Woodruff, Surface Sci., 40 (1973) 669.
5. J.E. Demuth, Ph.D. Thesis, Cornell University (1973).
6. R.H. Tait, S.Y. Tong & T.N. Rhodin, Phys. Rev. Lett., 28 (1972) 553.
7. J.E. Demuth, P.M. Marcus & D.W. Jepsen, Phys. Rev. B, 11 (1975) 1460.
8. J.E. Demuth & T.N. Rhodin, Surface Sci., 42 (1974) 261; 45 (1974) 249.
9. K. Christmann, G. Ertl & O. Schober, Surface Sci., 40 (1973) 61.
10. T.N. Taylor & P.J. Estrup, J. Vac. Sci. & Technol., 11 (1974) 244.
11. L.H. Germer & A.U. McRae, J. Chem. Phys., 37 (1962) 1382.
12. C.W. Tucker, Surface Sci., 26 (1971) 311.
13. J.E. Demuth, J. Colloid & Interface Sci., 58 (1977) 184.

CHAPTER SIX

THE CLEAN NI(100) AND NI(100)(2x2)C-p4g SURFACES

6.1 Introduction

This chapter will follow the same basic format as that of Chapter Five. Firstly, there will be a presentation and discussion of the clean Ni(100) surface I-V data and a comparison will be made with other work. The I-V spectra obtained from the carbon adsorption on this surface will then be shown, and some possible structures described.

6.2 The Clean Ni(100) Surface

6.2.1 Experimental procedures

The preparation of a clean Ni(100) surface followed very similar lines to the (110) surface, except that AES revealed sulphur and carbon as contaminants until several more cycles of argon ion bombardment and heating had been carried out. The clean AES spectrum was similar to that obtained for the (110) surface, showing the same diffraction peaks, although slightly reduced in intensity.

A clean surface LEED pattern is shown in Plate 6.1, and Fig. 6.1 describes the beam and azimuthal nomenclature. All spectra presented here were taken at room temperature ($\sim 293^{o}$ K) and are shown in Figs. 6.2 and 6.3. (The scaling factor, S, is as defined at the end of Section 5.2.1). The specimen was cooled and a few spectra compared with those obtained at room temperature; differences occurred only in the absolute intensities of peaks, which were larger for the 150^{o} K specimen by $\sim 10\%$.

6.2.2 Discussion of clean surface data

The clean Ni(100) surface has been widely studied by many workers using a variety of techniques (1-6). In particular, a very detailed study of the clean surface and the same surface with chalcogen adsorbates has been made using LEED by Demuth (7). For a very thorough discussion of the clean surface, this latter work is recommended

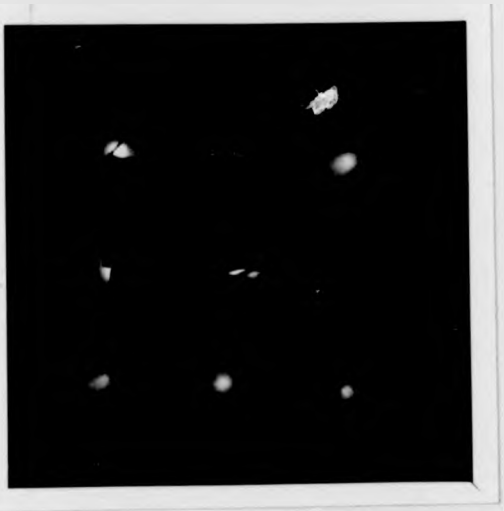

110 eV
PLATE 6·1

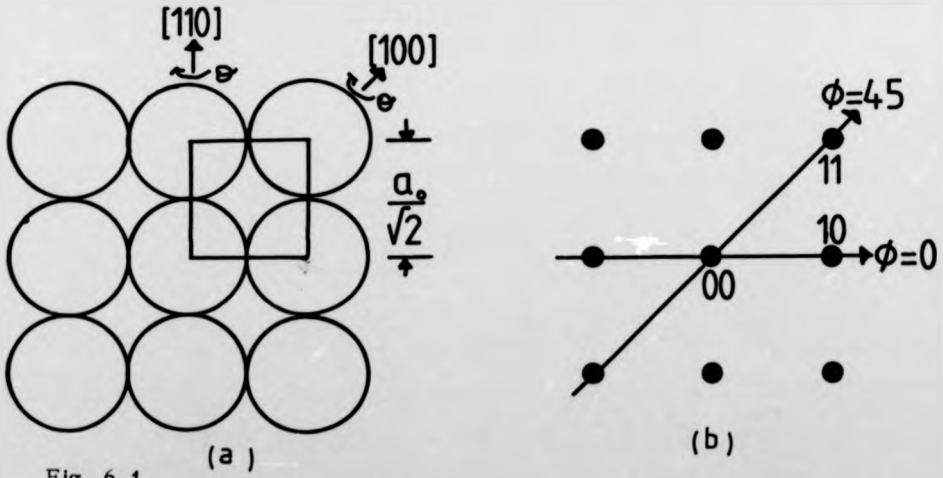

Fig. 6.1

Conventions for:

(a) azimuthal indexing (real space)

(b) beam indexing (diffraction pattern)

Fig. 6.2

Overleaf are presented specular beam I-V spectra for the $\varphi = 0^{o}$ and $\varphi = 45^{o}$ azimuths of clean Ni(100) at 290^{o} K.

Fig. 6.2

Overleaf are presented specular beam I-V spectra for the $\varphi = 0^{o}$ and $\varphi = 45^{o}$ azimuths of clean Ni(100) at 290^{o} K.

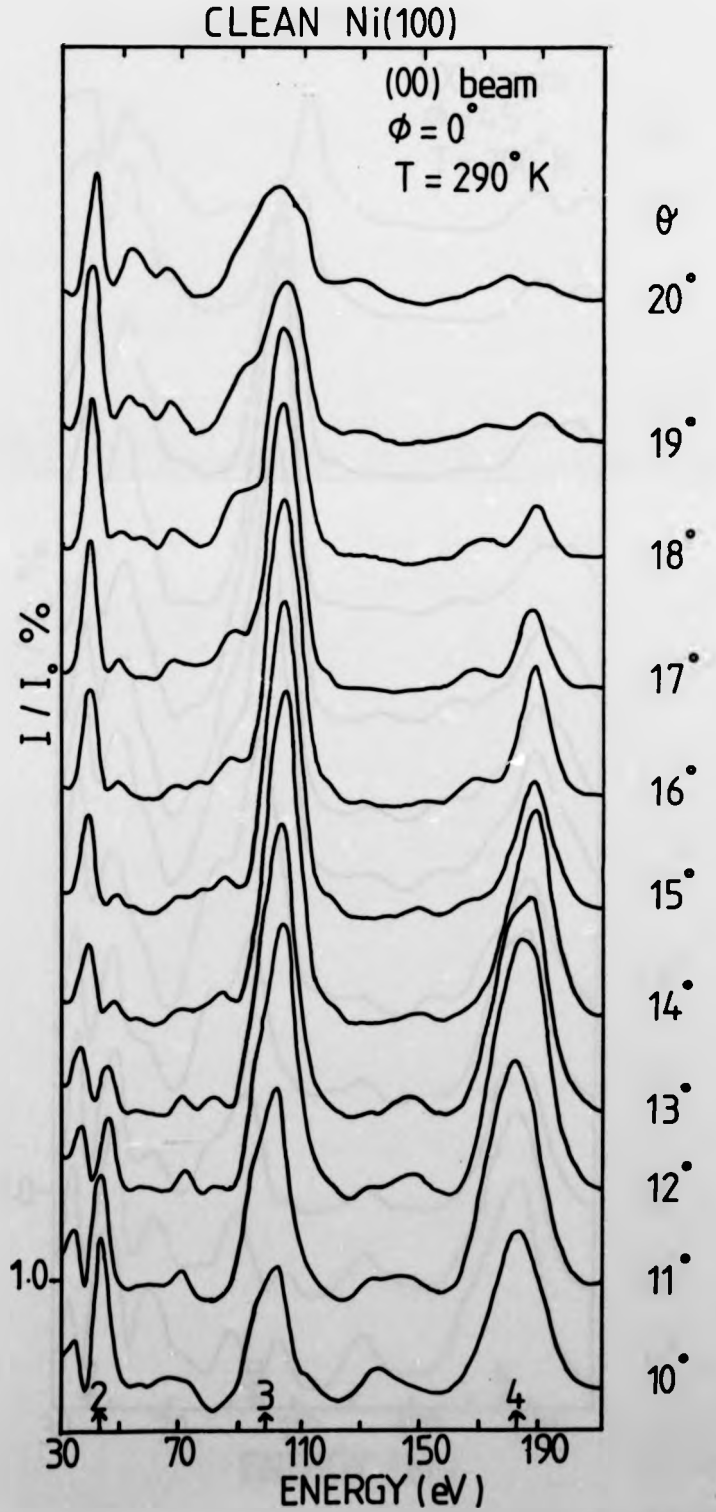
CLEAN Ni(100)
(00) beam
$\phi = 0^\circ$
T = 290° K
θ
20°
19°
18°
17°
16°
15°
14°
13°
12°
11°
10°
I / I₀ %
1·0
2
3
4
30
70
110
150
190
ENERGY (eV)

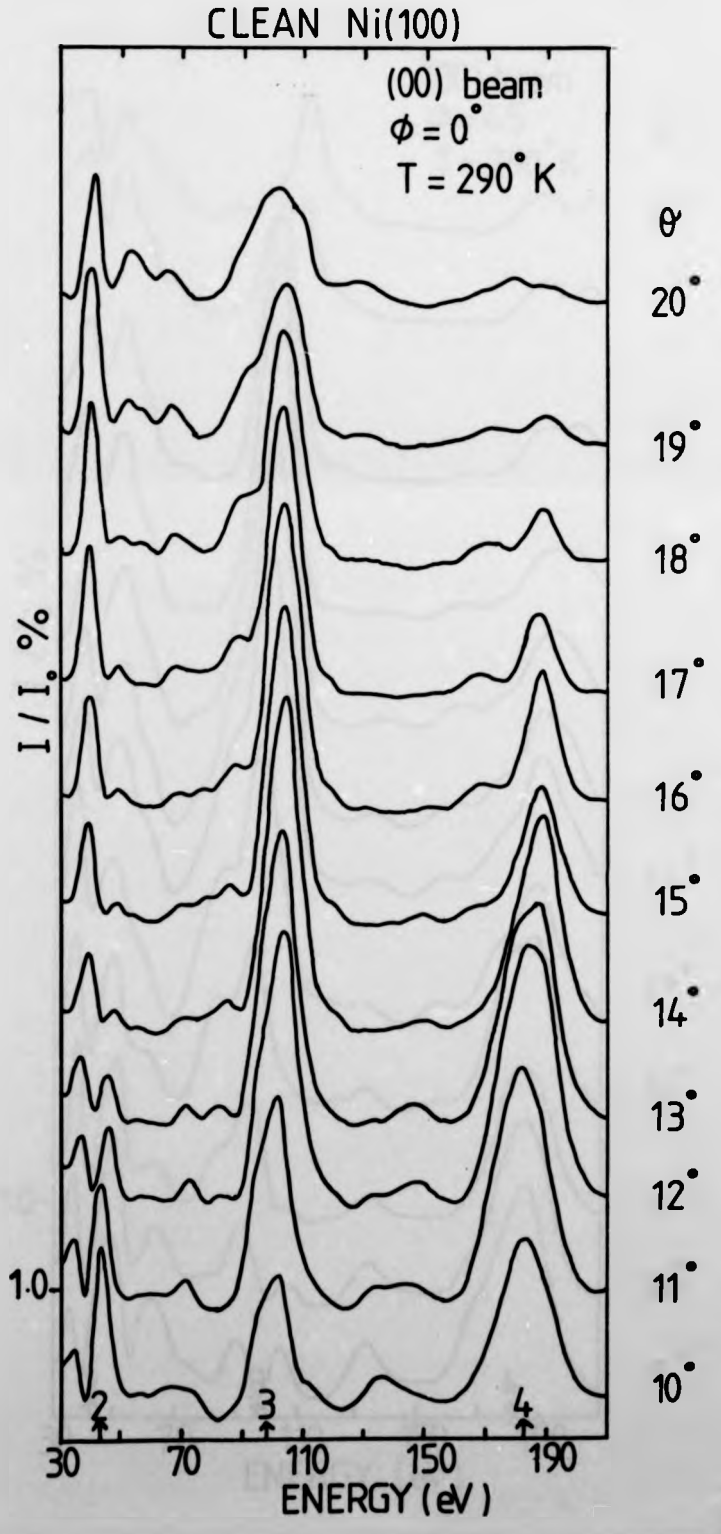
CLEAN Ni(100)
(00) beam
$\phi = 0^\circ$
T = 290° K
θ
20°
19°
18°
17°
16°
15°
14°
13°
12°
11°
10°
I/I₀ %
1.0
2
3
4
30
70
110
150
190
ENERGY (eV)

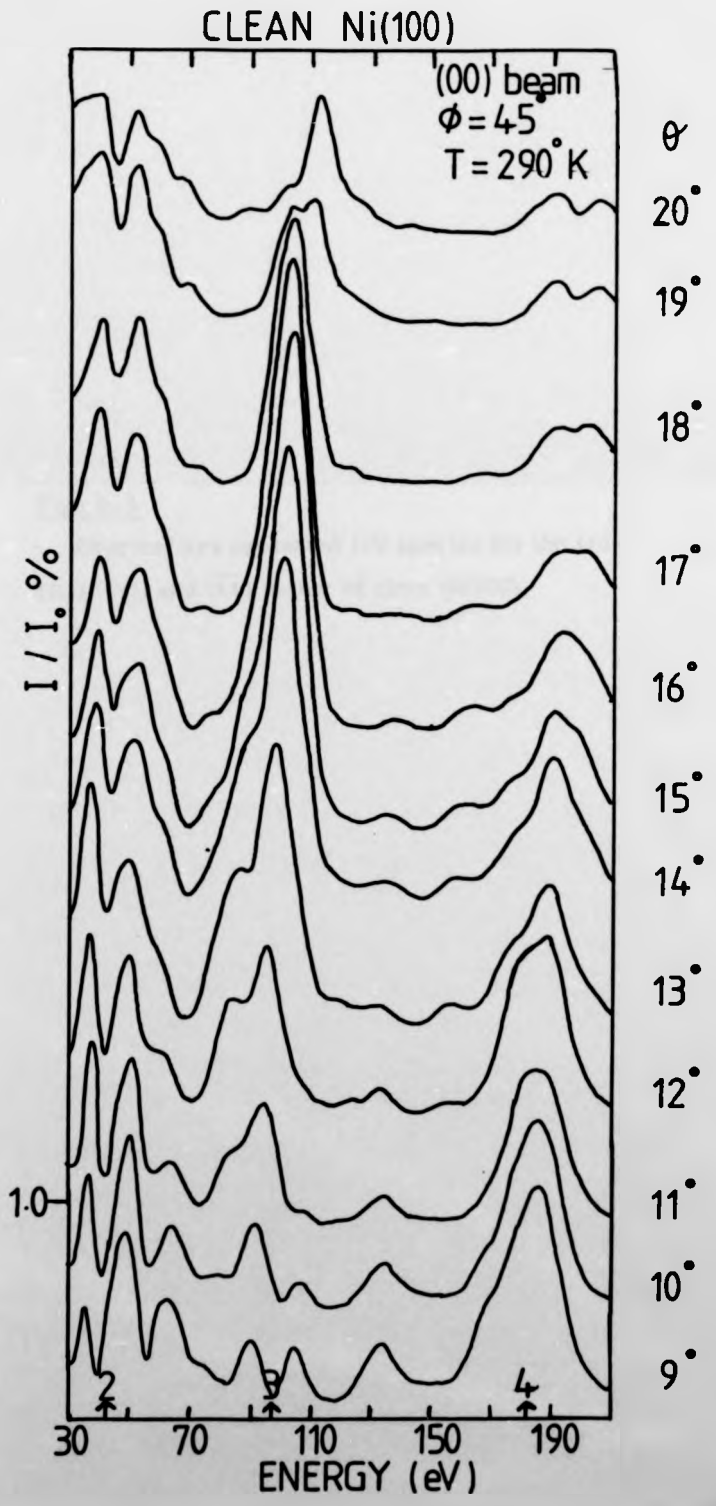
CLEAN Ni(100)
(00) beam
Φ = 45°
T = 290°K
θ
20°
19°
18°
17°
16°
15°
14°
13°
12°
11°
10°
9°
I / I₀ %
1·0
2
3
4
30
70
110
150
190
ENERGY (eV)

Fig. 6.3

Overleaf are presented I-V spectra for the (10), $(\bar{1}0)$, (11) and $(\bar{1}\bar{1})$ beams of clean Ni(100).

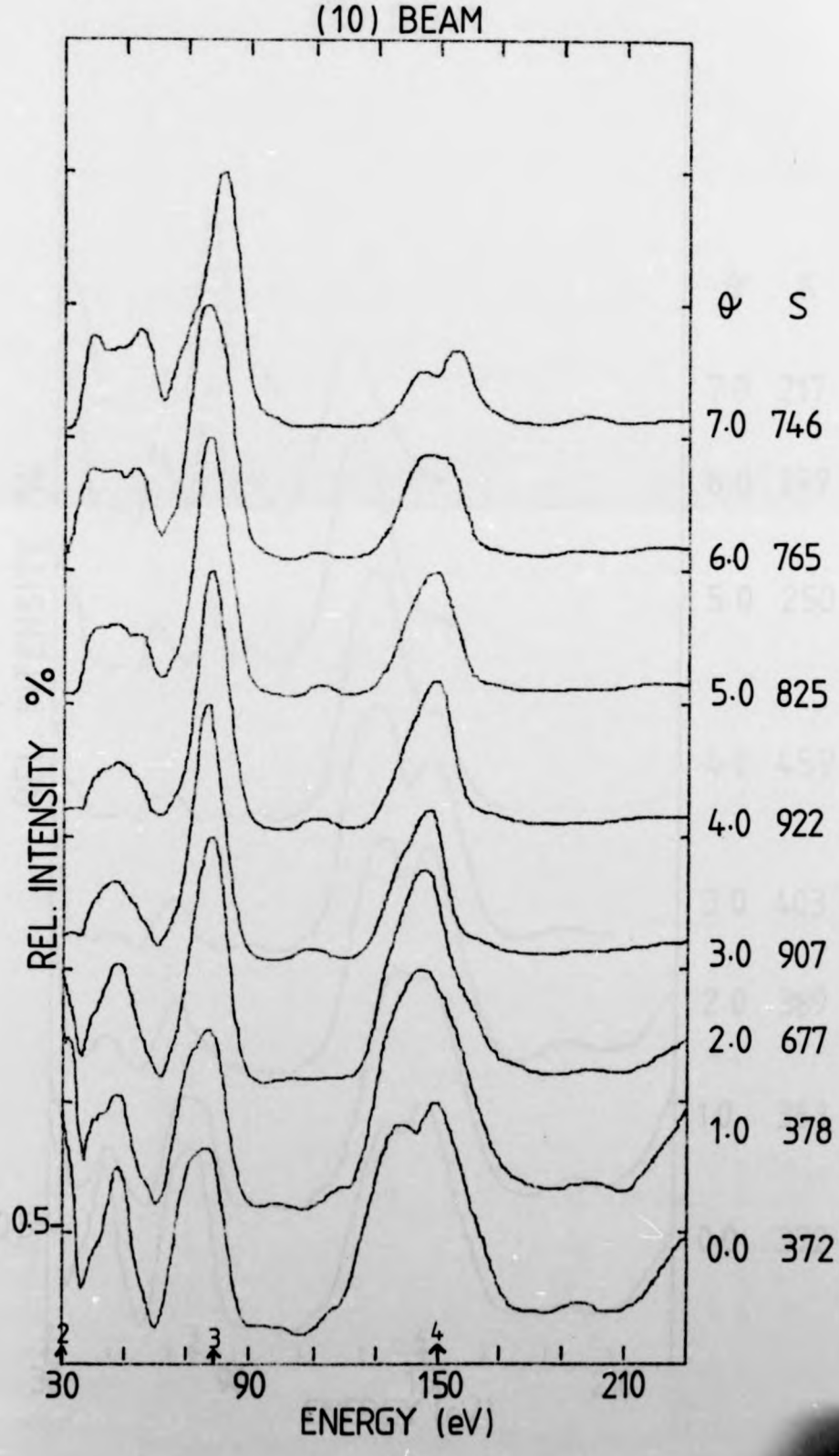
(10) BEAM
θ S
7·0 746
6·0 765
5·0 825
4·0 922
3·0 907
2·0 677
1·0 378
0·0 372
REL. INTENSITY %
0·5
2
3
4
30
90
150
210
ENERGY (eV)

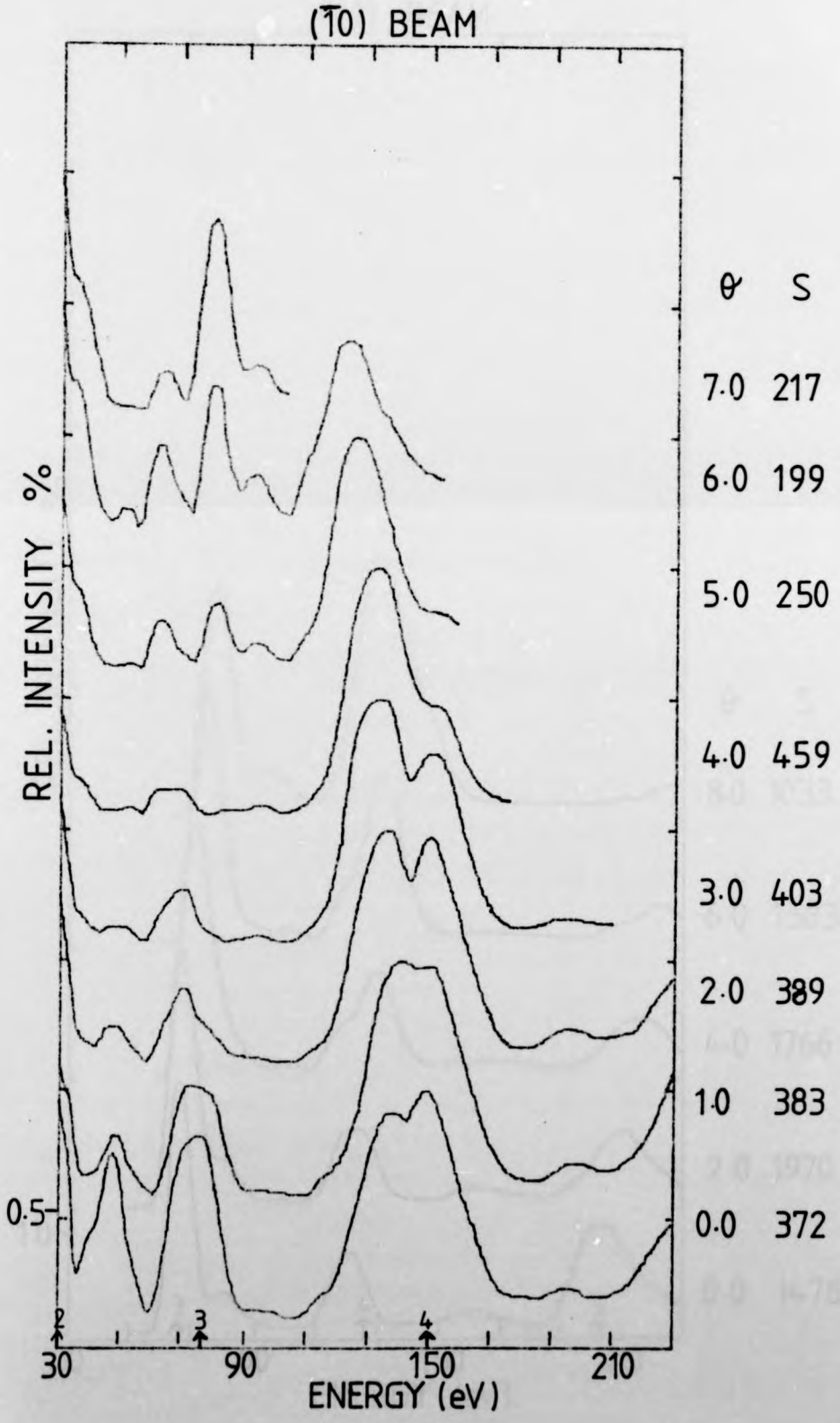
(10) BEAM
REL. INTENSITY %
0.5
θ S
7.0 217
6.0 199
5.0 250
4.0 459
3.0 403
2.0 389
1.0 383
0.0 372
2
3
4
30
90
150
210
ENERGY (eV)

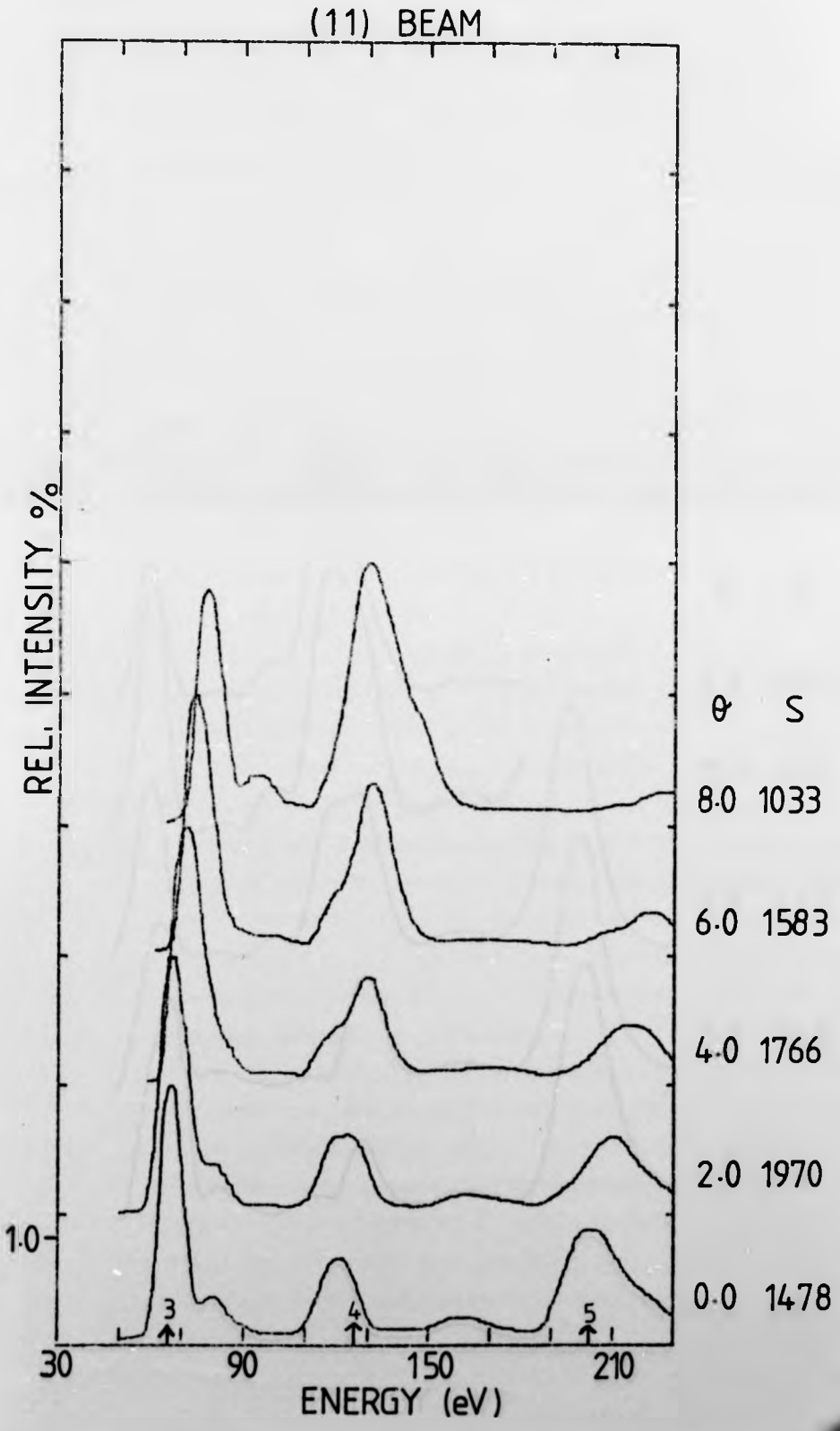
(11) BEAM
REL. INTENSITY %
1·0
θ S
8·0 1033
6·0 1583
4·0 1766
2·0 1970
0·0 1478
3
4
5
30
90
150
210
ENERGY (eV)

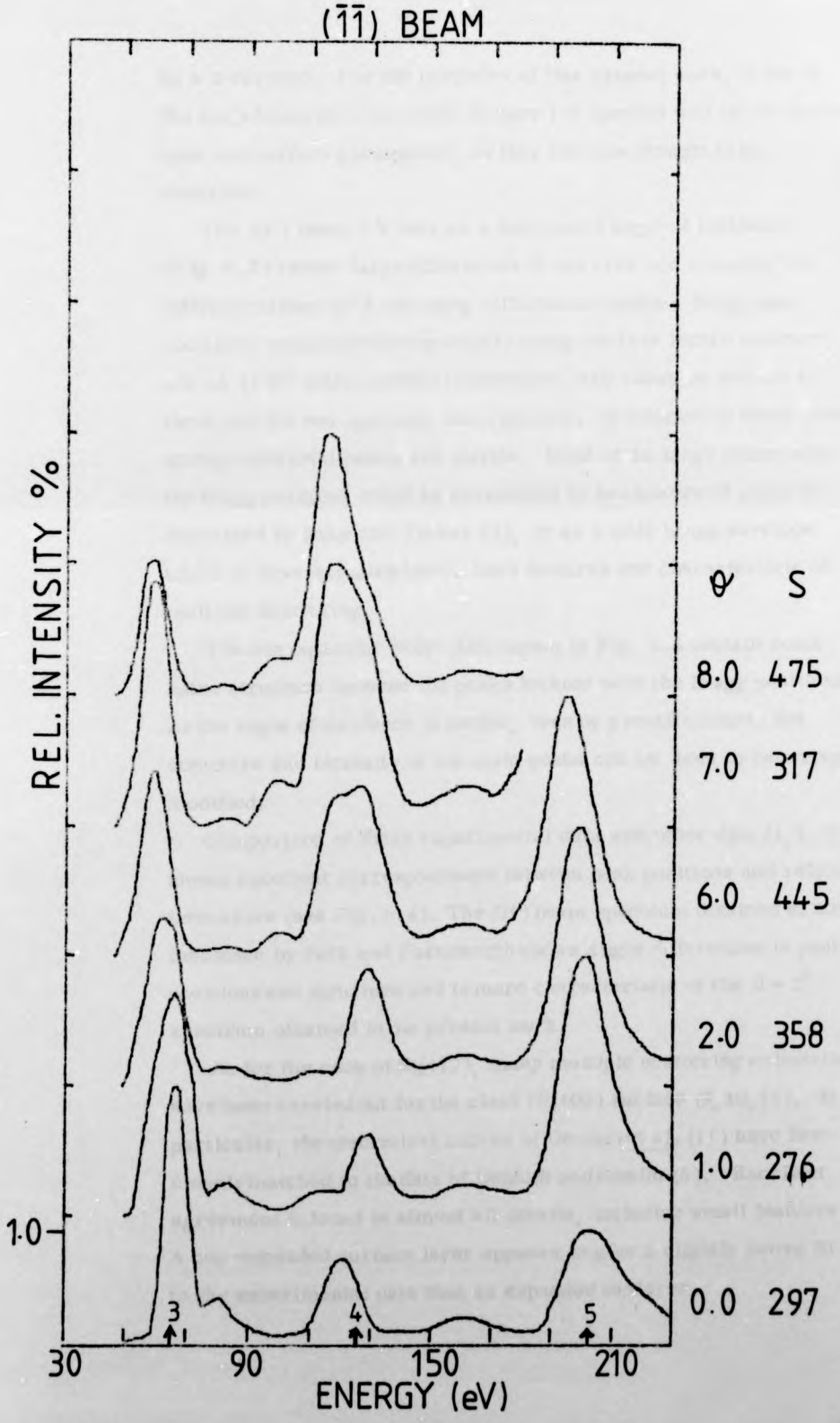
(1̄1̄) BEAM
REL. INTENSITY %
1·0
θ
S
8·0 475
7·0 317
6·0 445
2·0 358
1·0 276
0·0 297
3
4
5
30
90
150
210
ENERGY (eV)

as a reference. For the purposes of this present work, a few of the main features of the clean surface I-V spectra will be commented upon and surface parameters, as they are now thought to be, described.

The (00) beam I-V data as a function of angle of incidence (Fig. 6.2) reveal large differences in features and intensity for different values of θ and along different azimuths. Bragg peak positions, calculated kinematically using the bulk lattice constant and an 11 eV inner potential correction, are shown by arrows in these and the non-specular beam spectra. In addition to these peaks, strong additional peaks are visible. Most of the large peaks near the Bragg positions could be considered to be clusters of peaks as described by Duke and Tucker (8), or as a wide Bragg envelope which is severely modulated. Such features are characteristic of multiple scattering.

The non-specular beam data shown in Fig. 6.3 contain some extra structure between the peaks located near the Bragg positions. As the angle of incidence is varied, even by a small amount, the structure and intensity of the main peaks can be seen to be strongly modified.

Comparison of these experimental data with other data (1, 2, 7) shows excellent correspondence between peak positions and relative intensities (see Fig. 6.4). The (01) beam spectrum obtained at normal incidence by Park and Farnsworth shows slight differences in peak positions and structure and is more characteristic of the $\theta = 2^{o}$ spectrum obtained in the present work.

As for the case of Ni(110), many multiple scattering calculations have been carried out for the clean Ni(100) surface (9, 10, 11). In particular, the theoretical curves of Demuth et al. (11) have been closely matched to the data of Demuth and Rhodin (6). Excellent agreement is found in almost all details, including small features. A non-expanded surface layer appears to give a slightly better fit to the experimental data than an expanded top layer.

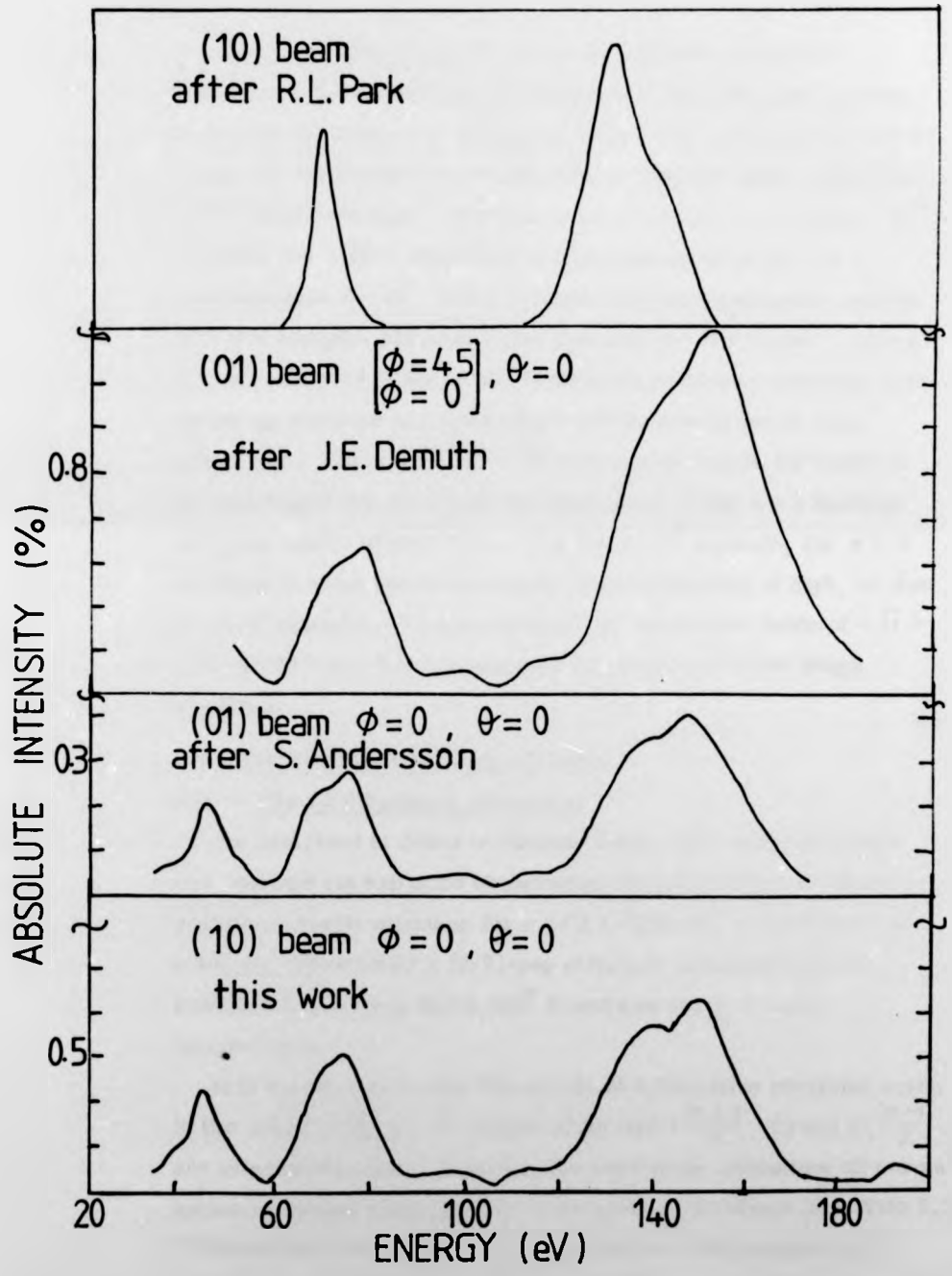

Fig. 6.4

Comparison of (10) beam data for Ni(100) obtained by various workers (1, 2, 7).

From a simple viewpoint, it can be seen how particular resonances affect the Bragg envelopes; for the (100) nickel surface at normal incidence, the emergence of the $< 20 >$ beams lies ~ 13 eV below the $n = 3$ kinematical peak for the specular beam, while the $< 12 >$ beams emerge ~ 11 eV above the $n = 3$ peak. For the $\varphi = 45^{o}$ azimuth, the $< \overline{12} >$ resonance causes a decrease in the $n = 3$ envelope up to $\theta = 12^{o}$, but as θ increases, this emergence moves to lower energies and lessens the effect on the $n = 3$ peak. Above $\theta = 16^{o}$, the $< 1\bar{1} >$ and $< 22 >$ emergence conditions converge upon the Bragg envelope and again cause severe attenuation of peak intensities. For $\varphi = 0^{o}$, the $< \overline{22} >$ resonance may be the cause of the splitting of the $n = 4$ peak and attenuation of the $n = 3$ envelope at higher angles of incidence. For the $\varphi = 0^{o}$ azimuth, the $n = 2$ envelope is narrower at low angles of incidence than at high, or than at other azimuths. This corresponds to the narrow bands of $< \overline{11} >$, $< \bar{1}1 >$, $< 1\bar{1} >$ and $< 11 >$ emergence conditions about the Bragg condition.

6.3 The Ni(100)(2x2) C-p4g Structure

6.3.1 The LEED pattern information

As described in detail in Chapter Four, this carbon structure was obtained via exposure of the heated Ni(100) surface to ethylene. A pattern, easily mistaken for a $(\sqrt{2} \times \sqrt{2})R\ 45^{o}$ structure at low energies, but actually a (2x2)-p4g structure (discussed below), intensified on cooling below 343^{o} K and was sharp at room temperature.

It is interesting to note the amount of information contained solely in the LEED pattern. All beams of the type $(\frac{2n+1}{2}, 0)$ and $(0, \frac{2n+1}{2})$ are missing at normal incidence, but have finite intensities off normal incidence except where they lie in the plane of incidence (see Plate 6.2). This indicates that the structure contains two perpendicular glide lines and must therefore be associated with the space-group p4g (12, 13) (Appendix III and Fig. 6.11).

Ni(100)

CLEAN (110 eV)

$\theta = 0^{\circ}$, $\phi = 0^{\circ}$, (120 eV)

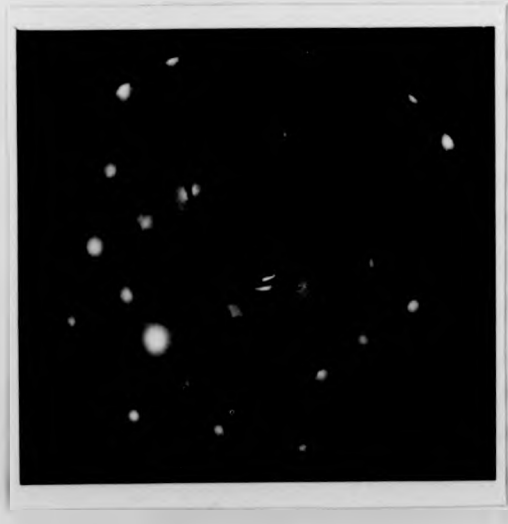

$\theta = 0^{\circ}$, $\phi \neq 0^{\circ}$, (140 eV)

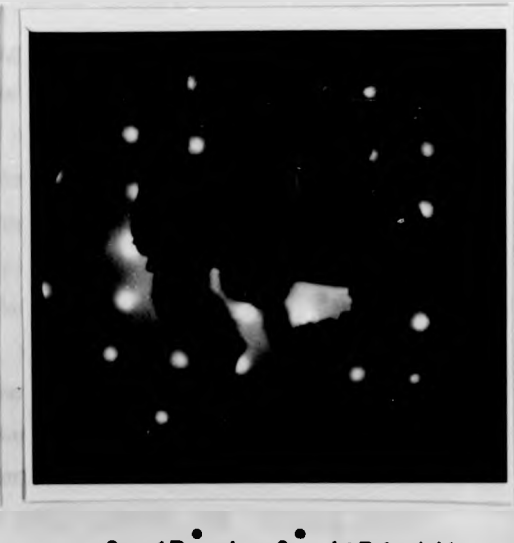

$\theta = 13^{\circ}$, $\phi = 0^{\circ}$, (131 eV)

PLATE 6·2

6.3.2 Discussion of intensity-energy spectra

Specular, integral and half-order beam spectra were obtained from the Ni(100)(2x2) C-p4g surface at room temperature and are presented in Figs.6.5 and 6.6.

The specular beam data show a marked change from the clean surface results; for example, in the $\varphi = 45^{o}$ azimuth, the Bragg peaks have been greatly reduced and are almost non-existent at higher angles of incidence. Peak intensities are generally reduced by about 30% as compared with clean surface intensities.

The (11) beam spectra are altered very little from those obtained from the clean surface. The n = 4 Bragg peak gains intensity with increasing angle of incidence, but the n = 5 Bragg peak is washed out.

The (10) beam shows more dramatic changes. The n = 3 Bragg peak is split into two and suffers a decrease in intensity relative to the lower energy features at ~ 40 eV, which are enhanced. The n = 4 Bragg peak also shows signs of splitting and is very much reduced in intensity, particularly as the angle of incidence is increased. Higher energy, (E > 200 eV) features are attenuated and a number of intensity maxima are shifted to lower energies.

A limited amount of data from a Ni(100) surface with a carbon overlayer are available for comparison. Demuth and Rhodin (14) have obtained specular beam data for the $\varphi = 0^{o}$ azimuth over a variety of angles of incidence. However, the non-specular beam data so far published are for the (11)(01) and $(\frac{1}{2}\frac{1}{2})$ at normal incidence only. These non-specular beam data are shown for comparison in Fig. 6.7. Demuth and Rhodin (14) describe the carbon structure obtained as a p(2x2) pattern; the "missing spots" were not reported. This was obtained by dissociating carbon monoxide, adsorbed from the gas phase, in a 2keV electron beam. The sample was then warmed, resulting in CO and CO_2 coming off, leaving an ordered carbon overlayer.

Fig. 6.5

Overleaf are presented the specular beam spectra from the Ni(100)(2x2)C-p4g surface at $\varphi = 0^{o}$ and $\varphi = 45^{o}$.

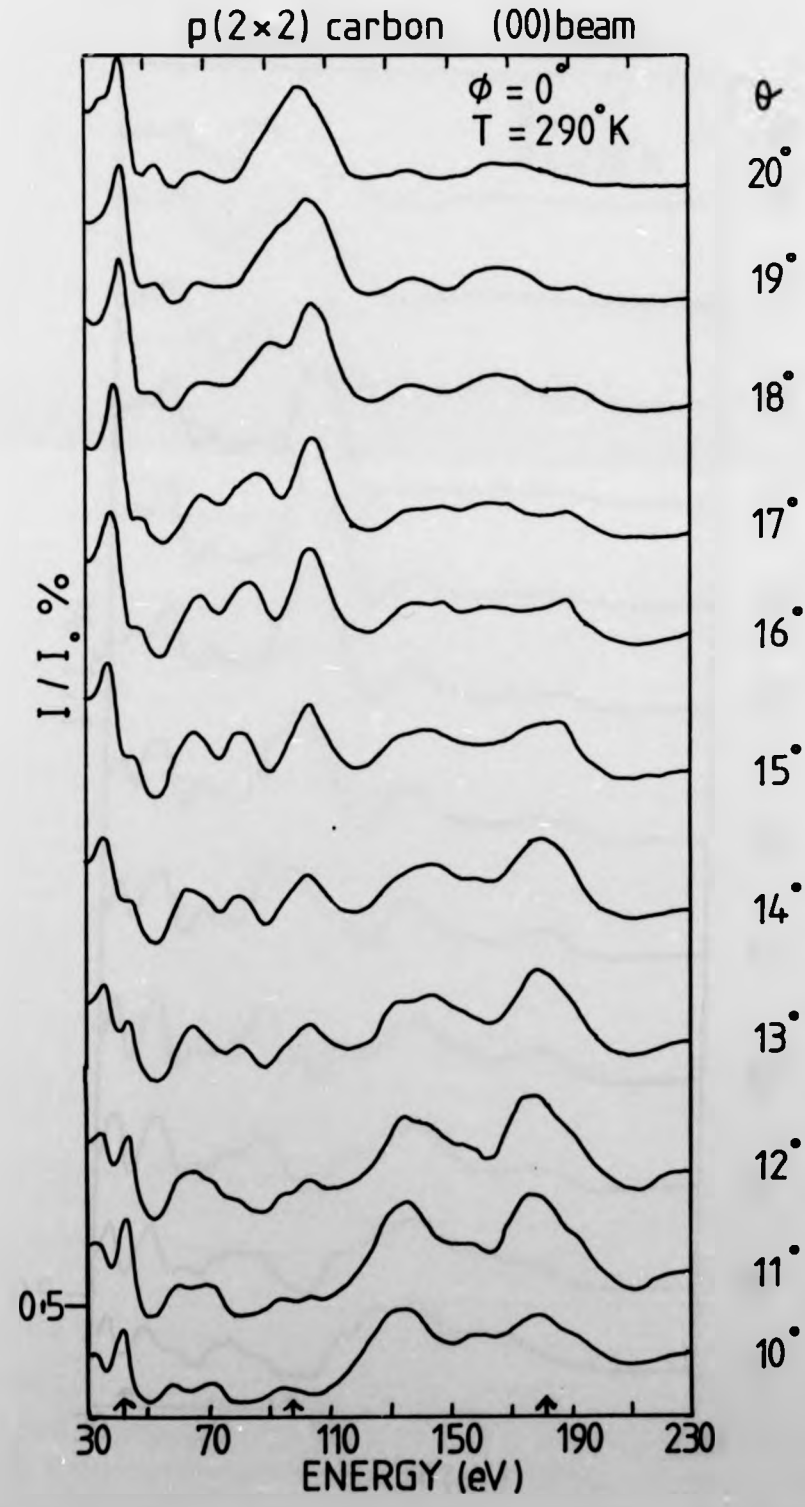
p(2×2) carbon (00)beam
Φ = 0°
T = 290°K
θ
20°
19°
18°
17°
16°
15°
14°
13°
12°
11°
10°
I/I₀ %
0·5
30
70
110
150
190
230
ENERGY (eV)

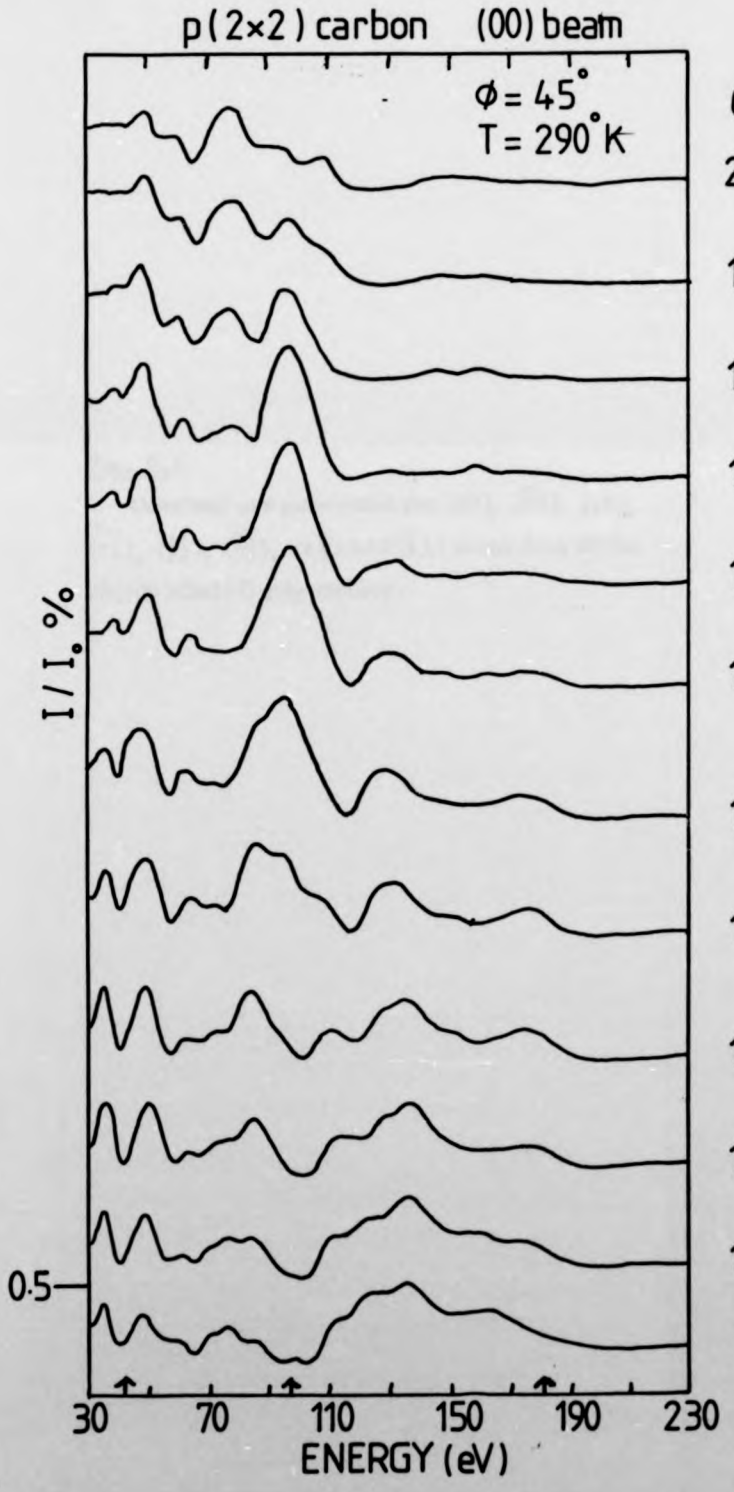
p(2×2) carbon (00) beam
φ = 45°
T = 290°K
θ
20°
19°
18°
17°
16°
15°
14°
13°
12°
11°
10°
9°
I/I₀ %
0·5
30
70
110
150
190
230
ENERGY (eV)

Fig. 6.6

Overleaf are presented the (10), $(\bar{1}0)$, (11), $(\bar{1}\bar{1})$, $(\frac{1}{2}\frac{1}{2})$, $(\frac{\bar{1}}{2}\frac{\bar{1}}{2})$, $(1\,\frac{\bar{1}}{2})$ and $(\bar{1}\,\frac{1}{2})$ beam data of the Ni(100)(2x2)C-p4g surface.

Fig. 6.6

Overleaf are presented the (10), $(\bar{1}0)$, (11), $(\bar{1}\bar{1})$, $(\frac{1}{2}\frac{1}{2})$, $(\frac{\bar{1}}{2}\frac{\bar{1}}{2})$, $(1\,\frac{\bar{1}}{2})$ and $(\bar{1}\,\frac{1}{2})$ beam data of the Ni(100)(2x2)C-p4g surface.

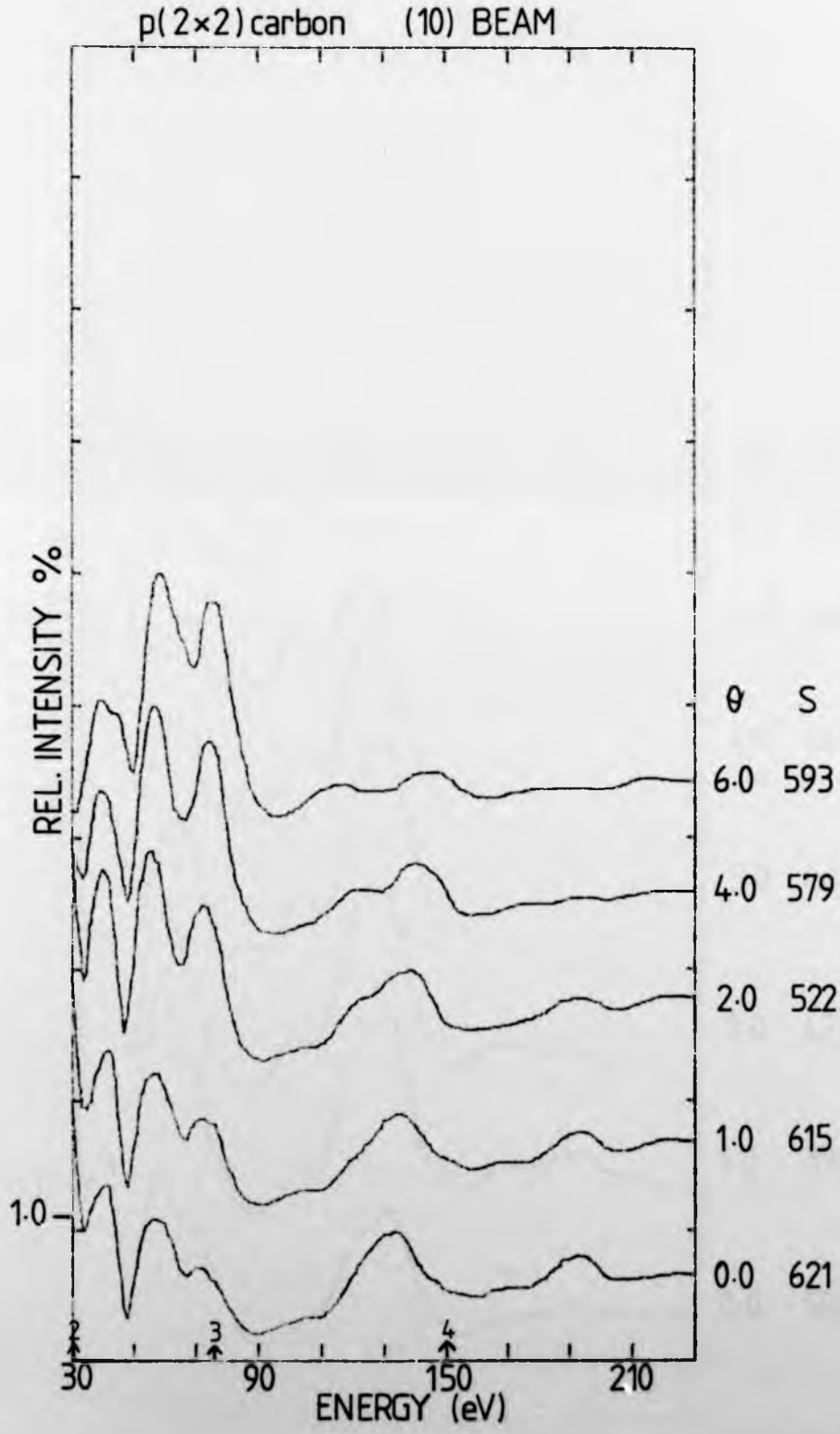
p(2×2) carbon (10) BEAM
REL. INTENSITY %
θ S
6·0 593
4·0 579
2·0 522
1·0 615
0·0 621
1·0
2
3
4
30
90
150
210
ENERGY (eV)

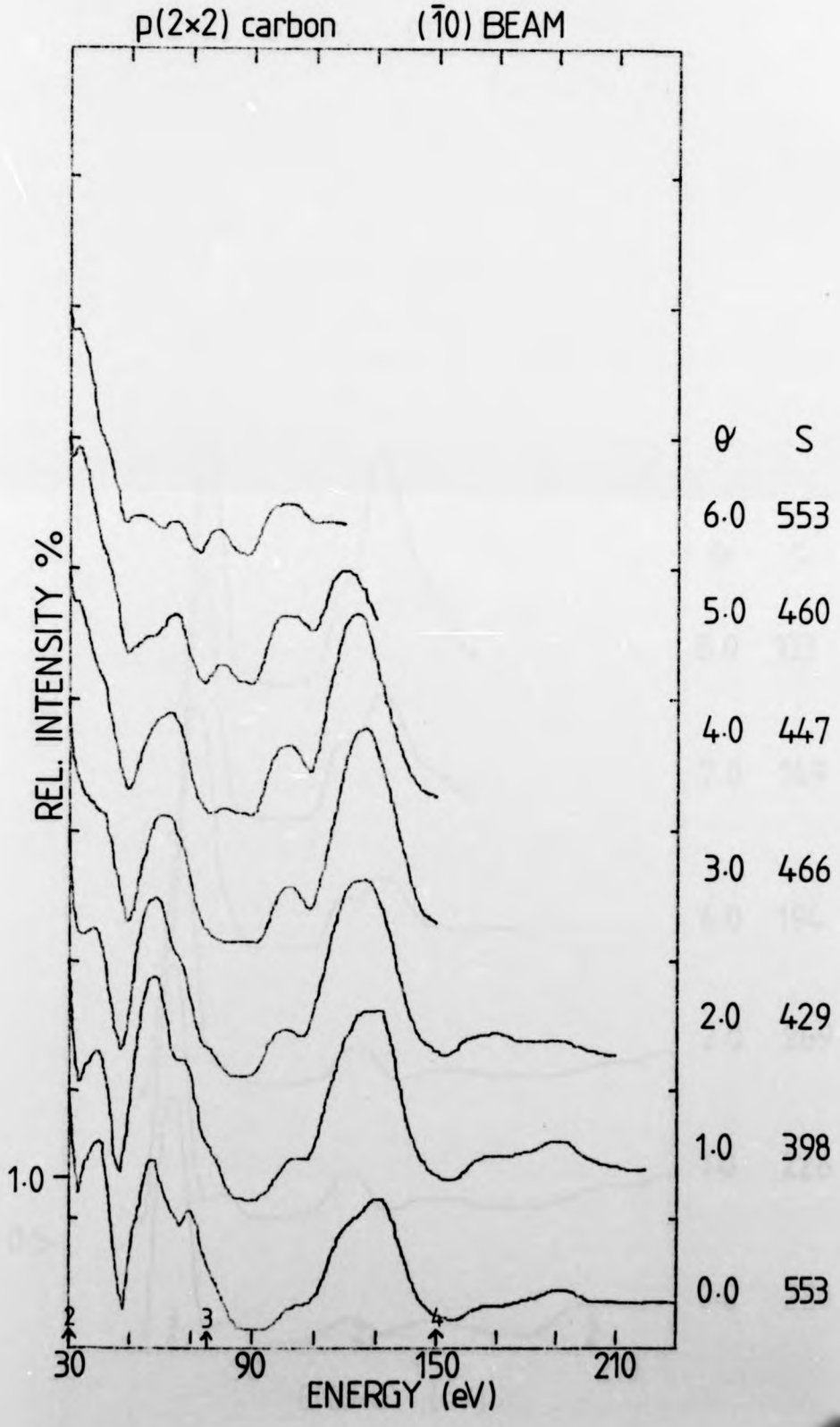
p(2×2) carbon
(1̄0) BEAM
REL. INTENSITY %
1·0
θ
S
6·0 553
5·0 460
4·0 447
3·0 466
2·0 429
1·0 398
0·0 553
2
3
4
30
90
150
210
ENERGY (eV)

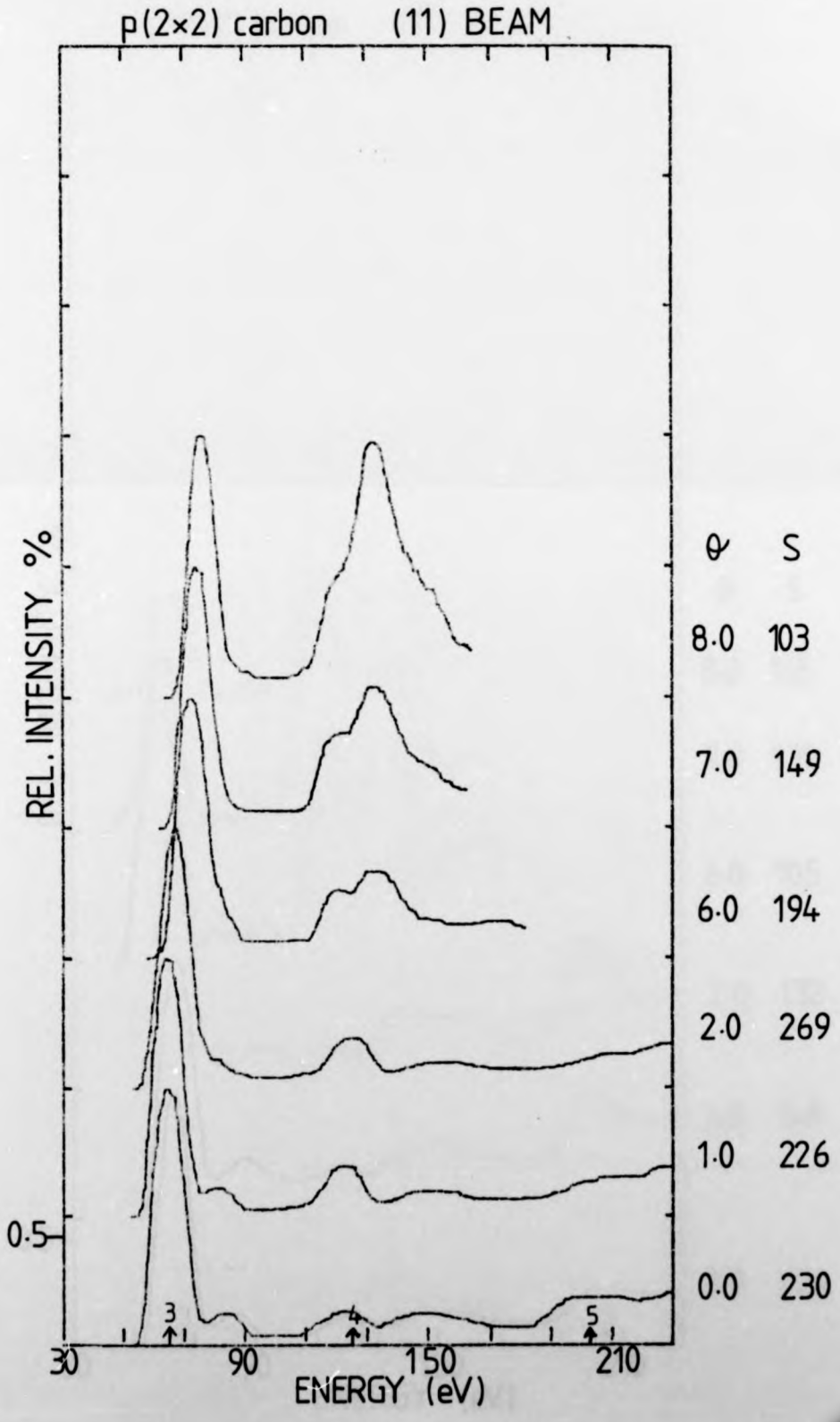
p(2×2) carbon (11) BEAM
REL. INTENSITY %
0·5
θ S
8·0 103
7·0 149
6·0 194
2·0 269
1·0 226
0·0 230
3
4
5
30
90
150
210
ENERGY (eV)

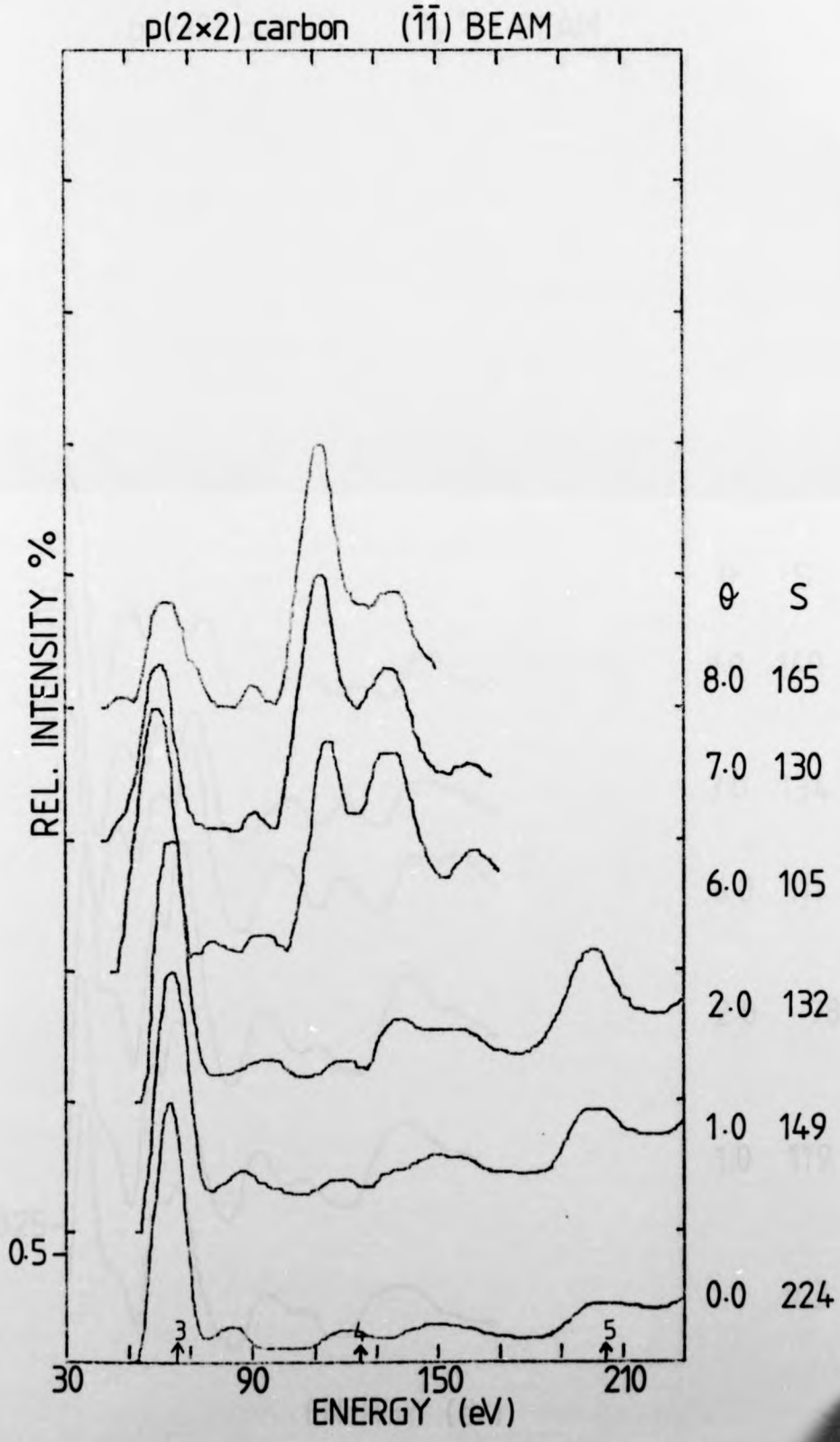
p(2×2) carbon (1̄1̄) BEAM
REL. INTENSITY %
θ S
8·0 165
7·0 130
6·0 105
2·0 132
1·0 149
0·0 224
0·5
3
4
5
30
90
150
210
ENERGY (eV)

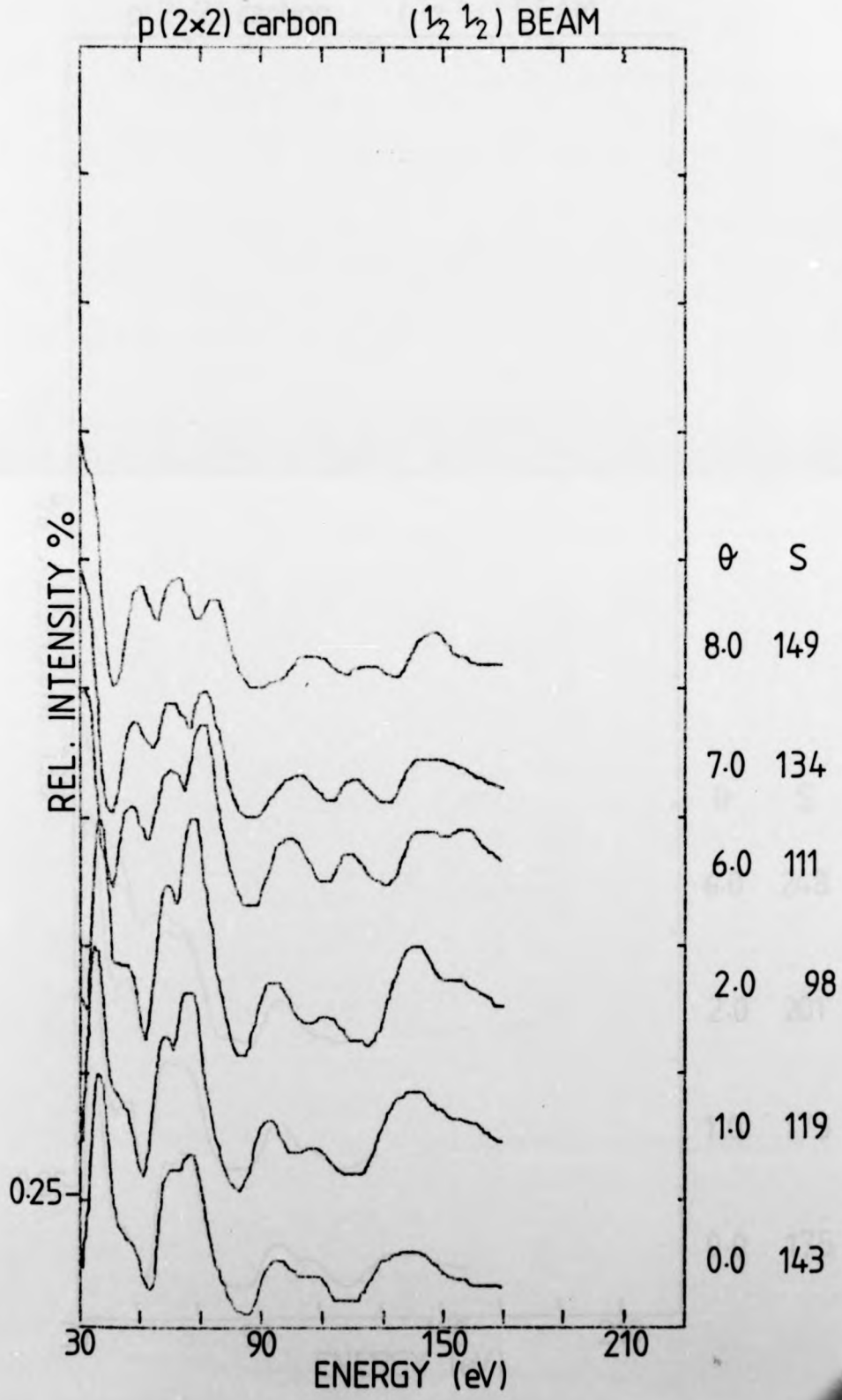
p(2×2) carbon (½ ½) BEAM
REL. INTENSITY %
0·25
θ S
8·0 149
7·0 134
6·0 111
2·0 98
1·0 119
0·0 143
30
90
150
210
ENERGY (eV)

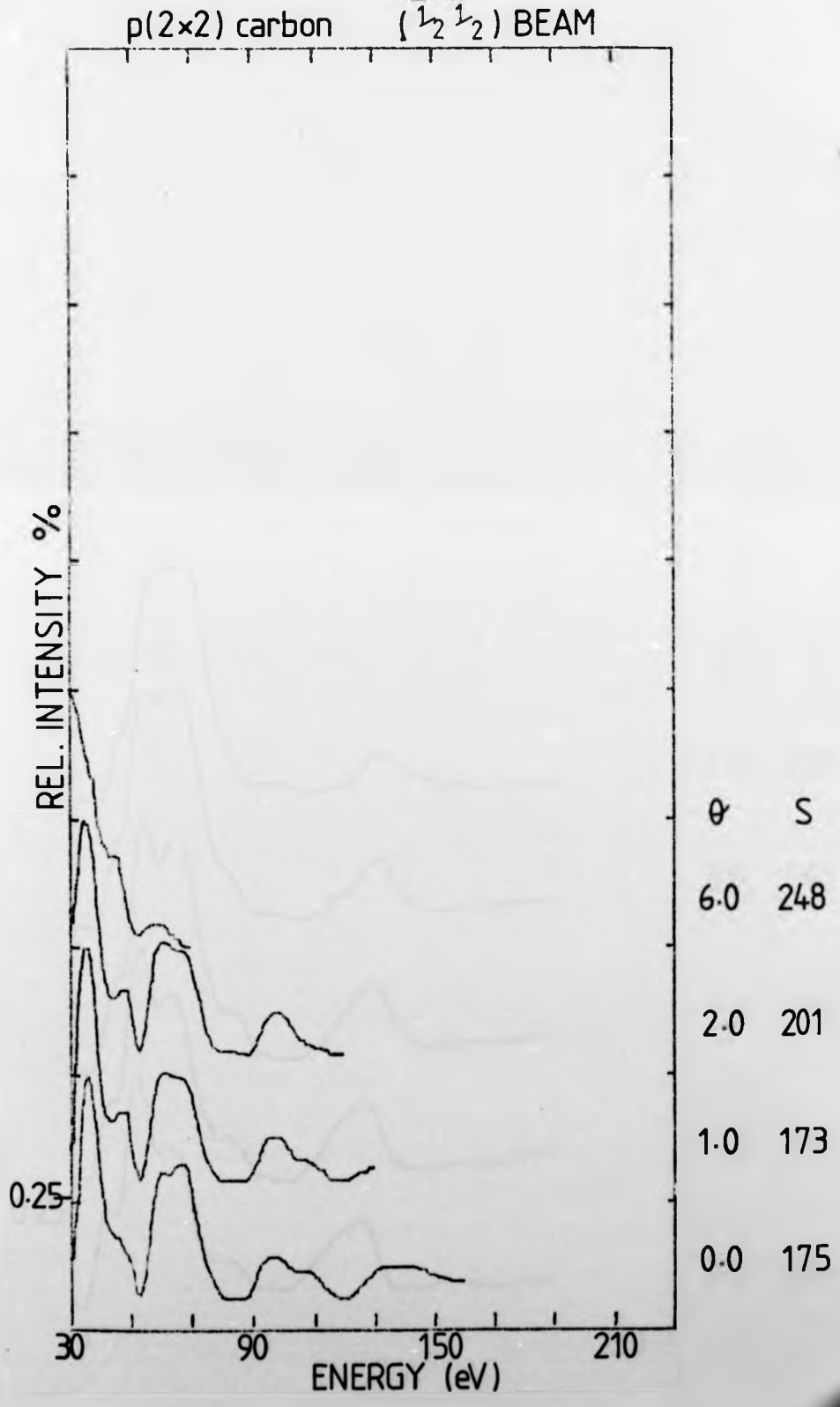
p(2×2) carbon (1/2 1/2) BEAM
REL. INTENSITY %
0·25
30
90
150
210
ENERGY (eV)
θ S
6·0 248
2·0 201
1·0 173
0·0 175

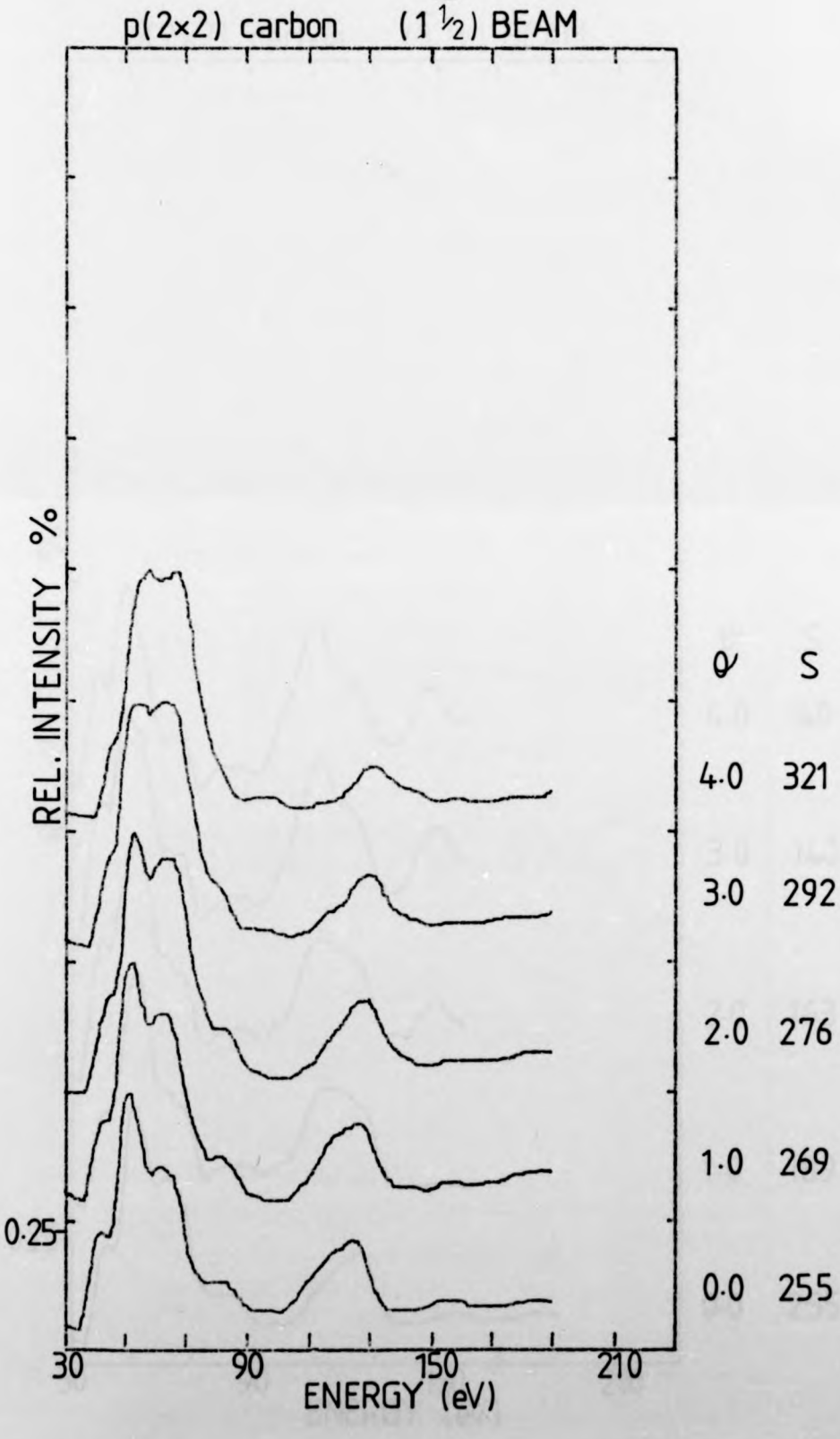
p(2×2) carbon (1 $\bar{1}$/2) BEAM
REL. INTENSITY %
0·25
30
90
150
210
ENERGY (eV)
ϑ S
4·0 321
3·0 292
2·0 276
1·0 269
0·0 255

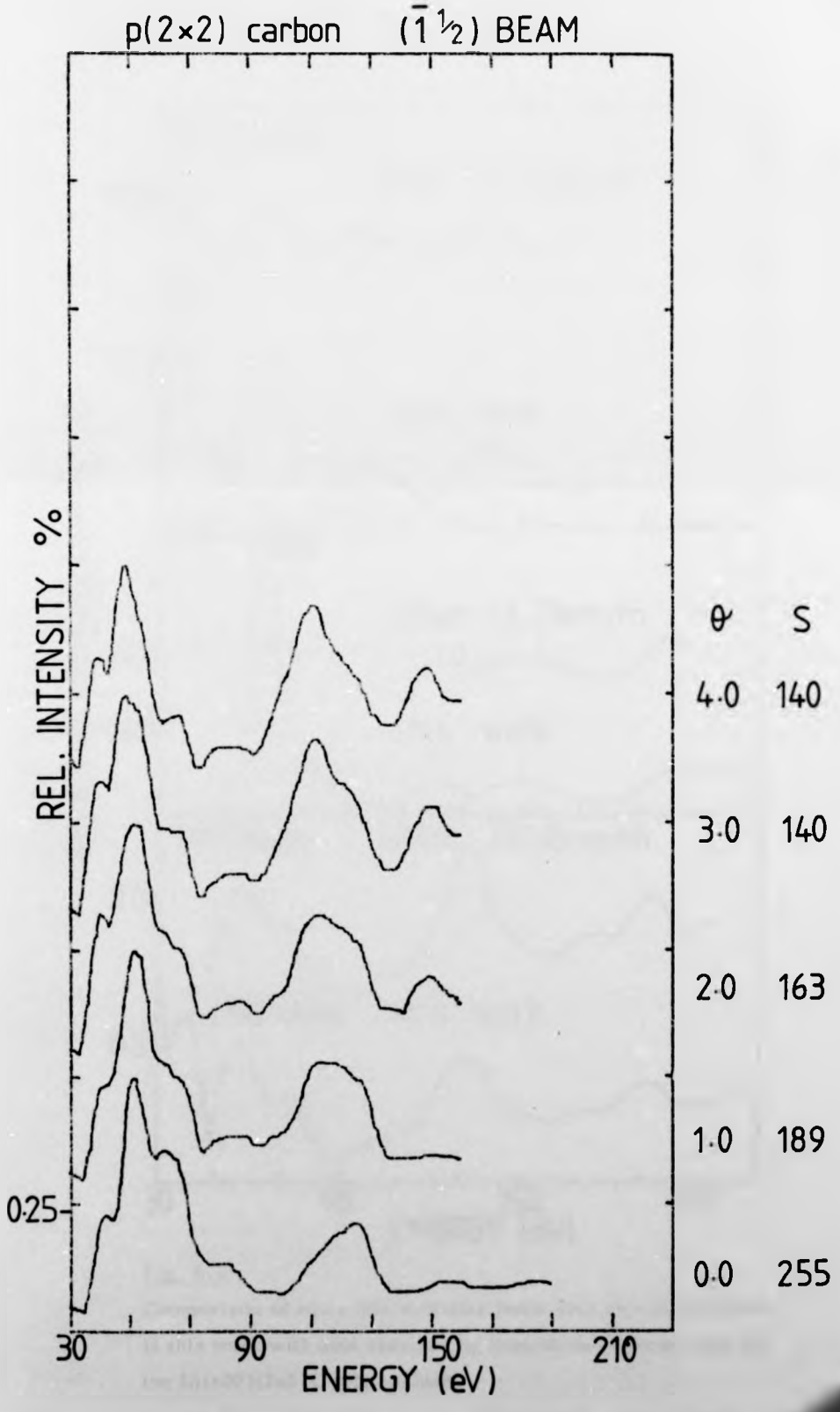
p(2×2) carbon (1̄ ½) BEAM
REL. INTENSITY %
0·25
θ S
4·0 140
3·0 140
2·0 163
1·0 189
0·0 255
30
90
150
210
ENERGY (eV)

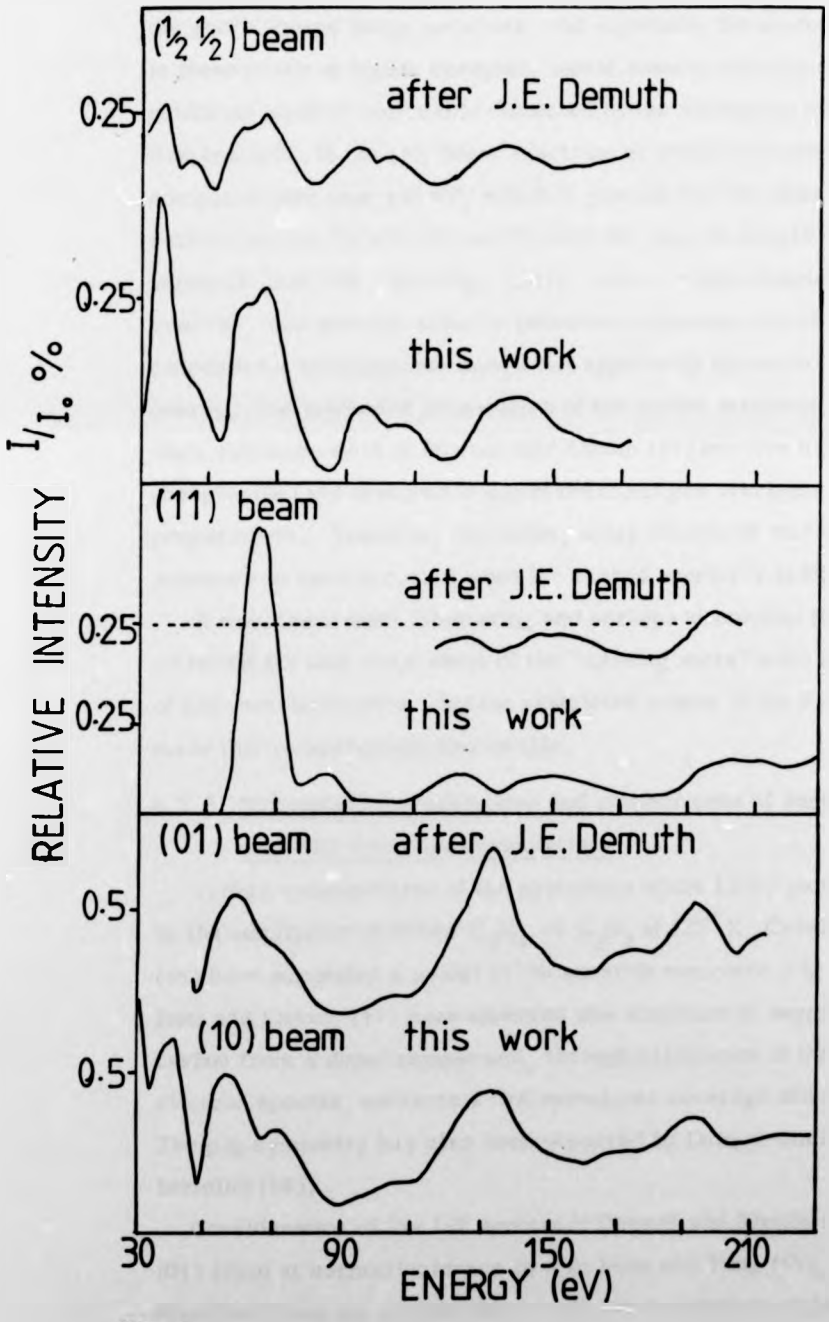

Fig. 6.7

Comparison of some non-specular beam data ($\theta = 0$) obtained in this work with data obtained by Demuth and Rhodin (14) for the Ni(100)(2x2)C-p4g surface.

The general tendency of the data to show a marked alteration in the peaks around Bragg positions, and especially the marked decrease in these peaks at higher energies, would seem to indicate that the substrate layer is noticeably disturbed by the adsorption of carbon. For example, in the (10) beam spectrum at normal incidence, a compound peak near 145 eV, which is present for the clean (100) surface and for Ni(100)-Te and Ni(100)-Se, can be thought of as a substrate peak (15). (See Fig. 6.8). With a carbon overlayer, however, this position actually becomes a minimum and the Bragg condition for the substrate layers has apparently moved to a lower energy. The method of preparation of the carbon structure in this work and in the work of Demuth and Rhodin (14) involves higher energies than are involved in any of the chalcogen overlayer preparations. There is, therefore, more likelihood that the nickel substrate is reconstructed when the carbon overlayer is formed.

It would have been interesting and perhaps instructive to have collected I-V data from some of the "missing spots" when they were of non-zero intensities, but the restricted motion of the Faraday cup made this measurement impossible.

6.3.3 Structural interpretations and comparisons of experimental data with dynamical calculations

From a consideration of the symmetry of the LEED pattern formed by the adsorption of either C_2H_4 or C_2H_2 at 423° K, Casalone et al. (16) have suggested a model of the possible structure (Fig. 6.9). Isett and Blakely (17) have observed this structure on segregation of carbon from a doped sample and, through calibration of the Auger electron spectra, estimate a half monolayer coverage of carbon. The p4g symmetry has also been observed by Dalmai-Imelik and Bertolini (18).

Consideration of the I-V spectra of Demuth and Rhodin (14) for the (01) beam at normal incidence by Van Hove and Tong (15), led to the hypothesis that the carbon atoms may displace the top nickel layer atoms

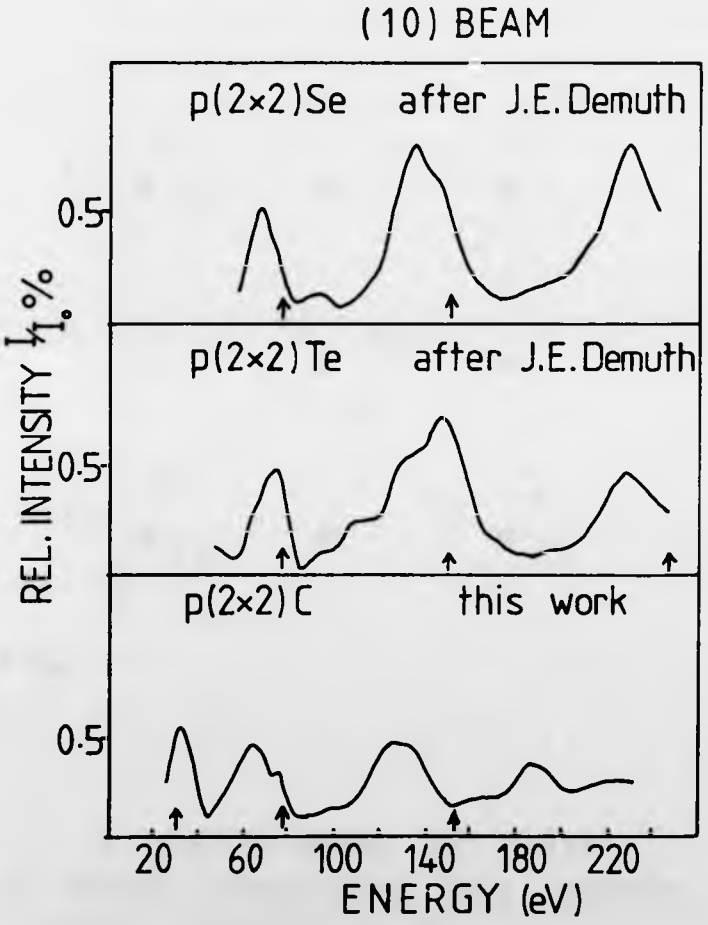

Fig. 6.8

(10) beam spectra obtained from the Ni(100)p(2x2)Se, Ni(100)p(2x2)Te and Ni(100)p(2x2)C surfaces.

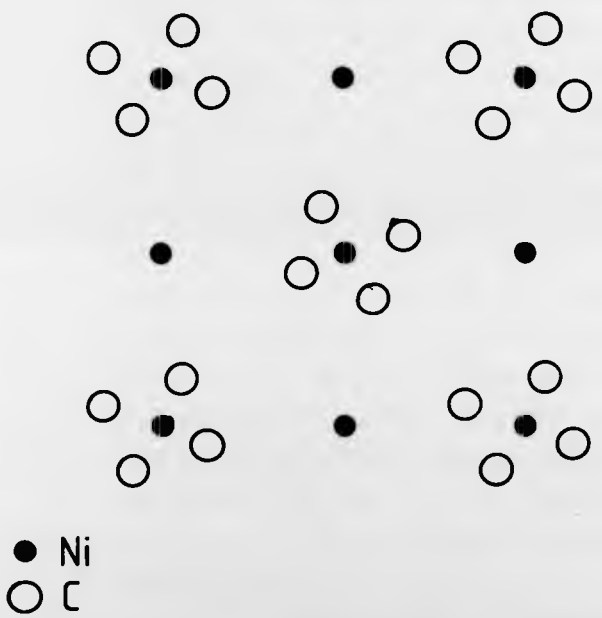

A possible model for carbon on Ni(100) incorporating p4g symmetry (after Casalone et al.)

Fig. 6.9

Model for the Ni(100)(2x2)C-p4g surface not incorporating expansion of the top Ni layer (16).

perpendicularly outwards from their ideal bulk positions. Such a displacement would shift the Bragg peaks to lower energies. Inelastic damping cuts down the effect of deeper layer disturbances and so, in their dynamical calculations, they consider only a top layer displacement. Fig. 6.10(a) shows their calculated curves for the p(2x2) carbon structure ($\frac{1}{2}$ monolayer) on a bulk-like Ni(100) substrate, with the carbon atoms sitting at various distances over the 4-fold sites. It is obvious that there is a systematic mismatch of peaks which could be corrected by increasing the nickel inner potential, but there is no obvious justification for this. An inner potential shift in the carbon layer cannot shift substrate peaks in the required way (19). Fig. 6.10(b) shows Van Hove and Tong's (15) calculated curves for a top nickel layer expansion of 0.15 Å (8.5%). The C-Ni interlayer spacing which best fits this single experimental curve is 1.2 Å. They report only a slight improvement in the correlation between theory and experiment for the $(\frac{1}{2}\frac{1}{2})$ beam for an 8.5% expansion and mention that the agreement is only fair, but this has not been published. However, from this work it would seem that an expansion of the top substrate layer could play a part in the model of carbon adsorption on Ni(100).

However, the observation of the p4g group symmetry when the carbon overlayer is present greatly restricts the number of possible structures. The symmetry requires that the unit mesh has a central motif which is the mirror image of that at the mesh corners in both directions of the primitive unit mesh vectors (Fig. 6.11). This suggests that the (2x2) structure corresponds to a half-monolayer coverage of carbon, which was found to be the case from AES studies by Isett and Blakely (17), and is thought to be approximately this coverage from AES spectra of Chapter Four. The carbon atoms must then cause some of the 4-fold symmetric sites of the clean surface to be reduced to 2-fold symmetry. Maglietta and Rovida (20) have reported a p(2x2) carbon structure on heating an f.c.c. form cobalt

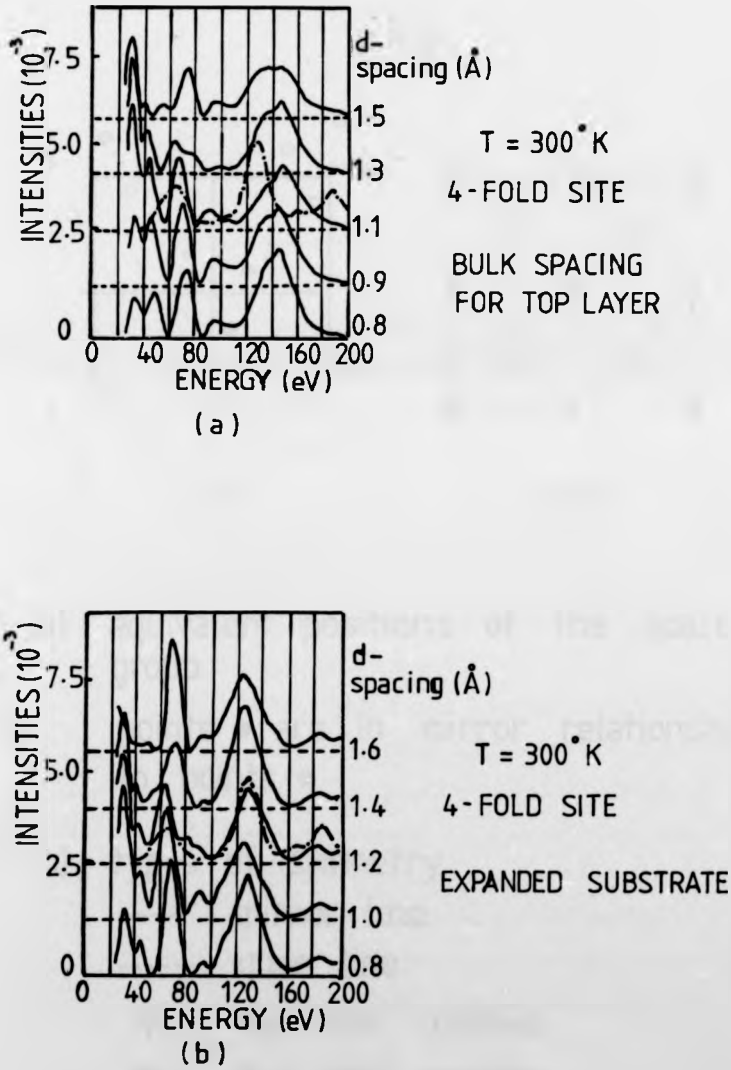

Fig. 6.10

Comparison of theoretical curves of Van Hove and Tong (15) with experimental spectra (dashed curves) of Demuth and Rhodin (14) for the Ni(100)(2x2)C-p4g structure.

(a) for carbon in 4-fold sites over an undistorted Ni substrate.

(b) for carbon in 4-fold sites over an expanded Ni substrate.

p 4 g

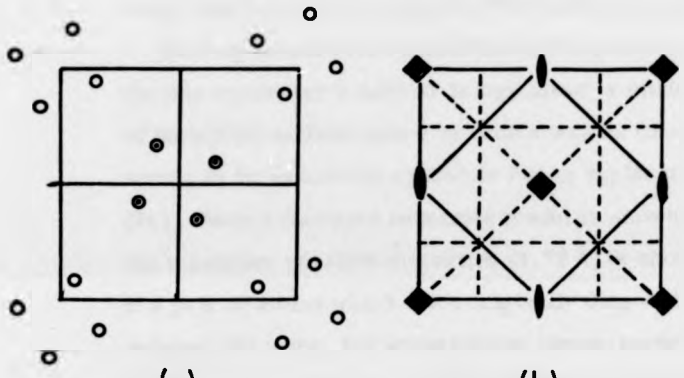

(a) (b)

(a) equivalent positions of the space group

points • are in mirror relationship to points ∘

(b) types of symmetry

—— mirror line

----- glide line

⬮ two-fold rotation

◆ four-fold rotation

Fig. 6.11

Illustration of p4g symmetry

(100) surface; they mention that the $(\frac{1}{2}, 0)$ and symmetric beams are very weak, particularly at normal incidence. An evaluation of the carbon concentration in this p(2x2) phase by AES resulted in a figure of $(1.4 \pm 0.3) \times 10^{15}$ atoms/cm^2, which would indicate that more than one carbon atom is present per unit mesh.

Bearing in mind the restriction of the possible structures which the p4g symmetry condition brings about, a model involving distortion of the nickel surface atoms in such a way as to satisfy the symmetry seems to be an obvious candidate for an explanation of the structure (21). Such a distorted substrate model is shown in Fig. 6.12; here the maximum possible distortion (1.52 Å) is shown and would occur if a pair of atoms which were originally diagonally opposite on the original net were, for some reason, drawn together until they touched. This distortion closes up some of the original 4-fold symmetric sites, and at the same time opens up the holes in the remaining 4-fold sites and causes a rotation of the surrounding nickel atoms. The radius of a hole in the undistorted surface is 0.52 Å and this is increased by 0.075 Å for maximum distortion.

Having arrived at this distortion model, the problem is now to decide where the carbon atoms are most likely to be located. Two possibilities are immediately obvious, namely in the enlarged 4-fold symmetric holes, or bridge-bonded diagonally with all top layer nickel atoms bonded to one carbon atom. These two models are shown in Fig. 6.13(a) and (b). The bridge-bonded model is attractive in that it would cause the required distortion by drawing the nickel atoms together when forming the bridge bond with the carbon. However, since in many cases carbon is found having four single bonds, the 4-fold site is a strong possibility, although it is more difficult to see why the carbon atoms thus adsorbed should cause the distortion necessary to explain the p4g symmetry. As was mentioned above, the increase in the radius of the hole site for maximum distortion is only 0.075 Å; the carbon atom has a covalent radius of 0.77 Å, and so it is not clear why this only marginally

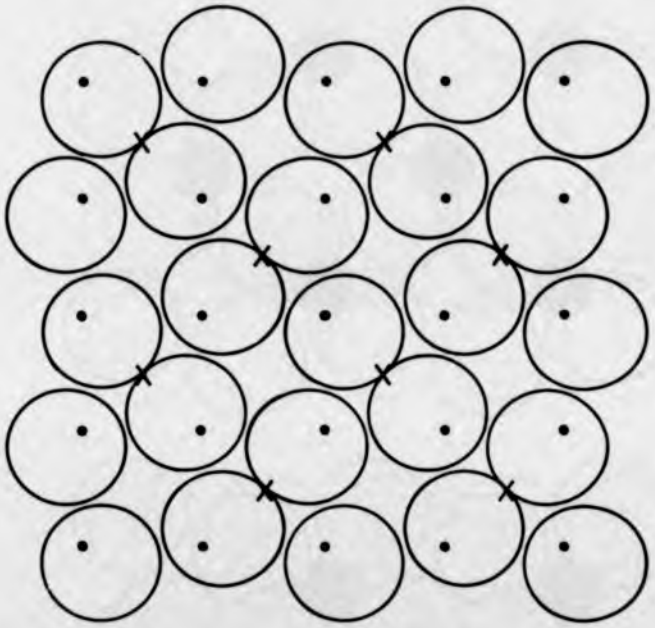

• undistorted Ni layer atom centres

Ni atoms in "distorted" model

N.B. the reduction of some 4-fold symmetric sites to sites of 2-fold symmetry (x)

Fig. 6.12

Distorted Ni substrate after adsorption of carbon to form the Ni(100)(2x2)C-p4g surface.

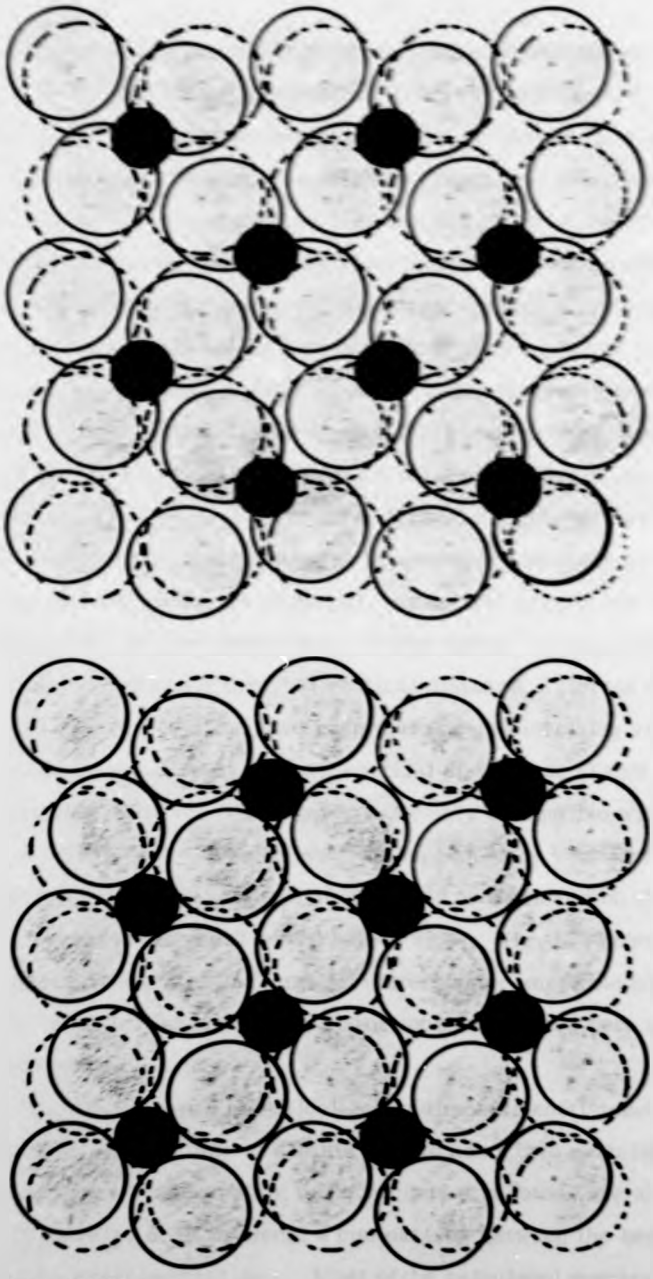

Fig. 6.13

Possible models of the Ni(100)(2x2)C-p4g structure.

(a) Carbon atoms in 2-fold bridge positions

(b) Carbon atoms in 4-fold hollows

The large circles represent the distorted Ni substrate. The undistorted Ni atoms (dashed circles) are shown as a reference. The carbon atoms are indicated by the small circles.

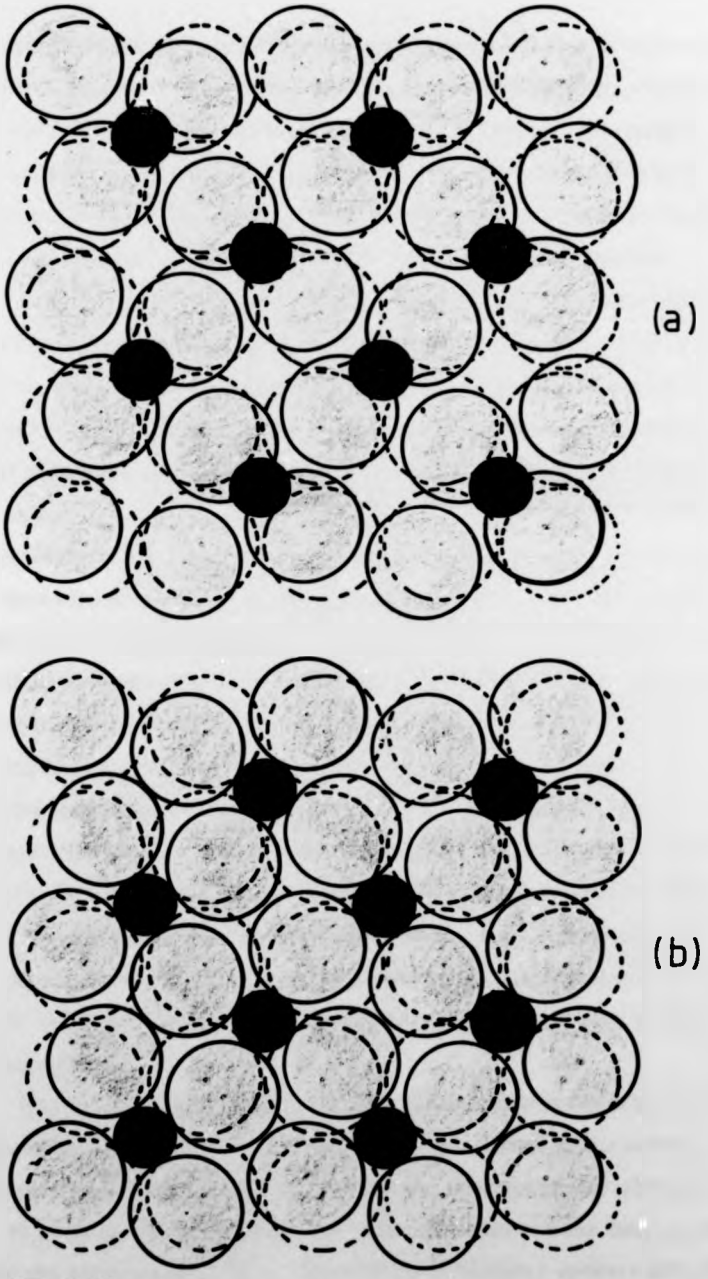

Fig. 6.13

Possible models of the Ni(100)(2x2)C-p4g structure.

(a) Carbon atoms in 2-fold bridge positions

(b) Carbon atoms in 4-fold hollows

The large circles represent the distorted Ni substrate. The undistorted Ni atoms (dashed circles) are shown as a reference. The carbon atoms are indicated by the small circles.

increased hole size should be energetically favourable enough to be the reason for such a distortion. From the AES spectra, a coverage of about $\frac{1}{2}$ monolayer is thought probable. However, if a larger coverage were the case, then perhaps two carbon atoms could be occupying the 4-fold sites or even the bridge sites, but this is not as readily believable as the two previously mentioned models.

A better understanding of this structure will only come about if the I-V spectra calculated by dynamical theory provide a good match to the experimentally obtained data. Using the multiple scattering programme of Holland and Zimmer (22) comparisons between theory and experiment have been made for a large number of structural parameters. These include considering an expanded and distorted top nickel layer, (this seems to be necessary in order to give the required peak shifts as in the (10) beam), and varying the carbon-nickel spacing for both the bridge and 4-fold sites. Having noted the peak trends upon varying the C-Ni vertical distance, different distortions of the nickel substrate have been investigated involving various combinations of horizontal and vertical distortions (Table 6.1). The distortion of the top nickel layer is readily compatible with the expanded nickel substrate layer as suggested by Van Hove and Tong (15), since the top layer atoms will be caused to be raised on the layer below and not sit in the usual 4-fold hollow sites. Fig. 6.14 shows the expected horizontal and vertical distortions compatible with a "billiard-ball" model of the structure ; distortions which have been examined are also marked.

Fig. 6.15 shows the calculated and experimental spectra for the clean Ni(100) surface as a basis for the adsorbate calculations. The calculated I-V spectra for these various structures are shown in Fig. 6.16, and Fig. 6.17 presents a comparison between the best of these and the experimental data. Most of the calculated spectra are for normal incidence conditions and after reasonable agreement for particular structures had been obtained, calculations were run for beams off normal incidence ($\theta = 8^{o}$)(Fig. 6.18).

Vertical distortion d_v Å		Horizontal distortion d_h Å			
		0.43	0.29	0.15	0.075
	0.43	4-fold (0.1)			
	0.29		4-fold (0.1)		
	0.28	4-fold (0.0) 4-fold (0.1) 2-fold (0.9)			
	022		4-fold (0.1)		
	0.15	4-fold (0.1) 2-fold (0.9)	4-fold (0.1)	2-fold (0.7) 2-fold (0.9) 2-fold (1.1) 4-fold (0.4) 4-fold (0.2) 4-fold (0.1) 4-fold (0.0) 4-fold (0.2)below monolayer below	
	0.075				4-fold (0.0) 2-fold (0.5) 2-fold (0.7) 2-fold (0.9)

Table 6.1

Combinations of the nickel atom distortions and carbon atom positions for which calculations have been performed. The figures in brackets following the carbon atom site indicate the carbon-nickel (d_z) spacing in Angstroms.

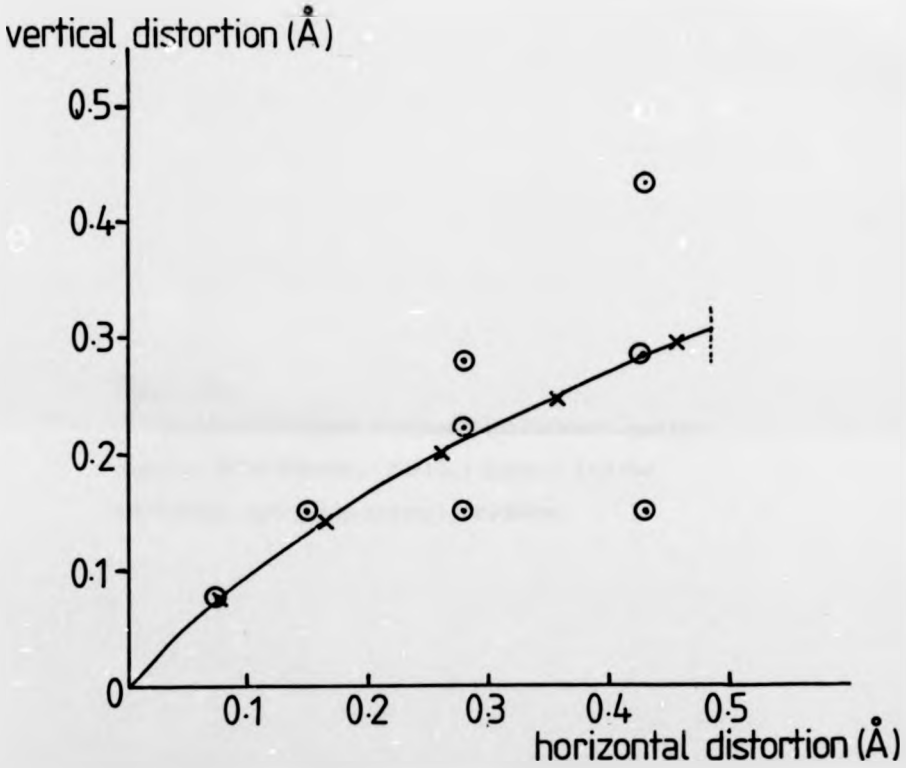

Fig. 6.14

Graph of vertical distortion against horizontal distortion of Ni atoms on the (100) surface.

The circles represent the co-ordinates of distortions for which full dynamical calculations for the Ni(100)(2x2)C-p4g structure have been performed.

Fig. 6.15

Overleaf is shown a comparison between spectra obtained from the clean Ni(100) surface and the theoretical spectra at normal incidence.

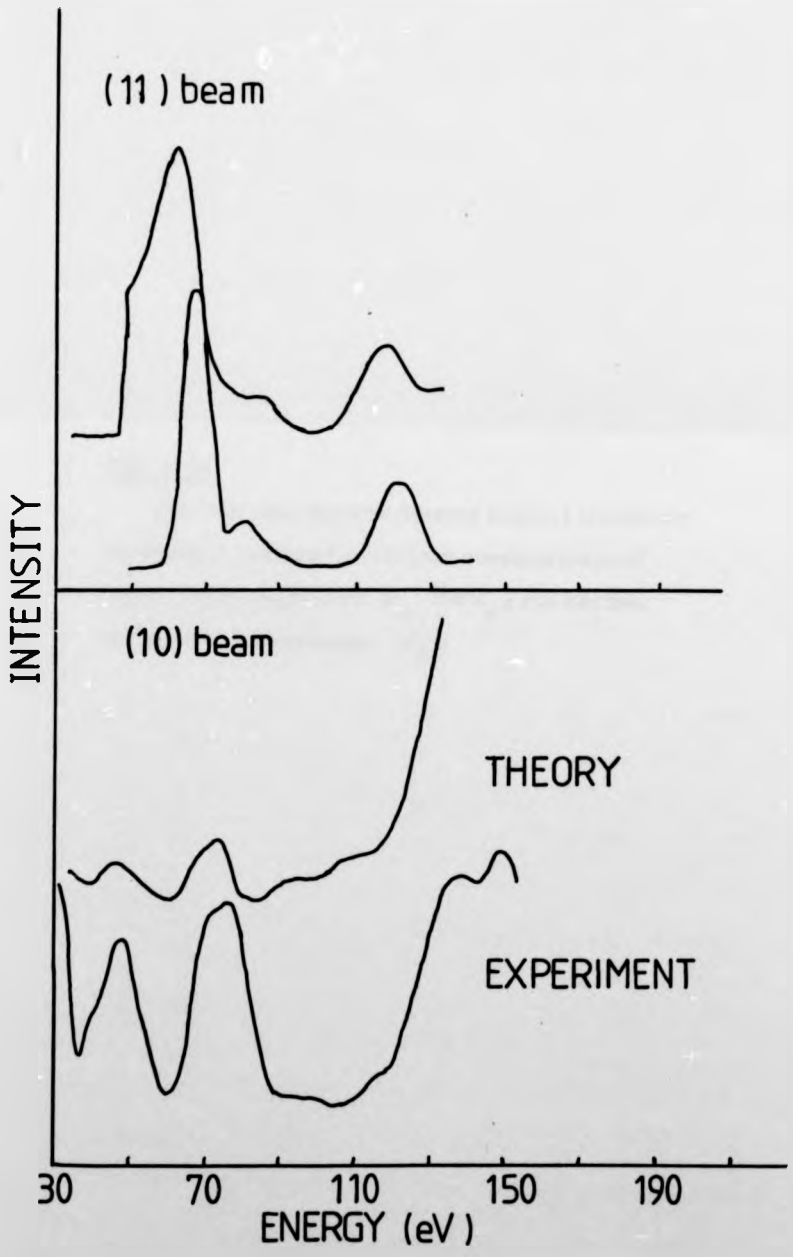
CLEAN Ni(100)
(11) beam
(10) beam
INTENSITY
THEORY
EXPERIMENT
30
70
110
150
190
ENERGY (eV)

Fig. 6.16

The following figures present normal incidence theoretical spectra for various combinations of nickel atom distortions (d_h and d_v) and carbon atom sites and spacings (d_z).

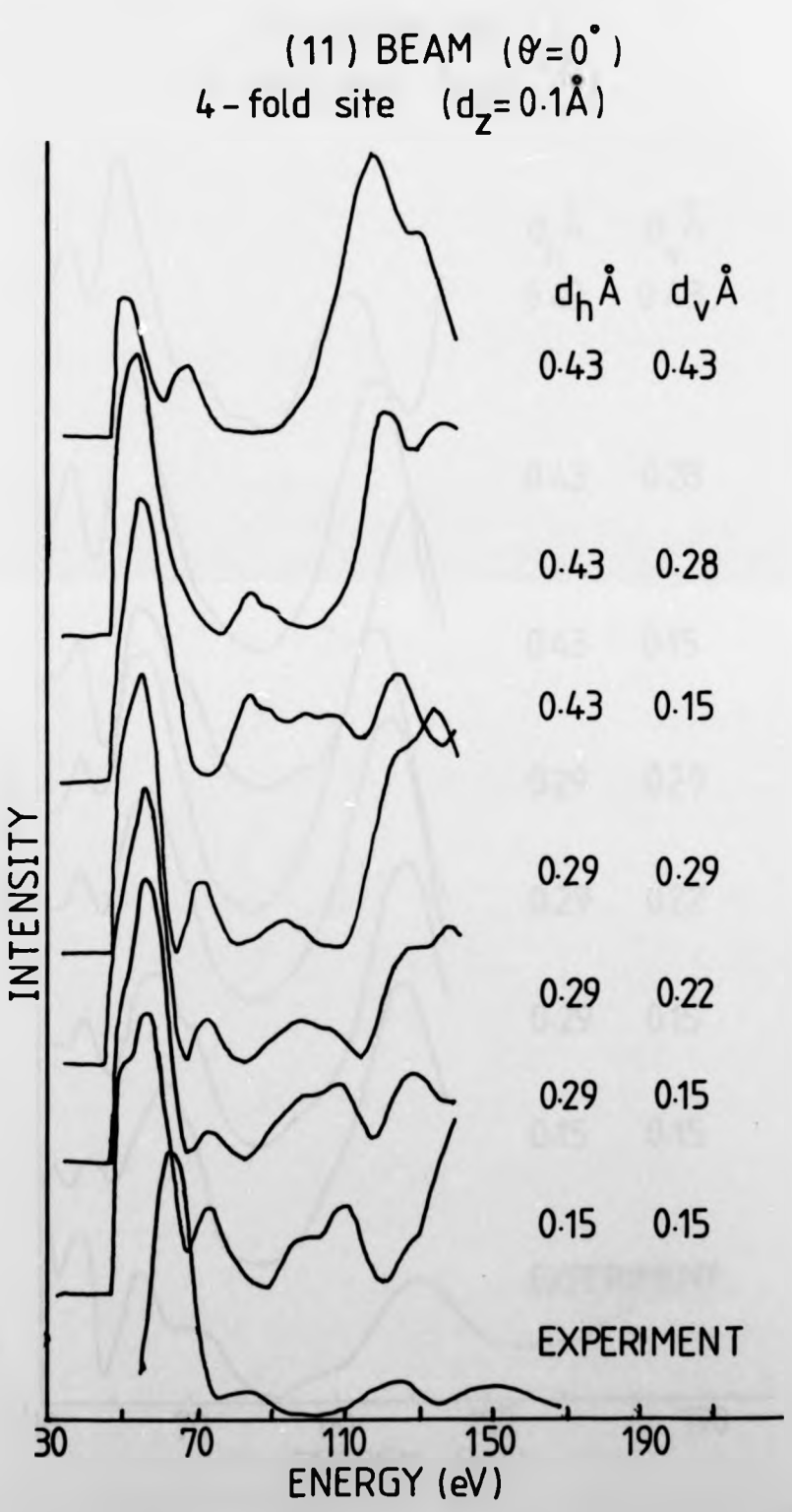
(11) BEAM (θ=0°)
4-fold site (dz=0·1Å)
dh Å dv Å
0·43 0·43
0·43 0·28
0·43 0·15
0·29 0·29
0·29 0·22
0·29 0·15
0·15 0·15
EXPERIMENT
INTENSITY
30
70
110
150
190
ENERGY (eV)

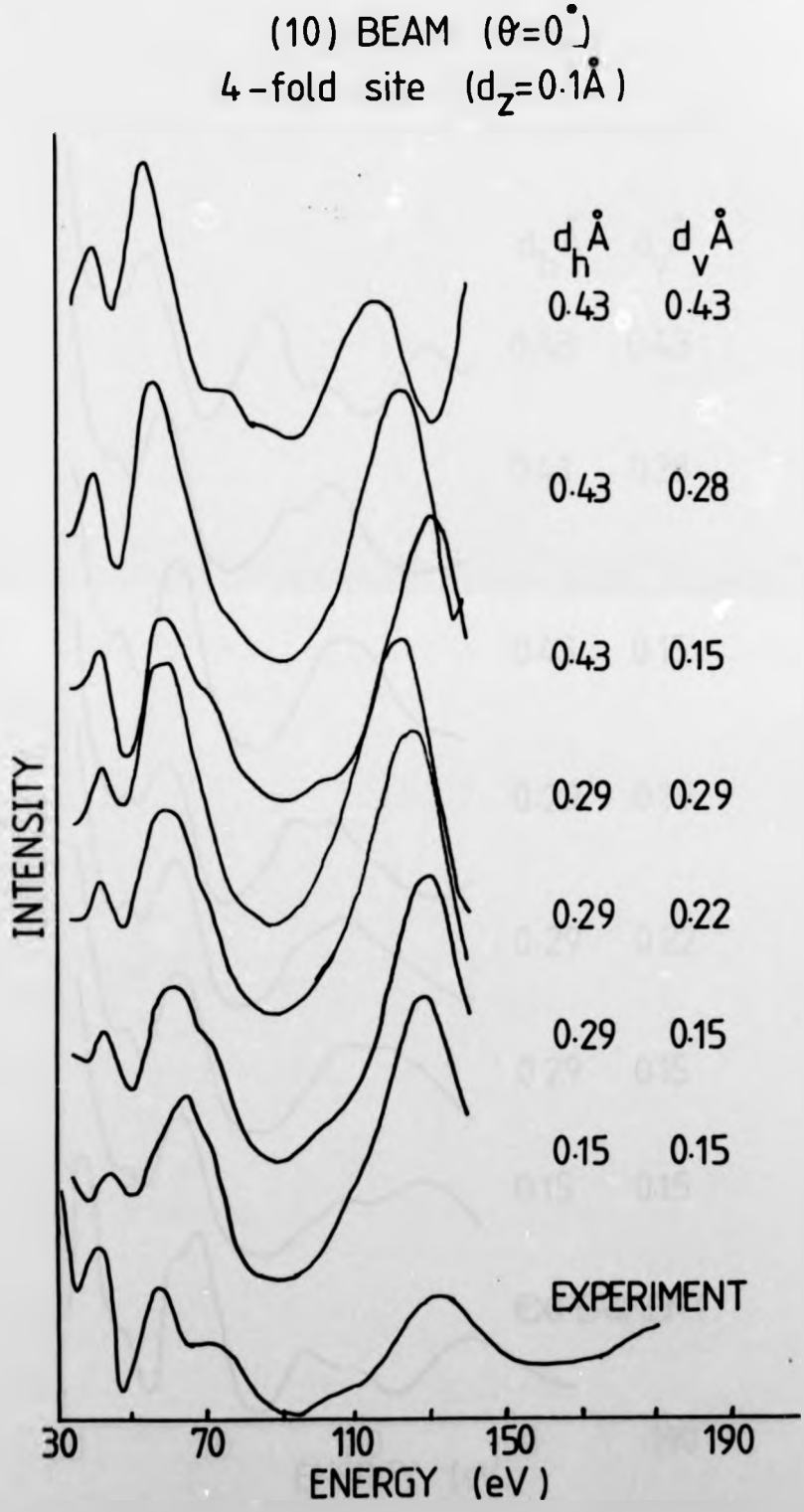
(10) BEAM (θ=0°)
4-fold site (d_z=0·1Å)
d_h Å
d_v Å
0·43 0·43
0·43 0·28
0·43 0·15
0·29 0·29
0·29 0·22
0·29 0·15
0·15 0·15
EXPERIMENT
INTENSITY
30
70
110
150
190
ENERGY (eV)

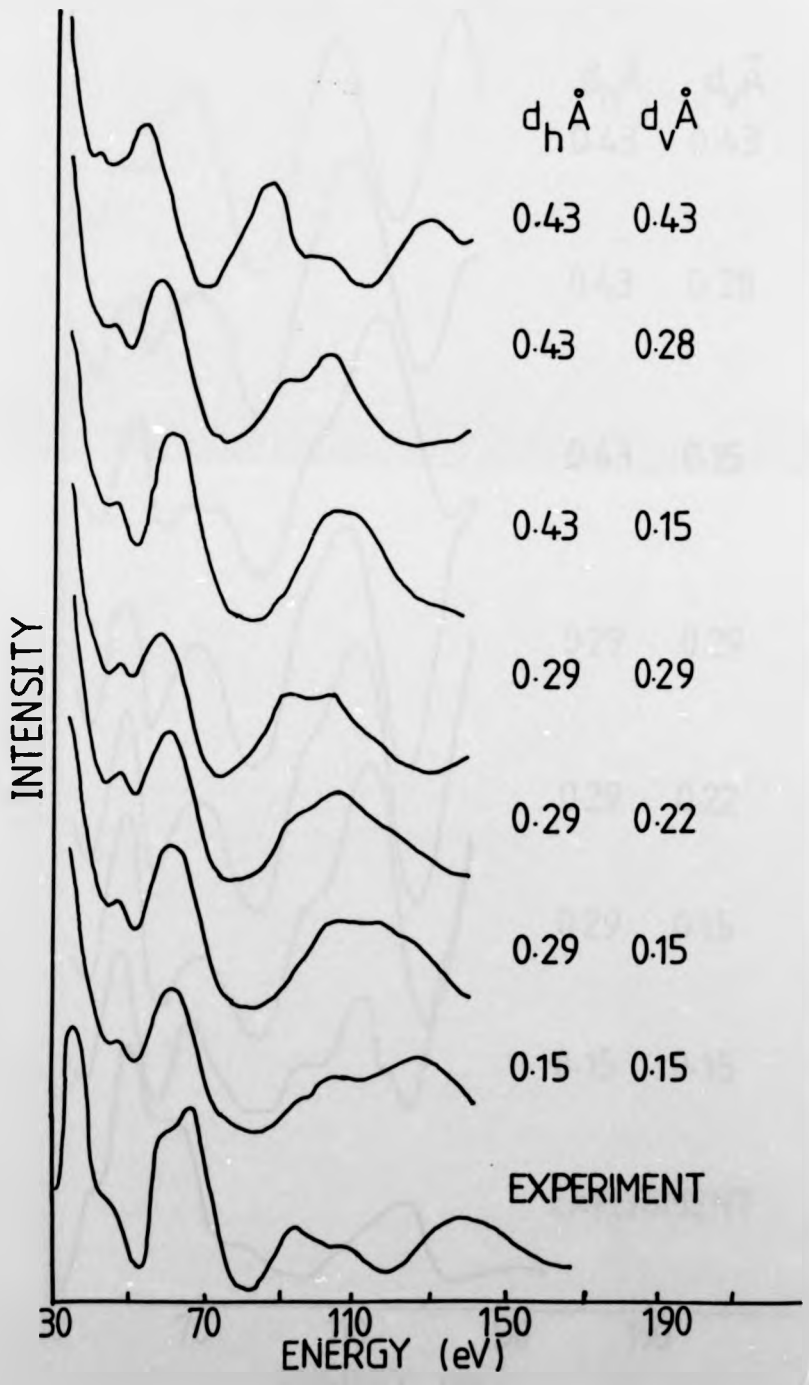
(1/2 1/2) BEAM (θ=0°)
4-fold site (dz=0.1Å)
dh Å
dv Å
0.43 0.43
0.43 0.28
0.43 0.15
0.29 0.29
0.29 0.22
0.29 0.15
0.15 0.15
EXPERIMENT
INTENSITY
30
70
110
150
190
ENERGY (eV)

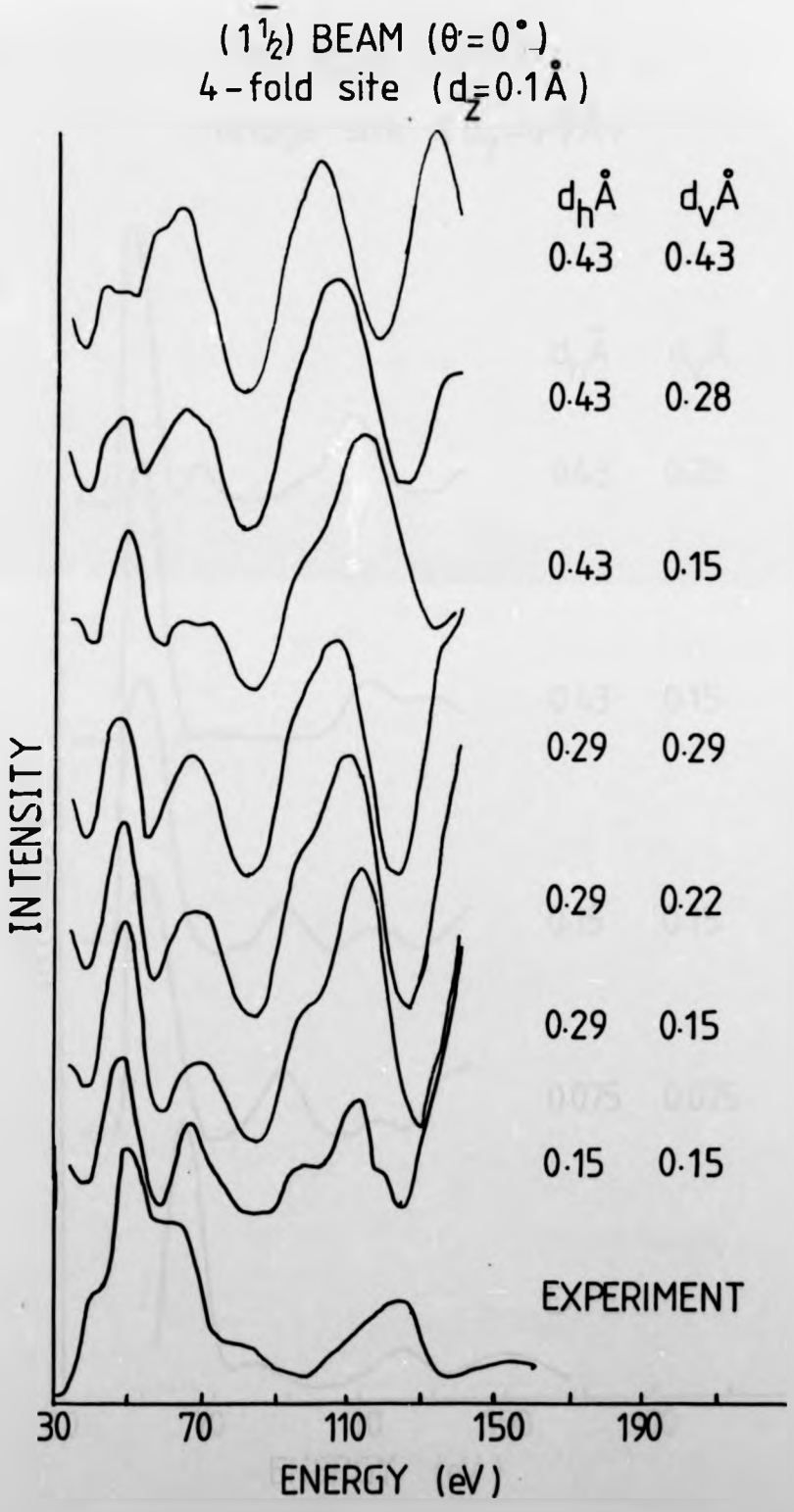
(1 $\bar{1}/2$) BEAM ($\theta = 0°$)
4-fold site ($d_z = 0.1$Å)
d_hÅ d_vÅ
0.43 0.43
0.43 0.28
0.43 0.15
0.29 0.29
0.29 0.22
0.29 0.15
0.15 0.15
EXPERIMENT
INTENSITY
30 70 110 150 190
ENERGY (eV)

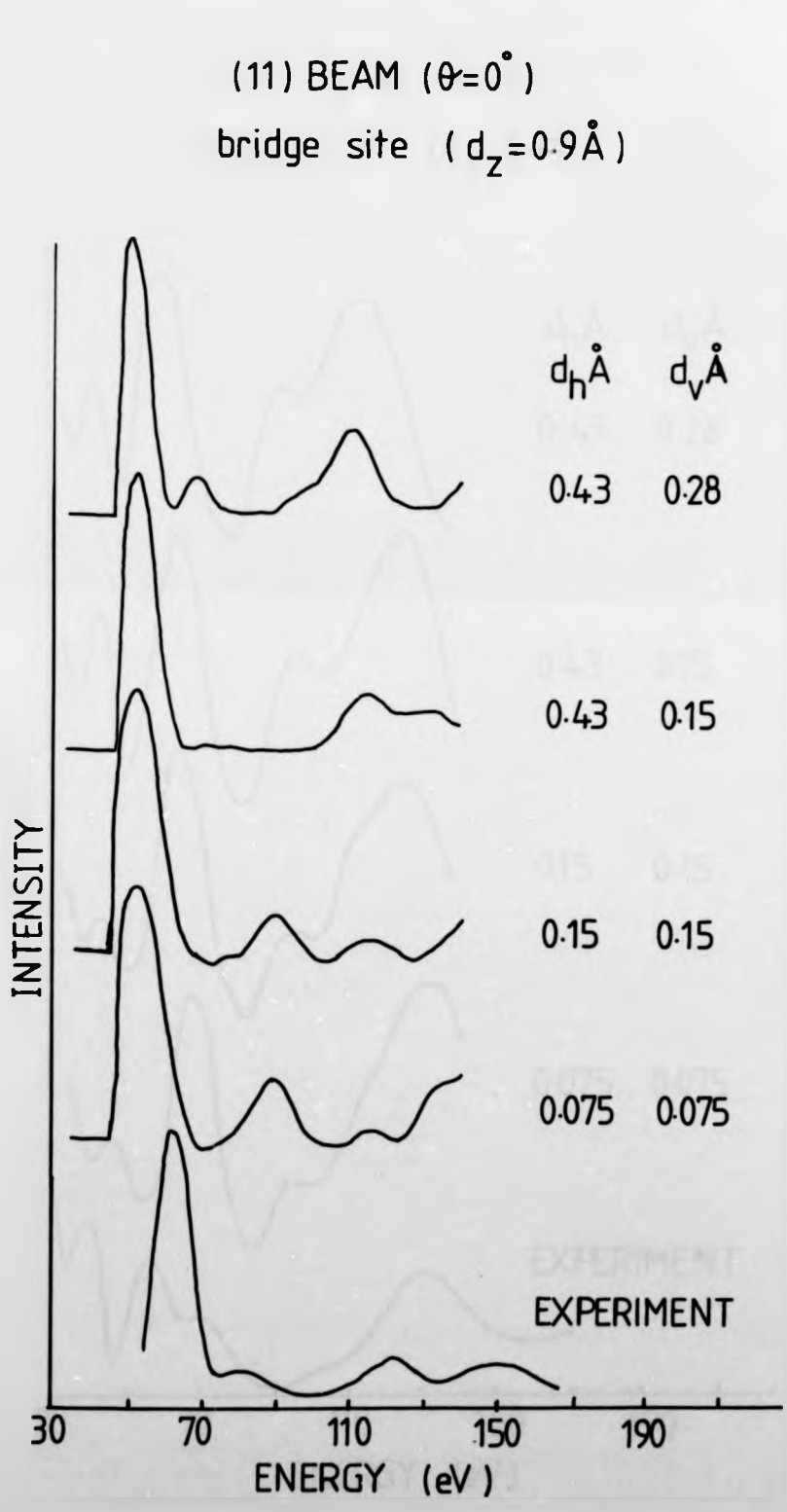
(11) BEAM (θ=0°)
bridge site (d_z=0·9Å)
d_hÅ d_vÅ
0·43 0·28
0·43 0·15
0·15 0·15
0·075 0·075
EXPERIMENT
INTENSITY
30
70
110
150
190
ENERGY (eV)

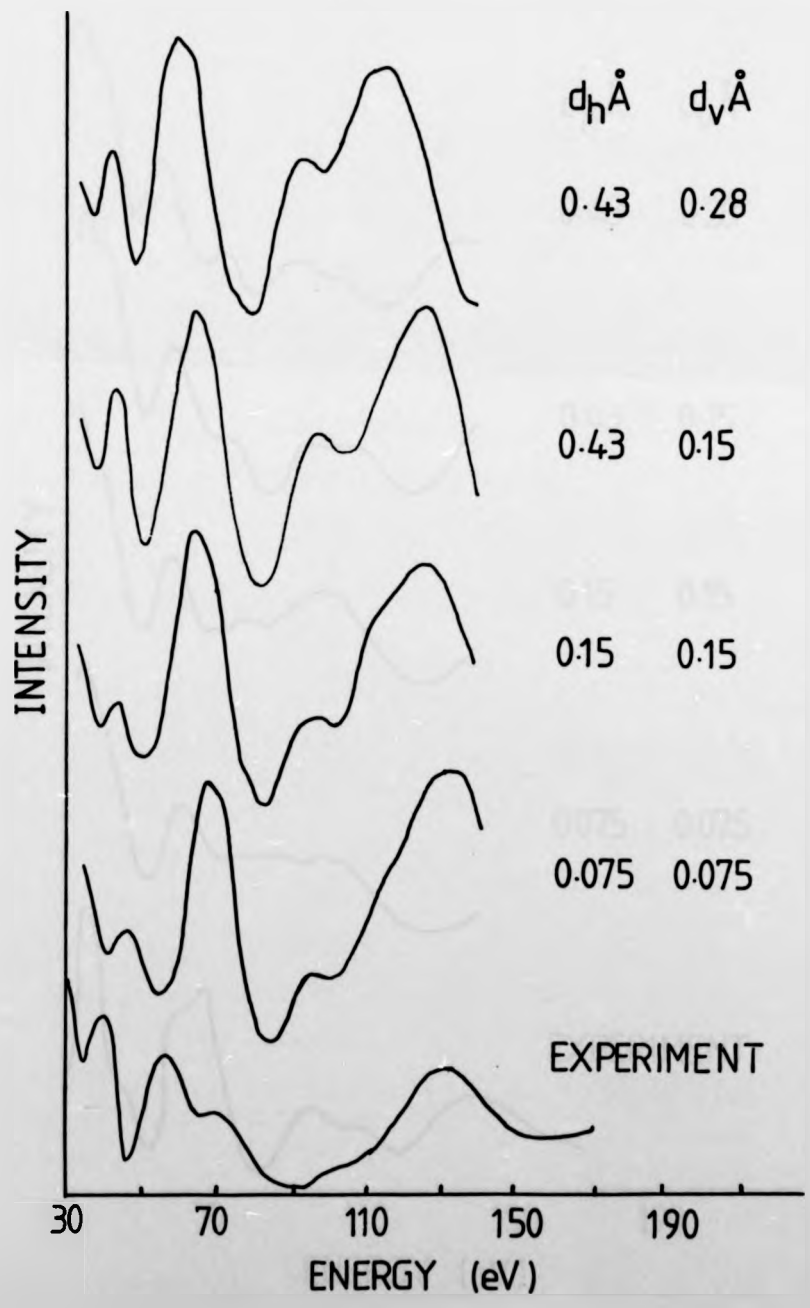
(10) BEAM (θ = 0°)
bridge site (dz = 0·9Å)
dhÅ dvÅ
0·43 0·28
0·43 0·15
0·15 0·15
0·075 0·075
EXPERIMENT
INTENSITY
30
70
110
150
190
ENERGY (eV)

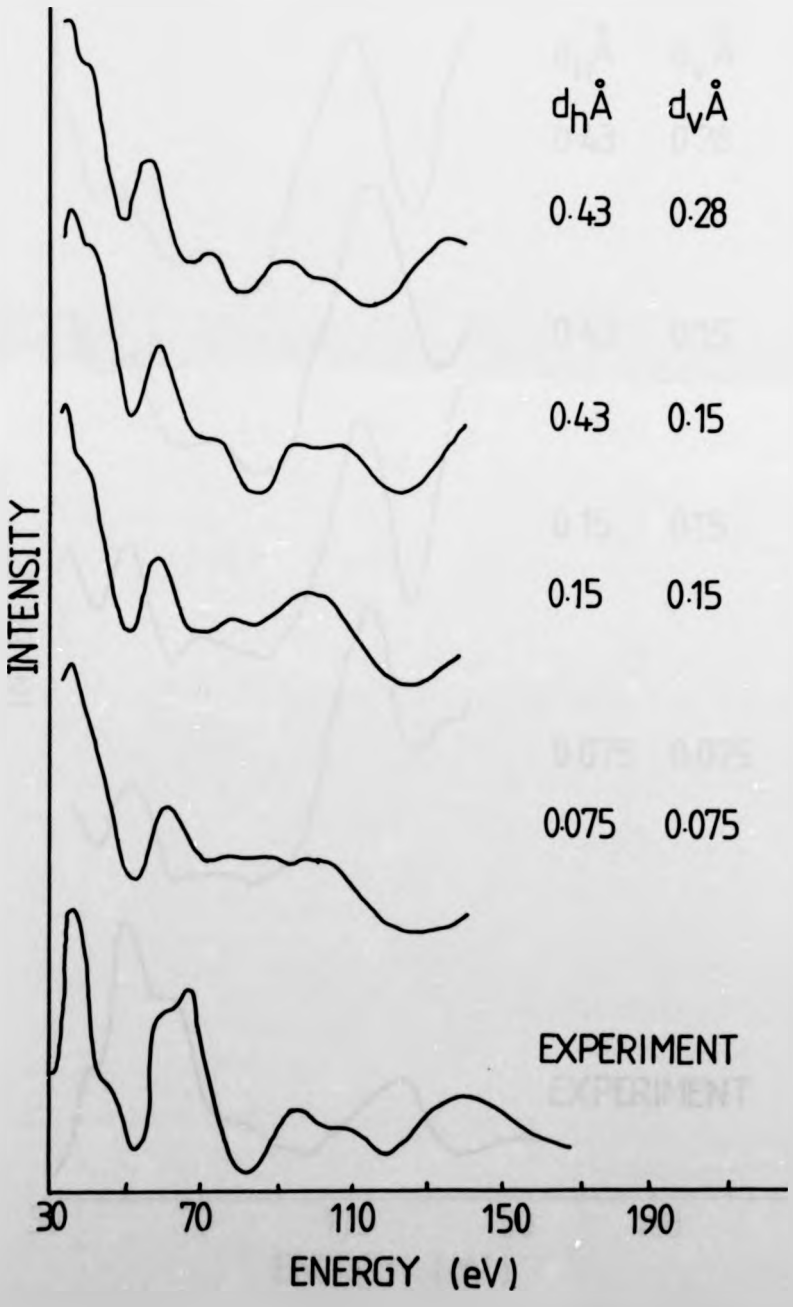
(½ ½) BEAM (θ=0°)
bridge site (dz=0·9Å)
dhÅ dvÅ
0·43 0·28
0·43 0·15
0·15 0·15
0·075 0·075
EXPERIMENT
INTENSITY
30
70
110
150
190
ENERGY (eV)

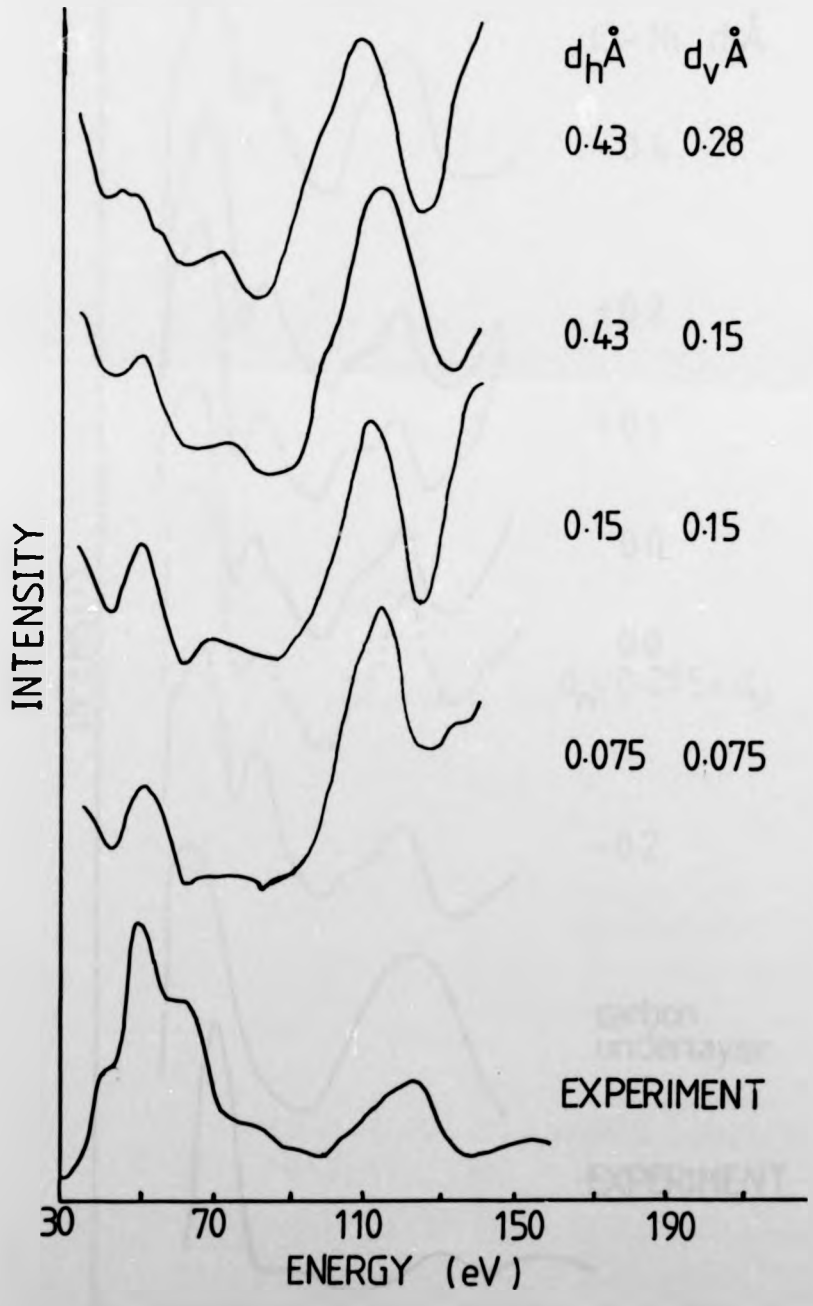
(1 $\bar{1}$/2) BEAM (θ=0°)
bridge site (d$_z$=0·9Å)
d_hÅ d_vÅ
0·43 0·28
0·43 0·15
0·15 0·15
0·075 0·075
EXPERIMENT
INTENSITY
30
70
110
150
190
ENERGY (eV)

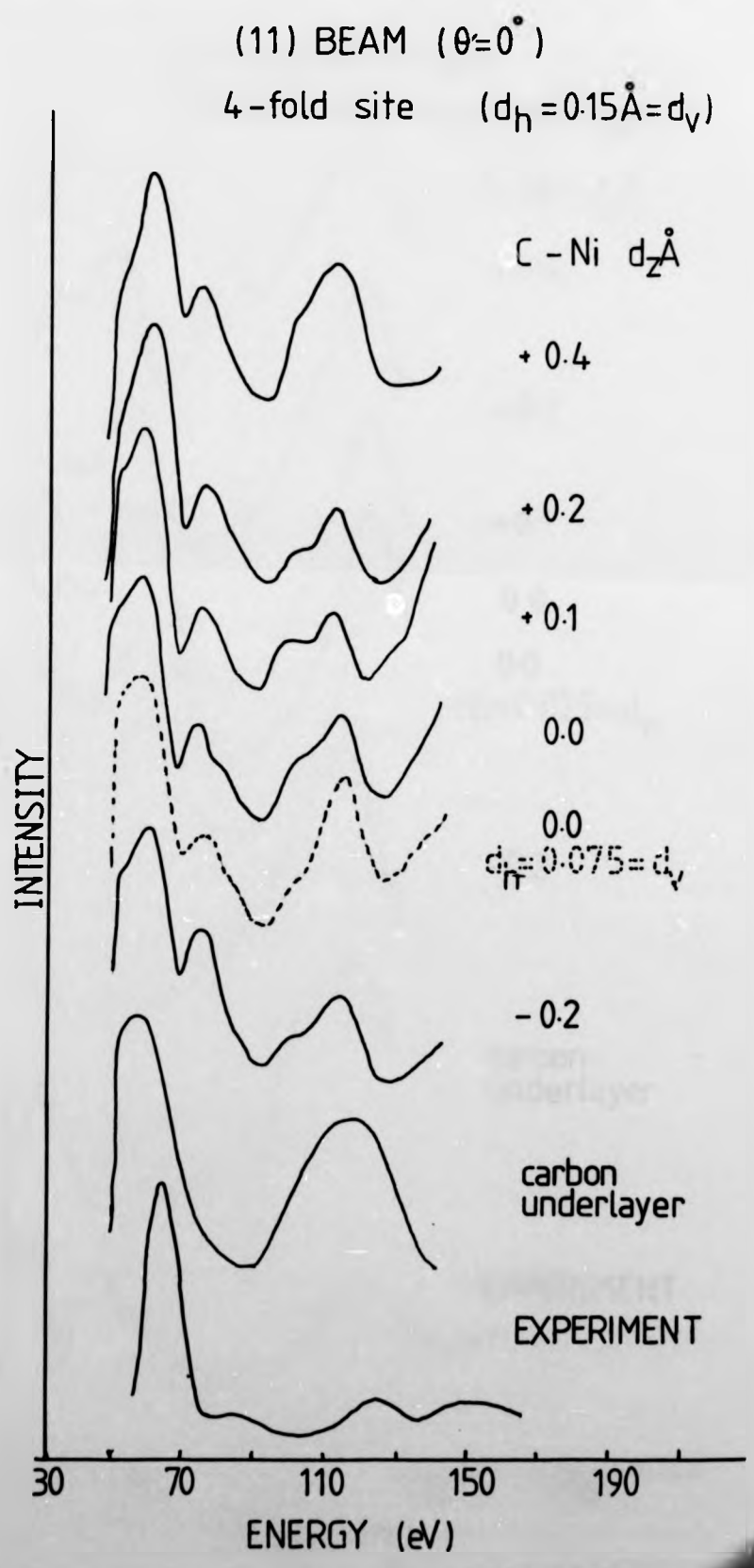
(11) BEAM (θ=0°)
4-fold site (dh=0·15Å=dv)
C-Ni dzÅ
+0·4
+0·2
+0·1
0·0
0·0
dh=0·075=dv
-0·2
carbon underlayer
EXPERIMENT
INTENSITY
30
70
110
150
190
ENERGY (eV)

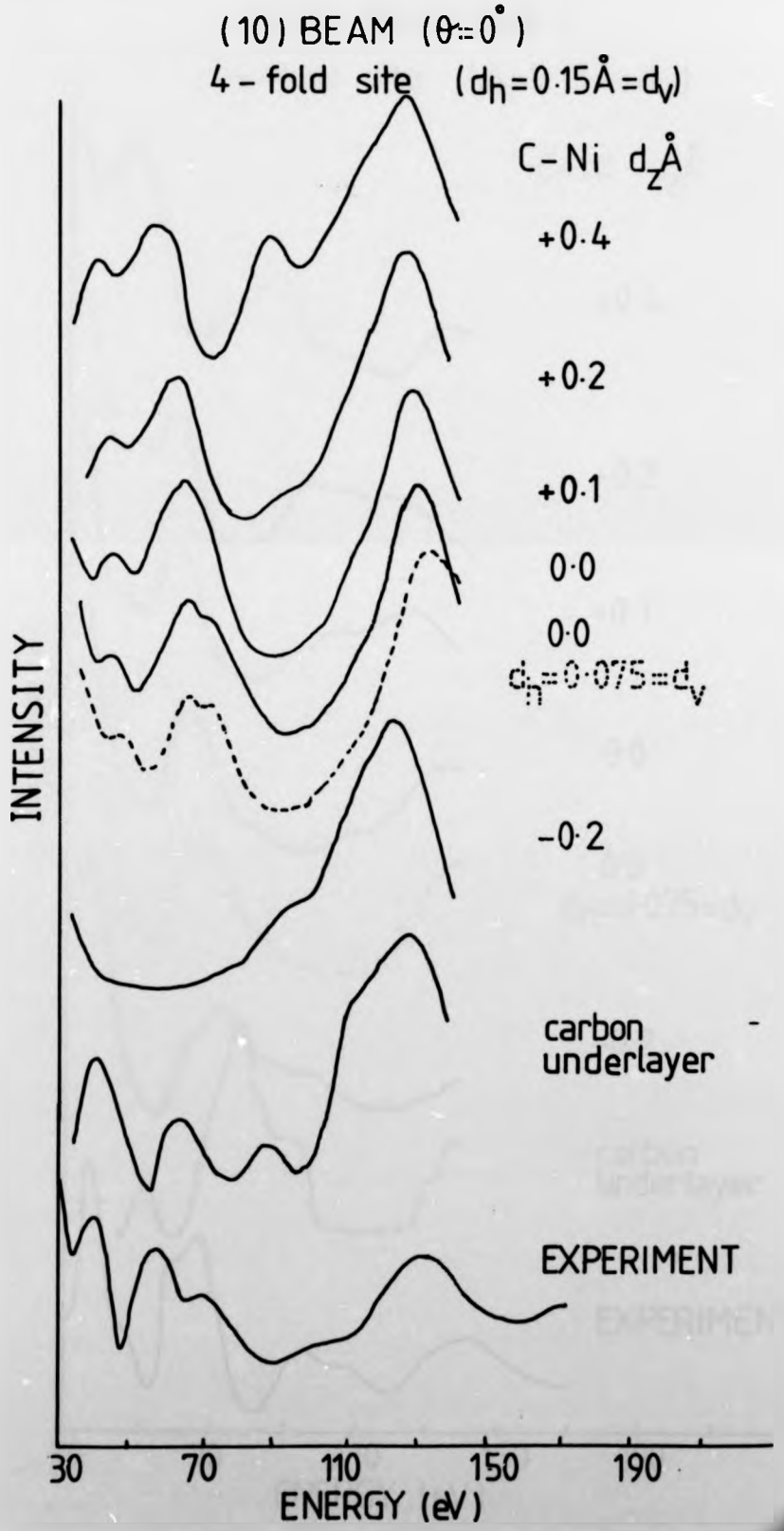
(10) BEAM (θ=0°)
4 – fold site (dh=0·15Å=dv)
C – Ni dzÅ
+0·4
+0·2
+0·1
0·0
0·0
dh=0·075=dv
–0·2
carbon underlayer
EXPERIMENT
INTENSITY
30
70
110
150
190
ENERGY (eV)

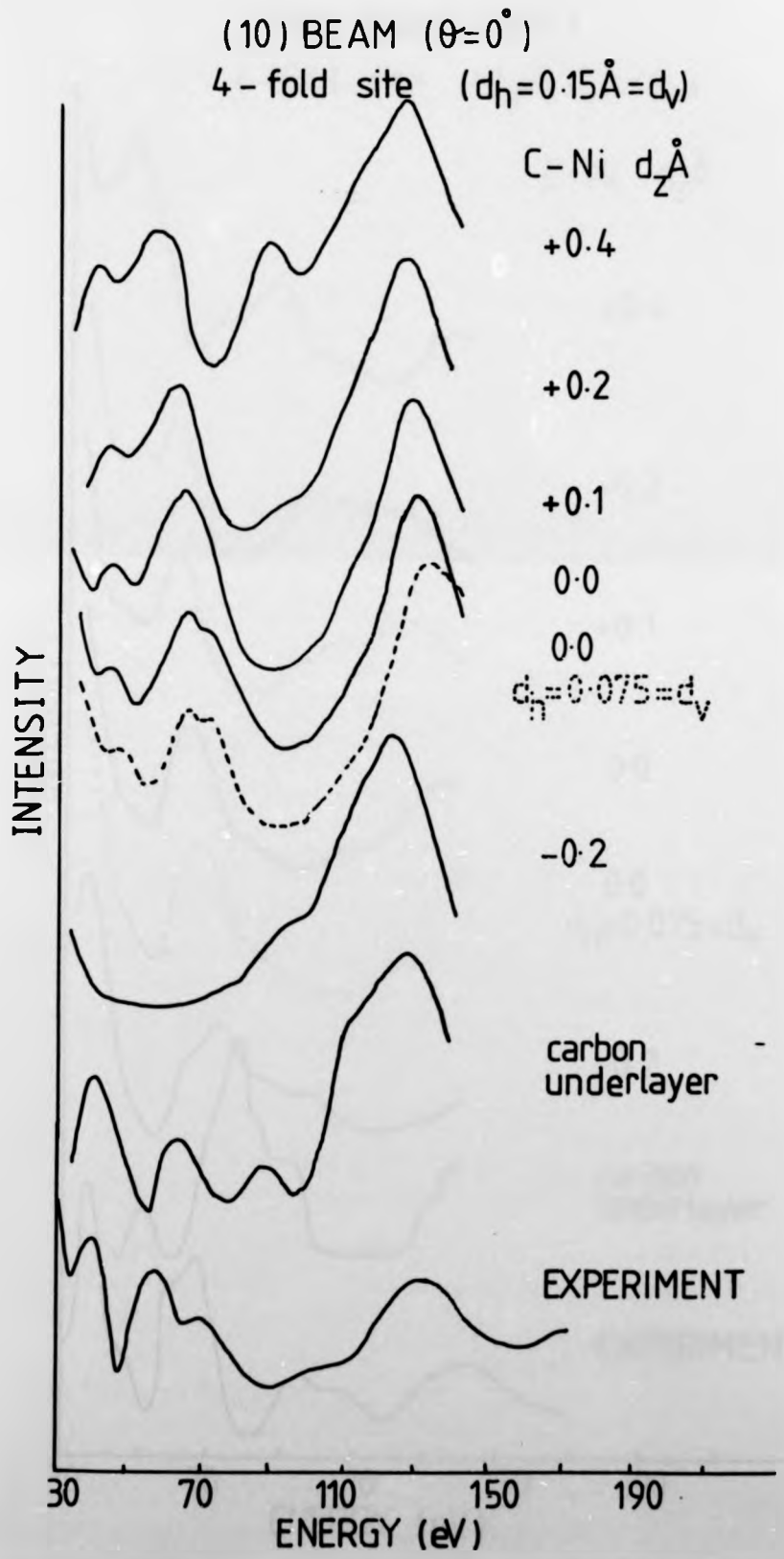
(10) BEAM (θ=0°)
4 - fold site (dh=0·15Å=dv)
C-Ni dzÅ
+0·4
+0·2
+0·1
0·0
0·0
dh=0·075=dv
-0·2
carbon underlayer
EXPERIMENT
INTENSITY
30
70
110
150
190
ENERGY (eV)

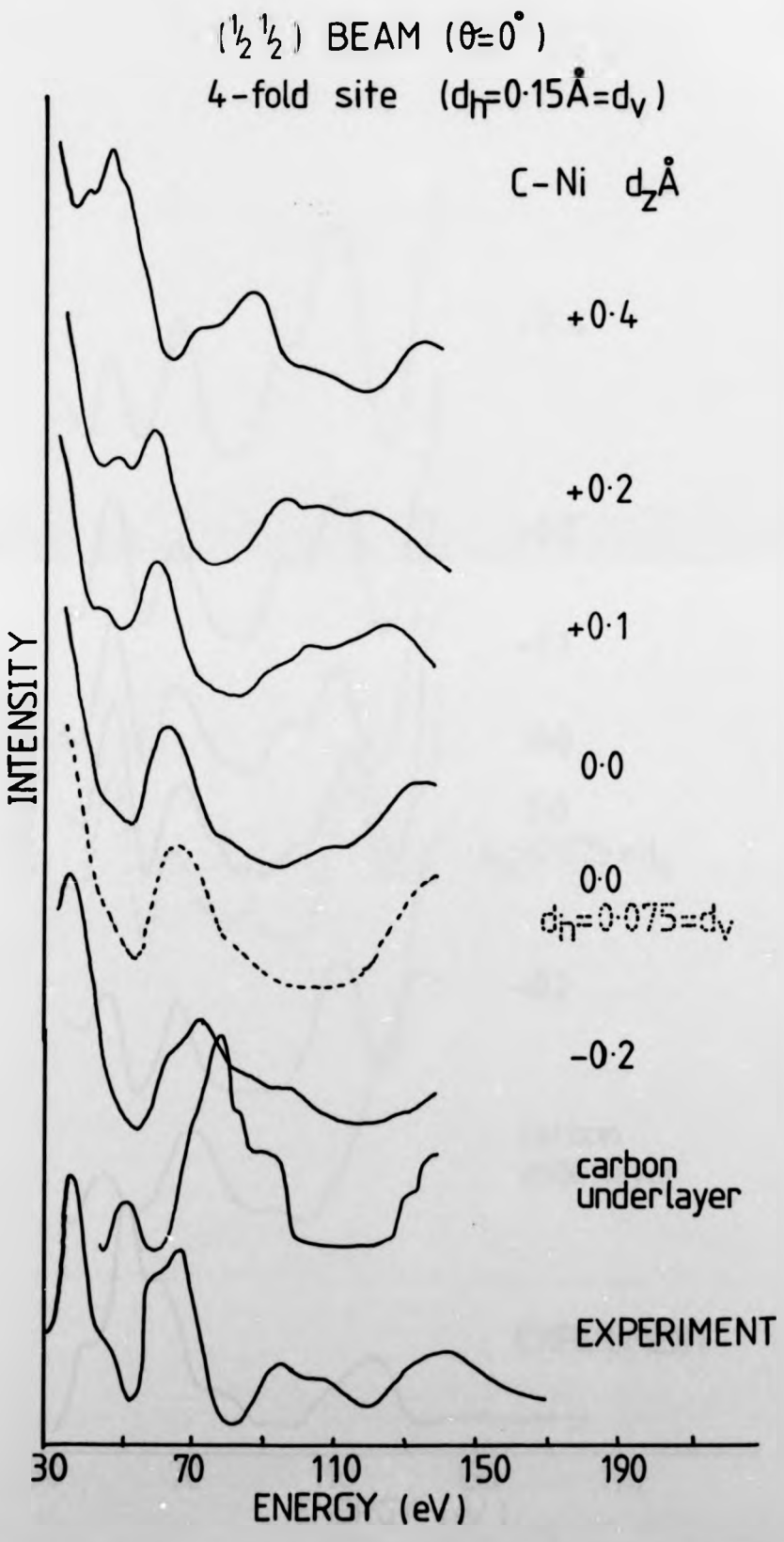
(½ ½) BEAM (θ=0°)
4-fold site (dH=0·15Å=dV)
C-Ni dZÅ
+0·4
+0·2
+0·1
0·0
0·0
dH=0·075=dV
-0·2
carbon underlayer
EXPERIMENT
INTENSITY
30
70
110
150
190
ENERGY (eV)

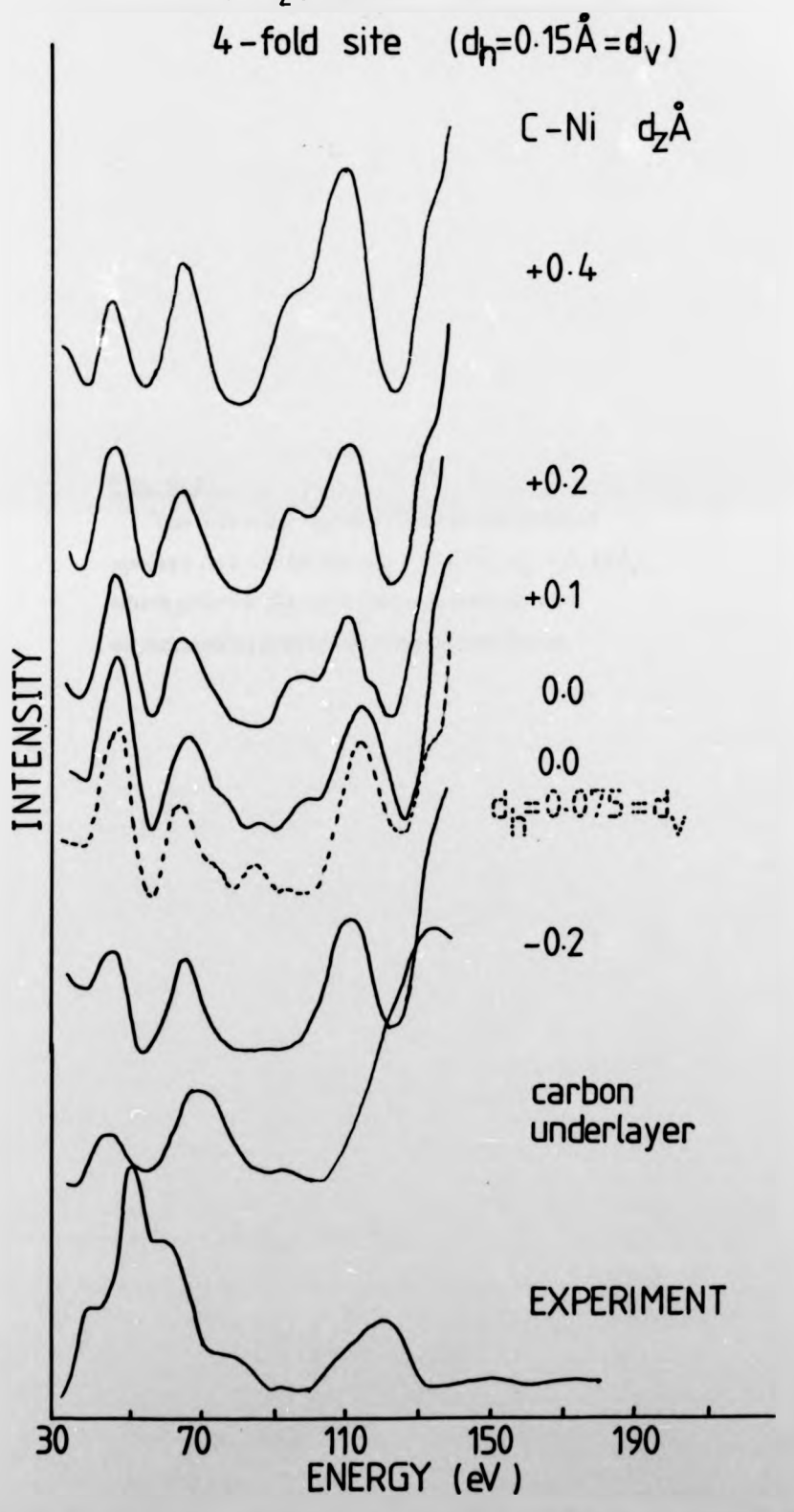
(1 $\bar{1}_2$) BEAM (θ=0°)
4-fold site (d_h=0·15Å=d_v)
C-Ni d_zÅ
+0·4
+0·2
+0·1
0·0
0·0
d_h=0·075=d_v
-0·2
carbon underlayer
EXPERIMENT
INTENSITY
30
70
110
150
190
ENERGY (eV)

Fig. 6.17

The following figures present theoretical spectra calculated for $d_h = 0.43$ Å, $d_v = 0.15$ Å, which provide the best correspondence with experimental spectra at normal incidence.

$\theta = 0^{\circ}$

$d_h = 0 \cdot 43$ Å, $d_v = 0 \cdot 15$ Å

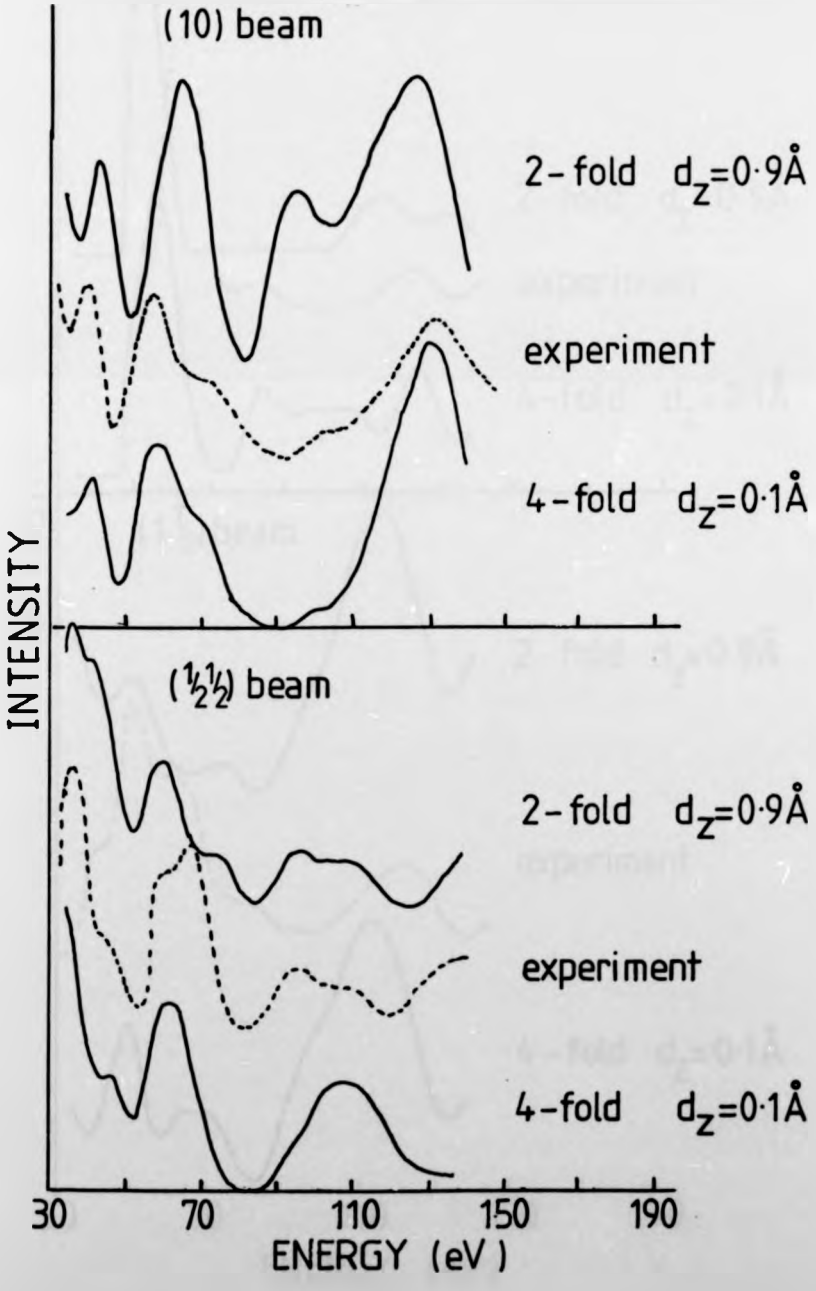

$\theta = 0^{\circ}$

$d_h = 0{\cdot}43\text{Å}$, $d_v = 0{\cdot}15\text{Å}$

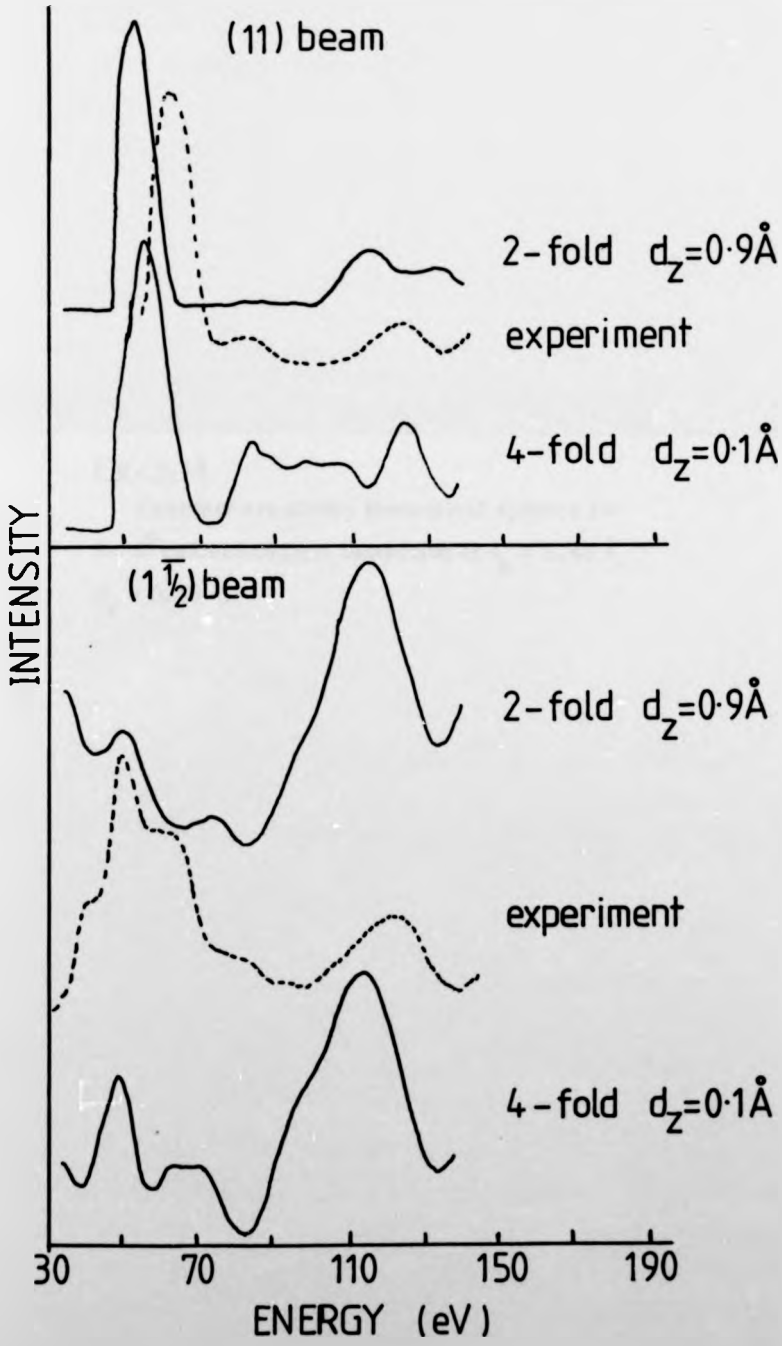

Fig. 6.18

Overleaf are shown theoretical spectra for $\theta = 8^{o}$ calculated for a distortion of $d_h = 0.43$ Å, $d_v = 0.15$ Å.

$\theta = 8^{\circ}$

$d_h = 0{\cdot}43\,\text{Å}$, $d_v = 0{\cdot}15\,\text{Å}$

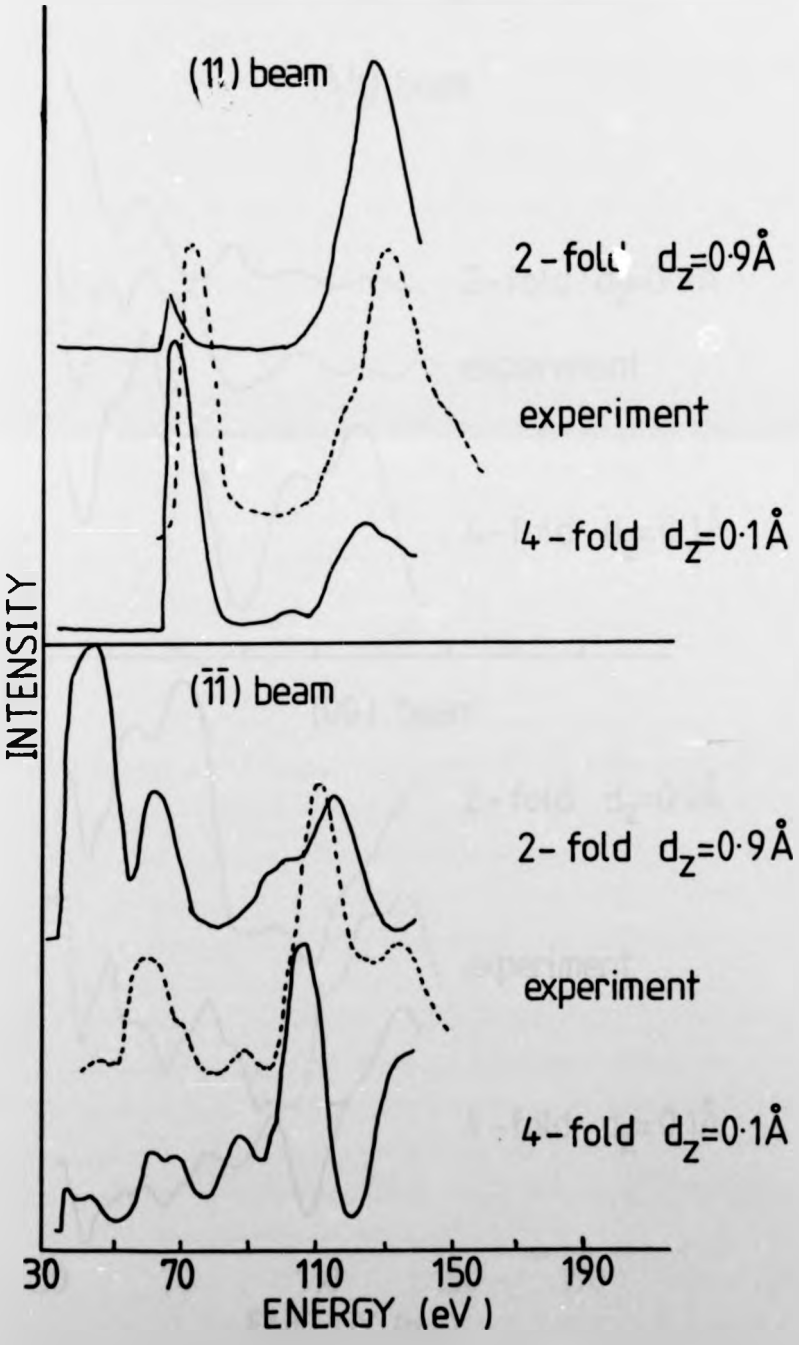

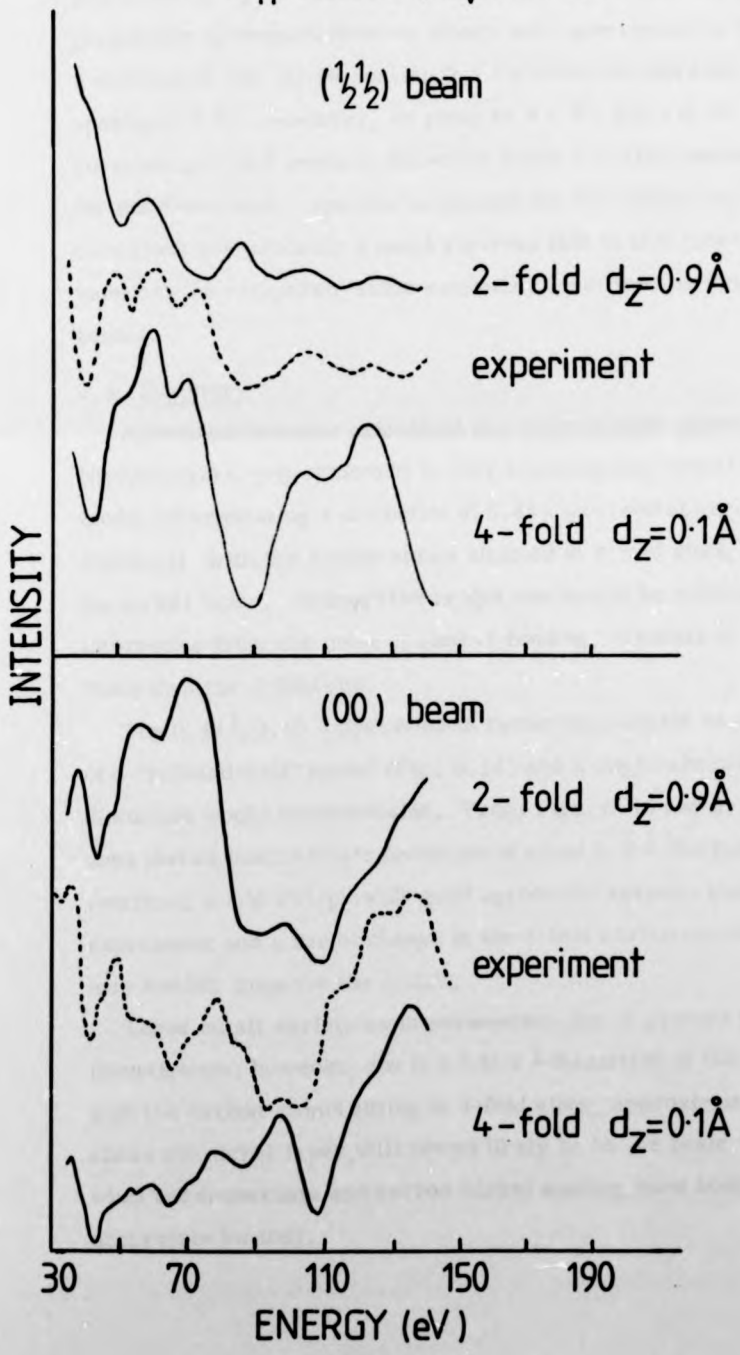
θ = 8°
d_h = 0·43Å , d_v = 0·15Å
(½½½) beam
2-fold d_z=0·9Å
experiment
4-fold d_z=0·1Å
INTENSITY
(00) beam
2-fold d_z=0·9Å
experiment
4-fold d_z=0·1Å
30
70
110
150
190
ENERGY (eV)

From Fig. 6.16 it will be seen that a distortion of around 0.43 Å (horizontal), 0.15 - 0.22 Å (vertical) provides some fairly reasonable agreement between theory and experiment for both the 4-fold hollow site (C-Ni spacing 0.1 Å) and the bridge site (C-Ni spacing 0.9 Å). However, on going to $\theta = 8^{o}$, for a 0.43 Å horizontal/0.15 Å vertical distortion there is plainly better agreement for the 4-fold site. Spectra calculated for off-normal incidence conditions are probably a more rigorous test in that more beams must now be compared, since symmetry conditions no longer equate beams.

6.4 Summary

Agreement between calculated and experimental spectra for the Ni(100)(2x2) C-p4g structure is very encouraging, especially for the model incorporating a distortion of 0.43 Å (horizontal) and 0.15 Å (vertical), with the carbon atoms situated in 4-fold sites, 0.1 Å above the nickel layer. Although the bridge site would be more unusual and interesting from the point of view of bonding, it seems to be less likely than the 4-fold site.

The 0.43 Å/0.15 Å distortion is rather improbable on consideration of a "billiard-ball" model (Fig. 6.14) and a slight alteration in this distortion would be reasonable. From Figs. 6.16 and 6.17 it can be seen that an intermediate distortion of about 0.3 Å (horizontal)/0.2 Å (vertical) would still provide good agreement between theory and experiment and a minor change in the 4-fold carbon-nickel spacing may further improve the match.

These small variations in parameters are at present under investigation; however, the 0.3 Å/0.2 Å distortion of the nickel atoms with the carbon atoms sitting in 4-fold sites, approximately 0.1 Å above the nickel layer, still seems likely to be the basic model, even when the distortions and carbon-nickel spacing have been more accurately located.

CHAPTER SIX
REFERENCES

1. R.L. Park & H.E. Farnsworth, Surface Sci., 2 (1964) 527.
2. S. Andersson & B. Kasemo, Surface Sci., 25 (1971) 273.
3. D.E. Eastman & J.K. Cashion, Phys. Rev. Lett., 27 (1971) 1520.
4. H.D. Hagstrum & G.E. Becker, J. Chem. Phys., 54 (1971) 1015.
5. J.E. Demuth, S.Y. Tong & T.N. Rhodin, J. Vac. Sci. & Technol., 9 (1971) 639.
6. J.E. Demuth & T.N. Rhodin, Surface Sci., 42 (1974) 261.
7. J.E. Demuth, Ph.D. Thesis, Cornell University (1973).
8. C.B. Duke & C.W. Tucker, Surface Sci., 15 (1969) 231.
9. J. Pendry, J. Phys. C., 4 (1971) 3095; Phys. Rev. Lett., 27 (1971) 856.
10. R.M. Tait, S.Y. Tong & T.N. Rhodin, Phys. Rev. Lett., 28 (1972) 553.
11. J.E. Demuth, P.M. Marcus & D.W. Jepsen, Phys. Rev. B., 11 (1975) 1460.
12. International Tables for X-ray Crystallography, Kynoch Press, Birmingham (1965).
13. B.W. Holland & D.P. Woodruff, Surface Sci., 36 (1973) 488.
14. J.E. Demuth & T.N. Rhodin, Surface Sci., 45 (1974) 249.
15. M.A. Van Hove & S.Y. Tong, Surface Sci., 52 (1975) 673.
16. G. Casalone, M.G. Cattania, M. Simonetta & M. Tescari, Surface Sci., 62 (1977) 321.
17. L.C. Isett & J.M. Blakely, Surface Sci., 58 (1976) 397.
18. G. Dalmai-Imelik & J.C. Bertolini, Compt. Rend. (Paris) C270 (1970) 1079.
19. M.A. Van Hove, Surface Sci., 48 (1975) 406.
20. M. Maglietta & G. Rovida, Surface Sci., 71 (1978) 495.
21. Julia H. Onuferko & D.P. Woodruff, First European Conference on Surface Science, Amsterdam (1978).
22. B.W. Holland & R.S. Zimmer, J. Phys. C., 8 (1975) 2395.

CHAPTER SEVEN

CONSTANT MOMENTUM TRANSFER AVERAGING

7.1 Introduction

A brief mention of CMTA was made in Chapter Two where some of the basic ideas were mentioned. A fuller description now follows, together with results obtained on the Ni(110) and (100) surfaces.

Lagally et al. (1, 2) proposed that I-V spectra, although containing a large number of multiple scattering contributions, also contain components from kinematical processes. If, by taking a large enough amount of data and applying an averaging procedure, the kinematical features can be enhanced while the dynamical features are diminished, the need to apply long, sophisticated computer programmes to interpret individual spectra may not arise. Their CMTA scheme supposes that kinematical features will be strengthened if the constraint of maintaining constant momentum transfer is complied with, i.e.

$$\text{for } (\underline{k} - \underline{k}')\, d = \text{constant}$$

where d is the spacing between planes perpendicular to the surface, and $\underline{k}$ and $\underline{k}'$ are the incident and diffracted wavevectors respectively, we define

$$\underline{k} - \underline{k}' = \underline{S}$$

Then, defining

$$S_o = \frac{2\pi}{d}$$

we obtain

$$(S/S_o) = 2d \cos\theta \left(\frac{E}{150.4}\right)^{\frac{1}{2}}$$

E is the incident beam energy in electron volts.

Diagrams indicating the reciprocal space geometry are shown in Fig. 7.1. The normalizing factor S_o will, of course, mean that the abscissa, S/S_o, of a plot is numbered in Bragg peak orders.

Ngoc et al. (3) have shown that CMTA intensities obtained from clean Ni(111) and Ag(111) are very kinematical in nature, as have McDonnell et al. (4) for the Cu(111) surface and Unertl and Webb (5) for Ni(100). In these cases, the conclusion reached is that there is little or no surface layer expansion or contraction, which would manifest itself by

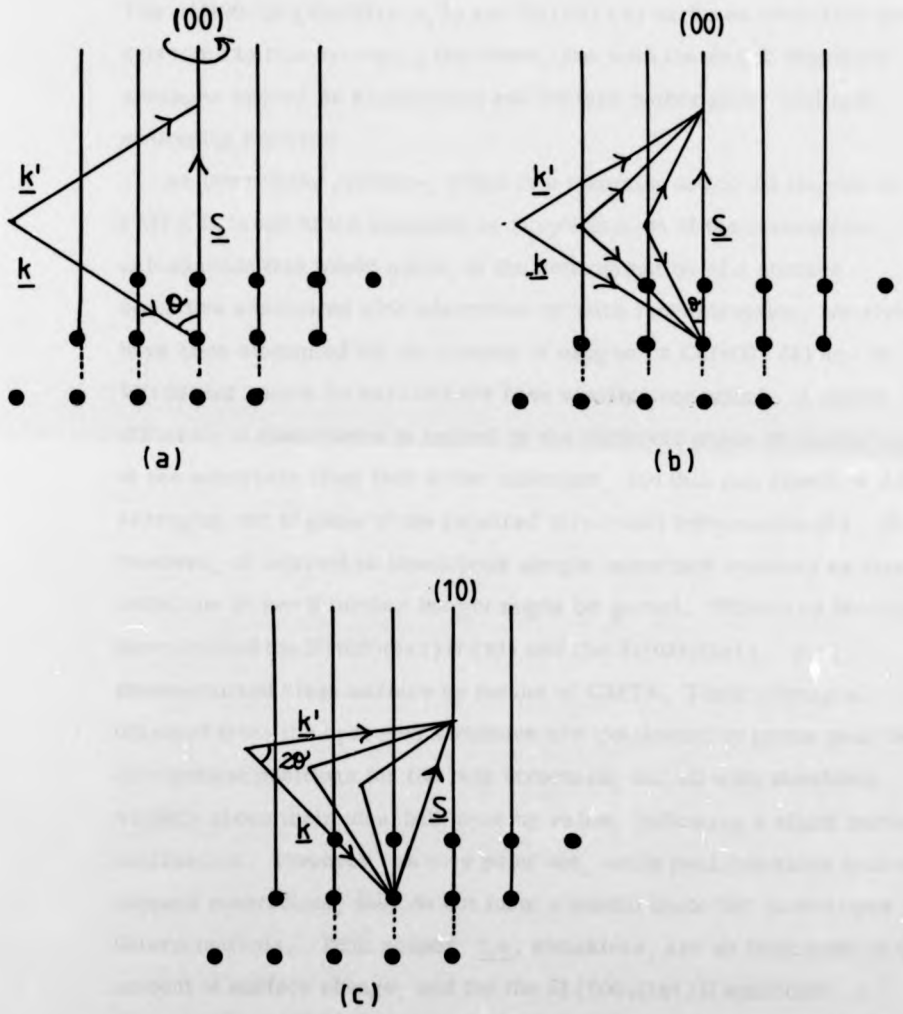

Fig. 7.1

Averaging geometries for

(a) the specular beam at constant polar angle, θ

(b) the specular beam at constant azimuth, φ

(c) the (10) beam

a shoulder appearing on the low or high side of the kinematical peaks. The Al(100) (6), Cu(100) (4, 7) and W(110) (8) surfaces have also been subjected to this averaging treatment, but with the result that their averages are not so kinematical and contain rather more multiple scattering features.

An interesting problem, which is a tempting one to be tackled by CMTA because of the enormity in simplification of the theoretical calculations this would mean, is the determination of a surface structure associated with adsorption or with reconstruction. Analyses have been attempted for the system of oxygen on Cu(100) (4) and on W(110) but cannot be said to have been wholly successful. A major difficulty in these cases is caused by the different phase of scattering at the adsorbate from that at the substrate, and this can result in the averaging out of some of the required structural information (9). It is, however, of interest to investigate simple adsorbate systems by this technique to see if further insight might be gained. White and Woodruff have studied the Si(100)(1x1)H (10) and the Si(100)(2x1) (11) reconstructed clean surface by means of CMTA. Their averages obtained from the hydrogen structure are dominated by peaks near the kinematical positions for the bulk structure, but all with shoulders slightly above their ideal bulk spacing value, indicating a slight surface contraction. However, as they point out, while peak positions tend to support contraction, they do not form a useful basis for quantitative determinations. Peak shapes, i.e. shoulders, are an indication of the amount of surface change, and for the Si(100)(1x1)H structure, a contraction of 3% ± 3% relative to the bulk spacing is suggested. In their study of the clean, reconstructed (2x1) structure, CMTA gives rise to many features other than the kinematical. This could be interpreted as being due to the reconstruction of quite a number of layers, but this solution is not readily justifiable and would need the support of dynamical calculations if it is to be believed.

In the present work, CMTA was carried out on the specular beam for the clean Ni(110) surface, both at room temperature and at 150° K. This is the only CMTA study known, to date, of a (110) face of an f.c.c.

a shoulder appearing on the low or high side of the kinematical peaks. The Al(100) (6), Cu(100) (4, 7) and W(110) (8) surfaces have also been subjected to this averaging treatment, but with the result that their averages are not so kinematical and contain rather more multiple scattering features.

An interesting problem, which is a tempting one to be tackled by CMTA because of the enormity in simplification of the theoretical calculations this would mean, is the determination of a surface structure associated with adsorption or with reconstruction. Analyses have been attempted for the system of oxygen on Cu(100) (4) and on W(110) but cannot be said to have been wholly successful. A major difficulty in these cases is caused by the different phase of scattering at the adsorbate from that at the substrate, and this can result in the averaging out of some of the required structural information (9). It is, however, of interest to investigate simple adsorbate systems by this technique to see if further insight might be gained. White and Woodruff have studied the Si(100)(1x1)H (10) and the Si(100)(2x1) (11) reconstructed clean surface by means of CMTA. Their averages obtained from the hydrogen structure are dominated by peaks near the kinematical positions for the bulk structure, but all with shoulders slightly above their ideal bulk spacing value, indicating a slight surface contraction. However, as they point out, while peak positions tend to support contraction, they do not form a useful basis for quantitative determinations. Peak shapes, i.e. shoulders, are an indication of the amount of surface change, and for the Si(100)(1x1)H structure, a contraction of 3% ± 3% relative to the bulk spacing is suggested. In their study of the clean, reconstructed (2x1) structure, CMTA gives rise to many features other than the kinematical. This could be interpreted as being due to the reconstruction of quite a number of layers, but this solution is not readily justifiable and would need the support of dynamical calculations if it is to be believed.

In the present work, CMTA was carried out on the specular beam for the clean Ni(110) surface, both at room temperature and at 150° K. This is the only CMTA study known, to date, of a (110) face of an f.c.c.

crystal. The specular beam data from the (1x2) H structure formed at 150°K were also subjected to CMTA.

The clean, room temperature Ni(100) surface has already been studied by CMTA by Unertl and Webb (5) for the specular beam in one azimuth and for the $(\bar{1}0)$ beam. It was thought to be a worthwhile exercise to repeat this work, if only to be reassured as to the reliability of the averaging procedures. CMTA was carried out on the (00), (11) and (10) beams. The Ni(100)(2x2)C - p4g structure was also made the subject of averaging, the (00), (11), (10) and $(\frac{1}{2}\ \frac{1}{2})$ beams being investigated.

7.2 Experimental Arrangement

Specular beam data were collected directly by an on-line GEC-4080 computer, which provided the primary beam energy ramp and an "instant feedback" display of the spectrum being stored. Data were collected for values of θ increasing in 2° steps from 8° to 30° or 32° at several azimuths, and each spectrum was normalized before averaging was done.

Non-specular beam spectra were taken by hand in the way described in Chapter Three. These were then digitised in 2 eV steps and the intensities stored in the computer to be normalized and subjected to the CMTA programme.

7.3 Results and Discussion

7.3.1 The clean Ni(100) surface

The intensity profiles for the (10) and (11) beams are shown in Fig. 7.2. Since the specular beam data were collected for five azimuths (0°, 10°, 20°, 30°, 45°), individual spectra are not presented here; instead, the averages obtained from five different azimuths are shown in Fig. 7.3. Fig. 7.4 shows the grand averages of the (00), (10) and (11) beams. For a value of V_o = 14eV, the agreement with the experimental data averages of Unertl and Webb is good. Fig. 7.5 shows a comparison between their experimentally obtained (00) and $(\bar{1}0)$ beam intensities and the present work. The only important structure in the

Fig. 7.2

Overleaf are shown the I-V data from clean Ni(100) for the (10) and (11) beams which were used to compute the constant momentum transfer averages.

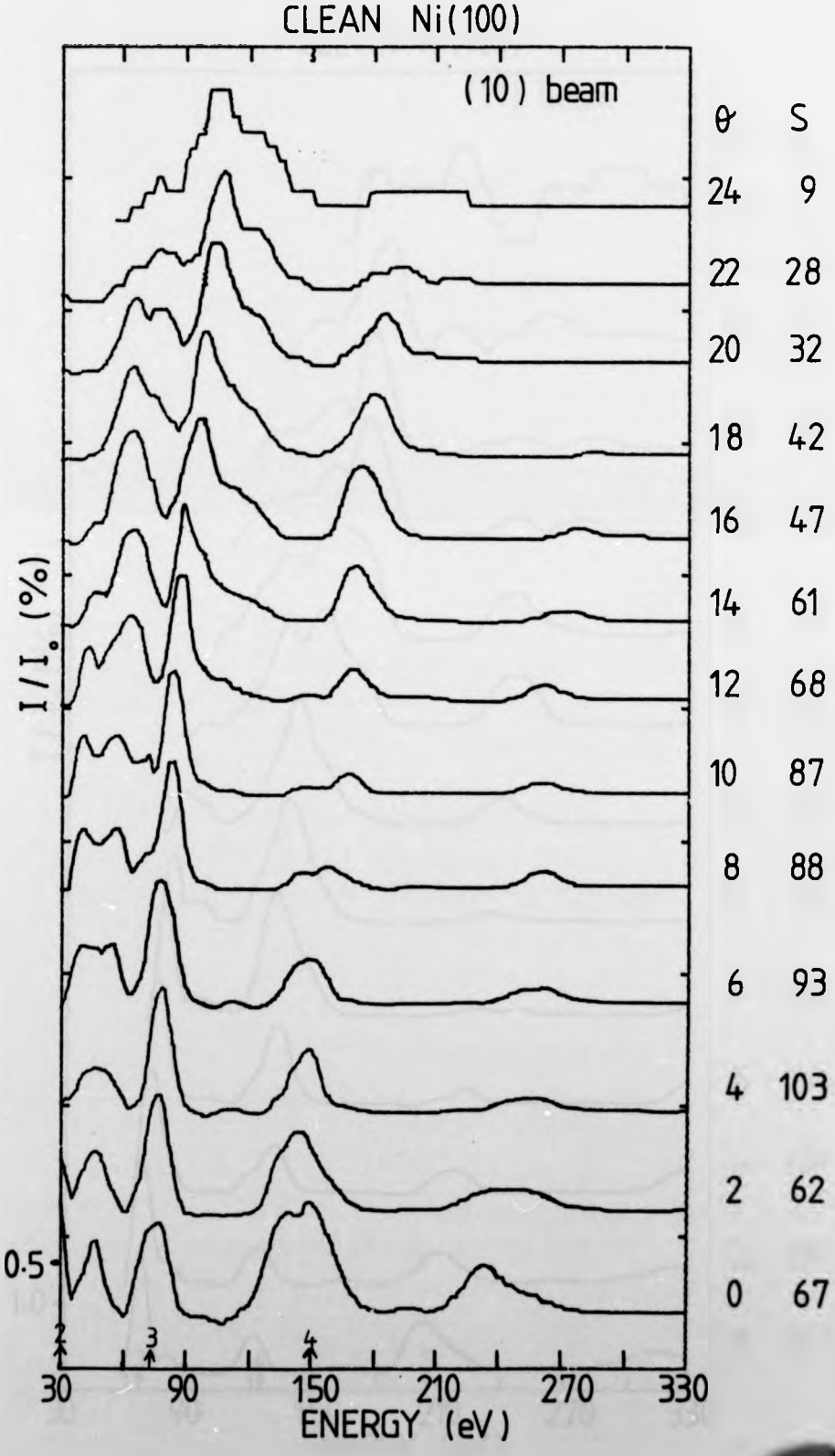
CLEAN Ni(100)
(10) beam
θ
S
24 9
22 28
20 32
18 42
16 47
14 61
12 68
10 87
8 88
6 93
4 103
2 62
0 67
I/I₀ (%)
0·5
2
3
4
30
90
150
210
270
330
ENERGY (eV)

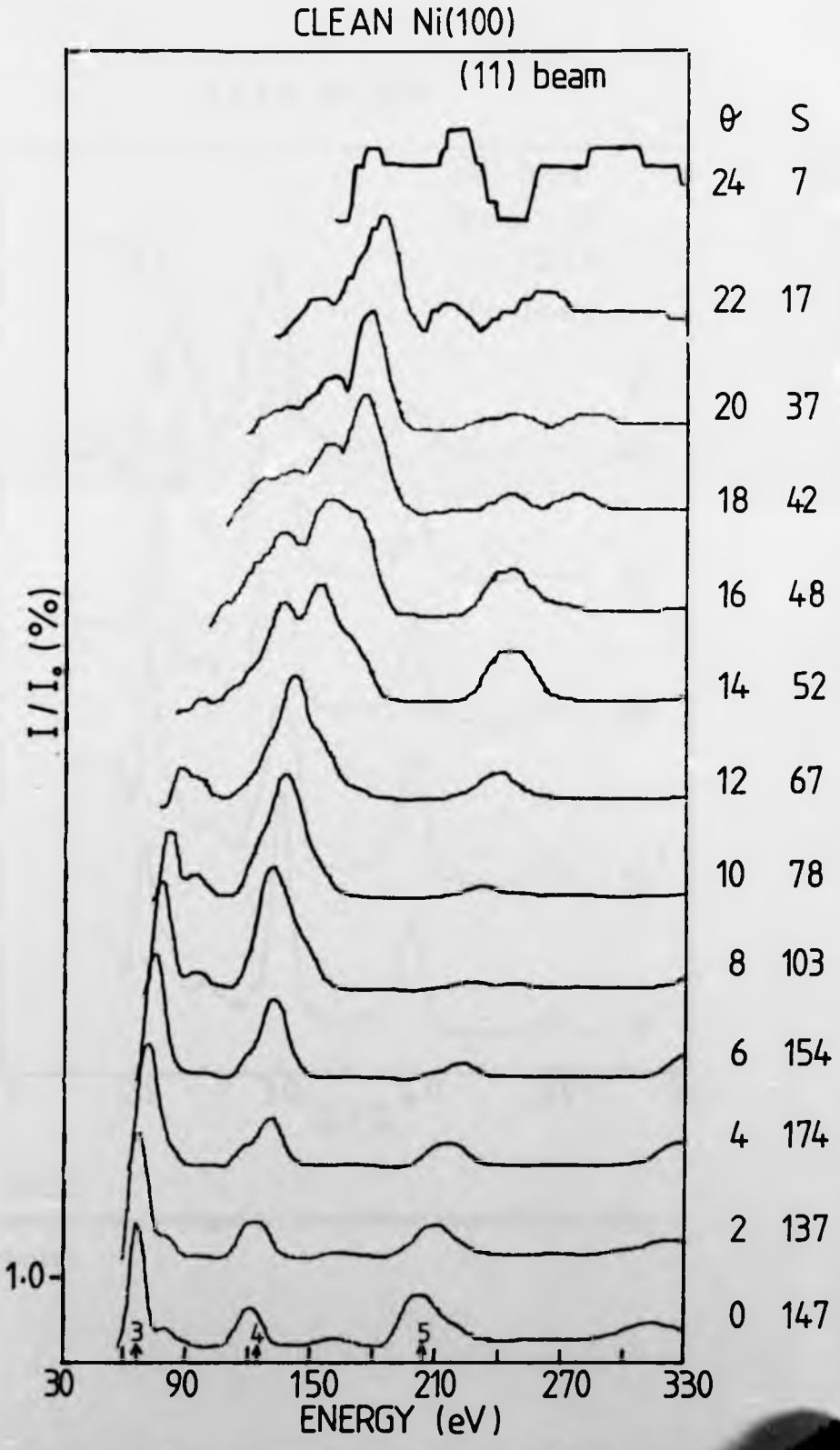
CLEAN Ni(100)
(11) beam
θ S
24 7
22 17
20 37
18 42
16 48
14 52
12 67
10 78
8 103
6 154
4 174
2 137
0 147
I/I₀ (%)
1·0
3
4
5
30
90
150
210
270
330
ENERGY (eV)

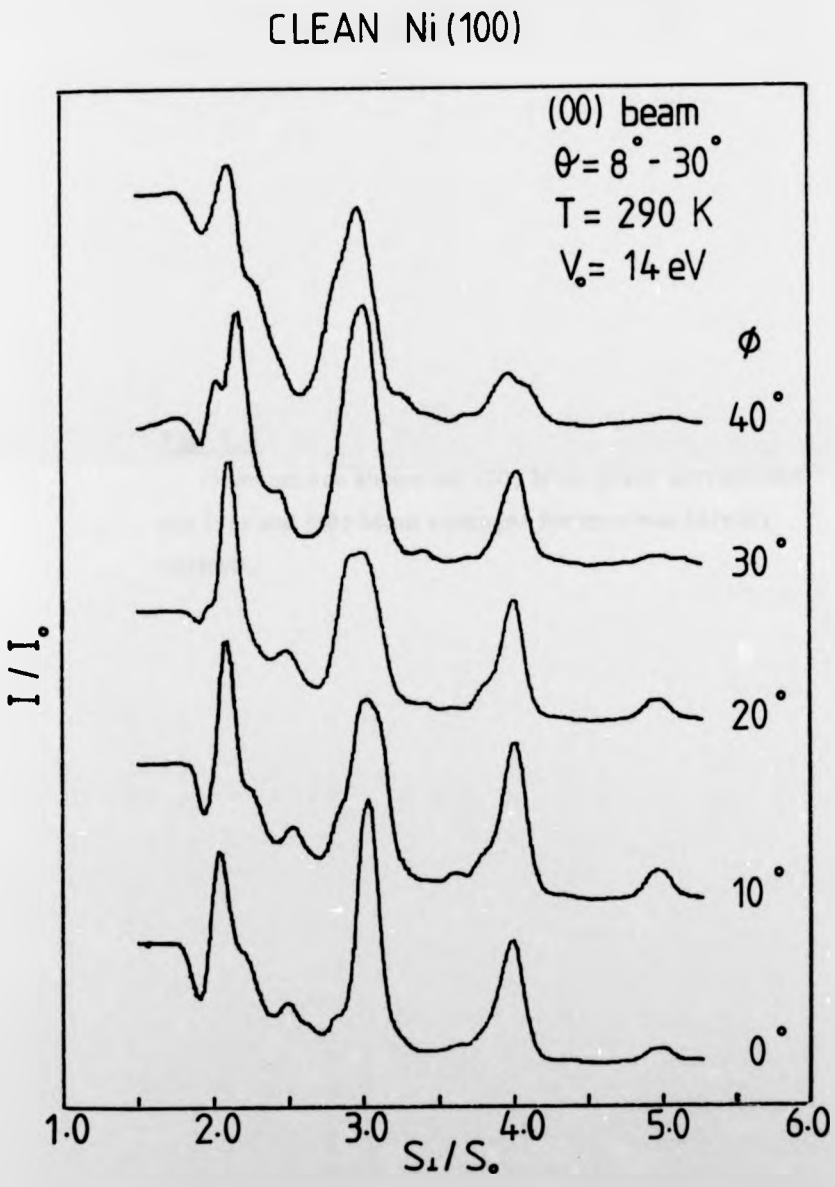

Fig. 7.3

Specular beam averages for five different azimuths from clean Ni(100)

Fig. 7.4

Overleaf are shown the (00) beam grand average and the (11) and (10) beam averages for the clean Ni(100) surface.

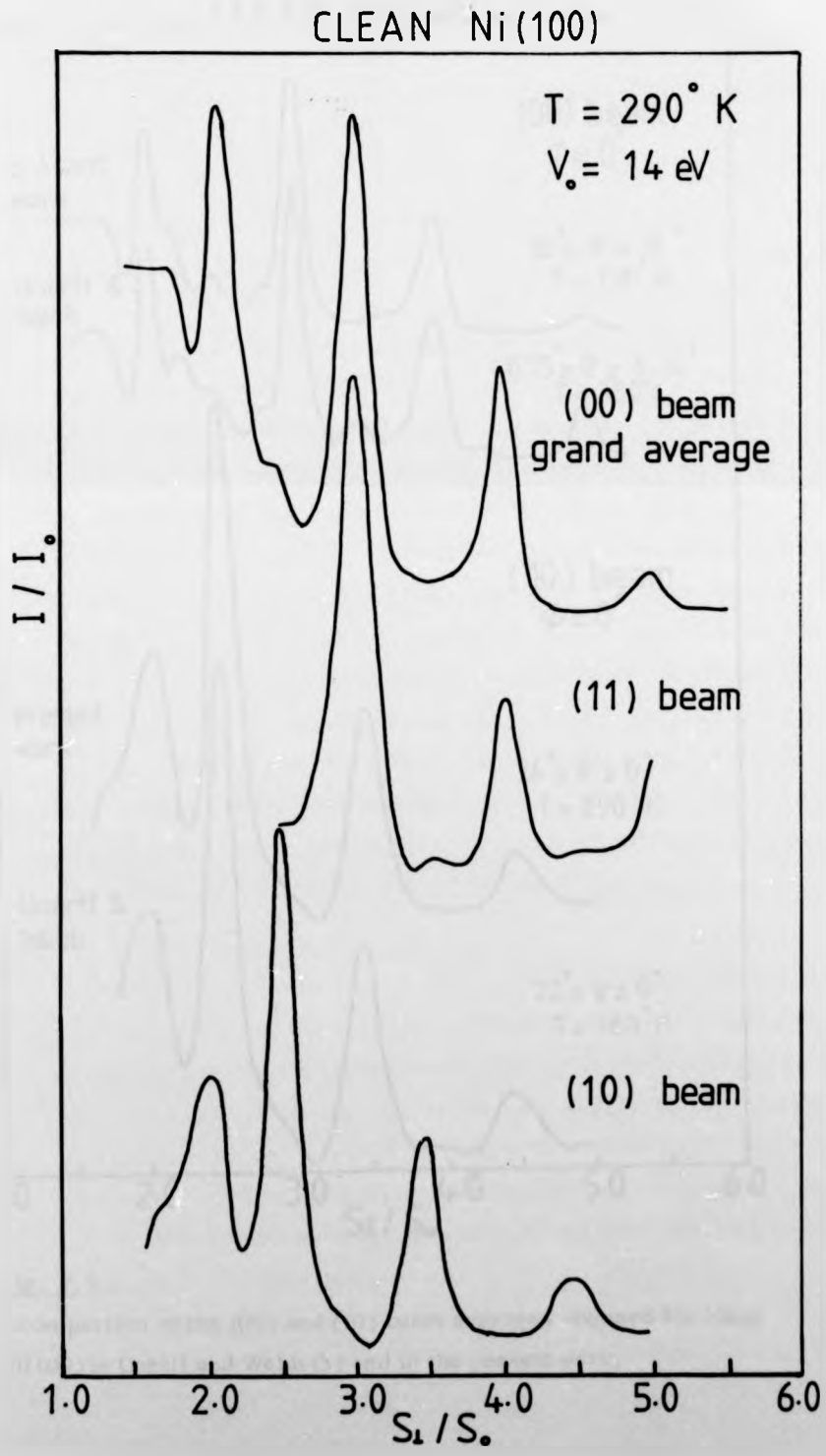
CLEAN Ni(100)
T = 290° K
V₀ = 14 eV
(00) beam
grand average
(11) beam
(10) beam
I / I₀
1·0
2·0
3·0
4·0
5·0
6·0
S₁ / S₀

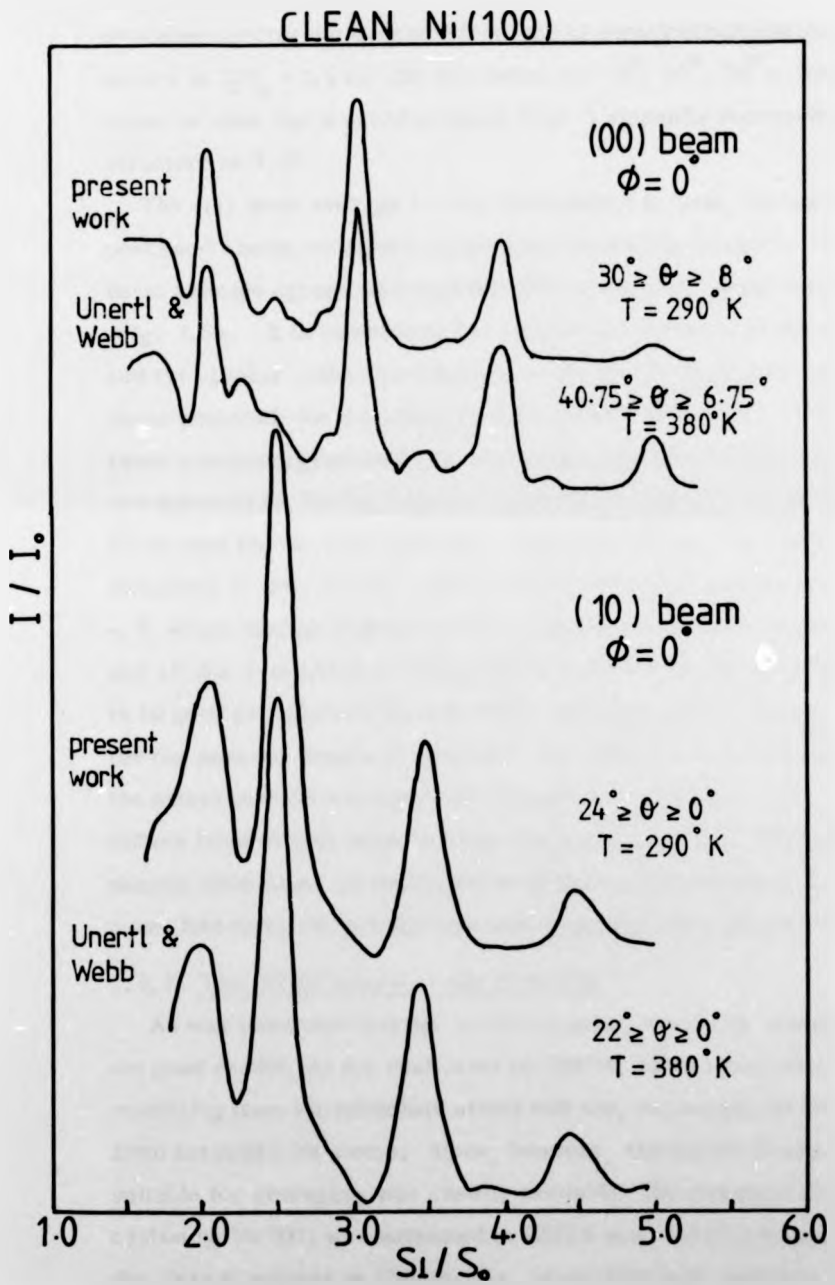

Fig. 7.5

A comparison of the (00) and (10) beam averages obtained for clean Ni(100) by Unertl and Webb (5) and in the present work.

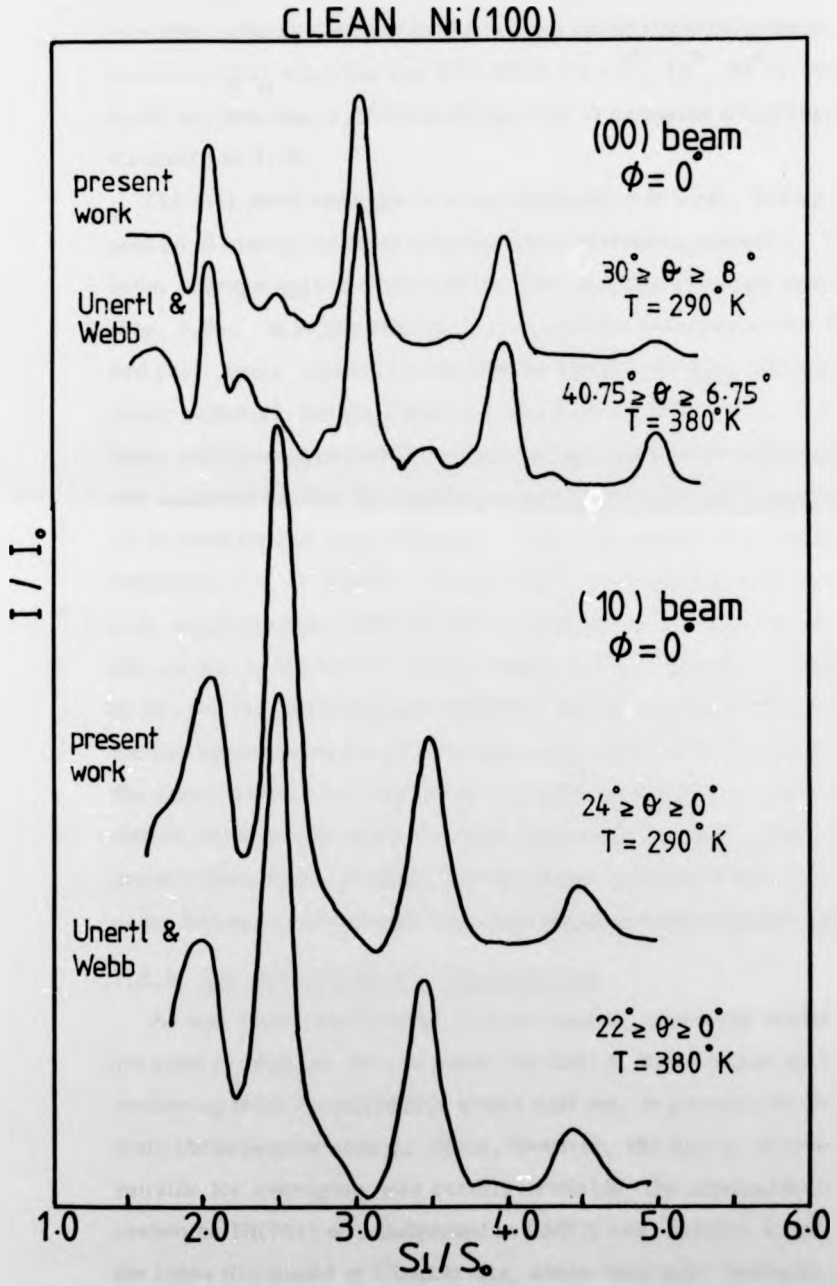

Fig. 7.5

A comparison of the (00) and (10) beam averages obtained for clean Ni(100) by Unertl and Webb (5) and in the present work.

averaged spectra not expected from the kinematical calculations, occurs at $S_i/S_o = 2.4$ for the (00) beam ($\varphi = 0^o$, 10^o, 20^o); however, it can be seen that a grand average over 5 azimuths decreases the structure at 3.45.

The (11) beam average is very kinematical in form, having symmetric peaks and almost no remaining multiple scattering features. The (10) beam average agrees well with the $(\bar{1}0)$ average of Unertl and Webb (5) (Fig. 7.5). It is interesting to compare the averages of the (00), (10) and (11) beams with those obtained by McDonnell et al. (4) using a 14 eV inner potential, for the clean Cu(100) surface (Fig. 7.6). The (11) beam averages agree well, except for the slight half-order peaks which are apparent for the Ni surface; a good fit is obtained if a value of 14 eV is used for the inner potential. The (10) beams have peaks and shoulders at very similar values of S_i/S_o and disagree only around $S_i/S_o \simeq 2$, which may be understandable owing to the fact that these features are all due to the lowest energy peaks where averaging is least likely to be good and data are less reliable. A comparison of the grand averages for the specular beams (5 azimuths for nickel and 10 for copper) shows the nickel surface average to be far more kinematical. This also differs from an (00) beam average from another f.c.c. (100) surface, namely aluminium, as described by Quinto and Robertson (6). In that case, however, the average was performed for one azimuth only.

7.3.2 The Ni(100)(2x2)C - p4g structure

As was mentioned earlier in this chapter, overlayer structures are not good candidates for evaluation by CMTA, since phase shifts due to scattering from the adsorbate atoms will not, in general, be the same as from the substrate atoms. Since, however, the means of acquiring data suitable for averaging was readily available, the structure formed by carbon on Ni(100) was subjected to CMTA and, bearing in mind some of the ideas discussed in Chapter Six, some "tell-tale" features in the averaged data were sought.

Fig. 7.6

Overleaf are shown (00), (11) and (10) beam averages for the clean Cu(100) (4) and Ni(100) surfaces.

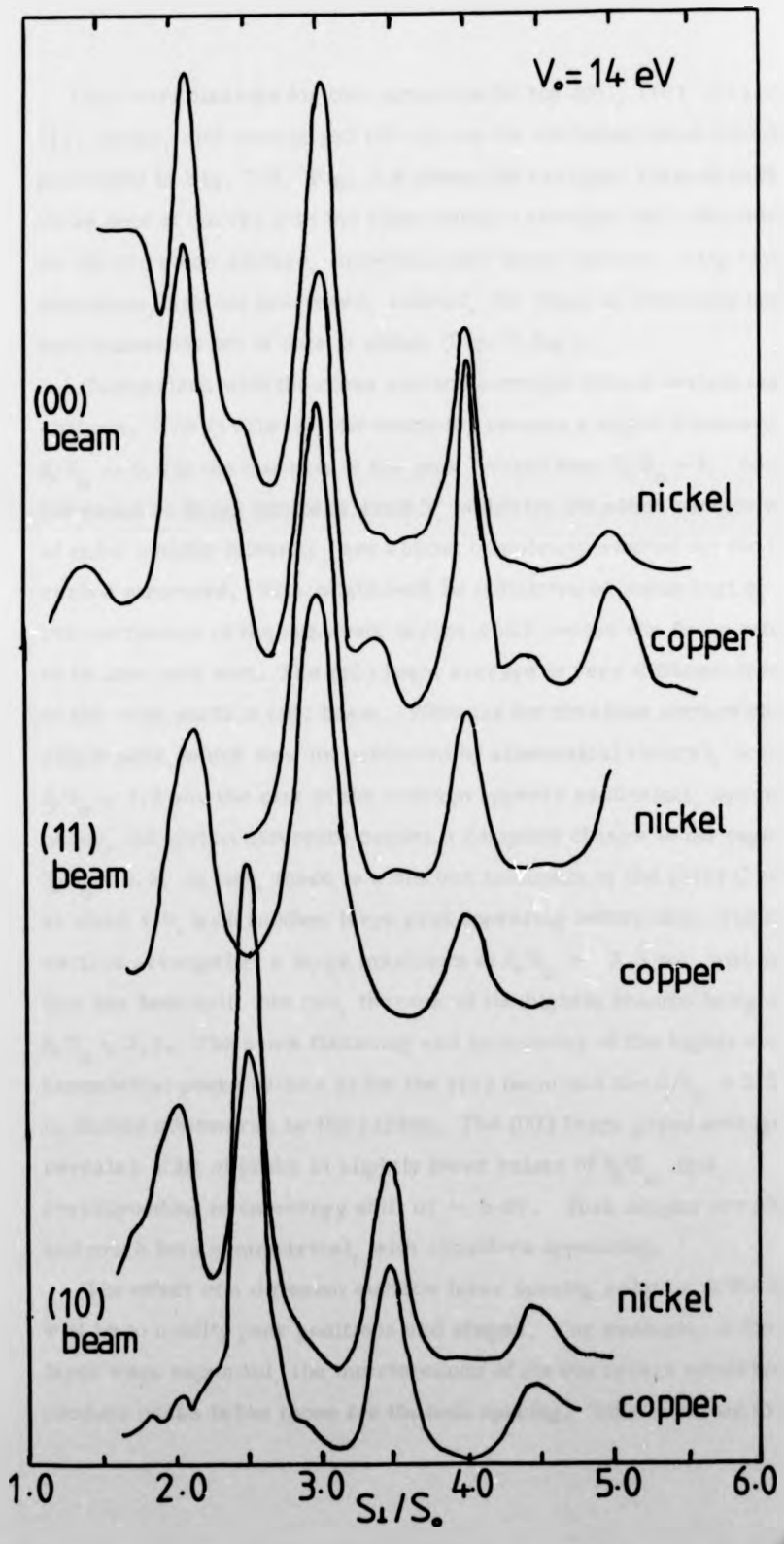
V₀= 14 eV
(00)
beam
nickel
copper
(11)
beam
nickel
copper
(10)
beam
nickel
copper
1·0
2·0
3·0
4·0
5·0
6·0
S₁/S₀

Data were obtained for this structure for the (00), (10), (11) and $(\frac{11}{22})$ beams, and normalized I-V curves for the latter three beams are presented in Fig. 7.7. Fig. 7.8 shows the averaged form of each of these sets of curves with the clean surface averages for comparison. As for the clean surface, individual (00) beam spectra, being rather numerous, are not presented: instead, the effect of averaging upon each azimuthal set of data is shown (Fig. 7.8(a)).

Comparison with the clean surface averages shows certain marked changes. The (11) beam, for example, reveals a slight downward shift, $S_i/S_o \simeq 0.2$ in the position of the peak located near $S_i/S_o = 3$; however, the peaks at Bragg numbers 4 and 5, which for the clean surface were of quite notable intensity, are almost completely washed out for the carbon structure. This might well be indicative of some sort of reconstruction of the substrate layers which causes the Bragg condition to be less well met. The (10) beam average is very different from that of the clean surface (10) beam. Whereas for the clean surface only one single peak, (which was not predicted by kinematical theory), occurs at $S_i/S_o \simeq 1.9$ and the rest of the average appears as distinct, symmetrical peaks, the carbon structure causes a complete change in the region below $S_i/S_o = 2.5$. In fact, there is a distinct minimum in the (2x2) C average at about 1.9, with another large peak appearing before this. The clean surface average has a large maximum at $S_i/S_o \simeq 2.5$ but, with carbon, this has been split into two, the peak of the highest feature being at $S_i/S_o \simeq 2.3$. The same flattening and broadening of the higher energy kinematical peaks occurs as for the (11) beam and the $S_i/S_o = 3.5$ peak is shifted downwards by the carbon. The (00) beam grand average reveals a shift of peaks to slightly lower values of S_i/S_o, this corresponding to an energy shift of $\sim$ 5 eV. Peak shapes are altered and much less symmetrical, with shoulders appearing.

The effect of a different surface layer spacing relative to the bulk will be to modify peak positions and shapes. For example, if the surface layer were expanded, the interferences of the top layers would tend to produce peaks below those for the bulk spacing. This will lead to low

Fig. 7.7

The following figures show the I-V spectra obtained for the (10), (11) and $(\frac{11}{22})$ beam averages for the Ni(100) (2x2) C-p4g surface, subsequently used for CMTA.

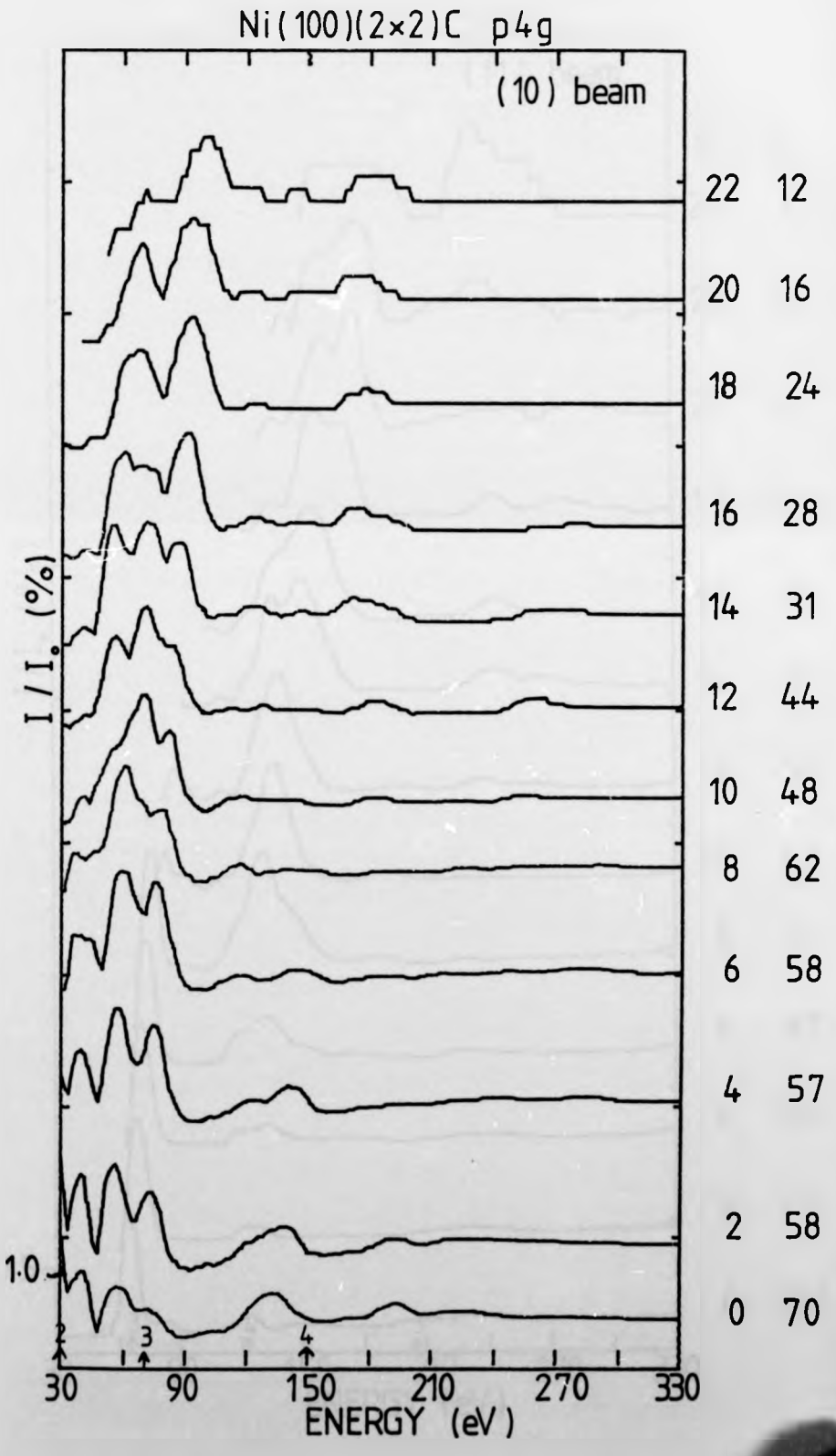
Ni(100)(2×2)C p4g
(10) beam
22 12
20 16
18 24
16 28
14 31
12 44
10 48
8 62
6 58
4 57
2 58
0 70
I / I₀ (%)
1·0
2
3
4
30
90
150
210
270
330
ENERGY (eV)

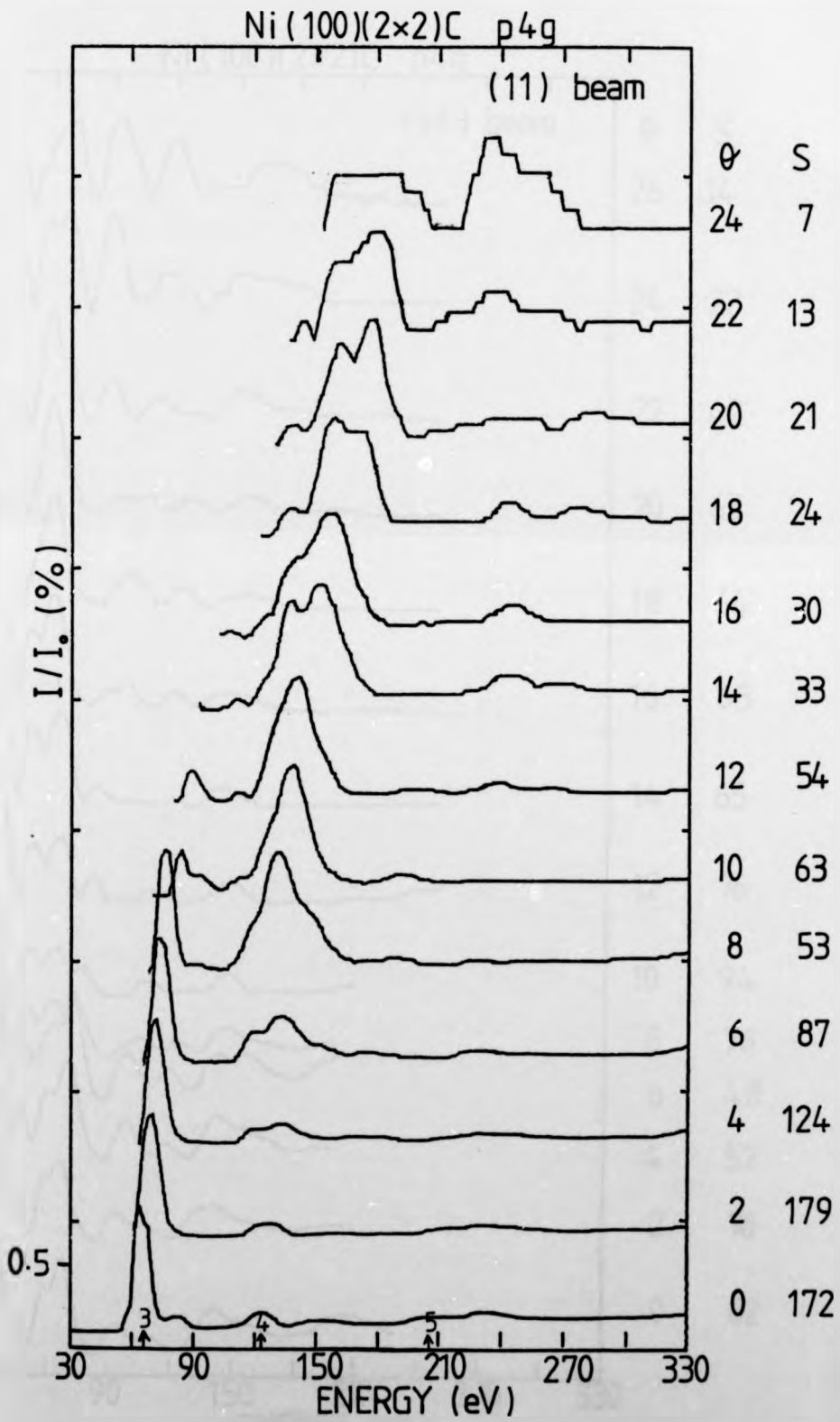
Ni (100)(2×2)C p4g
(11) beam
θ S
24 7
22 13
20 21
18 24
16 30
14 33
12 54
10 63
8 53
6 87
4 124
2 179
0 172
I/I₀ (%)
0.5
3
4
5
30
90
150
210
270
330
ENERGY (eV)

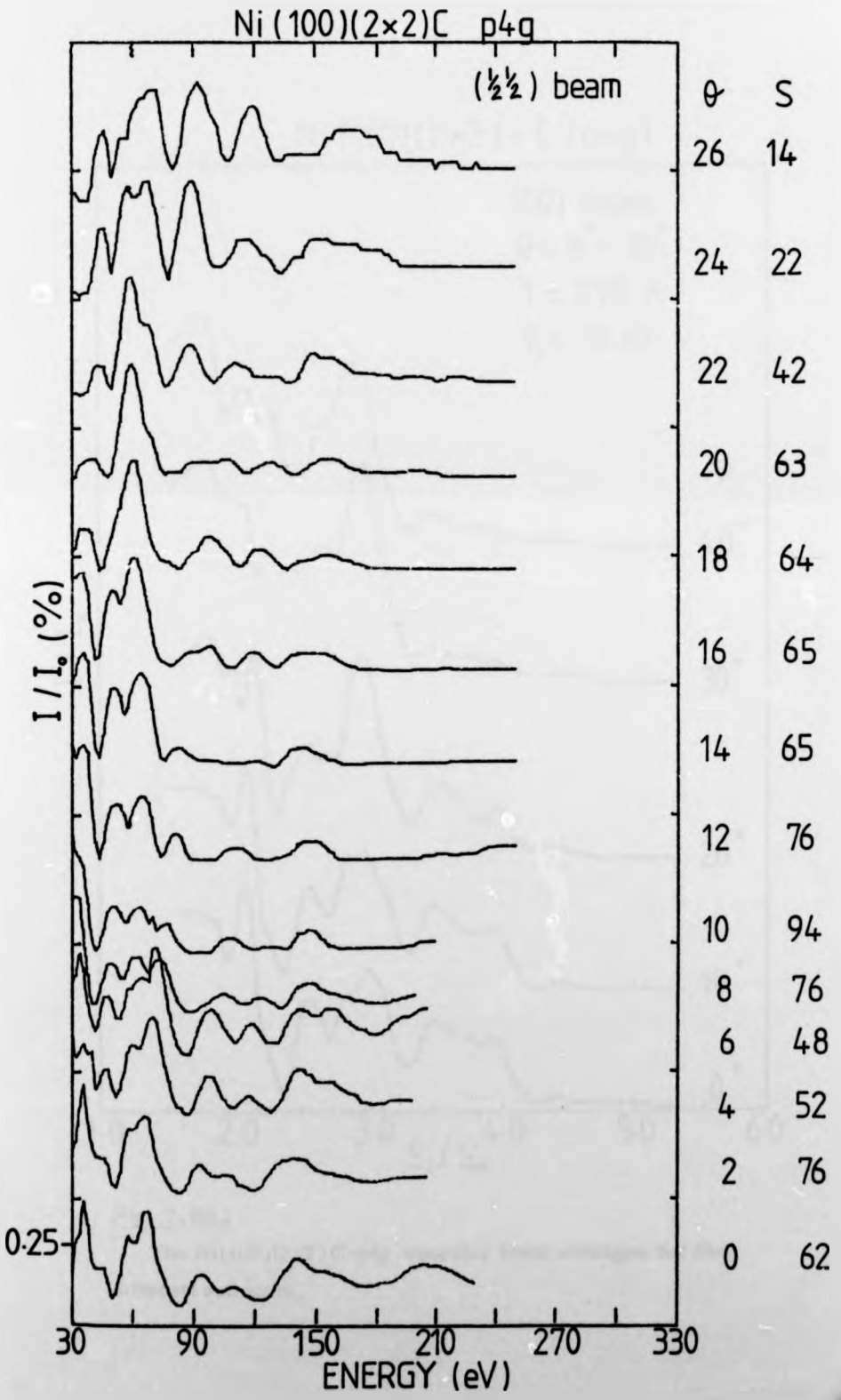
Ni (100)(2×2)C p4g
(½½) beam
θ S
26 14
24 22
22 42
20 63
18 64
16 65
14 65
12 76
10 94
8 76
6 48
4 52
2 76
0 62
I / I₀ (%)
0·25
30 90 150 210 270 330
ENERGY (eV)

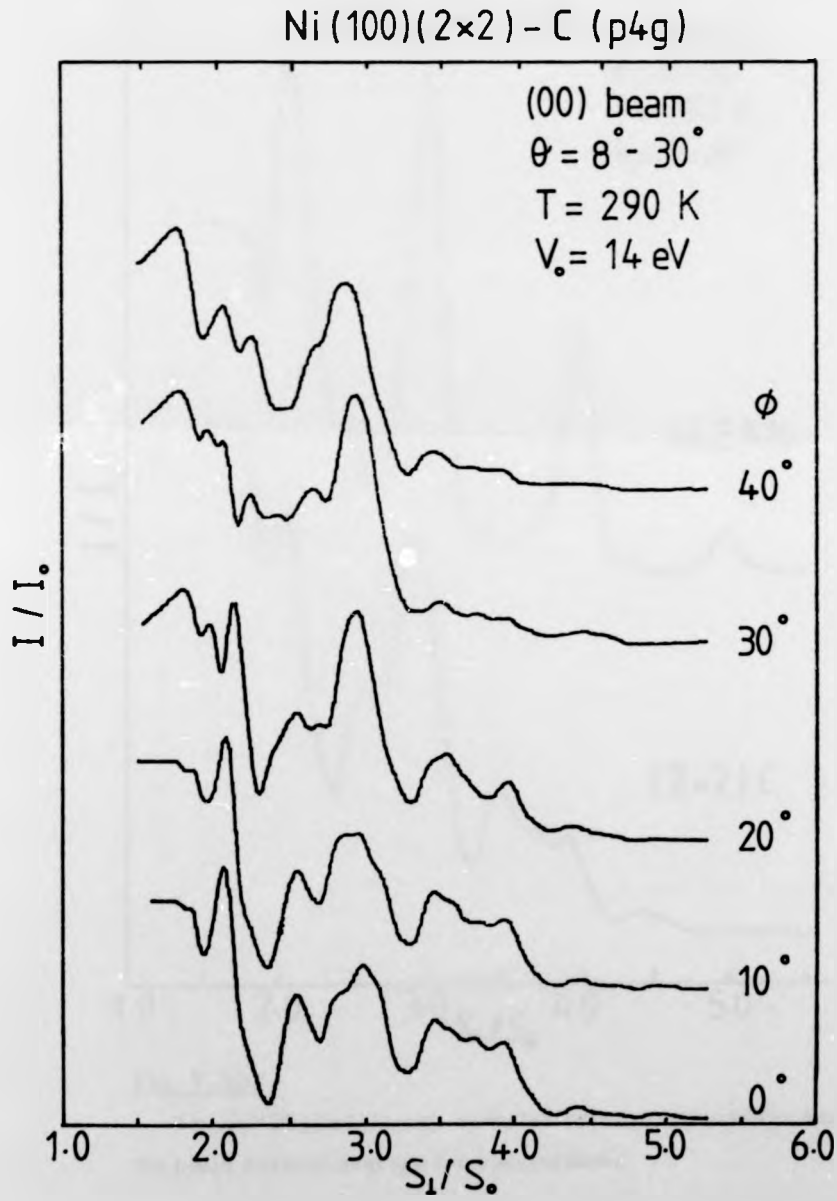

Fig. 7.8(a)

The Ni(100)(2x2)C-p4g specular beam averages for five different azimuths.

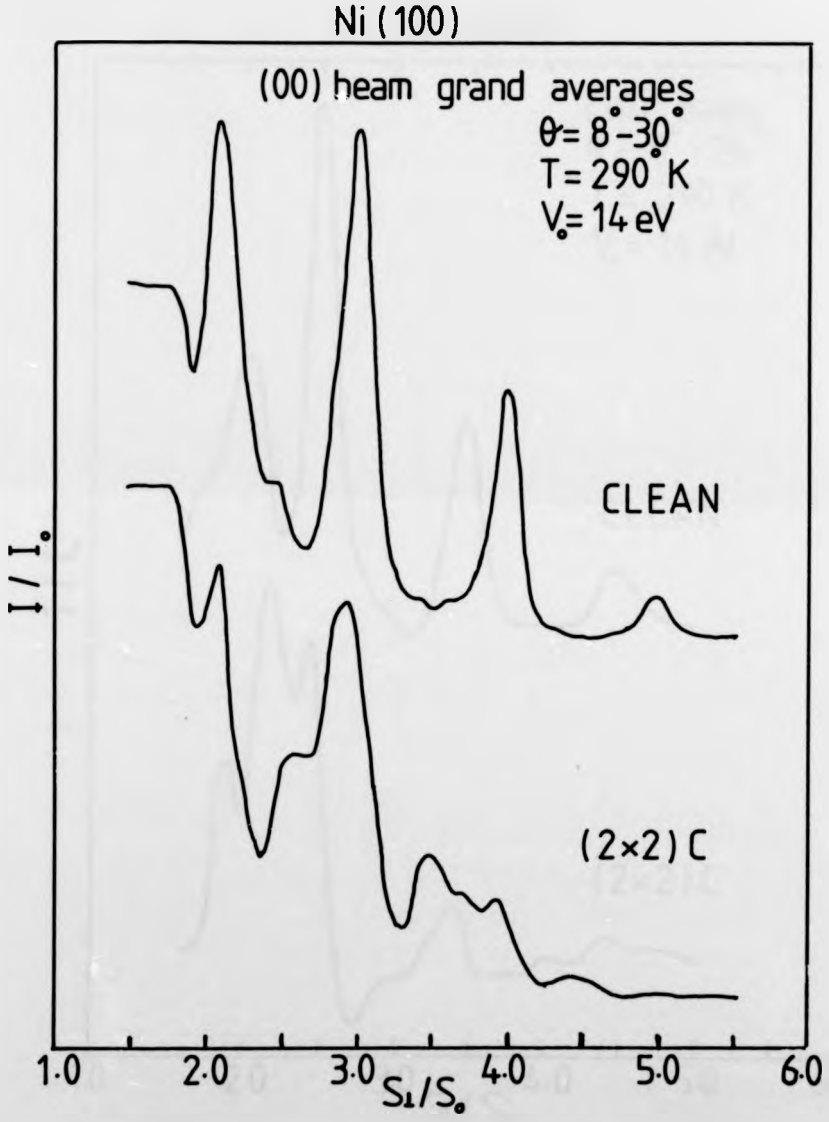

Fig. 7.8(b)

The Ni(100)(2x2)C-p4g specular beam grand average with the clean surface average for comparison.

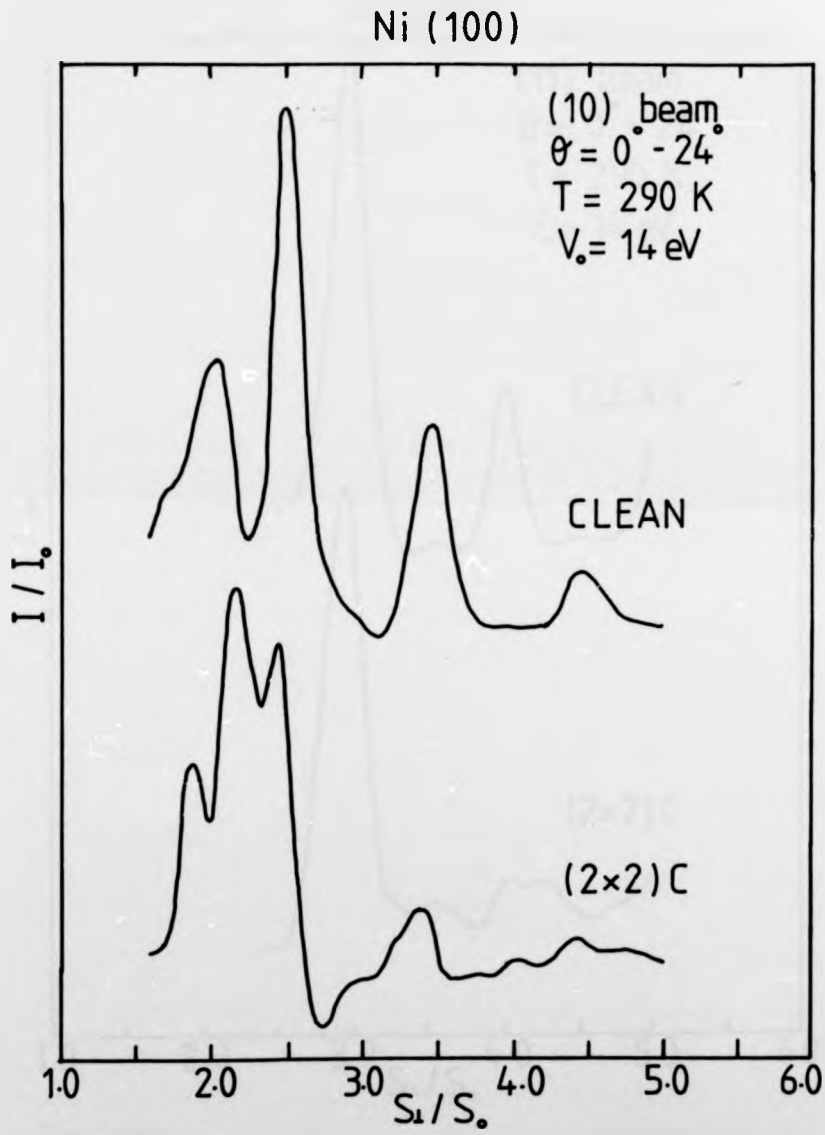

Fig. 7.8(c)

The Ni(100)(2x2)C-p4g (10) beam average with the clean surface average for comparison.

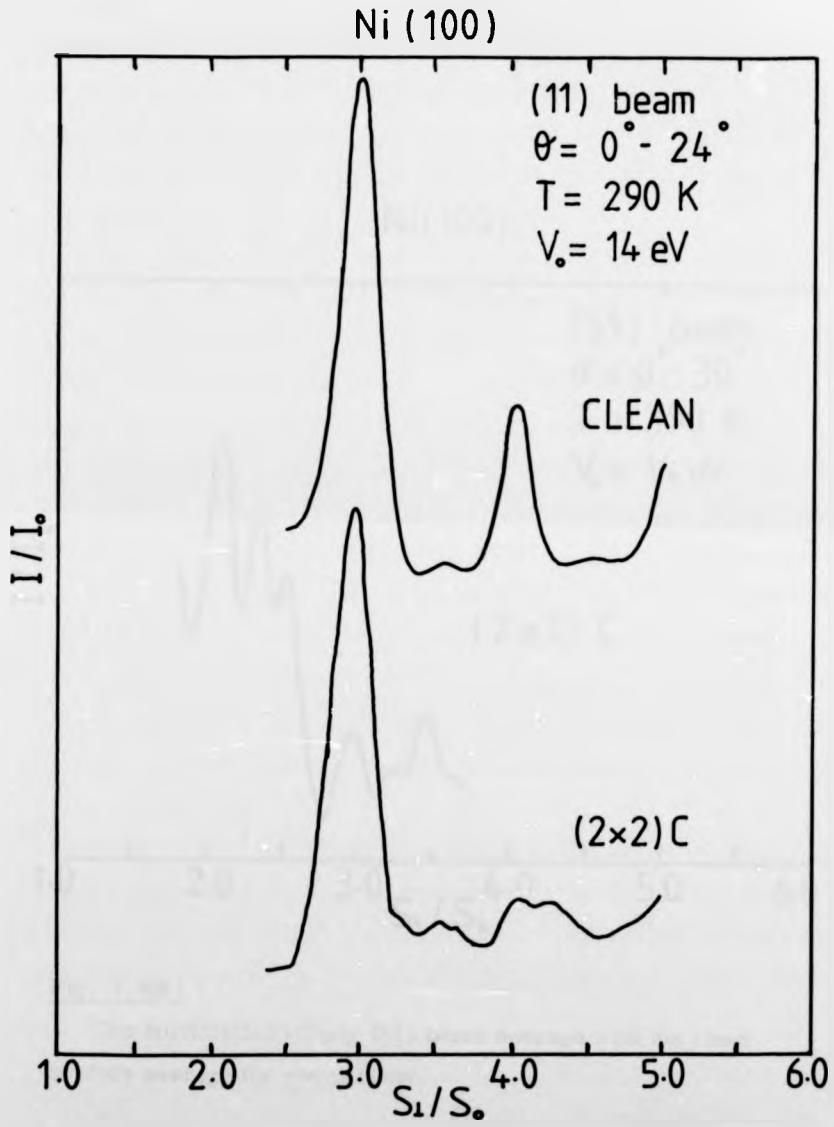

Fig. 7.8(d)

The Ni(100)(2x2)C-p4g (11) beam average with the clean surface average for comparison.

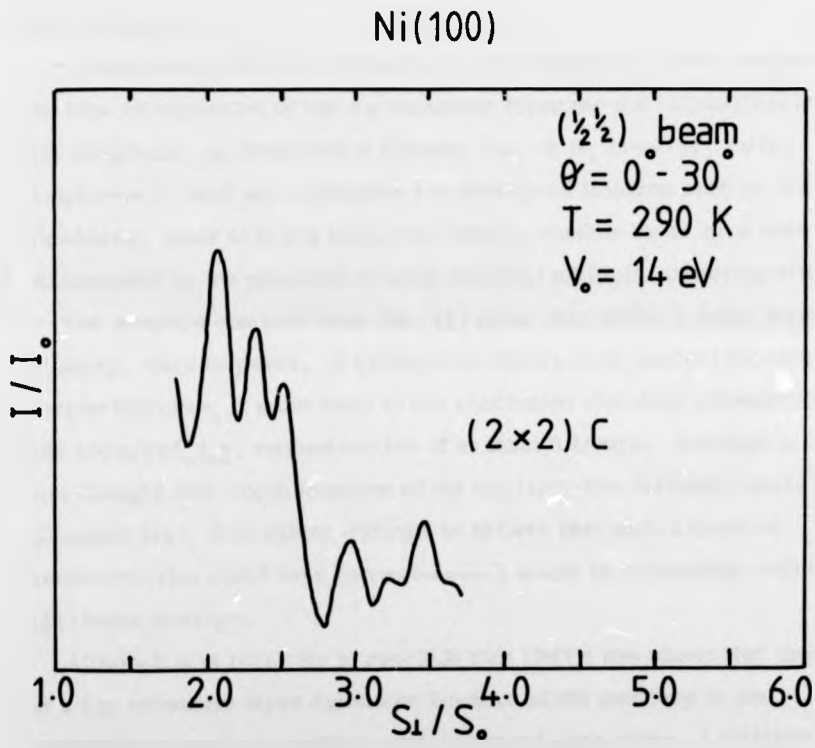

Fig. 7.8(e)

The Ni(100)(2x2)C-p4g ($\frac{1}{2}\frac{1}{2}$) beam average with the clean surface average for comparison.

momentum transfer shoulders on the peaks and a general shift to lower values of S_v/S_o. As has been pointed out by White and Woodruff (10), this effect is, in principle, exaggerated at high values of S_v/S_o, in reality, decreased inelastic scattering and the Debye-Waller factor suppress this sensitivity.

These results could be thought to provide further evidence supporting the idea of expansion of the top substrate layer for the Ni(100)(2x2) C-p4g structure, as described in Chapter Six. It is, however, rather dangerous to base any arguments too heavily on features such as low shoulders, since it is not known for certain whether these have been accentuated by the presence of weak residual multiple scattering effects.

The average obtained from the $(\frac{1}{2}\frac{1}{2})$ beam data shows a large number of sharp, narrow peaks. If kinematical theory is to account for these narrow features, it must point to the conclusion that deep reconstruction has occurred, i.e. reconstruction of at least 5 layers. Although it is now thought that reconstruction of the top layer has definitely occurred (Chapter Six), it is rather difficult to believe that such a depth of reconstruction could have happened which would be compatible with the $(\frac{1}{2}\frac{1}{2})$ beam average.

Although it is tempting to conclude that CMTA has shown that there is a top substrate layer expansion because of the tendency to low momentum transfer shoulders and downward peak shifts, a reliable quantification can really only be made by full dynamical calculations.

7.3.3 The clean Ni(110) surface

(a) Room temperature .- Specular beam data were collected for nine azimuths from the clean, room temperature (110) surface. These azimuths ranged from $\varphi = 90^o$ to $\varphi = 10^o$ in 10^o steps, each azimuth supplying spectra for the angle of incidence varying in 2^o steps from 0^o to 32^o. As for the Ni(100) surface, individual spectra will not be presented here, and only the average for each azimuth is shown (Fig. 7.9). It will be seen that in addition to the peaks at $S_v/S_o = 2$ and 3, a peak of comparable intensity is apparent near 2.5 and a small peak at ~ 3.5.

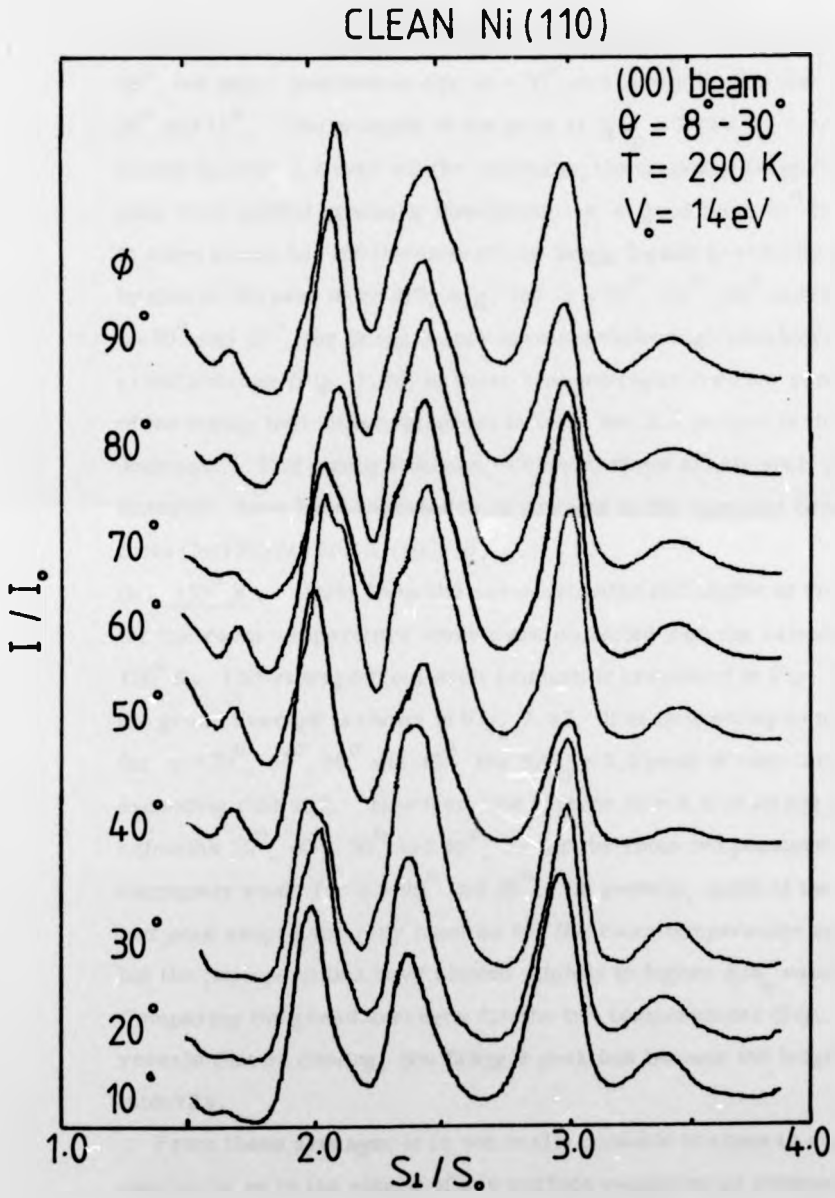

Fig. 7.9

Specular beam averages for 9 azimuths for the clean Ni(110) surface at room temperature.

A feature at ~ 1.6 is very strong for azimuths 90^{o}, 80^{o}, 60^{o}, 50^{o} and 40^{o}, but much less intense for $\varphi = 70^{o}$ and barely visible for $\varphi = 30^{o}$, 20^{o} and 10^{o}. The position of the peak at $S/S_{o} = 2$ (for $V_{o} = 14$ eV) varies by only 0.2 over all the azimuths, the tendency being for this peak to be shifted gradually downwards as φ goes from 90^{o} to 10^{o}. In some azimuths, the intensity of the Bragg 2 peak is actually exceeded by that of the peak near 2.5, e.g. for $\varphi = 70^{o}$, 60^{o}, 50^{o} and 30^{o}. For $\varphi = 50^{o}$ and 30^{o}, the Bragg 2 peak shows definite high shoulders. The grand average (Fig. 7.10) of these nine averages does not remove any of the strong half-order features; in fact, the 2.5 feature is the most dominant. Half-order features, although of not nearly such great intensity, have been reported to be present in the specular beam average from Cu(100)(4) and Al(100) (6).

(b) 150^{o} K.- Data from the same azimuths and angles of incidence as for the room temperature study were collected with the sample held at 150^{o} K. The average from each azimuth is presented in Fig. 7.11 and the grand average is shown in Fig. 7.12. It is interesting to note that for $\varphi = 70^{o}$, 60^{o}, 50^{o} and 30^{o}, the $S/S_{o} = 2.5$ peak is very large, exceeding that at 2. However, the feature at ~ 1.6 is strong for azimuths 70^{o}, 60^{o}, 50^{o} and 40^{o}, as for the room temperature case, but extremely weak for $\varphi = 90^{o}$ and 80^{o}. In general, most of the shoulders and peak shapes are very much as for the room temperature specimen, but the peak positions have shifted slightly to higher S/S_{o} values. Comparing the grand averages for the two temperatures (Fig. 7.12) reveals that on cooling, the Bragg 2 peak has become the largest in intensity.

From these averages it is not really possible to come to any conclusion as to the nature of any surface expansion or contraction. A surface contraction of 5% relative to the bulk is in no way apparent. It would be thought that data taken at 150^{o} K would show noticeable differences from that obtained at 293^{o} K, since the vibrational amplitude of the surface will have been considerably reduced; this did not prove to be the case. Nevertheless, the clean, 150^{o} K surface averages can be compared with those obtained from the Ni(110)(1x2)H structure.

A feature at ~ 1.6 is very strong for azimuths 90^{o}, 80^{o}, 60^{o}, 50^{o} and 40^{o}, but much less intense for $\varphi = 70^{o}$ and barely visible for $\varphi = 30^{o}$, 20^{o} and 10^{o}. The position of the peak at $S_f/S_o = 2$ (for $V_o = 14$ eV) varies by only 0.2 over all the azimuths, the tendency being for this peak to be shifted gradually downwards as φ goes from 90^{o} to 10^{o}. In some azimuths, the intensity of the Bragg 2 peak is actually exceeded by that of the peak near 2.5, e.g. for $\varphi = 70^{o}$, 60^{o}, 50^{o} and 30^{o}. For $\varphi = 50^{o}$ and 30^{o}, the Bragg 2 peak shows definite high shoulders. The grand average (Fig. 7.10) of these nine averages does not remove any of the strong half-order features; in fact, the 2.5 feature is the most dominant. Half-order features, although of not nearly such great intensity, have been reported to be present in the specular beam average from Cu(100) (4) and Al(100) (6).

(b) 150^{o} K.- Data from the same azimuths and angles of incidence as for the room temperature study were collected with the sample held at 150^{o} K. The average from each azimuth is presented in Fig. 7.11 and the grand average is shown in Fig. 7.12. It is interesting to note that for $\varphi = 70^{o}$, 60^{o}, 50^{o} and 30^{o}, the $S_f/S_o = 2.5$ peak is very large, exceeding that at 2. However, the feature at ~ 1.6 is strong for azimuths 70^{o}, 60^{o}, 50^{o} and 40^{o}, as for the room temperature case, but extremely weak for $\varphi = 90^{o}$ and 80^{o}. In general, most of the shoulders and peak shapes are very much as for the room temperature specimen, but the peak positions have shifted slightly to higher S_f/S_o values. Comparing the grand averages for the two temperatures (Fig. 7.12) reveals that on cooling, the Bragg 2 peak has become the largest in intensity.

From these averages it is not really possible to come to any conclusion as to the nature of any surface expansion or contraction. A surface contraction of 5% relative to the bulk is in no way apparent. It would be thought that data taken at 150^{o} K would show noticeable differences from that obtained at 293^{o} K, since the vibrational amplitude of the surface will have been considerably reduced; this did not prove to be the case. Nevertheless, the clean, 150^{o} K surface averages can be compared with those obtained from the Ni(110)(1x2)H structure.

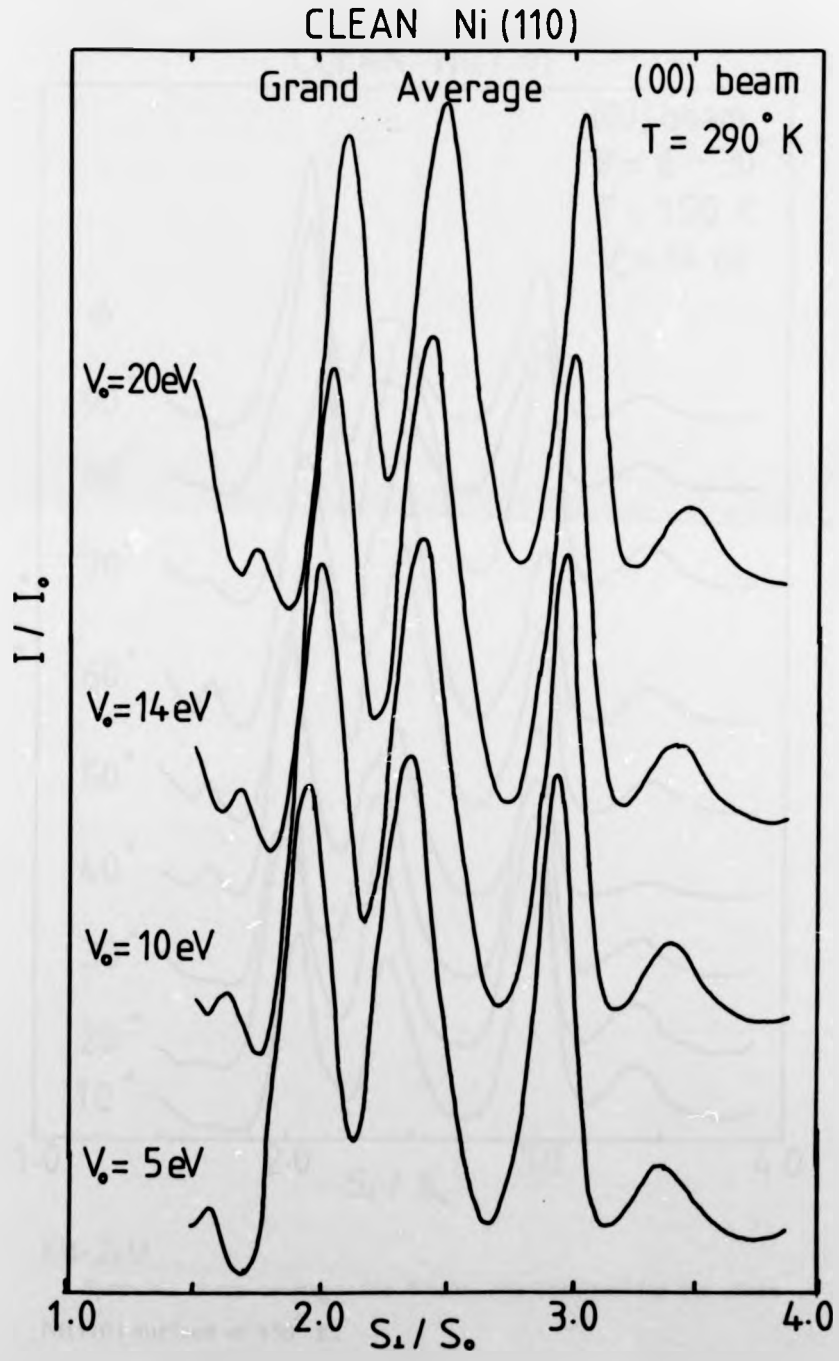

Fig. 7.10

The grand average of the averages obtained from 9 azimuths for room temperature clean Ni(110). The effect of varying the inner potential, V_o, is shown.

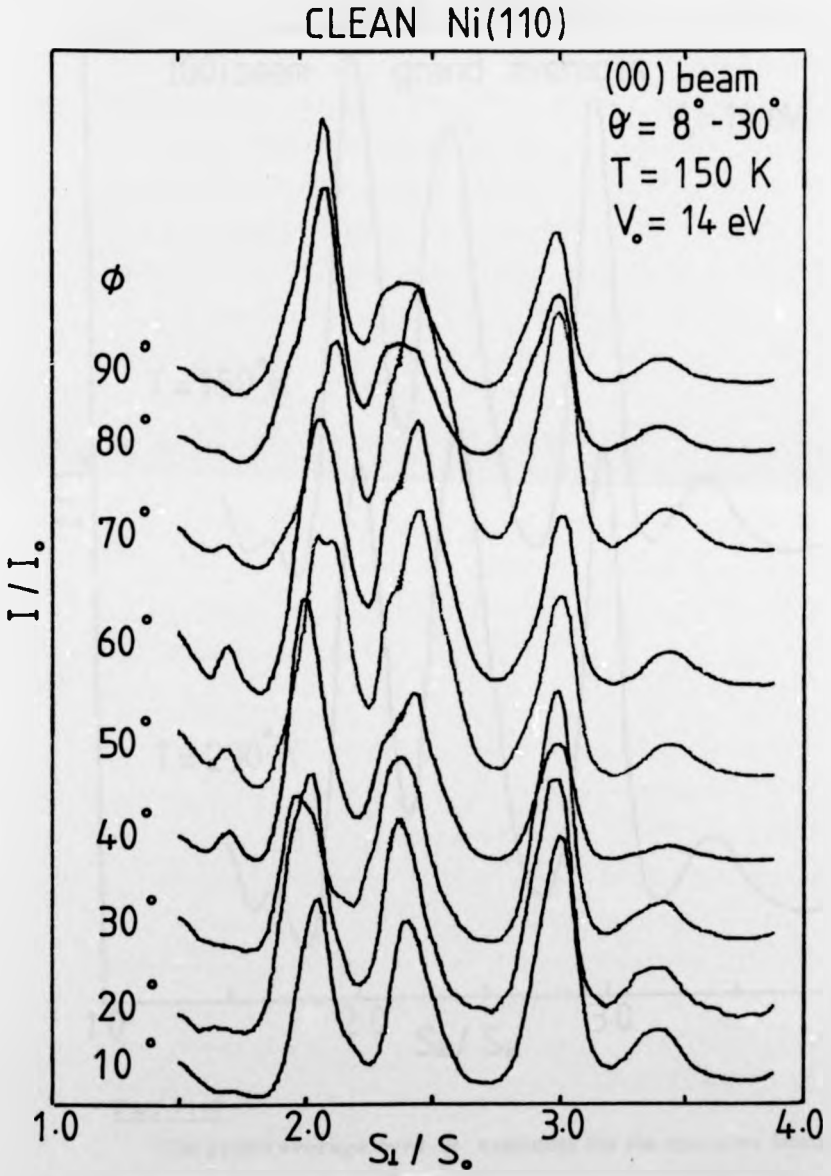

Fig. 7.11

Specular beam averages for 9 azimuths obtained for the clean Ni(110) surface at 150° K.

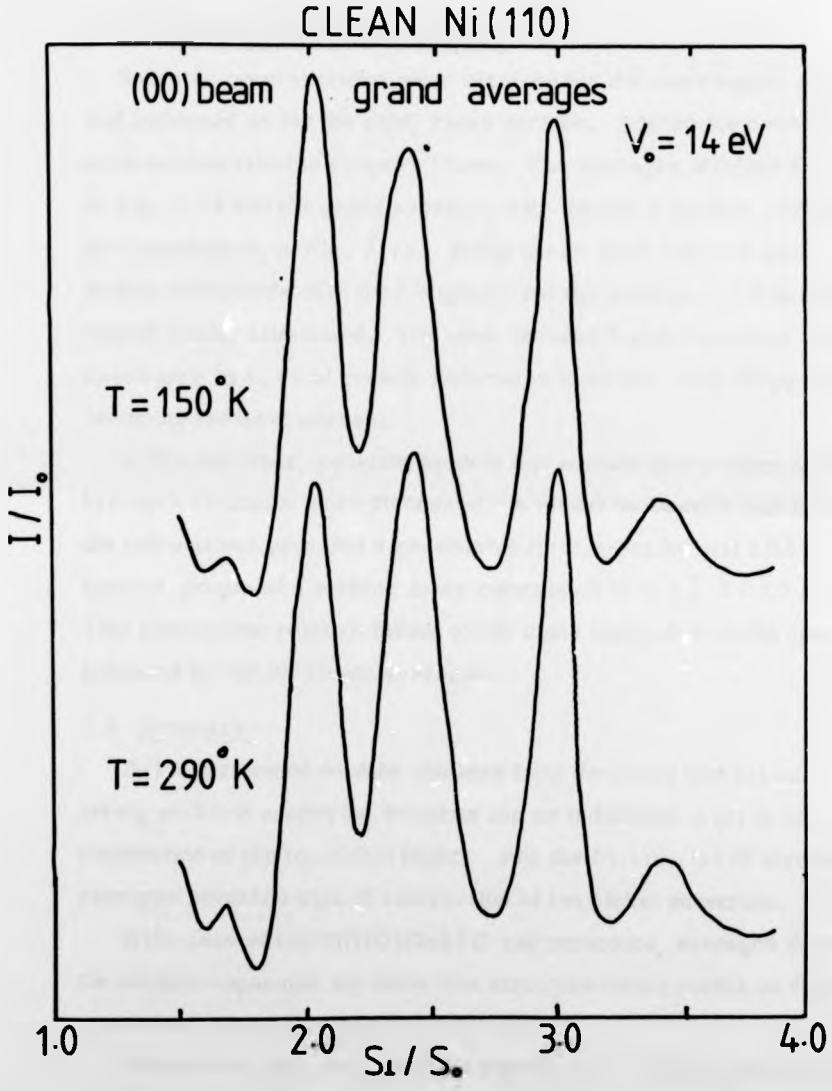

Fig. 7.12

The grand average over 9 azimuths for the specular beam for clean Ni(110) at 150° K with the room temperature grand average for comparison.

7.3.4 The Ni(110)(1x2)H structure

Specular beam averages were obtained for the same angles of azimuth and incidence as for the cold, clean surface. Adsorption conditions were as described in Chapter Three. The averages obtained are shown in Fig. 7.13 and the grand average, with the clean surface average for comparison, in Fig. 7.14. Bragg peaks 2 and 3 will be seen to have shifted downwards only very slightly, but the peak at ~ 1.6 has been almost totally eliminated. The peak between 2 and 3 has been shifted downwards by 0.1 and greatly reduced in intensity, with Bragg peak 3 becoming the most intense.

In Chapter Four, possible models and surface parameters for this hydrogen structure were discussed. A model by Demuth (12) for which the calculations provided a reasonable fit to experimental LEED I-V spectra, proposed a surface layer contraction of 0.1 Å $\pm$ 0.05 ($\sim$ 8%). This contraction relative either to the clean surface or to the bulk is not indicated by the (00) beam averages.

7.4 Summary

CMTA performed on data obtained from the clean Ni(110) surface shows strong multiple scattering features and no indication is given of contraction of the top nickel layer. For the Ni(110)(1x2)H structure, averages reveal no sign of contraction of the nickel substrate.

In the case of the Ni(100)(2x2) C-p4g structure, averages do support the surface expansion but show fine structure which cannot be explained in terms of single scattering processes.

For the two adsorbate systems studied here, CMTA analysis appears to be only partially consistent with the structures proposed by full dynamical calculations.

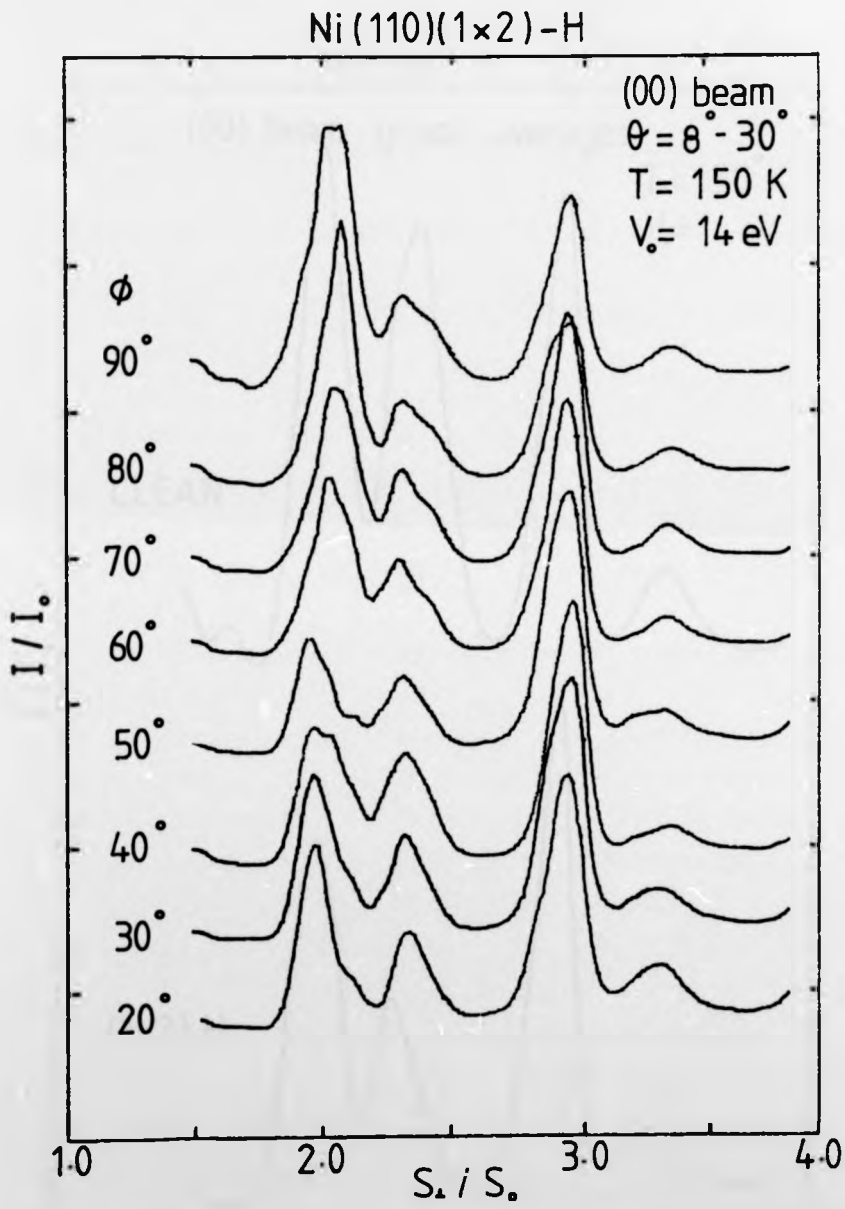

Fig. 7.13

Specular beam averages for 8 azimuths obtained for the Ni(110)(1x2)H surface at 150° K

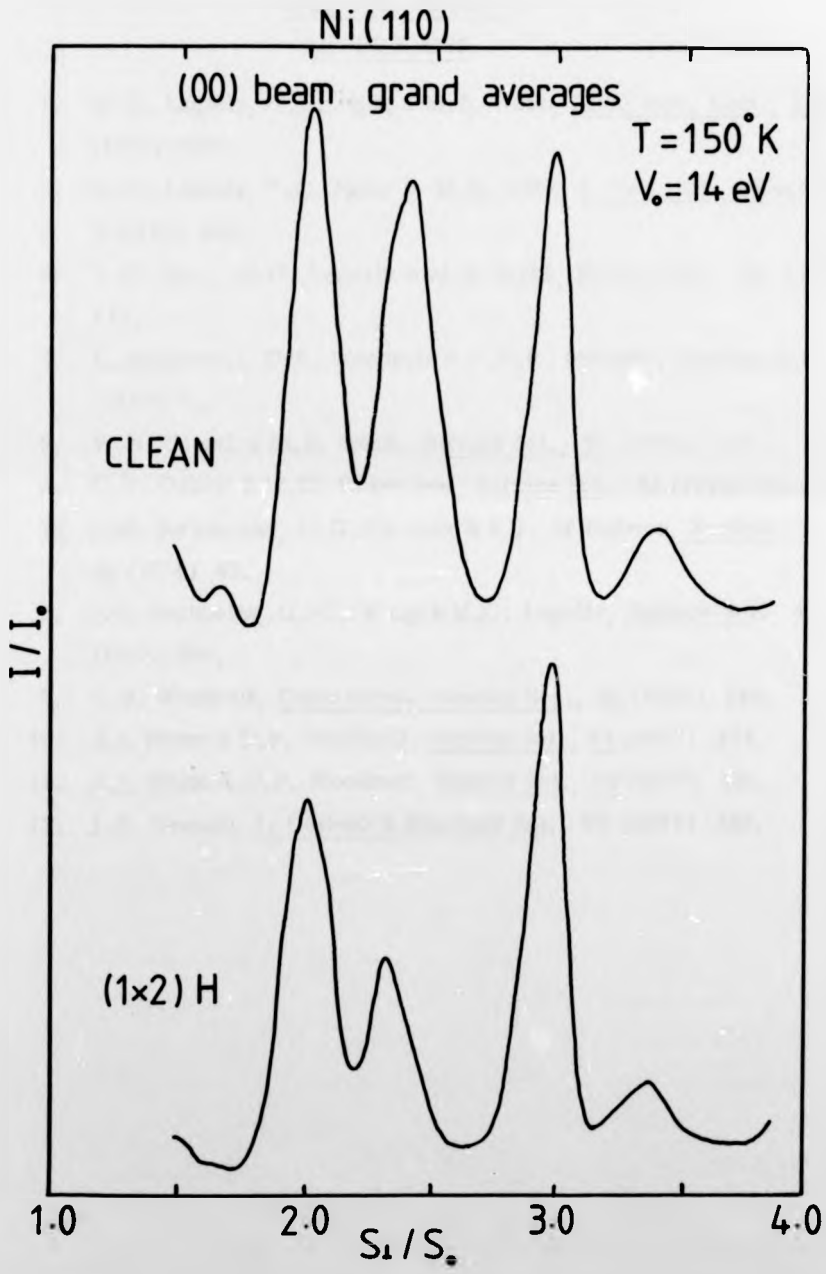

Fig. 7.14

The specular beam grand average for 8 azimuths obtained for the Ni(110)(1x2)H surface at 150° K with the cold, clean surface grand average for comparison.

CHAPTER SEVEN

REFERENCES

1. M.G. Lagally, T.C. Ngoc & M.B. Webb, Phys. Rev. Lett., 26 (1971) 1557.
2. M.G. Lagally, T.C. Ngoc & M.B. Webb, J. Vac. Sci. & Technol., 9 (1972) 645.
3. T.C. Ngoc, M.G. Lagally & M.B. Webb, Surface Sci., 35 (1973) 117.
4. L. McDonnell, D.P. Woodruff & K.A.R. Mitchell, Surface Sci., 45 (1974) 1.
5. W.N. Unertl & M.B. Webb, Surface Sci., 59 (1976) 373.
6. D.T. Quinto & W.D. Robertson, Surface Sci., 34 (1973) 501.
7. J.M. Burkstrand, G.G.Kleiman & F.J. Arlinghaus, Surface Sci., 46 (1974) 43.
8. J.C. Buchholtz, G.-C. Wang & M.G. Lagally, Surface Sci., 49 (1975) 508.
9. D.P. Woodruff, Discussions Faraday Soc., 60 (1976) 218.
10. S.J. White & D.P. Woodruff, Surface Sci., 63 (1977) 254.
11. S.J. White & D.P. Woodruff, Surface Sci., 64 (1977) 131.
12. J.E. Demuth, J. Colloid & Interface Sci., 58 (1977) 184.

CHAPTER EIGHT

SUMMARY

Extensive sets of I-V data have been obtained for the clean Ni(110) and Ni(100) surfaces and are found to compare very favourably with the more limited data previously available.

The effects of adsorption conditions, i.e. the presence of the electron beam, hot filaments and exposure pressures, have been a necessary subject of investigation in order to be certain of obtaining consistently reproducible I-V spectra for the various adsorption systems studied.

The nickel-hydrogen system (both the (100) and (110) surfaces) was found to be extremely prone to electron stimulated desorption by the electron beam and in order to obtain an I-V profile identical to that obtained immediately after hydrogen exposure, hydrogen had to be pumped continually through the experimental chamber during the data collection. In the case of the Ni(110)(1x2)H structure at 150° K, it can be concluded that hydrogen adsorbs atomically, since, in the absence of the electron beam and all hot filaments, no extra features have appeared when the diffraction pattern is examined, even after long exposures to hydrogen.

The Ni(110)(1x2)H surface was studied and an extensive set of I-V spectra obtained. Comparison of these data with the normal incidence data previously available showed good agreement for most beams. A model involving the pairwise distortion of rows of nickel atoms is thought to be the most likely model on comparison of experimental data with the theoretical spectra obtained elsewhere. However, since a larger amount of data are now available, it is intended to investigate this system more thoroughly theoretically.

Ethylene was not observed to form any structure on the Ni(110) surface at either 150° K or 290° K. On exposure of the hot (600° K) surface to ethylene, a (4 x 5) structure was formed, characteristic of a carbon overlayer. This is similar to the results obtained by other workers adsorbing methane on a hot Ni(110) surface, and is believed to be associated with a carbon structure.

Adsorption of ethylene on a 150° K Ni(100) surface gave rise initially to a very diffuse ($\sqrt{2} \times \sqrt{2}$) R 45° pattern which gradually grew slightly sharper on exposure to the electron beam or on warming to room temperature. Acquisition of I-V spectra from this surface was difficult in view of the diffuseness of the beams. However, the very limited data taken reveals a marked similarity between clean surface data and those obtained from the surface after exposure to 40 L ethylene at 150° K. Similarly, on warming to 290° K with the electron beam on, data are more like those obtained from the Ni(100)(2x2)C-p4g surface.

When the Ni(100) surface was exposed to ethylene whilst hot, (cooling from 600° K), the Ni(100)(2x2)C-p4g structure was formed. This was characterized by the systematic absence of some half integer beams in certain geometrical conditions. The implications of this symmetry, with its condition of requiring two perpendicular glide planes, have led to the postulation of a model which incorporates both a horizontal and a vertical distortion of the top layer of nickel atoms. Extensive sets of I-V spectra have been acquired and compared with those obtained from full dynamical calculations for a large number of distortions and for various carbon positions. The model which provides very encouraging agreement between theory and experiment is that involving a 0.43 Å horizontal, 0.15 Å vertical distortion of the nickel top layer atoms, with the $\frac{1}{2}$ monolayer of carbon atoms sitting in 4-fold sites, 0.1 Å above the nickel atoms. A modification of the distortion would be more acceptable on "billiard-ball" model considerations and may well give slightly better agreement for spectra; this work is continuing at present.

Constant Momentum Transfer Averaging of I-V data was performed for both of the clean surfaces and for the Ni(100)(2x2)C-p4g and Ni(110)(1x2)H surfaces. The averages obtained for the clean Ni(100) surfaces were very kinematical and compare well with previous work. The clean Ni(110) averages reveal no signs of features which would indicate the proposed 5% surface layer contraction; the Ni(110)(1x2)H surface

Adsorption of ethylene on a 150° K Ni(100) surface gave rise initially to a very diffuse ($\sqrt{2} \times \sqrt{2}$) R 45° pattern which gradually grew slightly sharper on exposure to the electron beam or on warming to room temperature. Acquisition of I-V spectra from this surface was difficult in view of the diffuseness of the beams. However, the very limited data taken reveals a marked similarity between clean surface data and those obtained from the surface after exposure to 40 L ethylene at 150° K. Similarly, on warming to 290° K with the electron beam on, data are more like those obtained from the Ni(100)(2x2)C-p4g surface.

When the Ni(100) surface was exposed to ethylene whilst hot, (cooling from 600° K), the Ni(100)(2x2)C-p4g structure was formed. This was characterized by the systematic absence of some half integer beams in certain geometrical conditions. The implications of this symmetry, with its condition of requiring two perpendicular glide planes, have led to the postulation of a model which incorporates both a horizontal and a vertical distortion of the top layer of nickel atoms. Extensive sets of I-V spectra have been acquired and compared with those obtained from full dynamical calculations for a large number of distortions and for various carbon positions. The model which provides very encouraging agreement between theory and experiment is that involving a 0.43 Å horizontal, 0.15 Å vertical distortion of the nickel top layer atoms, with the $\frac{1}{2}$ monolayer of carbon atoms sitting in 4-fold sites, 0.1 Å above the nickel atoms. A modification of the distortion would be more acceptable on "billiard-ball" model considerations and may well give slightly better agreement for spectra; this work is continuing at present.

Constant Momentum Transfer Averaging of I-V data was performed for both of the clean surfaces and for the Ni(100)(2x2)C-p4g and Ni(110)(1x2)H surfaces. The averages obtained for the clean Ni(100) surfaces were very kinematical and compare well with previous work. The clean Ni(110) averages reveal no signs of features which would indicate the proposed 5% surface layer contraction; the Ni(110)(1x2)H surface

averages do not indicate the $8\frac{1}{2}\%$ contraction postulated by dynamical theory. Averages obtained from the Ni(100)(2x2)C-p4g surface do contain features indicative of expansion of the surface layer but peak shapes and features are present which cannot be explained by purely kinematical considerations. These results do not give a favourable impression of the future potential of CMTA for use in the area where it was thought most promising, i.e. substrate layer expansion and contraction.

From the qualitative adsorption studies, it is clear that adsorption conditions and beam effects are very important areas for consideration. Obvious refinements in experimental techniques must be to use lower incident beam currents and acquire I-V data more rapidly. This would be of obvious benefit in the case of detailed hydrocarbon adsorption studies. The present work has provided a basis for such a study for nickel, both in characterizing adsorption conditions and in obtaining an insight into the Ni(100)-carbon structure.

APPENDIX I

AUGER ELECTRON SPECTROSCOPY (AES)

The Auger process occurs after an atomic level has been ionized by incident photons or electrons (1). It involves three energy levels (Fig. AI.1(a)): energy level E_W is ionized, an electron from level E_Y fills the hole and a second electron escapes into the vacuum with the remaining kinetic energy E given by

$$E \simeq E_W - E_Y - E_X \qquad [1]$$

These three levels are characteristic of the atom and are known from X-ray work. The Auger electrons do not possess exactly this energy since the atoms involved are not free and ionized levels are involved, but the initial and final states are sufficiently close in energy to make this a reasonable approximation (2).

At high primary energies, the beam is less effective at ionization (Fig. AI.1(c)) but more secondary electrons capable of ionizing are created.

Another process which can occur is the emission of X-rays (Fig. AI.1(b)).

For $E_I < 500$ eV the Auger process is much stronger;

for $E_I \simeq 2000$ eV the two processes are comparable

where E_I is the ionization energy.

So for elements of low atomic number, the Auger process dominates. Typically

$$I \sim 10^{-5} I$$

Auger current yield — primary current

The collected electron current can be written in a Taylor series in modulation $\Delta E = k \sin \omega t$

where k is the modulation amplitude and

ω is the angular frequency.

$$I(E + \Delta E) = I(E) + I'(E)\,\Delta E + \frac{I''(E)}{2!}\Delta E^2 + \frac{I'''(E)}{3!}\Delta E^3 + \ldots\ldots$$

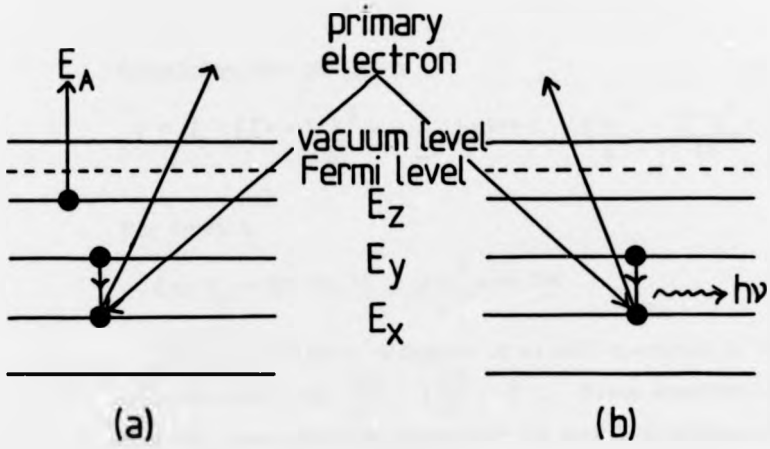

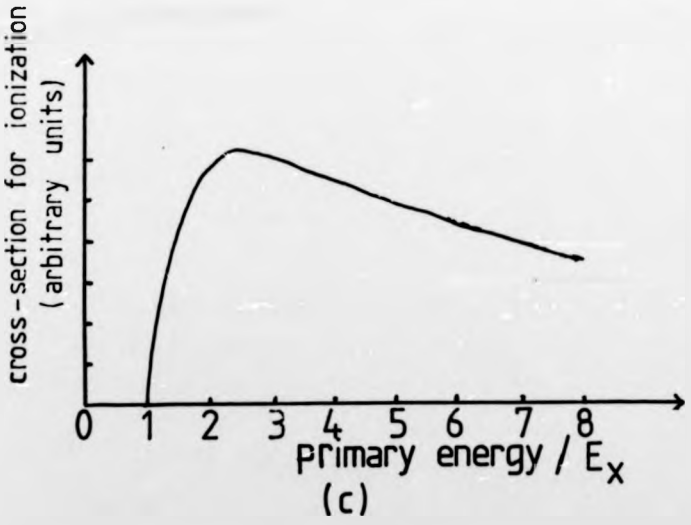

Fig. AI.1

(a) The Auger process

(b) X-ray emission

(c) variation of ionization cross-section with primary beam energy

Substituting for ΔE gives

$$I = I_o + [I'k + \frac{I'''k^3}{8} + ...] \sin \omega t - [\frac{I''k^2}{4} + \frac{I''''k^4}{48} + ...] \cos 2\omega t \text{ etc.}$$

For small k

$$I \simeq I_o + I'k \sin \omega t - \frac{I''k^2}{4} \cos 2\omega t \qquad [2]$$

The standard form of display of an AES spectrum is the double differentiated form $\frac{dN}{dE}$. ($\frac{dN}{dE} \propto I''$). From equation [2] it can be seen that the modulation amplitude must be small, otherwise the small k approximation breaks down. In practice, the amplitude of the modulation must be smaller than the width of the narrowest feature, otherwise it will not be resolved.

APPENDIX II

KINEMATIC CALCULATION OF PEAK POSITIONS AND BEAM ENERGIES

The Bragg Condition

$$(\underline{k} - \underline{k}') \cdot \underline{d} = 2\pi n$$

where $\underline{k}$ and $\underline{k}'$ are the incident and diffracted wavevectors respectively, $\underline{d}$ is the displacement from one plane to the next and n is an integer can be rewritten as

$$-\underline{g} \cdot \underline{d} + (\underline{k}_\perp - \underline{k}'_\perp)\, \underline{d}_\perp = 2\pi n$$

since by conservation of momentum $\underline{k}'_\parallel = \underline{k}_\parallel + \underline{g}$

where $\underline{k}_\parallel$ is the wavevector parallel to the surface and

$\underline{k}_\perp$ is the perpendicular component of the wavevector

The dashed notation represents the diffracted wavevector.

The reciprocal net vector $\underline{g} = h\underline{a}^* + l\underline{b}^*$

where $$\underline{a}^* = \frac{2\pi\, \underline{b} \wedge \underline{n}}{\underline{a} \cdot \underline{b} \wedge \underline{n}}$$

and $$\underline{b}^* = \frac{2\pi\, \underline{a} \wedge \underline{n}}{\underline{a} \cdot \underline{b} \wedge \underline{n}}$$

$\underline{n}$ is a unit surface normal and h and l are integers. $\underline{a}$ and $\underline{b}$ are two vectors describing the real surface unit mesh. Hence

$$\underline{a}^* \cdot \underline{a} = 2\pi \qquad \underline{a}^* \cdot \underline{b} = 0$$

and

$$\underline{b}^* \cdot \underline{b} = 2\pi \qquad \underline{b}^* \cdot \underline{a} = 0$$

Defining

$\underline{d}_\parallel = \alpha\underline{a} + \beta\underline{b}$, where α and β are half integers,

$$\underline{g} \cdot \underline{d} = 2\pi(\alpha h + \beta l)$$

This leads to the Bragg Condition

$$(\underline{k}_\perp - \underline{k}'_\perp)\underline{d}_\perp - 2\pi(\alpha h + \beta l) = 2\pi n \qquad [1]$$

By conservation of energy,

$$k^2 = k'^2 \quad \underline{i.e.} \quad k_\parallel^2 + k_\perp^2 = k'^2_\parallel + k'^2_\perp$$

$$k_\perp^2 - 2\underline{k}_\parallel \cdot \underline{g} - g^2 = k'^2_\perp$$

then

$$k^2 \cos^2\theta - 2kg \sin\theta \cos\theta_g - g^2 = k_\perp'^2 \qquad [2]$$

where θ_g is the angle between $\underline{g}$ and $\underline{k}_\parallel$

and θ is the internal angle of incidence.

The Bragg Condition now becomes

$$(k\cos\theta - [k^2\cos^2\theta - 2kg\sin\theta\cos\theta_g - g^2]^{\frac{1}{2}})\underline{d}_\perp - 2\pi(\alpha h + \beta l) = 2\pi n \qquad [3]$$

Therefore, if the angle of incidence, θ, is known, this equation can be solved for $\underline{k}$ and hence the position of the Bragg peaks can be found.

If the wave vector outside the surface is $\underline{p}$ and inside the surface is $\underline{k}$

(i) $\underline{p}_\parallel = \underline{k}_\parallel$ or $p \sin\theta' = k \sin\theta$

$$\therefore k\sin\theta = (\frac{2mE}{\hbar^2})^{\frac{1}{2}} \sin\theta'$$

(ii) $p^2\sin^2\theta' = k^2\sin^2\theta$

or $k\cos\theta = [k^2 - p^2 + p^2\cos^2\theta']^{\frac{1}{2}}$

$$\underline{\text{i.e.}}\ k\cos\theta = [\frac{2mV_o}{\hbar^2} + (\frac{2mE}{\hbar^2})\cos^2\theta']^{\frac{1}{2}} \qquad [4]$$

Substituting [4] into [3] gives the Bragg Condition as a function of the external energy and angle of incidence θ'.

It can be seen that for emergence

$$k_\perp'^2 = 0$$

must be substituted into equation [2], but the beam will still not emerge immediately because of total internal reflection at the potential step at the surface.

Since $k\sin\theta = p\sin\theta'$

$$k\sin\theta \leq p$$

$$\sin\theta \lesssim \frac{p}{k} = (\frac{E}{E+V_o})^{\frac{1}{2}}$$

So the emergence condition must be obtained by the substitution of

$$k_{\perp}'^2 = \frac{2mV_o}{\hbar^2} \quad \text{into equation} \quad [2]$$

This simple condition locates very approximately the positions of Bragg peaks, but examination of an experimental spectrum will quickly reveal many features, often of equal or even greater intensity, located at positions not predicted by simple Bragg theory.

APPENDIX III

SYMMETRY CONSIDERATIONS APPLIED TO LEED

The symmetry of a particular diffraction pattern can limit the number of possible surface structures. The way in which this can be concluded is described for the case of the Ni(100)(2x2)C - p4g structure.

By choosing the proper initial and final states, the matrix elements of the operator T give a complete description of a LEED experiment, so that

$$\psi_f = T \psi_i$$

The amplitude of any diffracted wave with wave vector $\underline{k}'$ is obtained from

$$< \underline{k}' \mid T \mid \underline{k} >$$

If the surface structure is invariant under a symmetry operator S, then the T matrix is also invariant so that

$$S^{-1} T S = T$$

and hence

$$< \underline{k}' \mid T \mid \underline{k} > = < S\underline{k}' \mid T \mid S\underline{k} > \qquad [1]$$

This treatment has been discussed with regard to symmetry properties of surfaces by Holland and Woodruff (3). While the basic translational and rotational symmetries and their effects are well known, the use of the glide symmetry operator has particularly interesting consequences.

A glide operation consists of a reflection across a line and a translation of half the repeat distance along the line. In the case of the translation, S can be written as

$$S \mid \underline{k} > = e^{i \frac{1}{2} \underline{k} \cdot \underline{a}} \mid \underline{k} >$$

where $\underline{a}$ is the net vector.

The glide operation is then written

$$S \mid \underline{k} > = e^{i \frac{1}{2} \underline{k} \cdot \underline{a}} \mid R_f \underline{k} > \qquad [2]$$

where R_f is the reflection operator.

From equations [1] and [2]

$$\langle S\underline{k}' \mid T \mid S\underline{k} \rangle = e^{i\frac{1}{2}(\underline{k}-\underline{k}').\underline{a}} \langle R_f\underline{k}' \mid T \mid R_f\underline{k} \rangle = \langle \underline{k}' \mid T \mid \underline{k} \rangle$$

If the projection of $\underline{k}$, i.e. $\underline{k}_{\parallel}$, lies in the direction of a glide line

$$R_f \mid \underline{k} \rangle = \mid \underline{k} \rangle$$

and if $\underline{k}'$ lies in the glide direction

$$R_f \mid \underline{k}' \rangle = \mid \underline{k}' \rangle$$

Hence either

$$\langle \underline{k}' \mid T \mid \underline{k} \rangle = 0$$

or $$e^{i\frac{1}{2}(\underline{k}-\underline{k}').\underline{a}} = 1$$

whereby $\frac{1}{2}(\underline{k}-\underline{k}').\underline{a} = 2\pi, 4\pi, \ldots\ldots$

But from translational symmetry

$$(\underline{k} - \underline{k}').\underline{a} = 2\pi n$$

so that for odd integer values of n, $\langle \underline{k}' \mid T \mid \underline{k} \rangle$ must vanish.

Therefore odd-order beams along glide directions will be missing (see Chapter Six, Plate 6.2).

APPENDICES

REFERENCES

1. C.C. Chang, Surface Sci., 25 (1971) 53.

2. W.A. Coghlan & R.E. Clausing, A Catalogue of Calculated Auger Transitions for the Elements, Oak Ridge National Laboratory (1971).

3. B.W. Holland & D.P. Woodruff, Surface Sci., 36 (1973) 488.

APPENDICES

REFERENCES

1. C.C. Chang, Surface Sci., 25 (1971) 53.

2. W.A. Coghlan & R.E. Clausing, A Catalogue of Calculated Auger Transitions for the Elements, Oak Ridge National Laboratory (1971).

3. B.W. Holland & D.P. Woodruff, Surface Sci., 36 (1973) 488.